2011

Synthesis and Characterization of Highly Porous Borazine-Linked Polymers via Dehydrogenation/Dehydrocoupling of Borane-Amine Adducts and Their Applications to Gas Storage

Karl Jackson
Virginia Commonwealth University

Synthesis and Characterization of Highly Porous Borazine-Linked Polymers via Dehydrogenation/Dehydrocoupling of Borane-Amine Adducts and Their Applications to Gas Storage

A dissertation submitted in partial fulfillment of the requirements for the degree of Doctor of Philosophy at Virginia Commonwealth University

By
Karl Thomas Jackson
B.S. at Virginia State University, 2006

Director: Dr. Hani M. El-Kaderi
Assistant Professor, Department of Chemistry

Virginia Commonwealth University
Richmond, Virginia
December, 2011

Acknowledgment

I would first like to give glory and honor to God for His many blessing throughout my life. I was able to have confidence throughout my graduate studies, not because of my own intelligence and capabilities, but because of the promise that I can do all things through Christ who strengthens me (Phil 4:13). I am especially thankful to my parents, James and Brenda Jackson, for raising me to be the man that I am today as well as my brothers Kevin and Keith Jackson for their companionship and moral support. I would like to give a special acknowledgement to my advisor Dr. Hani El-Kaderi, who has graciously and enthusiastically taught me so much over the past four years. His patience and individualized attention have been very instrumental to my successes in the laboratory. I would like to thank my committee members, Dr. Maryanne Collinson, Dr. Everett Carpenter and Dr. Puru Jena for their support and willingness to assist whenever needed. I'd like to thank all of the current and past members of Dr. El-Kaderi's research group for their encouragement and support. I am grateful to all of my teachers and professors throughout my education, particularly Dr. Ralph Gatrone and Dr. Colleen Taylor at Virginia State University for their great influence on my decision to further my education. To all of my friends and family from Petersburg, VA and to my church family at Good News Baptist Church I am forever thankful for their prayers and encouragement.

Table of Contents

List of Tables

List of Figures

Abstract

SYNTHESIS AND CHARACTERIZATION OF HIGHLY POROUS BORAZINE-LINKED POLYMERS

Karl T. Jackson, Ph.D.

A dissertation submitted in partial fulfillment of the requirements for the degree of Doctor of Philosophy at Virginia Commonwealth University.

Virginia Commonwealth University, 2011.

Major Director: Dr. Hani M. El-Kaderi, Assistant Professor Department of Chemistry

A new class of porous polymers has been designed and successfully synthesized by thermal dehydrogenation of several polytopic arylamine-borane adducts and has been designated Borazine-Linked Polymers (BLPs). The polymers reported are constructed of linear, triangular, and tetrahedral amine building units to form 2D and 3D frameworks. The boron sites of the pores are aligned with hydrogen atoms contrasted with the recently reported halogenated BLPs which consist of pore channels aligned with bromine or chlorine atoms. One of the reported BLPs, BLP-2(H), was proven to be crystalline by PXRD, matching the experimental pattern to theoretical patterns calculated from modeled structures. BLPs were found to be thermally stable by thermogravimetric analysis, decomposing at temperatures ~450 ºC. Infrared spectroscopy and ^{11}B MAS NMR spectra confirm the formation of borazine as reported in previous borazine-containing polymers and ^{13}C CP MAS spectra confirmed that the structural integrity of the amine building units were maintained and incorporated in the framework of BLPs. Nitrogen isotherms revealed that BLPs exhibit high surface areas ranging from 1132-2866 m^2/g (Langmuir) and 400-

2200 m^2/g (Brunauer-Emett-Teller, BET) with pore sizes from 7-14 Å. Hydrogen, methane, and carbon dioxide measurements were performed at low pressure (up to 1 atm) and were found to be among the best of organic polymers. High pressure isotherms (up to 40 bar) were also taken at various temperatures ranging from 77-298 K. Isosteric heats of adsorption were calculated using the virial method at low pressures. Gas storage performance of BLPs at 40 bar were found to be: 14.7-42.5 mg/g for H_2 uptake at 77 K; 348.9-717.4 mg/g for CO_2 uptake at 298 K; and 40.8-116.1 mg/g for CH_4 uptake at 298 K. The CO_2/CH_4 selectivity of BLPs at 298 K up to 40 bar was calculated using the Ideal Adsorbed Solution Theory (IAST) to determine their performance as carbon capture and sequestration materials. Additionally, non-borazine containing nanoporous organic polymers (NPOFs) consisting of all carbon and hydrogen atoms were also synthesized and subjected to low pressure hydrogen storage measurements. The results show that though NPOFs generally exhibit higher surface areas (SA_{Lang} = 2423-4227 m^2/g), the H_2 storage capacity of BLPs is superior.

Chapter 1: Introduction

Research in the field of porous polymers has grown exponentially over the last decade due to a recognized necessity to develop novel approaches to the synthesis of materials for various applications.[1] Increased attention has been focused specifically on the development of covalently-linked, purely organic materials, which have potential to outclass the established porous materials such as zeolites and metal organic frameworks (MOFs) in applications including gas storage and separation,[2-6] catalysis,[7-13] electronics,[14,15] and chemical sensing.[16-20] In a recent review, these materials have been described as "energy polymers," because of their potential to enable new energy systems, including production, storage, delivery, and preservation of energy.[14] While relevant and highly popular, the field is still in a relatively underdeveloped phase and there is much more to be explored in order to fully exploit the potential benefits. For instance, examples of catalysis in organic polymers are scarce and currently consist of a narrow range of polymers. Until recent years, the process of developing new tailored porous materials has been tedious in that much of the progress that has been made thus far has been through unsystematic high-throughput processing of parameters rather than through understanding of the chemical and physical mechanisms that influence the properties.[21] Gas storage and separation have been the most thoroughly and commonly explored applications in the field of organic polymers, yet there is much more room for improvement in this regard, as well. Hydrogen storage has been rigorously investigated over the past few decades because increased storage efficiency is a key requirement in the successful transition to a long sought-

after alternative energy system free of carbon-based fuels. This proposed method of deriving the energy needs of society by using hydrogen is referred to as the "Hydrogen Economy" and the development of the ideal porous polymers can be essential to its emergence.

1.1 The Hydrogen Economy

Due to a growing energy dependence around the world and inevitable technological advancements in growing and developed countries, the demand for fossil fuels is constantly increasing. Unfortunately, great drawbacks come along with this increase in fossil fuel consumption. For one, there is a devastating cost to the environment around us. The negative effect of the carbon emissions that are produced from the burning of fossil fuels, on Earth's protective ozone layer has been well-documented over the past several decades.[22] Besides the negative environmental impact, U.S. dependence on fossil fuel forces dealings with countries that produce the fossil fuels, which raises potential for negative geopolitical repercussions. Thirdly, fossil fuels take millions of years to produce, the sources of which are being rapidly depleted. For these reasons and others, there has been great interest in discovering alternative fuel. Renewable energy sources are greatly preferred because of their abundance and their minimal negative environmental impact. Among the most recognized renewable energy sources are wind, solar, hydrothermal, and geothermal, all of which have been thoroughly investigated, but have inherent limitations on consistency and locality. Hydrogen, which acts as energy carrier, has long been recognized as a major candidate for a clean alternative fuel. The great potential for hydrogen as an alternative fuel has been a chief impetus behind the research which will be presented in this dissertation.

The vision of a widespread production and use of hydrogen as an energy carrier has become known as the "Hydrogen Economy." There are several reasons for this vast support

and vigorous push toward this direction among members of the scientific community. First of all, hydrogen is the most abundant element in the universe. Hydrogen's major source on earth is in the form of water, which is inexhaustible. Also, with the use of the hydrogen fuel cell there is zero carbon emissions, which makes it an excellent alternative in terms of environmental pollution. Combined with oxygen, hydrogen "burns" cleanly in fuel cells to generate the desired electric power and water.[23-28] Thus, a successful conversion to hydrogen as a major energy supply could eliminate the problems that currently exist when it comes to carbon emissions, energy independence and depleting resources. With zero negative impact on the environment and accessibility from water it would seem that hydrogen is the ultimate alternative fuel of the future. However, there are several components that must be considered when addressing the issue including production, storage, and fuel cell efficiency, i.e. the conversion of hydrogen to electrical or thermal power, delivery and storage among others.[29]

Hydrogen may be produced directly from renewable sources such as wind, water, or sun; however currently, commercially applied methods are primarily based on fossil raw materials. These processes include natural gas reforming (48%), partial oxidation of refinery residues (30%) and coal gasification (18%).[30] The process of natural gas reforming involves the conversion of natural gas to hydrogen with steam (steam reforming), oxygen (partial oxidation) or both in a sequence (autothermal reforming)[31] and is not suitable for hydrocarbons heavier than napthalene. Steam reforming, which is the most commonly used method is done by applying heat (800 – 900 °C) and pressure (20 – 40 bar) over a nickel catalyst.[31] Partial oxidation is applied to hydrocarbons ranging from methane to heavy oil and coal. The current use of renewable resources such as wind, hydrothermal and solar to produce hydrogen involves

the generation of electricity needed for electrolysis, i.e. the splitting of water into hydrogen and oxygen by applic-

Figure 1.1. Components of the hydrogen economy according to the U. S. Department of Energy

ation of direct current electricity. There is also research being done on the producing hydrogen by photochemical reactions. Here, a photocatalytic semiconductor with an energy gap so large that electrons are extracted from water absorbs energy-rich photons from solar radiation,[31] resulting in water splitting. Other methods of hydrogen production include the Kvaerner Process, thermochemical methods, biomass gasification and biological hydrogen production.[30,31]

The most important benefits of hydrogen can only be manifested if hydrogen is used in a fuel cell. Recent advances in fuel cell technology have been a primary inspiration behind a more positive outlook on successful transition to a hydrogen economy. There are several types of fuel cells which differ according to the electrolyte, the chemical reaction, and working temperature.[31] Proton-Exchange or Polymer-Electrolyte Membrane (PEM) fuel cells, the most

commonly used, will be used in the description of the principle components of a fuel cell for the sake of brevity. A single cell consists of an anode, where hydrogen molecules are oxidized into protons (H^+); a cathode, where oxygen molecules are reduced into oxide ions (O^{2-}); and an ion-conducting electrolyte which separates the anode and cathode and allows protons to flow through but is impermeable to electrons. As electrons are released from hydrogen at the anode, they are directed to the cathode creating an electric current. The first fuel cell was modeled in 1839 by Sir William Grove where he was successful able to generate electricity from hydrogen and oxygen,[32] i.e. the reverse electrolysis using platinum electrodes and sulfuric acid as the electrolyte. Fuel cells are most promising in the automobile market although targets for cost are far from met. Current costs for PEM fuel cell stacks are around $2000/kW compared to the cost of today's internal combustion engine which is $50-70/kW.[31] Though, there have been over 200 new patent applications for fuel cell technologies each year since 2002,[31] there are still fundamental advances necessary to lower cost in fuel cell materials.

The delivery and storage of hydrogen are among the most critical issues to be solved in order to establish a viable hydrogen economy. In a hydrogen-fueled car, 4-5 kg of H_2 (130-160 kWm) are needed to drive 500 km.[31] At ambient temperature and pressure, 5 kg of H_2 would fill a ball 5 m in diameter. While hydrogen has a relatively high energy per unit mass (142 MJ/kg),[33] its volumetric density is very low (12.7 MJ/m^3)[33] and inefficient. Hence, the efficient on-board storage of hydrogen is a great challenge which inhibits commercialization and widespread use. These limitations are due specifically to the very weak intermolecular interactions among hydrogen molecules. The small quadrupole and low polarizability of hydrogen gas do not provide significant binding through electrostatic, induction or dispersion interactions. Consequently, the van der Waals forces between two hydrogen molecules are

negligible compared with the strength of a hydrogen bond or a chemical bond. Currently, liquid hydrogen, which requires four times the storage space of conventional petroleum-based fuels, is the preferred form of hydrogen. In addition, the low temperature requirements propose difficulties with on-board storage. Hydrogen can also be physically stored in the gas phase; however, high pressure is necessary to achieve sufficient energy densities comparable to gasoline. A 350 bar system which holds approximately 6 wt% H_2 holds more than a 700 bar system (~4.5 wt%) showing that gravimetric capacity does not increase proportionally to pressure at high values.[31] The U.S. Department of Energy has set storage system performance target for 2015 at 5.5 wt% H_2 and 40 g H_2/L;[33] thus the scientific community has begun extensive investigations to develop alternative storage methods. Efforts now are being put forth to study hydrogen storage in systems such as chemical hydrides[34-40], metal hydrides,[41] and porous materials[42-55], however these are still a developing area.

Other essential components necessary for a successful hydrogen economy program include application and technological validation, safety, codes and standards and education according to the "Hydrogen Program," which is the U.S. Department of Energy's plan to usher the U.S into a future hydrogen economy.

1.2 Pore Characterization using Small Gas Adsorption

One promising method for improving hydrogen storage is the confinement of molecular hydrogen to the walls of porous materials such as coordination polymers,[42-47] porous carbon,[48-49] and organic polymers.[3,50-55] Here, the adsorbate, e.g. hydrogen, interacts with the host material, or adsorbent in a manner by which it can easily be released under ambient conditions. The process of adsorption differs from absorption in that the absorption process involves the trapping of a bulk phase absorbate inside relatively large volumes of space of the absorbent

while adsorption requires an interaction between the adsorbate and surface of the adsorbent forming a new chemical species. The amount of adsorbent which can be held and how easily it can be released are dependent on textural properties i.e., size, shape, and volume of the pores, all of which can be determined by conducting gas sorption experiments. This physical adsorption, or physisorption, involves electrostatic interactions between the guest molecules and atoms which make up the pore walls and should be clearly be distinguished from chemical adsorption, or chemisorption, by which the guest molecules are chemically bonded to the host and cannot easily be removed. Besides the information on pore metrics that can be collected, adsorption analysis is the direct method by which we can determine maximum loading of hydrogen, carbon dioxide, methane and many other gases at various temperatures and pressures in a given material. The adsorbed molecules can be removed by decreasing the pressure of the system in a process referred to as desorption.

The amount of gas adsorbed or desorbed as a function of relative pressure, P/P_o, is known as the adsorption or desorption isotherm. An isotherm is a sorption measurement in which the temperature remains constant for the entire experiment while the pressure is varied. Relative pressure is the ratio of absolute pressure, P, to the saturation pressure, P_o, which is the vapor pressure of a pure liquid (around 1 bar in the case of nitrogen or argon). Textural properties of microporous solids can be determined by analysis of their isotherm. In 1940, Brunauer, Demming, Demming, and Teller[56] classified isotherms into five types and there has subsequently been a type VI isotherm recognized by IUPAC.[57]

A type I isotherm is characterized by a sharp initial uptake of adsorbate at low pressures followed by a plateau in which very little gas is being adsorbed as pressure increases. This type of isotherm is representative of a microporous material (pore size less than 2 nm). The sharp

initial uptake represents the interaction of an adsorbent monolayer onto the surface of the pore walls. Because the pores are narrow, a saturation point is reached at very low pressures, usually before 0.1 P/Po. Type II isotherms, usually representative of nonporous or macroporous material

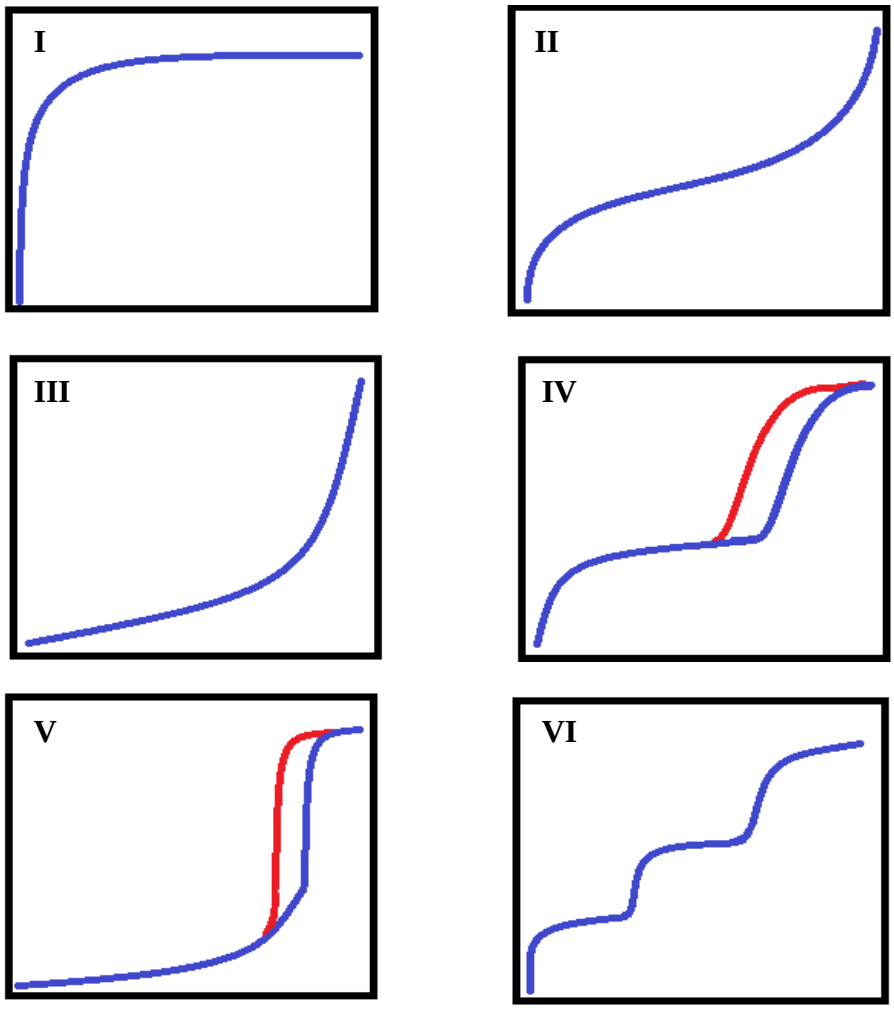

Figure 1.2. Six types of isotherms as identified by Brunauer, Demming, Demming, Teller and Sing.[57]

are characterized by a minimal initial slope followed by a linearly increasing central portion. The start of this linear region indicates the saturation of the surface monolayer followed by an indefinite multilayer formation. Type III isotherms are rarely occurring isotherms which are

characterized by a concave curve (relative to x-axis) showing no signs of monolayer adsorption (at low pressures) or saturation (adsorption increasing indefinitely with pressure). This usually occurs when the attraction between two adsorbate molecules is much stronger than the attraction between the adsorbent and the adsorbate. A type IV isotherm is similar in appearance to type II isotherms except they exhibit a second steep slope at higher pressures and may exhibit hysteresis. Hysteresis is the separation between the adsorption isotherm and the desorption isotherm. The second steep slope is due to capillary condensation, where adsorbate molecules are thought to condense inside the small pores (capillaries) with a finite multilayer corresponding to the filling of the pores, followed by saturation at a pressure close to 1 bar. Hysteresis signals that desorption takes place by a different mechanism than adsorption. Type IV isotherms are usually representative of mesoporous materials (pore size between 2 and 50 nm). Type V isotherms are similar to type III isotherms except that pores in the mesoporous range maybe present evident by slightly linear central portion where pores are being filled and uptake reaches saturation close to unity. Type VI isotherms, identified in relatively recent years, are indicative of more than one type of sorption site.

Since the actual adsorption process of gas storage measurements occurs at the interface between the adsorbate molecules and the adsorbent, maximum uptake in most cases is dependent on the surface area of the material. We determine surface area by calculating the amount of molecules that are adsorbed as a monolayer onto the pore walls of the adsorbate. Surface area is usually calculated based on two main theories: the Langmuir theory[58] and the BET theory[59] resulting in Langmuir or BET surface area values, respectively.

Irving Langmuir articulated one of the early adsorption models in 1916 which is based on the assumptions that: (1) the surface of the adsorbent is uniform, that is, all the adsorption

sites are equivalent, (2) adsorbed molecules do not interact with each other, (3) all adsorption occurs through the same mechanism, and (4) at the maximum adsorption, only a monolayer is formed. It is assumed that adsorbate molecules do deposit on other, already adsorbed, molecules of adsorbate, but only on the free surface of the adsorbent. After the appropriate sorption measurement we can calculate the Langmuir surface area of a given material using the Langmuir equation:

$$\theta = \frac{aP}{1 + aP}$$

where θ represents fractional coverage, P is pressure and a is a constant. If fractional coverage is represented as W/W_m, where W is weight of the adsorbate at some pressure and W_m is the weight of a monolayer; the equation can be rewritten in linear form as:

$$\frac{P}{W} = \frac{1}{aW_m} + \frac{P}{W_m}$$

By plotting P/W as a function of P this equation we can determine the slope, $\frac{1}{W_m}$, and the weight of the monolayer W_m. Total surface area, S_T, and specific surface area, S, are calculated usingthe following equations where N is Avogadro's number (6.023×10^{23}), A_{cs} is the cross-sectional area of the adsorbate, M is the molecular weight of the adsorbate and w is the sample weight.[60]

$$S_T = \frac{W_m N A_{cs}}{M}$$

$$S = \frac{S_T}{w}$$

The Langmuir model was later expanded upon by Brunauer, Emmet, and Teller in 1938 by what is known as the BET model or theory. The BET model accounts for the formation of multiple layers of adsorbate onto the adsorbent surface during which case the Langmuir model

is invalid. Here, gas molecules beyond the monolayer are speculated to interact with already adsorbed layers as expressed in the following:

$$A_{(g)} + S \rightleftharpoons AS$$

$$A_{(g)} + AS \rightleftharpoons A_2S$$

$$A_{(g)} + A_2S \rightleftharpoons A_3S\ldots$$

where A is the adsorbate molecule and S is the sorption site. With this in mind, the Langmuir equation can be modified to get the BET equation, accounting for multilayer adsorption:

$$\frac{1}{W[\left(\frac{P}{P_0}\right) - 1]} = \frac{1}{aW_m} + \frac{a-1}{W_m a}\left(\frac{P}{P_0}\right)$$

A linear plot of $1/[W((P/P_0)-1)]$ vs P/P_0 which is limited to relative pressures of ≤ 0.2 P/P_0 for microporous material gives us a slope of $s = \frac{a-1}{W_m a}$ and a y-intercept of $i = \frac{1}{aW_m}$.[8] From these two equations we can determine the weight of a monolayer to be $W_m = \frac{1}{s+i}$. By plugging this value into the equations the BET surface area of a material can be calculated. Because BET surface area is thought to more accurately portray the interaction between adsorbate and adsorbent molecules and is valid in micro-, meso- and macroporous materials, it is more commonly reported, though the Langmuir model, resulting in higher values, is still frequently used in microporous materials. Once surface area is established, total pore volume and the average pore radius can be calculated. Total pore volume, that is, the volume of liquid nitrogen contained in the pores can be calculated using the following equation:

$$V_{liq} = \frac{P_a V_{ads} V_m}{RT}$$

P_a and T are ambient pressure and temperature, respectively and V_m is the molar volume of liquid adsorbate (34.7 cm^3/mol for nitrogen).

Pore size of a material can be described in more detail from isotherms using one of several established theories. The Density Functional Theory (DFT) gives a more realistic description of the filling of micropores and narrow mesopores than classical macroscopic theories such as Dubinin-Radushkevich; Barrett, Joyner and Halenda (BJH); and Horvath and Kawazoe (HK), which are also commonly used. Local fluid structures near curved solid walls are more correctly described using the Non-Local Density Functional Theory (NLDFT), which will be used in data presented in later chapters. In the NLDFT approach, adsorption isotherms in model pores are determined based on the intermolecular potentials of the fluid-fluid and solid-fluid interactions as a function of temperature and pressure. NLDFT, which is most commonly encountered when investigating the porosity of porous organic polymers, will be overviewed briefly. The experimental isotherm is described as a combination of theoretical isotherms in individual pores, i.e. the experimental isotherm is the integral of the single-pore isotherm multiplied by the pore size distribution (PSD). The relationship between theoretical isotherms and the experimental isotherm can be interpreted in terms of a Generalized Adsorption Isotherm (GAI) equation or the Fredholm-type integral equation:[60]

$$N\left(\frac{P}{P_0}\right) = \int_{W_{min}}^{W_{max}} N\left(\frac{P}{P_0}W\right) f(W) dW$$

where $N\left(\frac{P}{P_0}\right)$ is the experimental adsorption isotherm, $N\left(\frac{P}{P_0}W\right)$ is the kernel (set) of theoretical isotherms in model pores of width, W, and f(W) is the PSD function. To find the PSD from the experimental isotherm, the kernel must first be calculated using DFT or Monte Carlo computer simulation. Kernels are described based on a specific pore shape (e.g. cylindrical, spherical, or

slit pores) and range of pore diameters. The solution is then found by solving the GAI equation using multilinear least-square fitting procedures.

For calculations of surface area, pore volume, pore size distribution etc., a gas probe is used, which is in most cases nitrogen. Other commonly used gas probes include argon and carbon dioxide. Nitrogen is most commonly used because it is inert, it has a relatively small diameter (~3.56 Å), fitting well within the confines of most microporous materials and its vapor pressure at liquid temperature (77 K) is ~1 atm, which reveals analyte properties at normal conditions. One disadvantage is that, at 77 K, the low relative pressure range (10^3–10^8) data are not useful. This could be due to diffusional problems of the molecules inside the narrow pores (<0.7 nm), density changes of the adsorptive, lack of applicability of the DR equation in such low relative pressure range, or different adsorption mechanisms according to the nature of the adsorbent/adsorptive.[61] Argon, much like N_2 is inert, a small gas (3.39 Å), and has a vapor pressure near atmospheric pressure at its boiling point (87 K). An advantage of using Ar at 87 K is that the lower limit of measurable pressures are extended down to 4.0 Å pores.[62] CO_2 molecules are used because of the higher adsorption temperatures, in contrast to N_2 at 77 K, resulting in a larger kinetic energy of the CO_2 molecules, and these are able to enter into the narrow pores.[61] CO_2 adsorption allows valuable parameters to be obtained such as surface area, volume, and size distribution of micropores.

1.3 Porous Polymers for Gas Storage

1.3.1 Traditional Gas Storage Materials

Traditionally, materials used for gas storage and separation consisted of naturally occurring carbon-based materials which are activated at high temperatures. Effective adsorbents must have high thermal stability, high rigidity and will usually have small pore diameters,

which results in higher surface area and therefore a high capacity for gas adsorption. The use of porous carbons date back to 2000 BC when ancient Egyptians used charcoal to purify water for medicinal purposes.[63] Activated carbons are very versatile adsorbents and are used in various applications mostly relating to the removal of gaseous contaminations by adsorption from liquids or gases. Other related applications include solvent recovery, air purification, food processing and chemical industry, for removal of color from various types of sugar syrup, and in air pollution control.[63] Carbon molecular sieves, having small pore sizes with a sharp pore size distribution compared with other activated carbons, have important uses in gas separation systems; particularly in the separation of nitrogen and oxygen having the advantages of low energy cost, room temperature operation, compact equipment, etc.[63] Activated carbon fibers having pore volumes of up to 1.6 cm^3/g and surface areas up to 2500 m^2/g, have advantage over traditional materials for effective elimination of SO_2 and NO_x from flue gases from combustion of coal and gasoline fuels.[64,65]

Porous silica-based materials are also well documented for their applications in gas storage because of their chemical inertness and stability. Porous silica is a form of amorphous silica first prepared by acidification of basic silicate solutions.[66] Using this method, catalyst, catalyst-supports, and adsorbents are commercially prepared. Another method to prepare silica is by hydrolysis of a silicon alkoxide, to form silicic acid.[66] Silicic acid condenses to form polysilicates, which connect together to form a network whose pores are filled with solvent molecules or a gel. Other forms of silica include pyrogenic silica or mineral opals. The silica surface is generally terminated with hydroxide (OH) groups bounded to a silicon atom. These hydroxide groups are particularly reactive to water and other polar molecules such as SH_2, CO, N_2O CH_3Cl, CH_3F, HCl, and ammonia.[66] These molecules are likely to be physisorbed to form

multiple hydrogen-bond layers. It is possible that porous silica can be used for hydrogen storage by adsorption of NH_3, since ammonia storage in silica is highly reversible.[67] This can be done by physical adsorption of NH_3, in microporous materials followed by the decomposition of the accumulated NH_3 into N_2 and H_2. Recent reports show silica materials with surface areas up to 2200 m^2/g, thus having an extremely high NH_3 uptake potential.[67] Porous silicas are also often used for the removal of volatile organic compounds in industrial settings. MCM-41 (Mobil Composition of Matter), synthesized by researchers at Mobil, is an example of a material constructed of amorphous porous silica possessing long range order to form uniformed mesopores.[68]

Zeolites are another class of porous materials traditionally used for gas storage and separation. Zeolites are synthesized or naturally occurring crystalline materials, unlike porous carbons and silicas, with open 3D framework structures made of SiO_4 and AlO_4 tetrahedra linked to each other by oxygen atoms to form porous channels,[69] Natural zeolites form where volcanic rocks and ash layers react with alkaline groundwater or in post-depositional environments, over periods ranging from thousands to millions of years in shallow marine basins. Because of a growing interest in materials with larger pore sizes, new synthetic zeolites began to be heavily researched. The first zeolitic structure with pores larger than 10 Å was reported in 1988,[70] with a pore diameter of 12 Å. Synthetic zeolites are typically between 3 and 15 Å, which can limit gas storage capacity, but can be advantageous in many other respects.[66] These materials are used in various applications such as waste-water cleaning, fertilizer, aquaculture, deodorization, gas separation, solar refrigeration, solid electrolytes construction materials, etc.[71]

1.3.2 Metal-Organic Frameworks

Organic-inorganic hybrid materials have long been investigated for a myriad of applications. In order to optimize and thoroughly characterize these materials, a method of crystallization had to be developed, which was first realized by the combination of nitrogen-containing linkers such as bypyridine and nitriles with metal clusters to form coordination polymers.[73] These materials were held together by weak interactions between the metal cation and the nitrogen sites of the linkers, which made them thermally and chemically unstable. One example was reported in 1989 on the synthesis of $(Cu[C(C_6H_4CN)_4])_n^{n+}$, which was described as having a tetragonal unit cell with adamantane like cavities.[72] This area was more recently developed with the introduction of Metal-Organic Frameworks (MOFs), which are highly crystalline porous frameworks where the metal-nitrogen interactions are replaced with the much stronger metal oxide bonds such as Zn-O, increasing overall stability. MOFs, generally made up of metal ion clusters connected by organic linkers, have been found to have exceptional applications in gas storage. The term MOF, though often used interchangeably with coordination polymers or networks, has been clearly distinguished by Yaghi *et al* in a recent review:[73]

> "The term coordination compound originally referred to compounds such as $Co(NH_3)_6Cl_3$ studied by Alfred Werner over 100 years ago. Here the Co–N bond has zero formal bond valence… In a MOF, such as MOF-5, the Zn–O bond has a formal valence of 1/2 and indeed the energy of the two Zn–O bonds acting as a framework link is expected to be close to that of a typical C–C bond. An essential point is that a MOF such as MOF-5 is the salt of the conjugate base of weak acid and the Zn–O bonding is no different in kind from the Zn–O bonding in, say, $ZnCO_3$…"

By careful selection of the organic linker and the metal ion building units, MOFs can be tailored for several applications including gas storage and separation, catalysis, luminescence and photovoltaics. This design principle allowing control and prediction of framework structure referred to as reticular chemistry. The stability of MOFs is evident, due to the ability to reversibly introduce and freely exchange solvent molecules from the pores. The first instance of gas sorption evaluation on a MOF was in 1998 on Zn(benzenedicarboxylate) where N_2 and CO_2 isotherms were taken,[74] revealing a relatively low surface area of 270 m^2/g. As a result of the exponential growth in research on MOF chemistry, targeted properties such as increased surface area, have drastically improved reaching Langmuir values of up to 10,000 m^2/g.[75] MOFs, though a ground-breaking addition to porous polymers, have some limitations that may impede them from optimal performance as gas storage materials. For one, they are relatively dense materials due to the metal composition in their framework, which could make storing a high mass percent of gas difficult. Second, their metal-oxide bonds, while stronger than coordination polymers, are non-covalent, which limits their chemical stability.

1.3.3 Covalent Organic Frameworks

In 2005, covalent-organic frameworks (COFs)[76], a new group of crystalline porous materials, were introduced to the field by Yaghi's gruoup at University of Michigan. The interest in developing in crystalline covalent organic polymers stems from the fact that such materials would be of low density because they are made from atoms of low molecular weight (C, H, B, O) and are strongly linked by covalent bonds. Before this development, the synthesis of crystalline extended organic structures linked by strong covalent bonds was an undeveloped field. The basis of COF chemistry relies on the fact that as long as there is some degree of reversibility in the formation of linking unit (e.g. boroxines or boranate esters), the

crystallization of purely covalent frameworks, should be possible. It was widely believed this required reversibility would be very difficult if not impossible to achieve (the crystallization problem).[77]

The strategy to overcome the crystallization problem involves a one-step condensation reaction of discrete molecules that can be adopted for the synthesis of their extended analogs. The first reported COF was an extension of a simple organic molecule, triphenylboroxine (COF-1) and a triboronate ester of triphenylene (COF-5, Figure 3). Triphenylboroxine, can be synthesized by the dehydration of three phenyl boronic acid molecules forming a planar conformation held together by hydrogen bonds. The extension of this reaction using 1,4-benzenediboronic acid, as expected, formed the layered hexagonal framework, COF-1. Here, the framework takes on a graphite topology (gra) i.e. a staggered AB arrangement analogous to the packing of graphite sheets where the tri-coordinate vertices (boroxine rings) lie over the center of the hexagonal pores of neighboring layers. Similarly, the synthesis of COF-5 was developed by an appropriation of the reaction between phenylboronic acid and hexahydroxyphenylene (HHTP), which forms the triboronate ester. Using 1,4-benzenediboronic acid instead of phenylboronic acid, a new extended sheet structure, COF-5 was formed. COF-5 adopts a boron nitride topology (bnn), an eclipsed arrangement, in which atoms of adjacent sheets lie directly over each other. Like MOFs, COFs are designed using concepts of reticular chemistry allowing for strict control over pore size and framework structure, which is confirmed using experimental measurements such as powder x-ray diffraction (PXRD) and gas sorption analyses. From N_2 adsorption experiments, COF-1 and COF-5 were determined to have permanent porosity with Brunauer Emmet Teller (BET) surface areas of 711 and 1590 m^2/g,

respectively. Using the HHTP molecule combined with linear or other triangular building units, COF-6, -8 and -10 were developed soon after, all having 2D boron nitride topologies.[77]

The first 3D COFs were published by El-Kaderi et al, showing a drastic increase in surface area when incorporating tetrahedral building units tetra(4-dihydroxyborylphenyl)methane (TBPM) and its silane analog (TBPS). The self-condensation of TBPM and TBPS yields COF-102 and COF-103, respectively.[78] The reaction of the tetrahedral building units with the HHTP yielded COF-105 and COF-108. Of the two networks which could possibly have formed, COFs 102, 103, and 105 took on the carbon nitride (ctn) topology and COF-108 forms a borocite (bor) topology. Gas sorption measurements confirm that 3D frameworks, due to low densities coupled with a maximized fraction of surface sites, are likely to have higher surface area and porosity: with surface area values for COF-102 (3472 m^2/g).

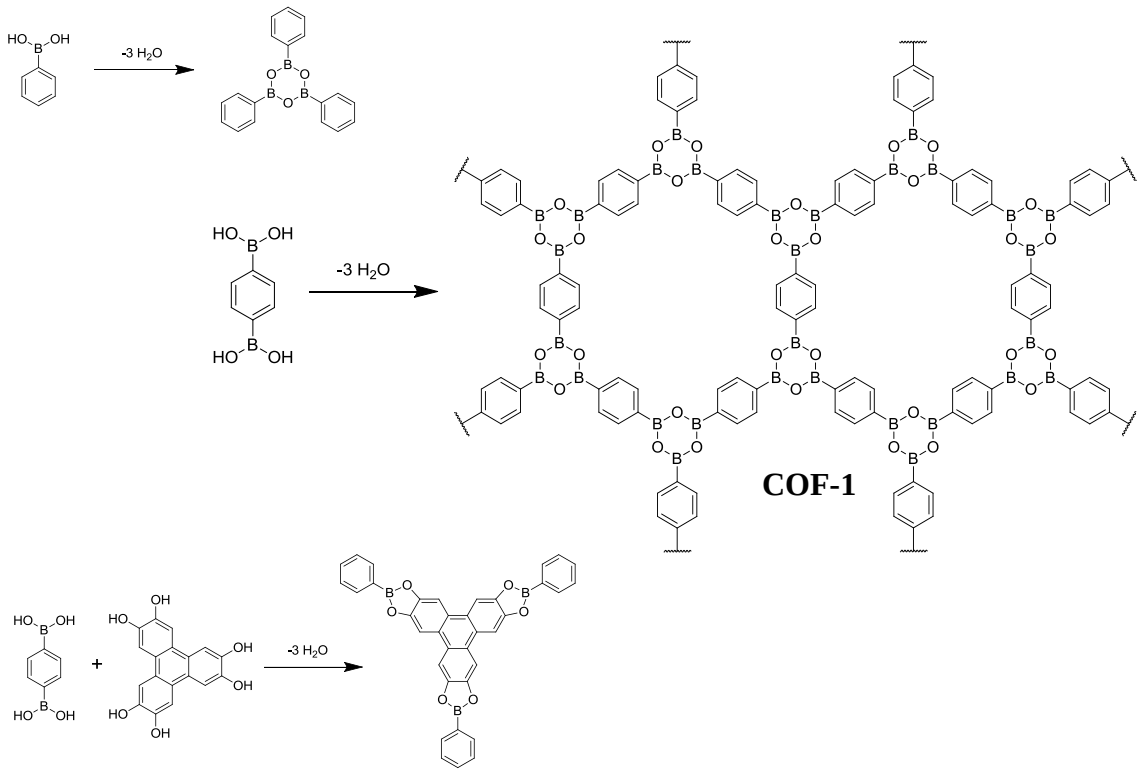

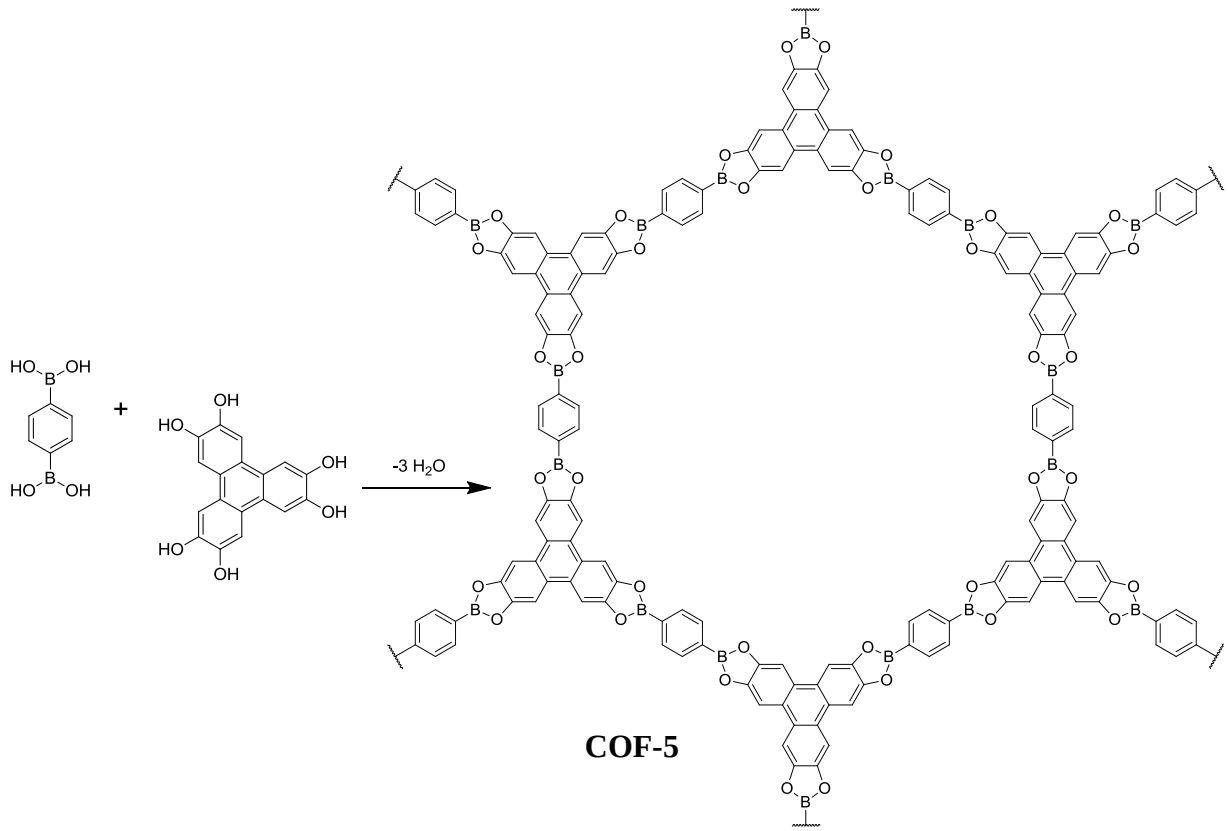

Figure 1.3. Condensation reactions of boronic acids used to produce discrete molecules and extended COFs.

and COF-103 (4210 m^2/g) exceeding those of most MOFs. As other groups began to explore the area of COF chemistry, Kuhn *et al*. published the first of a new class of crystalline polymers by the trimerization of nitriles, forming a covalent triazine-linked framework or CTF-1.[79] CTF-1 has similar porosity features to COF-1, being isoelectric, replacing the boroxine units with triazine rings. Subsequently, COF-300,[80] a 3D crystalline framework, was later published from the condensation of an aldehyde and an amine to form C-C and C-N covalent bonds, demonstrating structure interpenetration of struts in a diamond (dia) like structure.

To date, there are no reported polymers besides COFs and CTFs which exhibit crystallinity. However, the synthesis and characterization of several new organic polymers have been reported proving that crystallinity is not a requirement for high surface area material. Polymers of intrinsic microporosity (PIMs)[1,53] are constructed of highly rigid and nonlinear

linking group that would ensure space-inefficient packing, prevent structural relaxation and loss of microporosity. PIMs have been thoroughly explored as porous materials, with BET surface areas ranging from 450 – 1000 m^2/g. Another class of microporous organic materials is hypercrosslinked polymers (HCPs) which also exhibits high surface areas.[81-85] The permanent porosity of HCPs materials is a result of extensive crosslinking of organic linkers that prevent the porous structure from collapsing. Conjugated microporous polymers (CMPs) are another class of porous polymers, consisting purely of carbon and hydrogen atoms, which exhibit extremely high surface areas. CMPs are usually synthesized from the coupling of highly symmetric organic building units.[86-92] Because of their carbon composition, CMPs are extremely thermally and chemically stable as well. For example, Ben et al reported that PAF-1[93] (Porous Aromatic Framework), synthesized by Yamamoto homo-coupling of tetrakis(4-bromophenyl)-methane, has a BET value of 5640 m^2/g. PAF-1 had the highest reported surface area for porous organic polymers until the recent publication of PPN-4 (Porous Polymer Network) synthesized by the homocoupling of tetrakis(4-bromophenyl)silane from Zhou's group at Texas A&M with a BET value of 6461 m^2/g.[94]

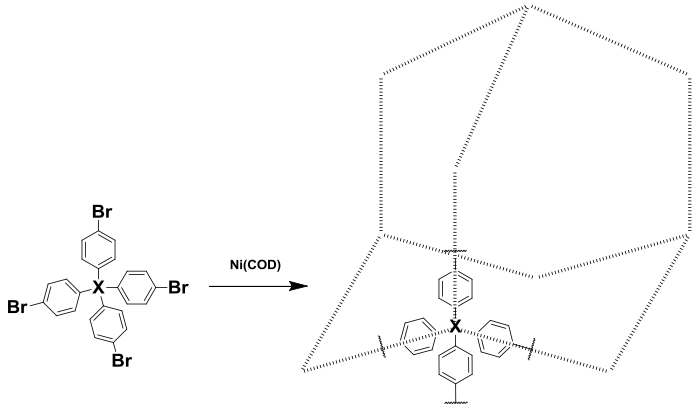

Figure 1.4. Synthetic route for PPN-3 (X: Adamantane), PPN-4 (X: Silicon), PPN-5 (X: Germanium), and PAF-1 (X: Carbon).

1.3.4 Borazine-Linked Polymers

Despite much recent advancement in the field of designed porous polymers, we recognize that there is still much more work to be done. The previously mentioned hydrogen storage targets have not yet been met, in addition to targets of other applications that could be improved. It is our belief that the relatively undeveloped area of covalent-organic frameworks should be given particular attention due to their exceptional exhibitions of gas storage. Extra efforts aimed at fine tuning the structures and electronic properties of COFs, in our opinion will have a substantial effect on their ability to confine hydrogen. This objective is addressed in this dissertation, which describes the design and synthesis of a new class of polymers aided by reticular chemistry for enhanced gas storage capabilities. We have extended this area of research by investigating the effects of including an alternate functionality i.e. borazine into the framework of porous organic polymers, known as Borazine-Linked Polymers.[95,96]

1.4 Boron-Nitrogen Bond Formation by Dehydrogenation of Amine-Borane Adducts

Before successful incorporation of borazine rings into porous polymers, the various methods of B-N bond formation had to be investigated. The study of B-N compounds date back to over two centuries ago with the preparation of ammonia-boron trifluoride, NH_3•BF_3, by Gay-Lussac in 1909[97] and Davy, J. in 1812.[98] Since the ring structure of borazine was discovered in 1926 by Alfred Stock,[99] B-N compounds start to attract more attention due to their resemblance to carbon structures. However, it was not until the 1950's, that research groups devoted major effort into the exploration of this area.[100] Besides the intriguing similarity of borazine to benzene, B-N compounds have primarily been studied for their use as a preceramics to boron nitride. Boron nitride, having a close resemblance to the carbon structure, graphite, is one of the

oldest known boron-nitrogen materials, dating back to the mid-19th century. Amine-borane complexes also have great potential use in hydrogen storage fuels due to their stability and the high gravimetric content of hydrogen.[101] With the numerous applications of BN compounds, there was much background information to refer to in pursuing a facile route to the synthesis of Borazine-Linked Polymers.

In the following section, the physical and chemical properties of borazine as well as the various reported synthetic routes will be discussed. It is important to recognize that in an aminoborane such as (dimethylamino)dimethylborane, boron is covalently bonded to nitrogen as opposed to an amine-borane such as aniline-borane, where the lone pair of electrons from the nitrogen source interacts with the empty p-orbital of boron in a donor-acceptor association however not a covalent bond. Amine-boranes are sometimes referred to as adducts or complexes. Besides borazine, other boron nitrogen ring systems that will be mentioned include saturated boron-nitrogen rings, called borazanes which act as intermediates in many cases between adducts and borazines or larger rings.

Borazine, or as it has been called, inorganic benzene, is a planar molecule similar in structure to boroxine and triazine, both of which have been used in the construction of crystalline covalently linked polymers. There have been various synthetic methods reported since its discovery almost a century ago. Stock first synthesized borazine, using diborane and ammonia. The two starting materials were introduced into solvent in gas phase and heated to ~300 ºC resulting in about a 50% yield.[101] Another early synthetic route involved the reaction of lithium borohydride with ammonium chloride in the absence of a solvent at a temperature around 300 ºC (30-35% yield).[102] It was then discovered that borazine could be synthesized from the direct thermal conversion of ammonia-borane (69-73% yield), but the process requires

specialized equipment.[103] In 1995, Sneddon was able demonstrate this process in laboratory glassware using tetraglyme as the solvent giving a 67% isolated yield of borazine.[104] Primary and secondary amine-borane adducts have been shown to undergo thermally induced dehydrocoupling to cyclic aminoborane $[R_2B\text{-}NR_2]_2$ (x = 2 or 3) and borazine derivatives.[105-109] Manners and co-workers have reported this dehydrocoupling under milder conditions using transition metal-catalysts, improving routes to boron-nitrogen rings and chains.[110-111] This work was used in initial attempts

Scheme 1.1. Synthetic route to borazine derivatives from amine-borane adducts through borazane formation.

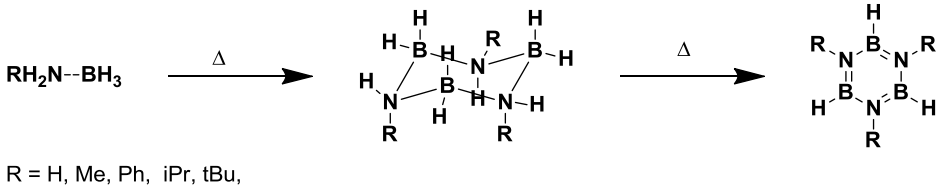

to synthesize BLPs using catalysts, as well as current research involving the incorporation of metal nanoparticles into BLP pores. It was upon the foundations of these initial works that the eventual success of synthesizing porous BLPs was built.

1.5 Characterization of Porous Organic Polymers

Since interest has risen in porous organic polymers, there has evolved a standard set of characterization techniques which have been adapted by many in the field. In general, scientists try to use techniques that will most completely describe the chemical composition, morphology, and physical and textural properties of a powder sample. Since slight variations from author to author may be encountered, briefly described here will be the techniques reported in recent

publications from El-Kaderi's group which include the characterization of covalent-organic frameworks (COFs), nanoporous organic frameworks (NPOFs), Benzimidazole-linked polymers (BILPs), as well as borazine-linked polymers (BLPs).

Textural properties such as pore size, pore volume, density and surface area were characterized by using an Autosorb-1C volumetric analyzer. The Autosorb uses nitrogen or argon isotherms to characterize the porous nature of a powder sample. The amount adsorbed is a function of temperature, pressure and the strength of attraction or interaction potential. In a typical experiment, a sample is activated, or heated under vacuum, in order to evacuate any guest molecules form the pores. At the start of the experiment, the evacuated sample is then brought to a constant temperature of 77 K using liquid nitrogen. Once the temperature has equilibrated, small amounts of the adsorbate are admitted in step. Adsorbate molecules quickly diffuse onto the surface of the pores of the sample (the adsorbent) as adsorption takes place.

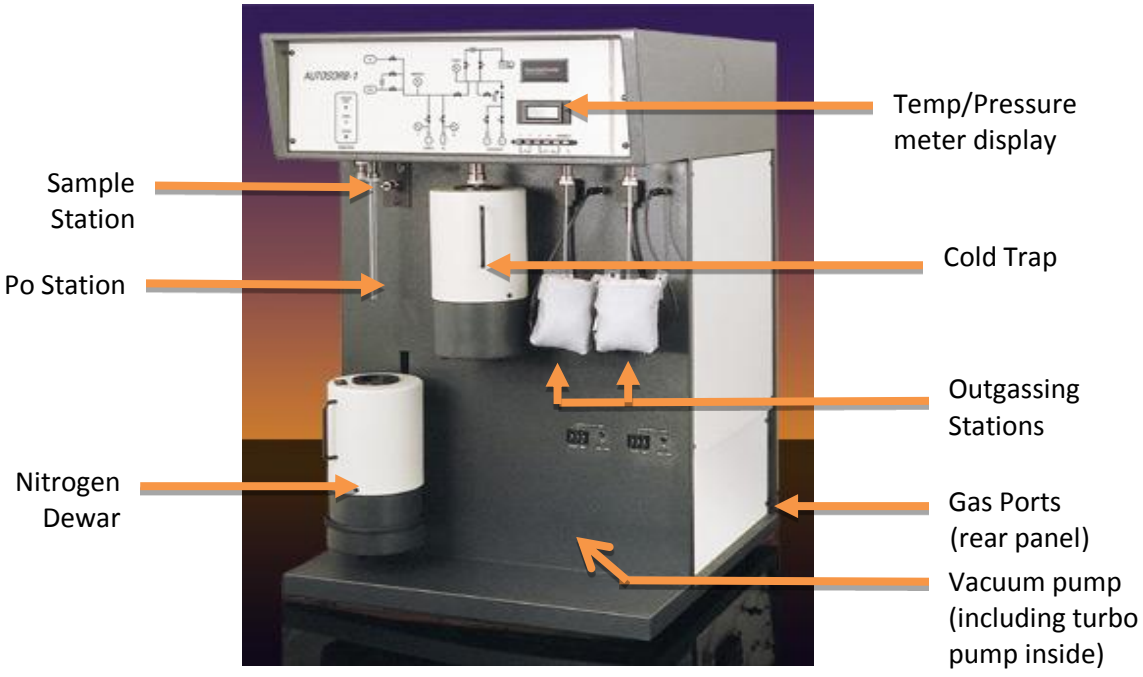

Figure 1.5. Image of Autosorb-1C with essential components labeled.

A high precision pressure transducer monitors pressure changes due to the adsorption process. This process is repeated until a set pressure level is reached. These points are plotted on a graph to produce an isotherm. From a nitrogen or Argon isotherm it is possible to calculate surface area, pore volume, and pore size distribution.

Fourier Transform-Infrared Spectroscopy (FT-IR) is used in the characterization of porous polymers to confirm that the target bonds are formed and/or broken. In most cases there are discernible differences in starting material and final product which can give insight on the chemistry occurring during the polymerization process. For example, in the synthesis of CTF-1, the nitrile starting material should be converted in a cyclotrimerization reaction to triazine rings.[79] Therefore in the IR spectra of the starting material, the peak at ~2225 cm^{-1} which is indicative of the carbon-nitrogen triple bond, is noticeably absent in the product spectra. The new peak appearing at ~1350 cm^{-1} arises from the formation of the triazine ring.

Similarly, solid state NMR spectroscopy is also used to confirm structural composition of insoluble polymers. Since, we are concerned with organic polymers, ^{13}C NMR is always relevant. Depending on the elemental composition of the reaction sites of the molecular building units, NMR signals can shift drastically or hardly at all. When characterizing BLPs, since there is no carbon-carbon bond cleavage or formation, the ^{13}C peaks of the polymer is hardly differentiable form those of the amine-borane adduct. However, in all cases, the addition of borane to the amine causes a noticeable shift in carbon atoms closest to nitrogen. Elemental analysis is typically done by combustion analysis where a sample is heated in either oxygen or an inert gas atmosphere and the relevant combustion products are measured. This method is not very accurate in determining composition due to side reactions that may occur or incombustible materials, but it can be helpful in giving a general idea of the relative abundance of the each

element. It is common to find lower carbon values. Organoboron compounds, for example, typically give lowered carbon values in elemental microanalysis due to the formation of noncombustible boron carbide byproducts.[76]

Thermogravimetric analysis (TGA) is another common technique used in the characterization of porous polymers. During a TGA, a sample is heated slowly under a flow of an inert gas, as the mass of a sample is recorded. There are several data that can be obtained by performing TGA on a sample. From a TGA plot, it is possible (1) to monitor whether any other reactions may be taking place during heating, (2) to determine the porosity of a polymer, i.e. the relative mass of solvent or unreacted material released from the pores, and (3) to determine the decomposition point of a sample.

Microscopy techniques such as scanning electron microscopy (SEM) and transmission electron microscopy (TEM) are often used when characterizing porous polymers to determine the purity and morphology of a sample, among other things. During SEM imaging, the surface of a sample is scanned with a beam of energetic electrons producing backscattered and secondary electrons. The backscattered electrons are the electrons that collide elastically with the sample, that is the direction changes but the speed is virtually unaffected.[112] Secondary electrons are produced as a result of interactions between energetic beam electrons and weakly bound conduction electrons, which leads to ejection of conduction band electrons with a few electron volts of energy.[112] TEM works using a similar concept, except the electrons are transmitted through a thin specimen. An image is formed from the interaction of the electrons transmitted through the sample. TEM can usually get to much higher magnifications than SEM, also capable of identifying the presence of doped species such as metal nanoparticles and clusters. Well defined particles indicate that there exists some degree of order in the formation

of a polymer. Homogeneity of particle sizes and shapes indicates that there exists one pure composition in the product. Several different particle sizes and shapes can suggest that there may be impurities or multiple phases.

To determine the crystallinity of these polymers, they are characterized by powder X-ray diffraction. In a typical XRD experiment, X-rays are passed through a sample causing scattering which is picked up by a detector. When a beam strikes a crystal surface, a portion of the beam is scattered by the layer of atoms at the surface. The unscattered portion penetrates to the second layer where diffraction again occurs. The cumulative scattering from the regularly spaced centers of the crystal results in an observable diffraction pattern.[112] Because of the difficulty to produce crystalline porous organic polymers, the overwhelming majority reported are amorphous evident by the absence of clear peaks in PXRD pattern or a broad hump from ~25 to 35 ° 2θ. Porous crystalline polymers such as COFs and CTF-1 are the only reported crystalline porous organic polymers besides BLP-2(H), which will be discussed in further detail later in Chapter 4.

1.6 Thesis Problem

The primary source of energy throughout the world by far is carbon-based fuels: more specifically oil, coal and natural gas. Consumption of fossil fuels is increasing as nations develop and automotive transportation becomes more prevalent which is a cause for major concerns. The use of hydrogen as an alternative fuel has become one of the most widely supported as a solution to the problem. However, there are some undeveloped areas regarding the use of hydrogen fuel, particularly when we consider methods of storage. The development of covalent-organic frameworks COFs has become of interest as hydrogen storage materials due to the fact that such materials are entirely composed of light elements (H, B, C, N and O) that

are linked by strong covalent bonds (B-O, C-C, C-N and B-C) to make a class of highly porous and low density polymers. The undeveloped area of covalent-organic frameworks should be given particular attention due to their exceptional potential in hydrogen storage. The objective of this dissertation is to present our efforts at fine tuning the structures and electronic properties of COFs, which should have a substantial effect on their ability to confine hydrogen, improving hydrogen storage capabilities. Described herein is the design and synthesis of a new class of borazine-linked polymers (BLPs) aided by reticular chemistry for enhanced gas storage capabilities. The design of the building blocks lead to high surface area and low-density polymers. With these considerations in mind, we first set out to prepare a library of building blocks to be used in the construction of BLPs. The diverse synthetic routes to amine building units allow systematic manipulations in porosity of the corresponding polymer, therefore having various potential applications in gas storage and separation. Polymers formed from linear and triangular shaped building units are expected to form 2D polymers while 3D polymers can potentially form from the tetrahedral building units; showing competitive low pressure gas storage capabilities. The crystallization of the first porous borazine-containing polymer will be described. The formation of the new polymers has been confirmed by the spectral and analytical methods mentioned above. Selected BLPs show impressive high pressure hydrogen, carbon dioxide and methane sorption performance. Also presented here, will be the synthesis and characterization of a set of nanoporous organic frameworks (NPOFs) constructed entirely of carbon and hydrogen with exceptional porosities.

Chapter 2: Design of Borazine-Linked Polymers

The design of porous organic polymers is as important as their synthesis and characterizations. When the word design is used in terms of polymer chemistry, it refers to the assembly of molecular building units to form predefined structures, often for targeted applications. Early on, it was realized by Wells,[113,114] that the ball and stick model could be considered as a representation of special kinds of abstract graphs called nets, with the vertices of the graph corresponding to the atoms and the edges (links) of the graph corresponding to the bonds. A net is an infinite array of nodes, each of which is connected to three or more other others by 2-connecting links. [115] Links must be 2-connecting; if they connect three or more nodes then they themselves are nodes. It is a very useful approach to both design and analysis of polymer frameworks to use nets making it possible to reduce complicated structures to simple networks in order gain a better understanding of the arrangement of the components. It was an important step forward when it was discovered that certain topologies could be targeted.

The discovery of MOFs led to the recognition that, in order to truly obtain structures by design, one had first to identify the principal topological possibilities for nets. These default structures were identified as those with high point symmetry at the vertices and with a small number of different kinds of vertices and edges.[116] The discipline of preparing materials of targeted geometry by design is termed reticular chemistry.[117,118] The principle topologies have been published in a recent review[119] and data for many of the nets most important for reticular

chemistry can be found in an online database known as the Reticular Chemistry Structure Resource (RCSR).[120]

Originally, the concepts of reticular chemistry had been used exclusively for metal-organic hybrid materials. However with the development of COFs,[76] the concept of reticular chemistry can be employed in the design of organic polymers. The synthesis of COF-1 was based on the molecular dehydration reaction of phenylboronic acid molecules to form a planar six-membered boroxine ring with the elimination of water molecules. The reaction was extended to 1,4- benzenediboronic acid in which a layered hexagonal framework was expected to form upon dehydration as mentioned in the previous chapter. We have extended these methods to the design of borazine-linked polymers constructed of various amine building units

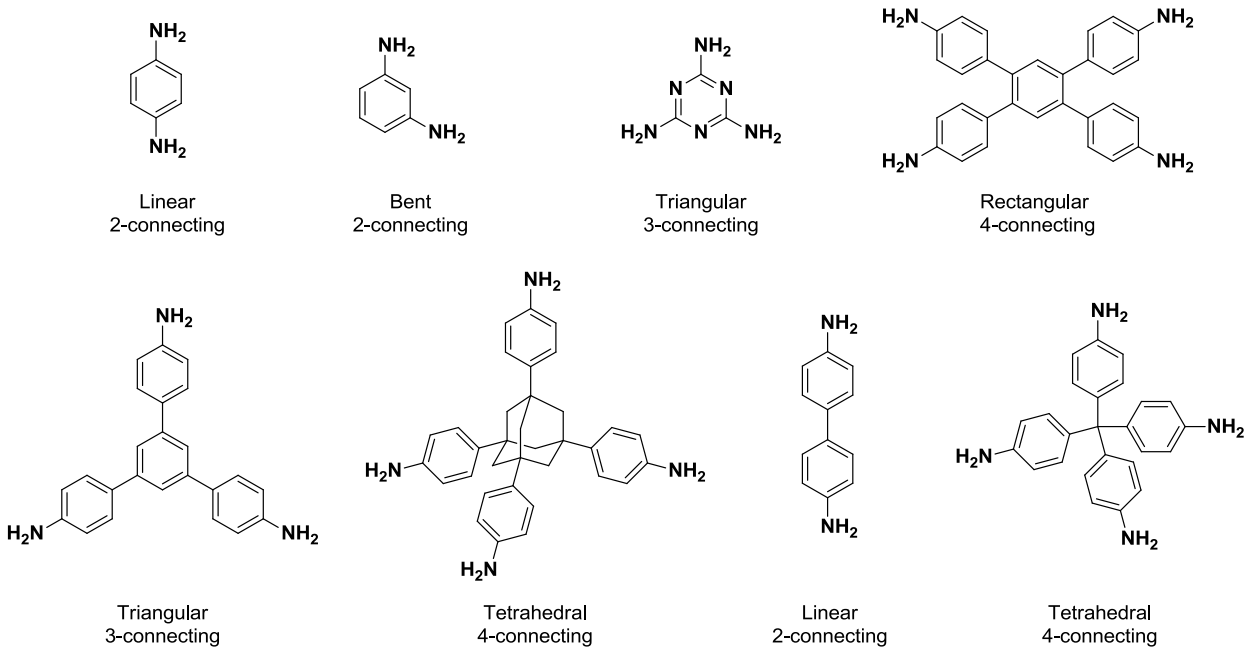

Figure 2.1. Amine building units with various shapes and connectivities.

according to the shape and dimensions of each amine. In each BLP, borazine acts as the triangular node. With these considerations in mind, we can rationally assign expected topologies to each polymer respective to their building units.

The selection of building units was not done randomly. Our strategy was based partly on the results of theoretical work demonstrated by Yaghi in 2004.[121] Here, the surface areas of a single infinite sheet of graphene, infinite chains of poly-p-linked six-membered rings, a graphene sheet divided into units of three six-membered rings that are 1,3,5-linked to a central ring, and isolated six-membered rings were compared. The surface area of graphene is shown to greatly increase when exposing the latent edges of the six-membered rings. This analysis suggests that by maximizing the number of exposed ring faces and edge on an organic linker, we can enhance the surface area of the polymer.

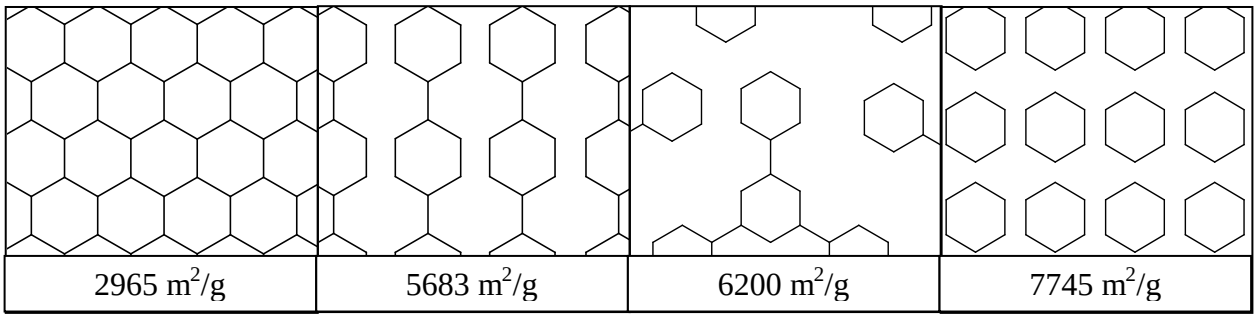

Figure 2.2. The Connolly surface area of graphite fragments of (a) a graphene sheet, (b) poly-p-linked six-membered rings, (c) 1,3,5–linked six-membered rings to a central ring (d) fully decomposed graphene sheets to individual six-membered rings.

The size and shape of each building unit will determine the size and shape of the pores of the corresponding polymer, which are key factor in determining gas uptake capacity such as H_2, CH_4, and CO_2. In hydrogen storage, reduction in pore size is known to enhance the interaction energy as the attractive potential fields of opposite walls overlap.[44,122-124] The ideal pore size seems to be approximately 5 Å considering the ~2.8 Å kinetic diameter of H_2.[44] Pores

of this size allow the H_2 molecule to interact with multiple portions of the framework, increasing the interaction energy between the framework and H_2. Larger pore size and surface area tend to hold higher volumes of methane. CO_2 storage, though also dependent on pore metrics, can greatly be influenced by the elemental composition of the pores. It has been shown for example that introducing amine functionality or accessible nitrogen sites into the pore wall of porous organic materials such as benzimidizole-linked polymers[125] can drastically impact their gas uptake and selectivity. The selective uptake of CO_2 over CH_4 or N_2 is believed to arise from enhanced CO_2-framework interactions through hydrogen bonding and/or dipole-quadrupole interactions.[126]

Operations in Materials Studio Modeling Software

The modeling software used in considering this pre-experimental data generation was Materials Studio 4.4.[127] Using Material Studio, we are able to clearly visualize the structure of the proposed polymer and obtain important information as to the feasibility of the formation of new polymers in terms of strain and energy of the system. Textural properties such as pore size and volume, and surface area can also be easily acquired from modeled structures. For these reasons, the first step in our investigations toward the synthesis of new polymer frameworks begins at the modeling stage. A brief overview of the general process of modeling these new structures using Materials Studio is presented.

1. **Building a Cell**. The first step in constructing a new model is to create a unit cell. A unit cell is the smallest cell which can describe the periodic arrangement of atoms within the crystal structure. A unit cell must be given a space group, which determines the symmetry of the cell and lattice parameters, which are the lengths of the cell edges and the angles between them. A space group is selected based on the coordination of the

building units and can be obtained from the Reticular Chemistry Structural Resource (RCSR) database or other existing databases for nets. RCSR will find the simplest target topology or default structure. The default structure is the structure which contains the minimum number of kinds of vertices and links.[128] For example, if there is a four-coordinated group and a three-coordinated group linked together, a search for nets with two kinds of vertices, 3 and 4, and one kind of edge yields the four nets: boracite (bor), carbon nitride (ctn), Pt_3O_4 (pto), and twisted boracite (tbo).

2. **Positioning Vertices.** The vertices are determined based on the space group chosen. Any atom can act as a vertex by inserting the atom into atomic coordinances found from the RCSR database. Vertices are then connecting revealing the basic crystal structure of the system.

3. **Introduction of Nodes and Linkers.** The nodes, are the functional groups which act as the vertices throughout the system. The group is superimposed onto the vertex, centered and the extensions are aligned with the bonds connecting each vertex. For example, all BLPs have a common triangular vertex which is borazine. The borazine ring would be centered over the vertex and the extensions from the nitrogen atoms would be aligned

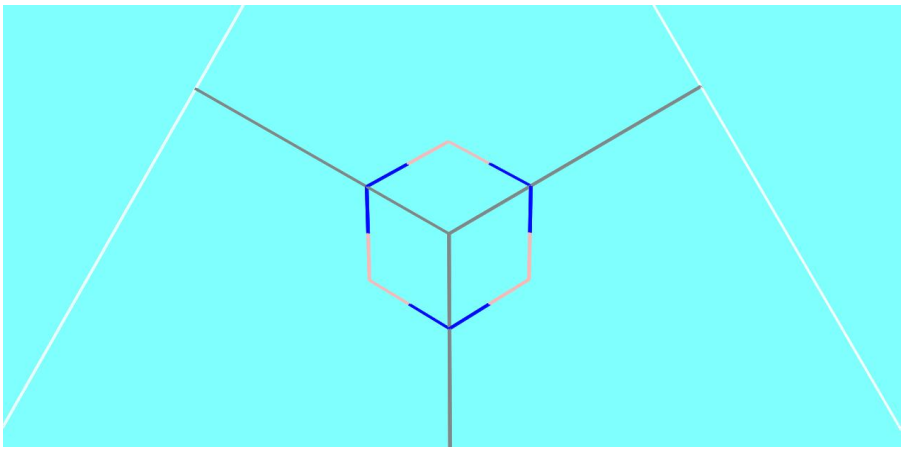

Figure 2.3. Borazine unit superimposed over triangular vertex in construction of BLP-1(H).

along the bonds connecting each vertex as shown in Figure 2.3. Linkers are inserted in a like fashion. The organic units are superimposed over the bonds connecting each node. Once all nodes and linkers are in place, the atomic vertices are deleted and bonds are connected in the appropriate positions.

4. **Geometry Optimization.** Finally, the geometry of the structure is optimized using the Forcite module. Forcite is an advanced classical molecular mechanics tool that allows energy calculations and reliable geometry optimization of the systems.[129] For periodic systems, Forcite allows the optimization of the cell parameters simultaneously with the molecular coordinates. [129] During a geometry optimization of a crystal structure, Forcite preserves the symmetry defined by the space group.

BLP-1(H) Structural Models

BLP-1(H) was modeled using boron nitride (**bnn**, P6/*mmm*) and graphite (**gra,** P63/*mmc*) topologies. Vertex positions were obtained from the Reticular Chemistry Structure Resource.[120] The dimensions of the unit cell were expanded beyond what any reasonable energetic minimization would result in to prevent overlapping of atoms. Subsequently, each vertex was replaced by a borazine ($B_3H_6N_3$) ring orientated such that the nitrogen atoms projected along the sites of extension. The midpoint of each extension was replaced by benzene and connected to the nitrogen atoms. The models were then geometrically optimized using the *Forcite* module as described above. The positions of atoms in the unit cell for the modeled topologies were visualized using *Mercury 2.4*[130] and are shown as fractional atomic coordinates in Table 2.1.

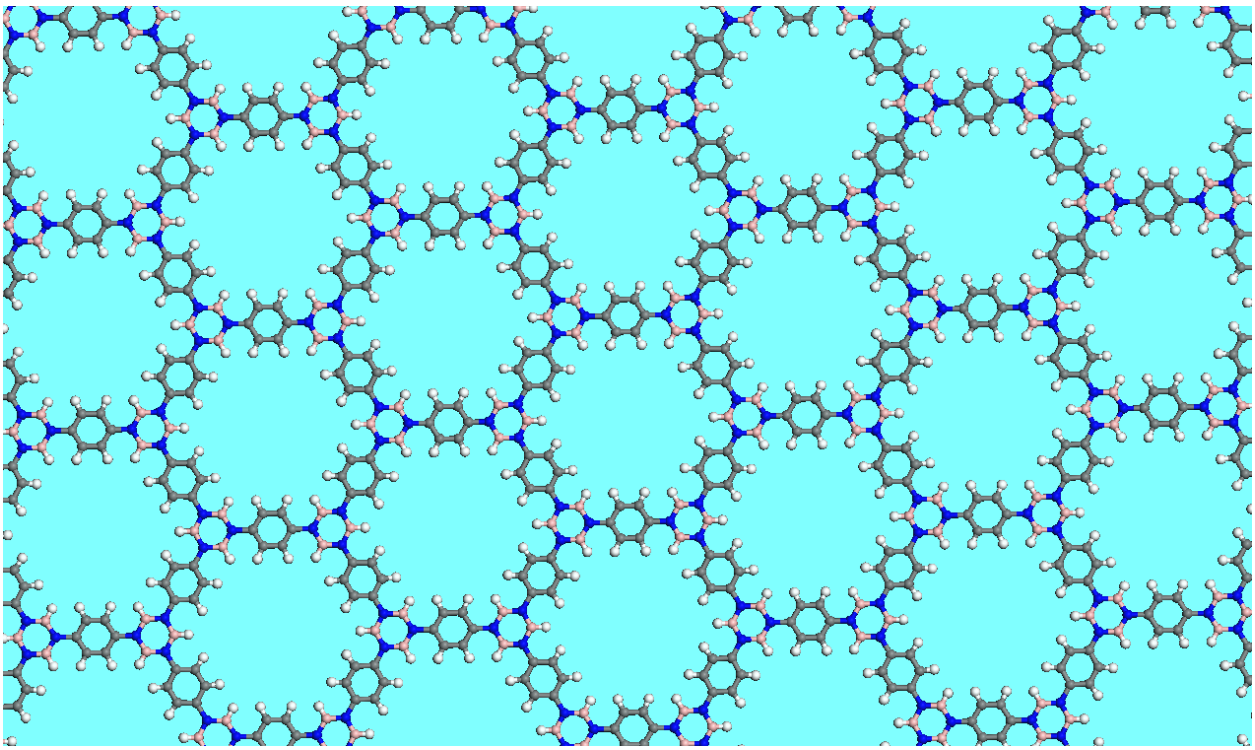

Figure 2.4. BLP-1(H) model using Materials Studio. *(pink spheres – boron; blue spheres – nitrogen; gray spheres – carbon; white spheres – hydrogen)*

Table 2.1. Fractional atomic coordinates for the eclipsed conformation of BLP-1(H).

BLP-1(H) *eclipsed*			
*P*6/*mmm* a = b = 15.2615 Å ; c = 3.4276 Å α = β = 90º ; γ = 120º			
Atom	X	Y	Z
B1	0.2808	0.5615	0.0000
N1	0.22503	0.6125	0.0000
C1	0.0528	0.6049	0.0000
C2	0.1095	0.5548	0.0000
H1	0.7806	0.2194	0.0000
H2	0.4055	0.0706	0.0000

Table 2.2. Fractional atomic coordinates for the staggered conformation of BLP-1(H).

BLP-1(H) *staggered*			
*P*63/*mmc* a = b = 15.3192 Å ; c = 6.5559 Å α = β = 90º ; γ = 120º			
Atom	X	Y	Z
B1	0.10715	0.05358	0.25
B2	0.38693	0.61307	0.25
N1	0.05553	0.11107	0.25
N2	0.27775	0.55551	0.25
C1	0.11155	0.2231	0.25
C2	0.22168	0.44336	0.25
C3	0.21834	0.28057	0.25
C4	0.27098	0.38581	0.25
H1	0.35134	0.41845	0.25
H2	0.26607	0.24793	0.25
H3	0.43018	0.56982	0.25
H4	0.19357	0.09679	0.25

BLP-2(H) Structural Models

BLP-2(H) was created using a space group of *P*-6*m2* in two different layer conformations, eclipsed and staggered. Vertex positions for the eclipsed structure were obtained from the Reticular Chemistry Structure Resource (http://rcsr.anu.edu.au) under the symbol acs-b. The vertices of the staggered structure were adapted from gra model. The two vertices were replaced by a benzene ring and a borazine ring such that the borazine nitrogen atoms were projected along the sites of extension. The midpoint of each extension was replaced by a benzene ring, which was connected at both sides to the adjacent atoms. The models were then geometrically optimized using the *Forcite* module as described above. The positions of atoms in the unit cell for the modeled topologies were visualized using *Mercury 2.4* and are shown as fractional atomic coordinates in Table 2.3.

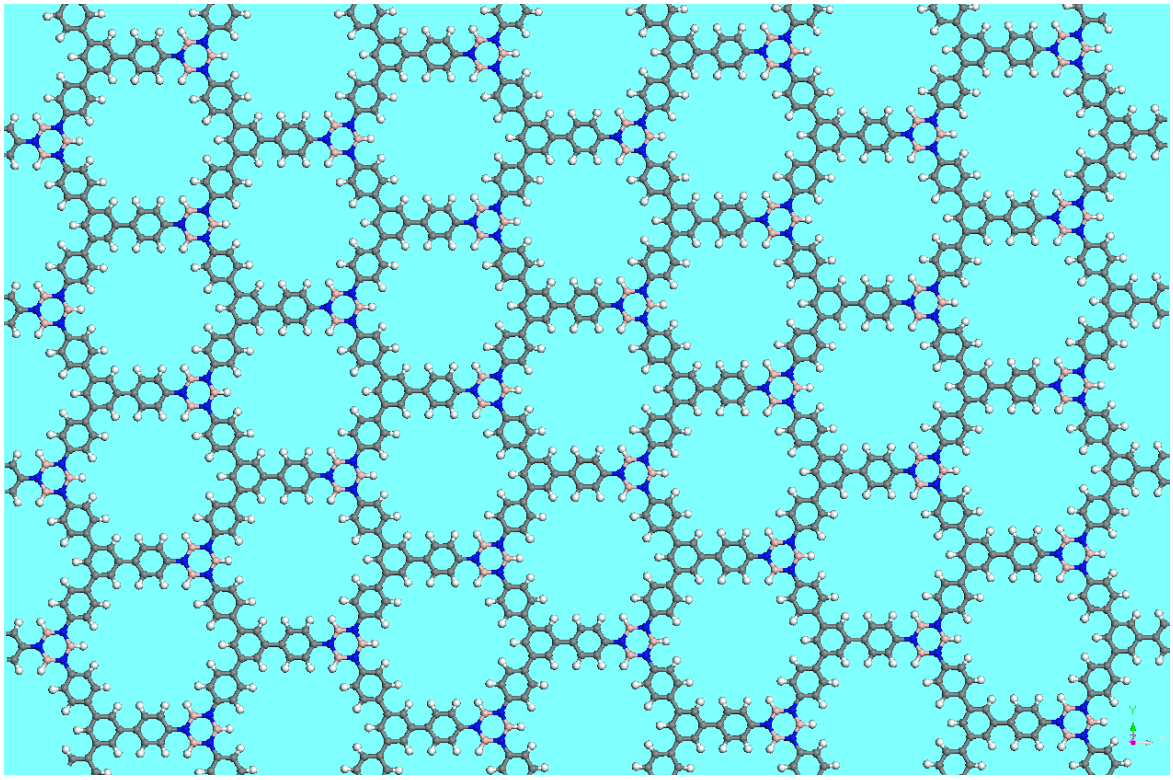

Figure 2.5. BLP-2(H) model using Materials Studio. *(pink spheres – boron; blue spheres – nitrogen; gray spheres – carbon; white spheres – hydrogen)*

Table 2.3. Fractional atomic coordinates for the eclipsed conformation of BLP-2(H).

BLP-2(H) *(Eclipsed)*			
P-6m2 a = b = 15.2905 Å ; c = 3.4579 Å α = β = 90º ; γ = 120º			
Atom	*x*	*Y*	*Z*
B1	0.4404	0.7203	0.0000
C1	0.5617	0.2808	0.0000
C2	0.6126	0.2252	0.0000
C3	0.5523	0.6044	0.0000
C4	0.6049	0.5515	0.0000
C5	0.5549	0.4451	0.0000
C6	0.4451	0.5549	0.0000
H1	0.5272	0.7636	0.0000
H2	0.4019	0.3143	0.0000
H3	0.3151	0.3999	0.0000
H4	0.7591	0.5182	0.0000
N1	0.3890	0.7780	0.0000

Table 2.4. Fractional atomic coordinates for the staggered conformation of BLP-2(H).

BLP-2(H) *(Staggered)*			
P-6m2 a = b = 15.2869 Å ; c = 6.3942 Å α = β = 90º ; γ = 120º			
Atom	*x*	*Y*	*Z*
B1	0.4407	0.7204	0.0000
B2	0.0537	0.9463	0.5000
C1	0.7283	0.1152	0.5000
C2	0.6126	0.3874	0.0000
C3	0.5550	0.4450	0.0000
C4	0.4452	0.5548	0.0000
C5	0.5617	0.2808	0.0000
C6	0.4485	0.0535	0.0000
C7	0.8881	0.7763	0.5000
C8	0.3956	0.9481	0.0000
C9	0.7783	0.5567	0.5000
C10	0.7207	0.4414	0.5000
C11	0.6142	0.3858	0.5000
C12	0.7809	0.0623	0.5000
H1	0.4211	0.3526	0.5000
H2	0.2488	0.2670	0.5000

(Table 2.4 continued)

H3	0.4818	0.2409	0.0000
H4	0.5274	0.7637	0.0000
H5	0.3151	0.3997	0.0000
H6	0.4019	0.3141	0.0000
H7	0.5742	0.4258	0.5000
H8	0.0970	0.9030	0.5000
N1	0.9443	0.8886	0.5000
N2	0.3890	0.6110	0.0000

BLP-3(H) Structural Models

BLP-3(H) was created using a space group of *P*-6*m2* in two different layer conformations, eclipsed and staggered. Vertex positions for the eclipsed structure were obtained from the Reticular Chemistry Structure Resource (http://rcsr.anu.edu.au) under the symbol acs-b. Dimensions of the unit cell were expanded beyond what any reasonable energetic minimization would result in to prevent overlapping of atoms. The vertices of the staggered structure were adapted from the gra model. The two vertices were replaced by a borazine rings and a triazine ring (C_3N_3) with the nitrogen atoms of borazine and the carbon atoms of triazine pointing along the sites of extension. The borazine nitrogen atoms were then bonded to the triazine carbon atoms. The models were then geometrically optimized using the *Forcite* module as described above. The positions of atoms in the unit cell for the modeled topologies were visualized using *Mercury 2.4* and are shown as fractional atomic coordinates in Table 2.5.

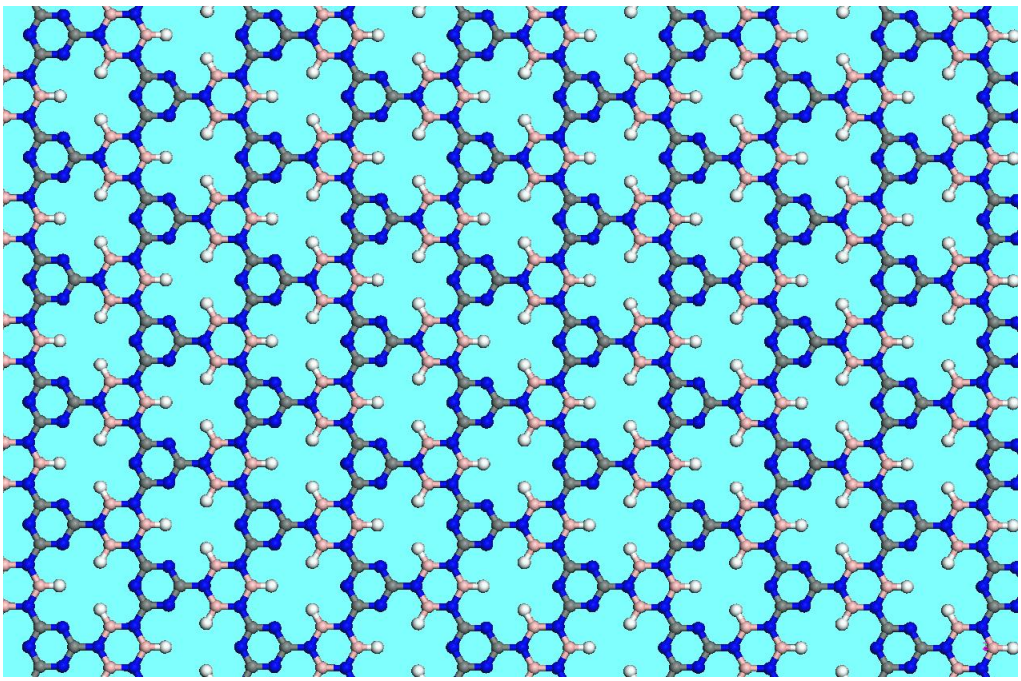

Figure 2.6. BLP-3(H) model using Materials Studio. *(pink spheres – boron; blue spheres – nitrogen; gray spheres – carbon; white spheres – hydrogen)*

Table 2.5. Fractional atomic coordinates for the eclipsed conformation of BLP-3(H).

BLP-3(H) *eclipsed*			
P-6m2 a = b = 7.5923 Å ; c = 3.4561 Å α = β = 90º ; γ = 120º			
Atom	*x*	*Y*	*Z*
B1	0.5492	0.7746	0.0000
N1	0.4616	1.2308	0.0000
C1	0.5606	1.1213	0.0000
H1	0.7214	0.8607	0.0000
H2	0.3081	1.1541	0.0000

Table 2.6. Fractional atomic coordinates for the staggered conformation of BLP-3(H).

BLP-3(H) *staggered*			
P-6m2 a = b = 7.6860 Å ; c = 6.5880 Å α = β = 90º ; γ = 120º			
Atom	*x*	*Y*	*Z*
B1	1.10655	0.89345	0.5
N1	0.88857	0.77714	0.5
C1	0.77573	0.55147	0.5
C2	0.56268	0.43732	0.5
H1	0.7214	0.8607	0.5
H2	0.3081	1.1541	0.5

BLP-10(H) Structural Models

BLP-10(H) was modeled in a similar fashion to BLP-1(H) using boron nitride (**bnn**, P6/*mmm*) and graphite (**gra,** P63/*mmc*). Here, the midpoint of each extension was replaced by biphenyl and connected to the nitrogen atoms. The models were then geometrically optimized using the *Forcite* module as described above. The positions of atoms in the unit cell for the modeled topologies were visualized using *Mercury 2.4* and are shown as fractional atomic coordinates in Table 2.7.

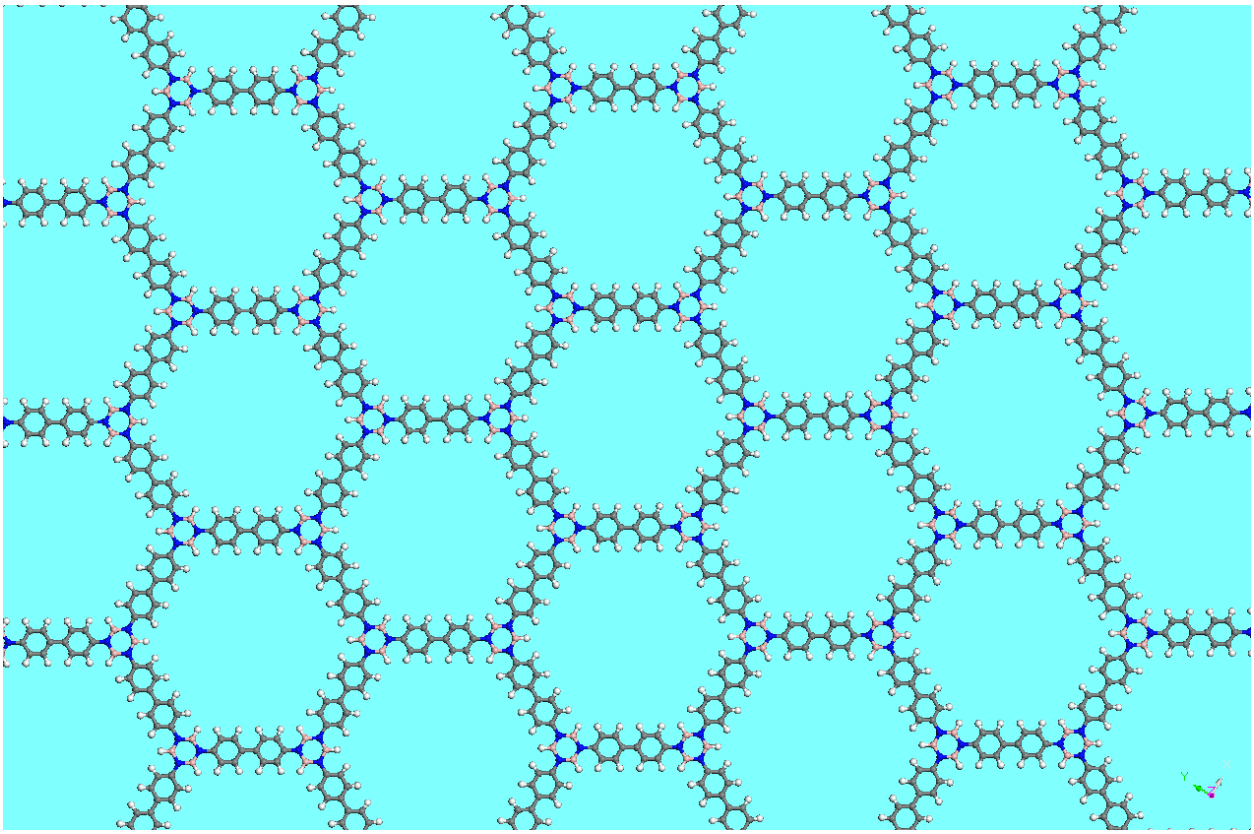

Figure 2.7. BLP-10(H) model using Materials Studio. *(pink spheres – boron; blue spheres – nitrogen; gray spheres – carbon; white spheres – hydrogen)*

Table 2.7. Fractional atomic coordinates for the eclipsed conformation of BLP-10(H).

BLP-10(H) *eclipsed*			
P-6m2 a = b = 22.9439 Å ; c = 3.4700 Å α = β = 90º ; γ = 120º			
Atom	*x*	*Y*	*Z*
B1	0.7024	0.4049	0.0000
N1	0.7409	0.3704	0.0000
C1	0.8157	0.4079	0.0000
C2	0.9618	0.4809	0.0000
C3	0.8541	0.3748	0.0000
C4	0.9244	0.4101	0.0000
H1	0.8324	0.3212	0.0000
H2	0.9480	0.3797	0.0000
H3	0.7313	0.4626	0.0000

Table 2.8. Fractional atomic coordinates for the staggered conformation of BLP-10(H).

BLP-10(H) *staggered*			
P-6m2 a = b = 22.9384 Å ; c = 6.5117 Å α = β = 90º ; γ = 120º			
Atom	*x*	*Y*	*Z*
B1	0.96422	1.03578	0.25
B2	0.36913	0.73826	0.25
N1	0.92584	0.96292	0.25
N2	0.40757	0.70379	0.25
C1	0.59125	0.74344	0.25
C2	0.52092	0.70817	0.25
C3	0.74239	0.8190	0.25
C4	0.81266	0.85403	0.25
C5	0.62861	0.81431	0.25
C6	0.48246	0.74123	0.25
C7	0.70505	0.85253	0.25
C8	0.85105	0.92552	0.25
H1	0.71884	0.76499	0.25
H2	0.83435	0.82206	0.25
H3	0.61483	0.7130	0.25
H4	0.49918	0.65451	0.25
H5	0.93536	1.06465	0.25
H6	0.39801	0.79602	0.25

BLP-12(H) Structural Models

BLP-12(H) was synthesized from tetra(4-aminophenyl)methane, a tetrahedral molecule. The polymer is expected to form as a 3D network having one 4-coordinate node which is the central methane atom and one 3-coordinate node which is the borazine. With this in mind, BLP-12(H) was modeled using a carbon nitride (**ctn**, *I*43d) and a borocite (**bor,** P43*m*) topology. Vertex positions were obtained from the Reticular Chemistry Structure Resource. Dimensions of the unit cell were expanded beyond what any reasonable energetic minimization would result in to prevent overlapping of atoms. Subsequently, each 3-coordinate node was replaced by borazine such that the nitrogen atoms projected along the sites of extension. Benzene was then placed at the midpoint between the nitrogen atoms of the borazine rings and the carbon atom (4-coordinate node), which was connected at both sides to the adjacent atoms. The models were then geometrically optimized using the *Forcite* module as described above. The positions of atoms in the unit cell for the modeled topologies were visualized using *Mercury 2.4* and are shown as fractional atomic coordinates in Table 2.9.

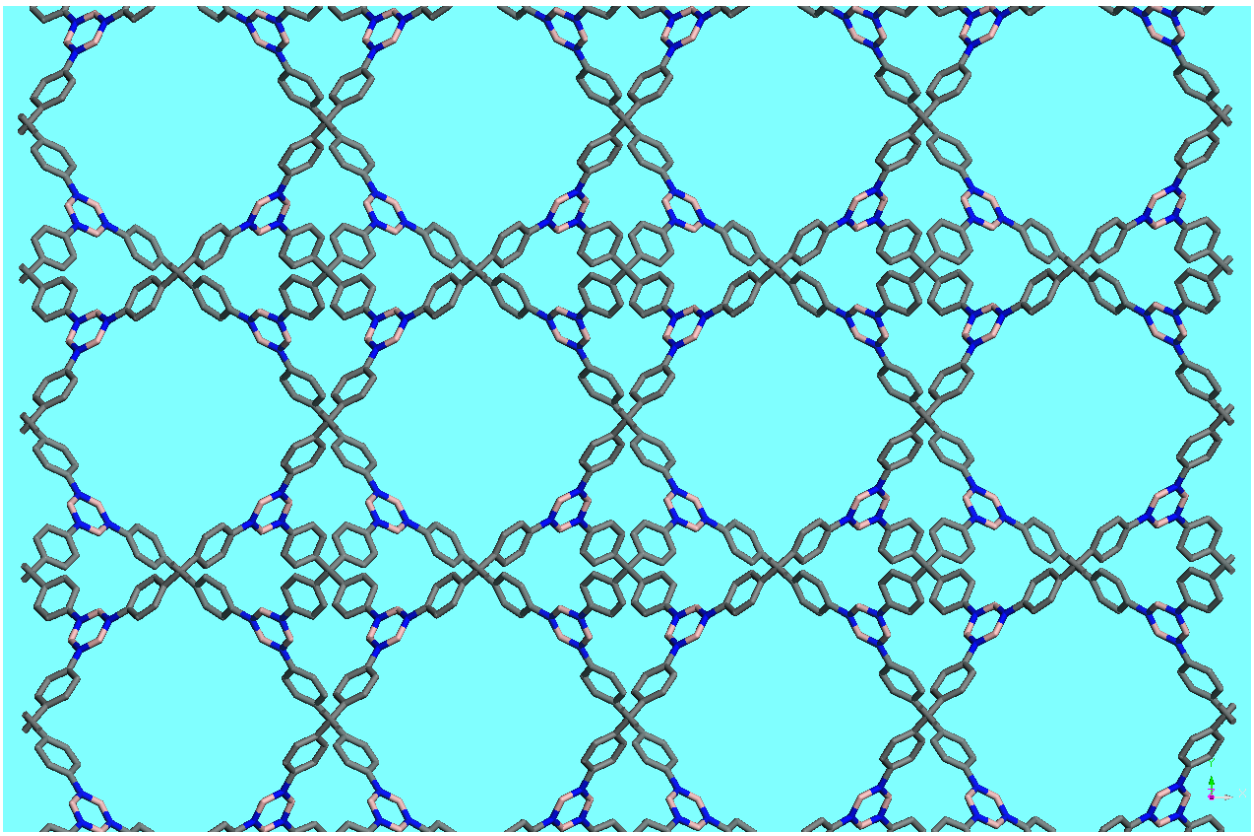

Figure 2.8. BLP-12(H) *bor* model using Materials Studio. *(pink spheres – boron; blue spheres – nitrogen; gray spheres – carbon; white spheres – hydrogen)*

Table 2.9. Fractional atomic coordinates for the **bor** conformation of BLP-12(H).

BLP-12(H)			
P-43m a = b = c = 18.0042 Å α = β = γ = 90º			
Atom	*X*	*Y*	*Z*
B1	0.77426	0.77426	0.12886
N1	0.74056	0.84111	0.15889
C1	0.64355	0.85014	0.05543
C2	0.58545	0.88694	0.01901
C3	0.67559	0.87749	0.12251
C4	0.55403	0.95244	0.04756
C5	0.50000	1.00000	0.00000
H1	0.66305	0.80145	0.02714
H2	0.56678	0.86491	0.03373
H3	0.74557	0.74557	0.07937

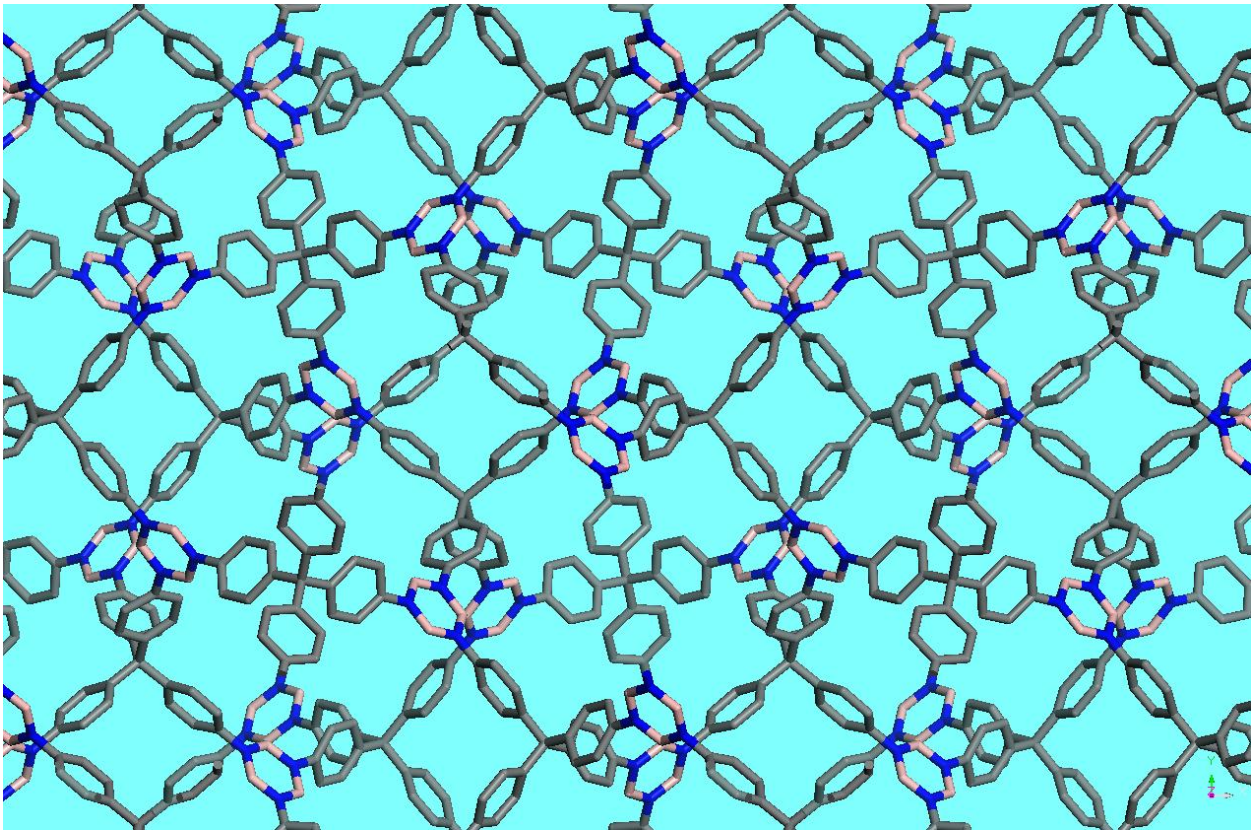

Figure 2.9. BLP-12(H) ctn model using Materials Studio. *(pink spheres – boron; blue spheres – nitrogen; gray spheres – carbon; white spheres – hydrogen)*

Table 2.10. Fractional atomic coordinates for the **ctn** conformation of BLP-12(H).

BLP-12(H)			
*I*43d a = b = c = 26.9355 Å α = β = γ = 90º			
Atom	*x*	*Y*	*Z*
B1	0.82636	0.74710	0.30364
N1	0.83594	0.71515	0.26197
C1	0.87962	0.77080	0.20401
C2	0.87674	0.72515	0.22895
C3	0.95321	0.69766	0.18886
C4	0.95576	0.74133	0.16024
C5	0.91397	0.68937	0.22170
C6	0.91820	0.78042	0.17098
C7	1.00000	0.75000	0.12500
H1	0.85174	0.79906	0.21036
H2	0.98139	0.66925	0.18501
H3	0.91259	0.65471	0.24203
H4	0.92041	0.81683	0.15426
H5	0.85263	0.78156	0.31113

BLP-15(H) Structural Models

BLP-15(H) is synthesized from the 1,3,5,7-tetrakis(4-aminophenyl)adamantane building unit which is tetrahedral in shape and modeled in a similar fashion to BLP-12(H). Only the ctn structure was considered due to incompatibility in the symmetry of the adamantane unit and the 4-coordinate node in the borocite structure. For the ctn model, the 4-coordinate vertices were replaced by adamntane. The model was then geometrically optimized using the *Forcite* module as described above. The positions of atoms in the unit cell for the modeled topologies were visualized using *Mercury 2.4* and are shown as fractional atomic coordinates in Table 2.11.

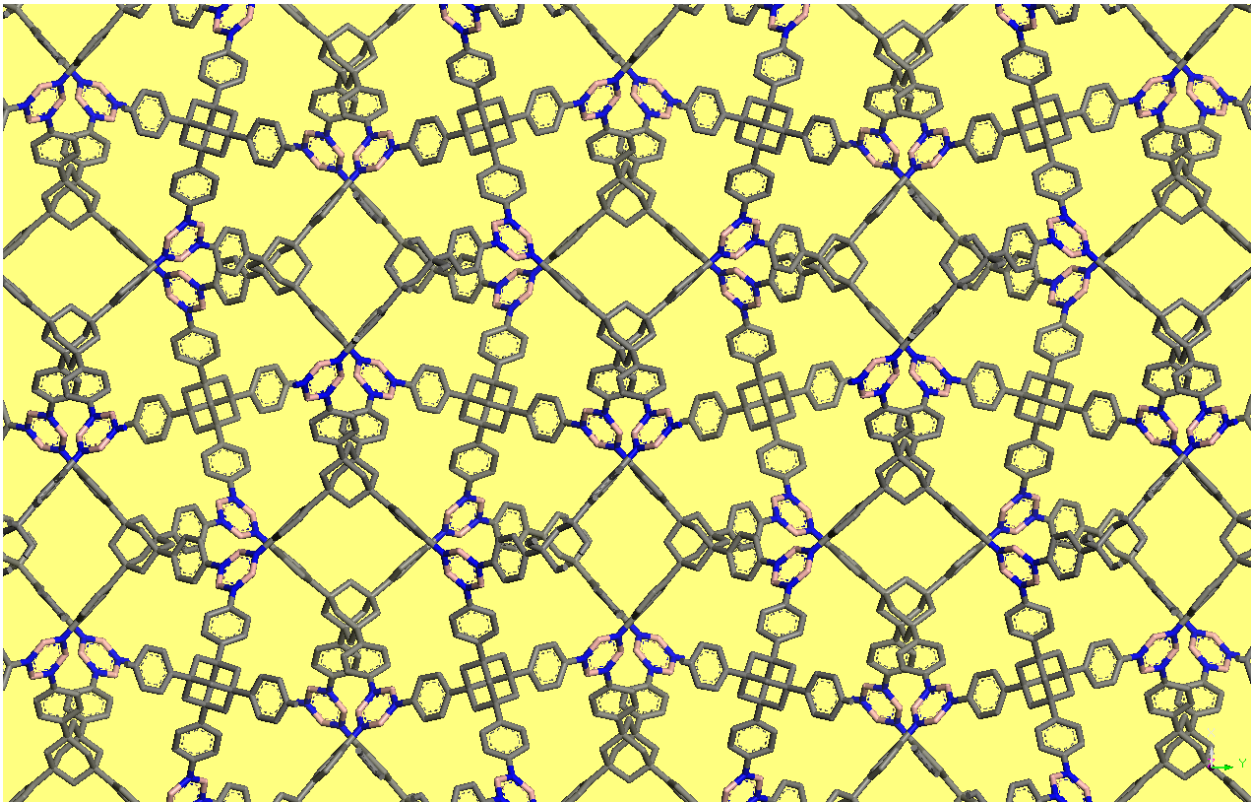

Figure 2.10. BLP-15(H) model using Materials Studio. *(pink spheres – boron; blue spheres – nitrogen; gray spheres – carbon; white spheres – hydrogen)*

Table 2.11: Fractional atomic coordinates for the **bor** conformation of BLP-15(H).

BLP-15(H)			
P-43*m* a = b = c = 32.8740 Å α = β = γ = 90º			
Atom	*x*	*y*	*Z*
B1	0.48655	-0.57405	-0.55269
N1	0.45947	-0.58049	-0.51874
C1	0.48913	-0.71292	-0.40312
C2	0.52502	-0.70217	-0.37379
C3	0.48040	-0.67747	-0.43254
C4	0.51272	-0.65920	-0.45406
C5	0.50607	-0.62690	-0.48072
C6	0.46639	-0.61355	-0.48994
C7	0.43375	-0.63332	-0.47024
C8	0.44063	-0.66388	-0.44142
C9	0.50000	-0.75000	-0.42924
H1	0.51509	-0.67619	-0.35451
H2	0.55261	-0.69254	-0.39055
H3	0.51413	-0.59650	-0.55754
H4	0.54365	-0.66971	-0.45068
H5	0.53243	-0.61255	-0.49415
H6	0.40257	-0.62550	-0.47720
H7	0.41421	-0.67712	-0.42714

Chapter 3: Synthesis of Highly Porous Borazine-Linked Polymers and Their Application to H_2, CO_2, and CH_4 Storage

3.1 Introduction

Recently there has been great interest in the design and synthesis of highly porous organic architectures due to their multifaceted potential use in applications that include storage, separation, conductivity, and catalysis.[131,132] The chemical composition, physical and textural properties are dictated during synthesis that allow for materials with enhanced properties relevant to their respective applications. With the exception of microcrystalline covalent-organic frameworks (COFs),[133,76-79] these polymeric materials are amorphous yet can possess considerable porosity and well-defined cavities which render them highly attractive especially in adsorptive gas storage.[5,134-140] Such desirable traits are imparted into organic materials through the use of rigid building blocks that direct the growth of polymer networks without the aid of templating agents.[131-140] In addition to customized porosity, polymerization processes can lead to pore wall functionalization that significantly enhance gas uptake and selectivity as demonstrated recently by El-Kaderi's group for benzimidazole-linked polymers.[125] Alternative methods for improved gas uptake (i.e. hydrogen) by porous architectures can also be accessed by the use of polarizable building units that increase hydrogen-framework interactions.[141] Along this line, we sought after the inclusion of borazine (B_3N_3) as a functionalized and polarizable building block into porous organic polymers.[95] Borazine is isostructural to the boroxine units found in COFs prepared

by boronic acid self-condensation reactions[76] and has been mainly used for the fabrication of BN-based ceramics or in organic optoelectronics.[142-146] However, up to date, the use of borazine for the preparation of porous polymers for gas storage remains fairly undeveloped.

Reported here are the synthesis and characterization of a new class of highly porous borazine-linked polymers and the investigation of their performance in gas (H_2, CO_2, CH_4) storage application under low pressure and cryogenic conditions. The synthesis of BLP-1(H) and BLP-12(H) was performed by thermolysis of 1,4-phenylenediamine and tetra-(4-aminophenyl)methane borane adducts in monoglyme to afford the corresponding polymers as white powders in good yields (Scheme 3.1).

Scheme 3.1. Synthesis of BLP-1(H) and BLP-12(H) from in situ thermal decomposition of arylamine-borane adducts.

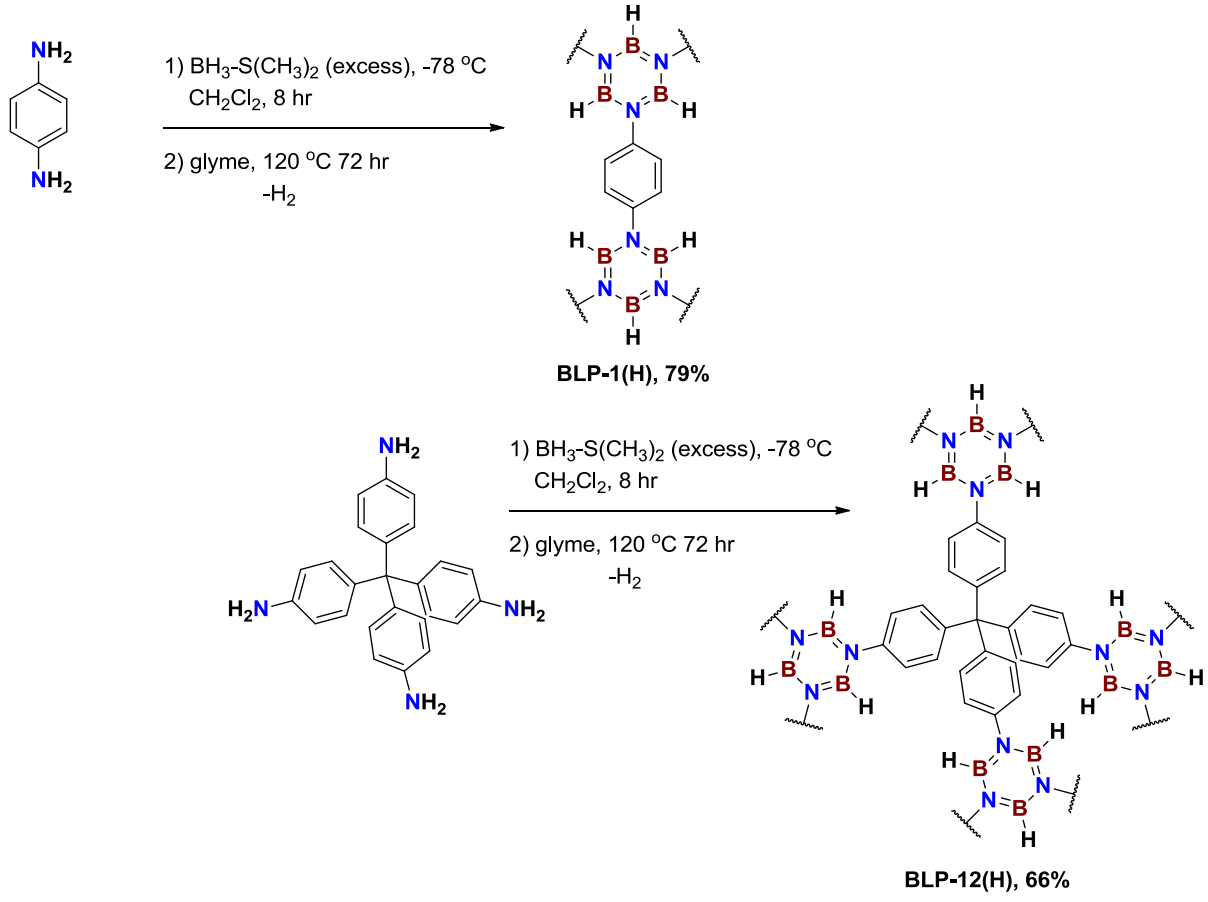

3.2 Experimental

All starting materials and solvents, unless otherwise noted, were obtained from the Acros Organics Co. and used without further purification. *P*-phenylenediamine was purified by sublimation. Tetrahydrofuran (THF) and monoglyme were distilled over sodium and benzophenone and dichloromethane (DCM) was distilled over CaH_2. *Tetra*-(4-aminophenyl)methane was synthesized according to a published method.[147] The isolation and handling of all products were performed under an inert atmosphere of nitrogen using either glove box or Schlenk line techniques.

p-phenylenediamine-borane, $C_6H_4(NH_2{\cdot}BH_3)_2$. A 100 ml Schlenk flask was charged with *p*-phenylenediamine (200 mg, 1.85 mmol) and 100 ml of anhydrous DCM. The solution was cooled to -78 ºC in an acetone/dry ice bath and treated with borane-dimethylsulfide (1.05 ml, 11.1 mmol, Aldrich) drop-wise under a flow of nitrogen. The clear solution was allowed to warm to room temperature while stirring overnight. On the following day, the white solid material is filtered and washed with DCM (3x15ml). ^{1}H NMR (300 MHz, DMSO-d_6): δ 7.39 (s, 4H), 7.11 (s, 4H), 1.51 (s, br, 6H). ^{13}C NMR (75 MHz, DMSO-d_6): δ 123.1, 141.3.

BLP-1(H). A Pyrex tube was charged with *p*-$C_6H_4(NH_2{\cdot}BH_3)_2$ (35 mg, 0.26 mmol) and 2 ml of glyme. The tube was flash frozen at 77 K, evacuated and flame sealed. The reaction mixture was heated in a programmable oven at 0.1 ºC/min to 120 ºC for 24 h to afford a fluffy white polymer which was isolated by filtration over a medium glass frit and washed with anhydrous THF (3 x 15 ml). Anal. Calcd.for ($C_9H_9B_3N_3$): C, 56.4%; H, 4.7%; N, 21.9%. Found: C, 55.9%; H, 5.1%; N, 18.2%.

***tetra*(phenyl)methane:** A mixture of triphenylmethylchloride (18.4 g, 66 mmol) and aniline (16.8 g, 177 mmol) were heated to 200 °C for five minutes and cooled to 90 °C. This was

treated with 100 ml of 2M HCl and 90 ml of methanol and refluxed briefly. A hard gray solid formed which had to be pulverized with mortar and pestle. The gray solid was then filtered and dissolved in 130 ml of ethanol and 20 ml of concentrated sulfuric acid. The mixture was cooled to -10 °C and 15 ml of isoamylnitrite was added. After stirring the mixture for about thirty minutes 30 ml of 50% hypophosphorous acid was added at -10 °C and heated to reflux. An light solid was filtered off. This crude product was washed with ethanol and 1,4-dioxane to yield *tetra*(phenyl)methane solid at 78% yield. Melting Point: 275 °C.

Scheme 3.2. Synthesis of tetraphenylmethane

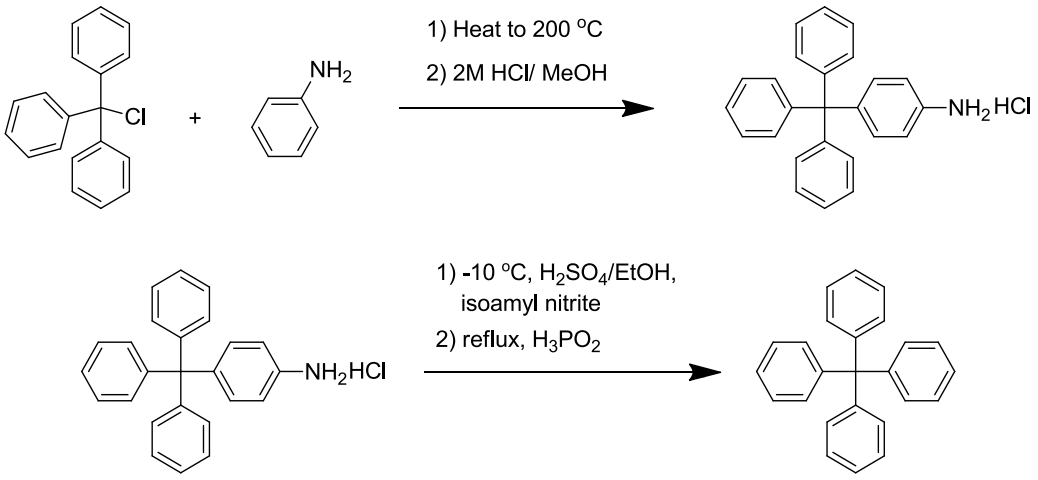

***tetra*(*p*-nitrophenyl)methane.** To tetraphenylmethane (10.0 g, 46.8 mmol) 60 ml of fuming nitric was added in portions at -10 °C with vigorous stirring. To this mixture 17 ml of acetic anhydride and 34 ml of glacial acetic acid was slowly added and stirred for about 15 minutes. Finally the reaction mixture was diluted with 100 ml of glacial acetic acid. The resulting yellow solid washed with acetic acid and methanol. The crude product was recrystallized with DMF to get yellow crystals of *tetra*(*p*-nitrophenyl)methane (8.9 g, 38.0% yield). ^{1}H NMR (300 MHz,

DMSO-d_6): δ 8.51 (d, 8H, Ar-H, J = 9.0 Hz), 7.85 (d, 8H, Ar-H, J = 8.9 Hz) d; ^{13}C NMR (75 MHz, DMSO-d_6): δ 146.6, 136.9, 132.1, 113.6, 62.2.

Scheme 3.3. Synthesis of tetra(p-nitrophenyl)methane

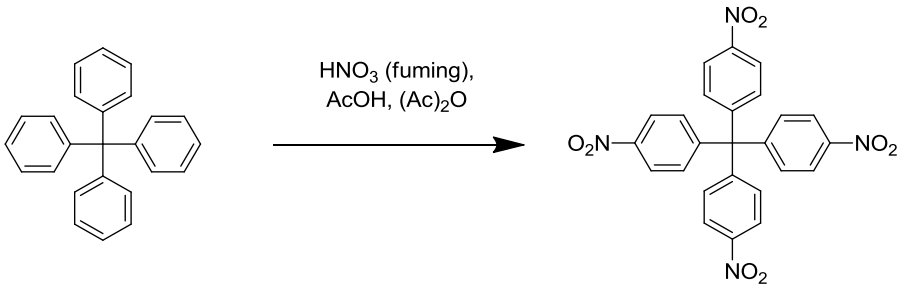

***tetra*(*p*-aminophenyl)methane.** To tetra(p-nitrophenyl)methane (1.50 g, 2.99 mmol) in 100ml of THF, 2.00 g (excess) of hydrazine monohydrate and ~10.0 g of Raney-nickel were added and refluxed for about 3 hours. The mixture was hot filtered and washed with ethanol. Solvent evaporated and the residue washed with ethanol and dried to get 0.70 g of *tetra*(*p*-aminophenyl)methane in 61% yield. ^{1}H NMR (300 MHz, DMSO-d_6): δ 6.67 (d, 8H, Ar-H, J = 8.7 Hz), 6.38 (d, 8H, Ar-H, J = 8.7 Hz), 4.96 (s, 8H, Ar-*NH2*); ^{13}C NMR (75 MHz, DMSO-d_6): δ 146.3, 136.5.0, 131.9, 113.4, 61.7.

Scheme 3.4. Synthesis of tetra(4-aminphenyl)methane

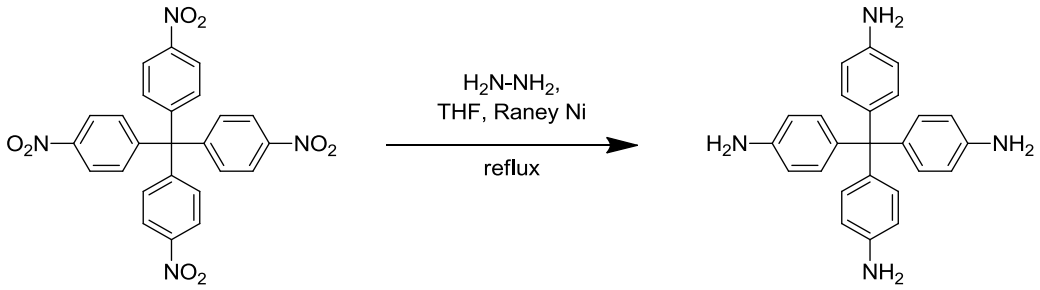

***tetra*-(4-aminophenyl)methane-borane, $C(C_6H_4NH_2{\cdot}BH_3)_4$.** A 100 ml Schlenk flask was charged with *tetra*-(4-aminophenyl)methane (100 mg, 0.26 mmol) and 100 ml of anhydrous DCM. The suspension was cooled to 0 ºC in an ice bath under a flow of nitrogen and treated with borane-dimethylsulfide (0.30 ml, 3.16 mmol) drop-wise. The clear solution was allowed to warm to room temperature while stirring overnight. On the following day, the white solid material is filtered and washed with DCM (3 x 15ml). ^{1}H NMR (300 MHz, DMSO-d_6): δ 7.47 (s, br, 8H), 7.14-7.17 (m, 16H), 1.59 (s, br, 12H). ^{13}C NMR (75 MHz, DMSO-*d_6*): δ 63.8, 122.4, 131.2, 141.7, 144.2.

Further characterization by Mass Spectrometry and elemental analysis were unsuccessful due to the instability of the amine-borane adduct in the absence of solvents and due polymerization upon heating under elemental analysis testing conditions.

BLP-12(H). A Pyrex tube was charged with 30 mg of $C(C_6H_4NH_2{\cdot}BH_3)_4$ (35.0 mg, 0.08 mmol) was dissolved in 2 ml of glyme. The tube was flash frozen at 77 K, evacuated and flame sealed. The reaction mixture was heated in a programmable oven at 0.1 ºC/min to 120 ºC for 24 h to afford a fluffy white polymer which was isolated by filtration over a medium glass frit and washed with anhydrous THF (3 x 15 ml).Anal. Calcd. for ($C_{75}H_{60}B_{12}N_{12}$): C, 71.54%; H, 4.80%; N, 13.35%. Found: C, 60.93%; H, 4.94%; N, 9.87%.

Organoboron compounds typically give lowered carbon values in elemental microanalysis due to the formation of non-combustible boron carbide byproducts.[76]

Inside a glove-box, about 150 mg of as-prepared sample of BLP was loaded into an Autosorb cell then heated to 120 °C under dynamic vacuum (1.0 x 10^{-5} torr) for 16 h. The

sample was back-filled with nitrogen to exclude adsorption of moisture prior to N_2 adsorption measurements.

Gas Sorption Measurements. Nitrogen experiments were run using a Quantachrome Autosorb 1-C analyzer at 77 K. Pore Size Distributions (PSDs) were calculated using Non-Local Density Functional Theory (NLDFT) on the adsorption branch with a spherical/cylindrical pore model. Hydrogen sorption experiments were run on the same Quantachrome Autosorb 1-C analyzer at both 77 K and 87 K. Methane and carbon dioxide experiments were run at 273 K and 293 K each. Ultrahigh purity helium (99.999%) was used to calibrate the free volume in the sample cell before each measurement. For H_2 uptake measurement, hydrogen with purity of 99.999% was used. CO_2 (99.9%) and CH_4 (99.999%) were obtained from Airgas Inc. (Radnor, PA).

Heat of Adsorption Calculations. Using the data taken at 77 K and 87 K, the isosteric heat of adsorption for each polymer was calculated according to previous reports[148] by solving the virial-type expression:

$$\ln P = \ln N + (1/T)\sum_{i=0}^{m} a_i N^i + \sum_{i=0}^{n} b_i N^i$$

where P is pressure in torr, T is temperature in Kelvin, and N is the mmol of gas adsorbed per gram of sample. The values for *m* and *n* were varied such that $m \geq n$ and resulted in the best fit as determined by the sum of the squares of the errors. The values for a_0, a_1,…a_m were used in the calculation for the isosteric heat of adsorption, Q_{st}:

$$Q_{st} = -R\sum_{i=0}^{m} a_i N^i$$

The calculated values were plotted as they relate to surface coverage, and the isosteric heat of adsorption values at the point of zero-coverage were highlighted in the text.

3.3 Results and Discussion

The chemical composition and connectivity of the building units were investigated by spectral and analytical methods which included FT-IR, solid-state ^{11}B and ^{13}C CP-MAS, and elemental analysis. By observing the loss of certain stretches expected for dehydrocoupling reactions combined with the appearance of borazine-characteristic peaks, the formation of the expected products can be confirmed. FT-IR spectra of starting materials, BLP-1(H) and BLP-12(H) were obtained as KBr pellets using Nicolet - Nexus 670 spectrometer. The bands at 3300-3500 cm^{-1} that correspond to the N-H stretching of amine/amine-borane adducts are significantly reduced after polymerization, however, the remaining weak signals are due to N-H stretches from unreacted $–NH_2$ on the surface of the polymers' particles and incompletely reacted groups at defects in the material. The aromatic C-H stretching was observed around 2800-3100 cm^{-1}. Borane B-H peaks in adducts were observed at approximately 2400 cm^{-1} while a slight shift to about 2550 cm^{-1} occurs after the formation of the borazine ring during polymerization. The intensity of the B-H band in the amine-borane adducts is significantly reduced upon borazine formation. The N-H band stretch of the amine is greatly reduced indicating a release of the amine hydrogen atoms from the starting material. The strong stretch appearing at 1400 cm^{-1} also supports the formation of the B-N bonds of the borazine ring.[95,149-151]

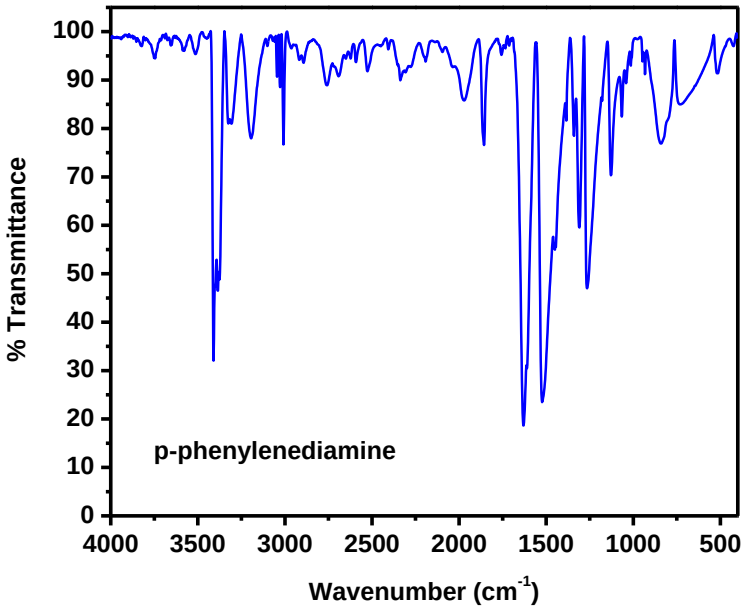

Figure 3.1: FT-IR spectrum of *p*-phenylenediamine.

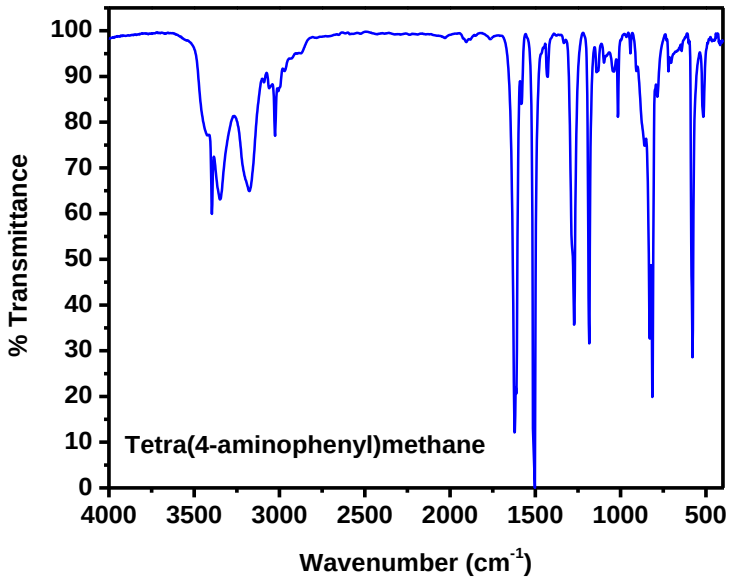

Figure 3.2: FT-IR spectrum of *Tetra*-(4-aminophenyl)methane.

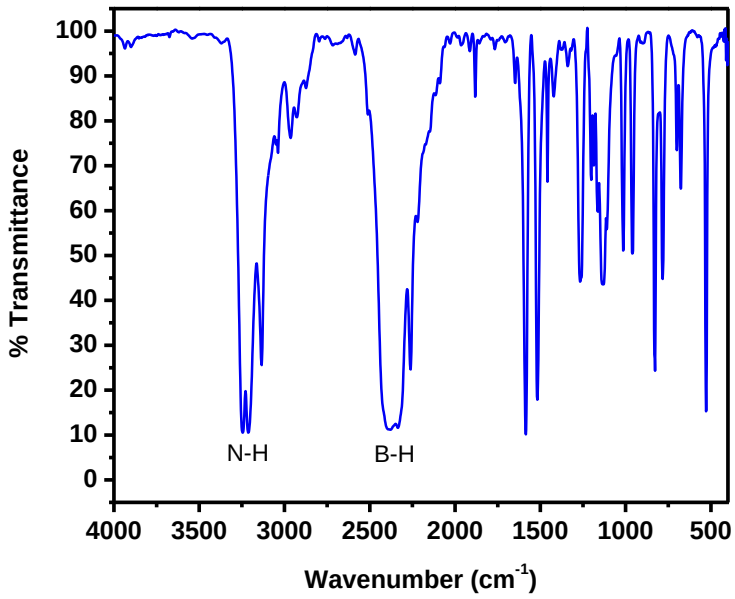

Figure 3.3: FT-IR spectrum of *p*-$C_6H_4(NH_2{\cdot}BH_3)_2$.

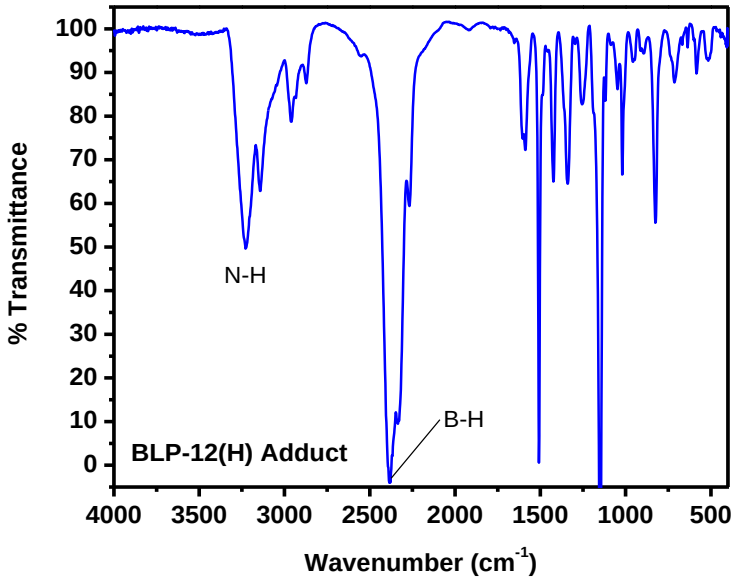

Figure 3.4: FT-IR spectrum of $C(C_6H_4NH_2{\cdot}BH_3)_4$.

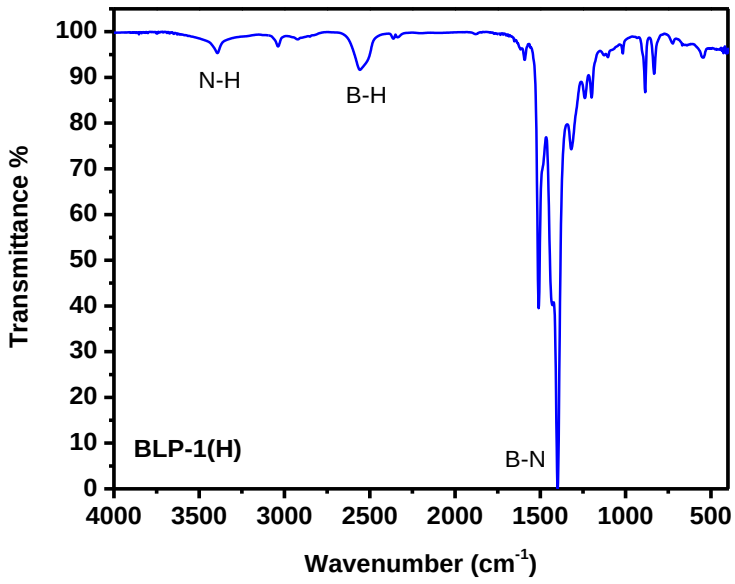

Figure 3.5: FT-IR spectrum of BLP-1(H).

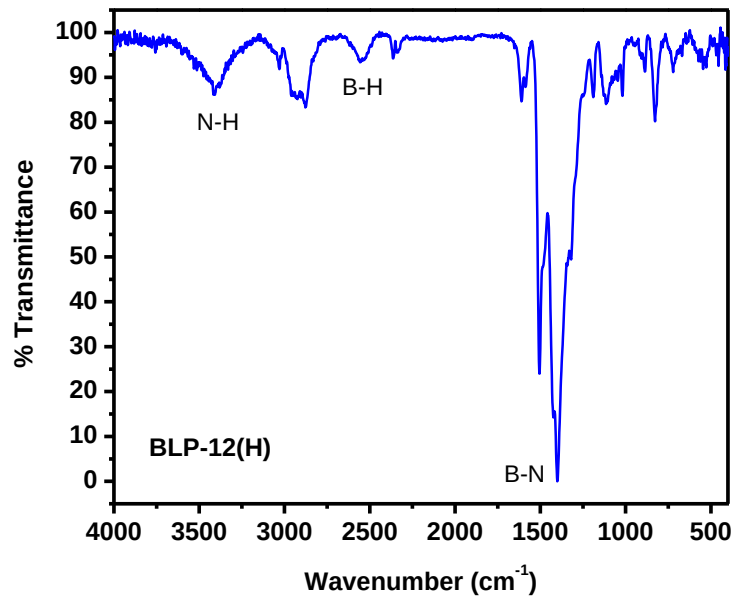

Figure 3.6: FT-IR spectrum of BLP-12(H).

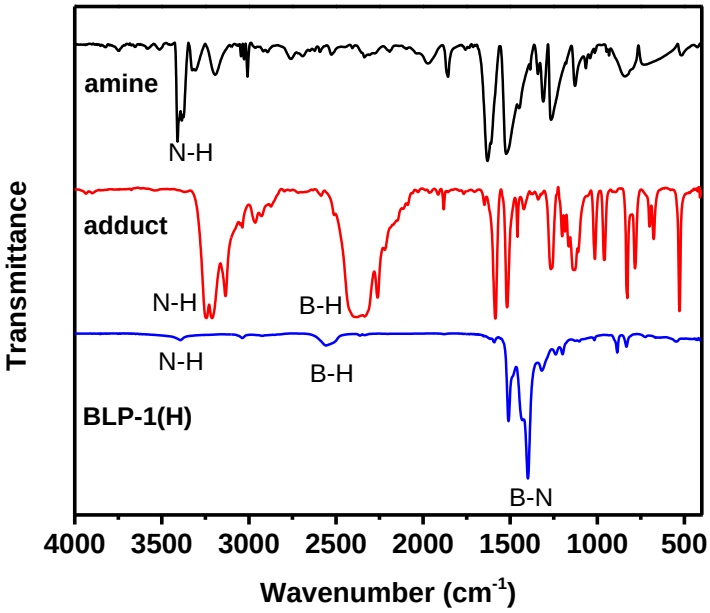

Figure 3.7: FT-IR spectrum of BLP-1(H) and starting materials.

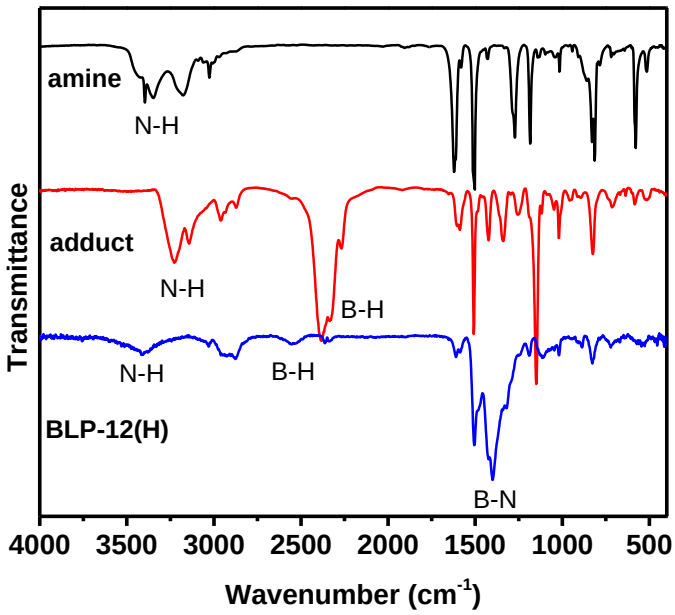

Figure 3.8: FT-IR spectrum of BLP-12(H) and starting materials.

We have also collected solid-state ^{11}B and ^{13}C CP-MAS to establish the connectivity and coordination number of boron and to verify the inclusion of intact building units into the framework of BLPs. Solid-state NMR spectra were recorded at ambient temperature on a 360-1 instrument by Spectral Data Services, Inc., Champaign, IL. ^{11}B MAS NMR data were collected with a 45 degree ^{11}B pulse length and a recycle delay of two seconds. High-power H-1 decoupling was employed during acquisition only. Samples were spun at the magic angle at about 7 kHz. Chemical shifts are referenced to external neat boron trifluoroetherate. The ^{13}C CP-MAS signals which appear as broad peaks in the aromatic range support the incorporation of intact phenyl and tetraphenylmethane cores into the networks of BLP-1(H) and BLP-12(H), respectively as seen in Figures 3.9 and 3.10 (*asterisks represent spinning side bands)*. The ^{11}B signals for both polymers appear as very broad peaks centered around 10.8 ppm for BLP-1(H) and 10.1 ppm for BLP-12(H). These measurements are consistent with reported values for borazine-containing polymers (0-40 ppm)[152,153] and are in sharp contrast to tetra-coordinated boron sites found in borane-amine adducts or cycloborazanes (0 to -45 ppm).[154-156]

A

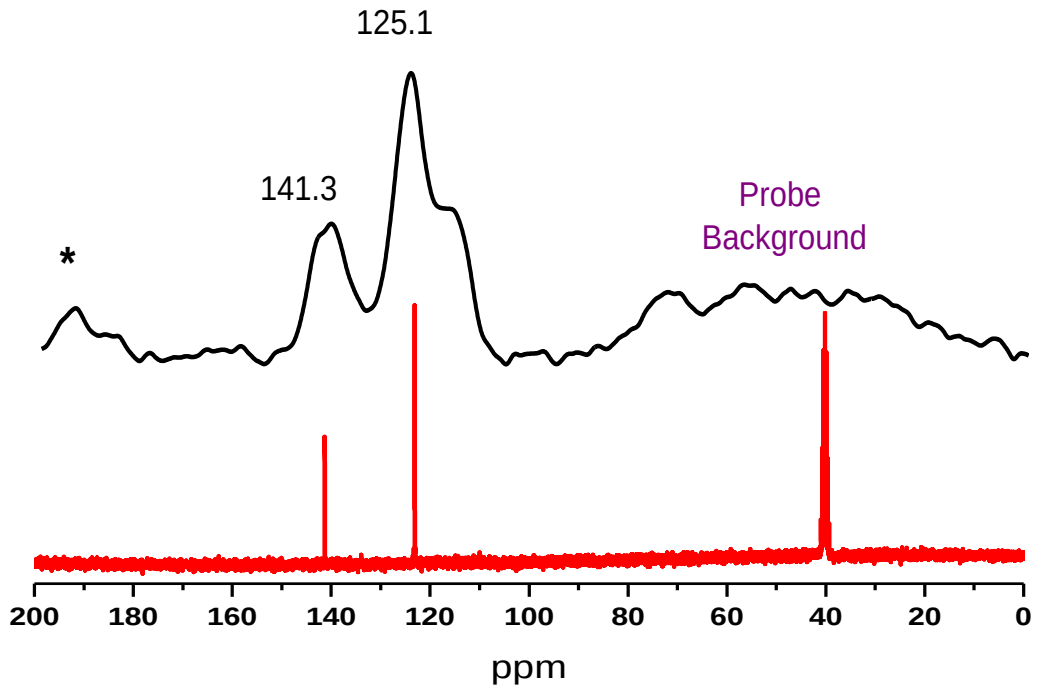

B

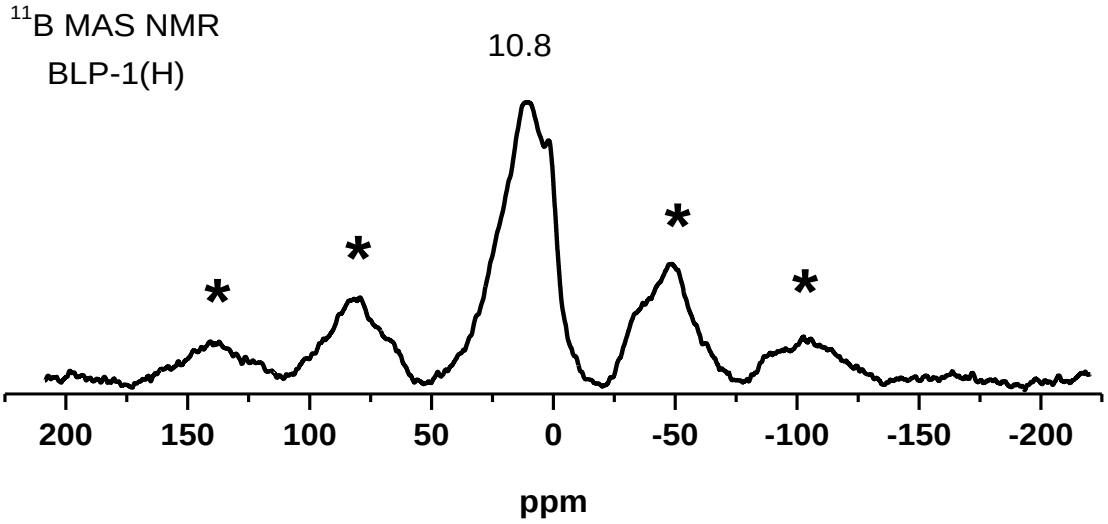

Figure 3.9: Solid state ^{13}C CP-MAS NMR (A) and ^{11}B MAS NMR (B) spectra for BLP-1(H). Red line – ^{13}C NMR of phenylenediamine-borane.

A

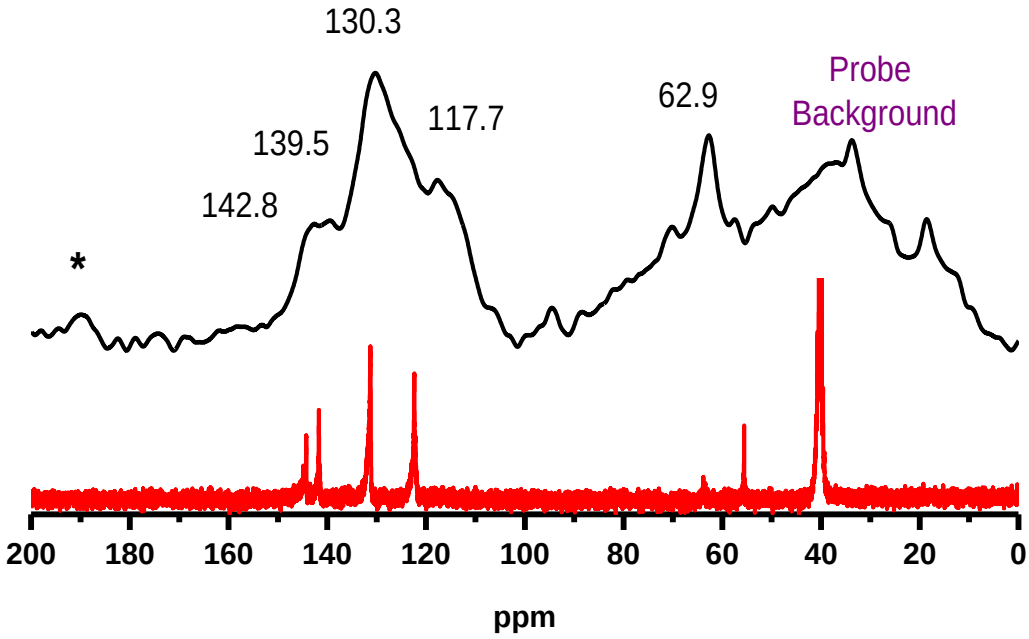

B

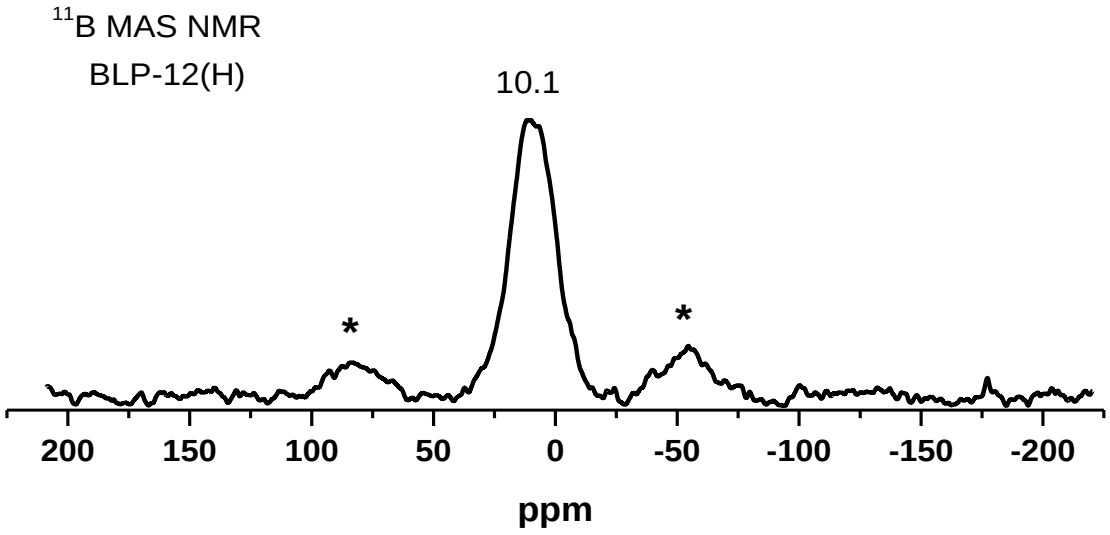

Figure 3.10: Solid state ^{13}C CP-MAS NMR (A) and ^{11}B MAS NMR (B) spectra for BLP-12(H). Red line – ^{13}C NMR of tetra(4-aminophenyl)methane-borane.

BLPs were isolated under an inert atmosphere followed by degassing at 120°C / 1.0 x 10^{-5} torr for 16 hrs. In order to determine the phase purity of products, scanning electron microscopy (SEM) was used to scan for the morphology present in the sample. A sample was prepared by dispersing the material onto a sticky carbon surface attached to a flat aluminum sample holder. The sample was then gold coated using an EMS (Electron Microscopy Sciences) 550x Sputter Coater at $1x10^{-1}$ mbar of pressure in a nitrogen atmosphere for 120 seconds while maintaining 20 mA of current. Samples were analyzed on a Zeiss EVO XVP Scanning Electron Microscope using the SEI detector with accelerating voltages ranging from 10 kV to 20 kV. SEM on as-prepared materials revealed a homogeneous morphology of spherical particles ~150 nm for BLP-1(H), and platelet particles ~200 nm for BLP-12(H) indicating phase purity (Figures 3.11 and 3.12). Only one type of morphology was found to exist in each polymer, confirming the purity of the material produced. Powder x-ray diffraction studies on as-prepared and activated materials indicated that both polymers are amorphous.

A

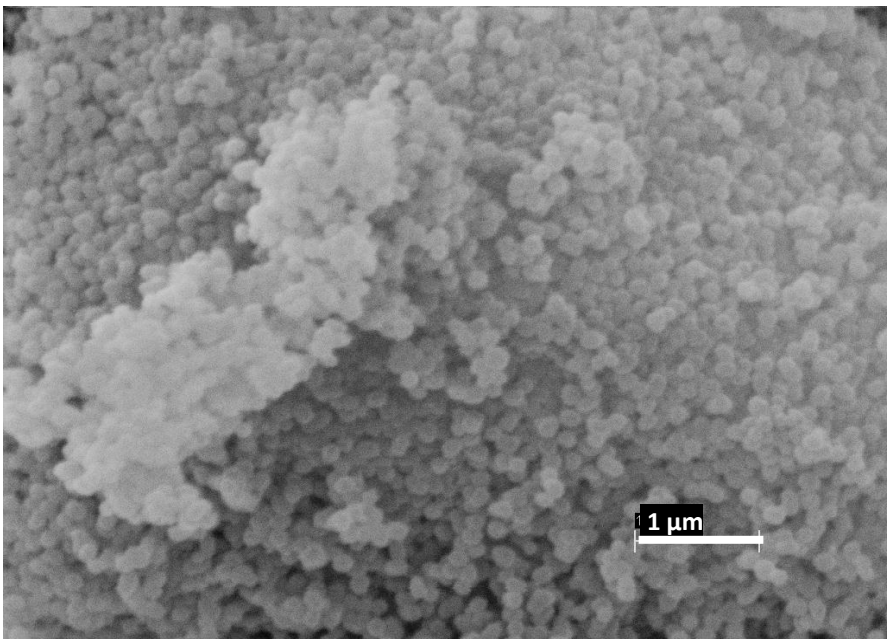

B

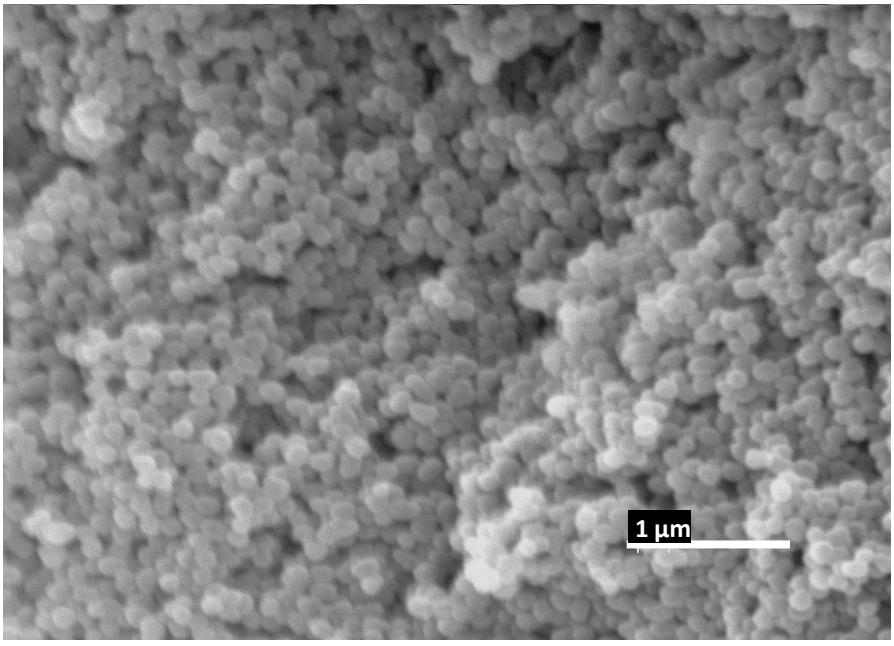

Figure 3.11: SEM image of BLP-1(H) revealing a uniform spherical morphology.

A

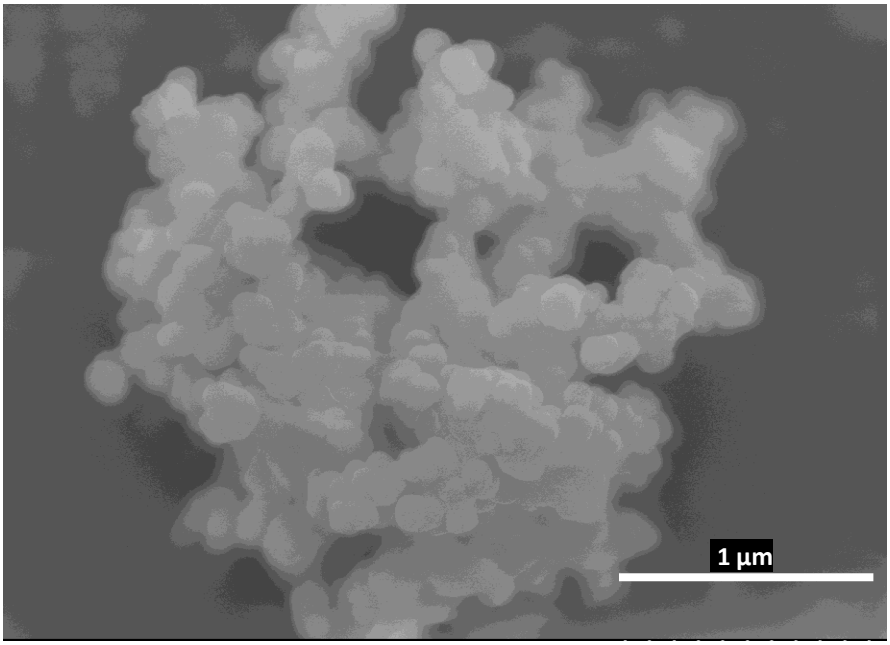

B

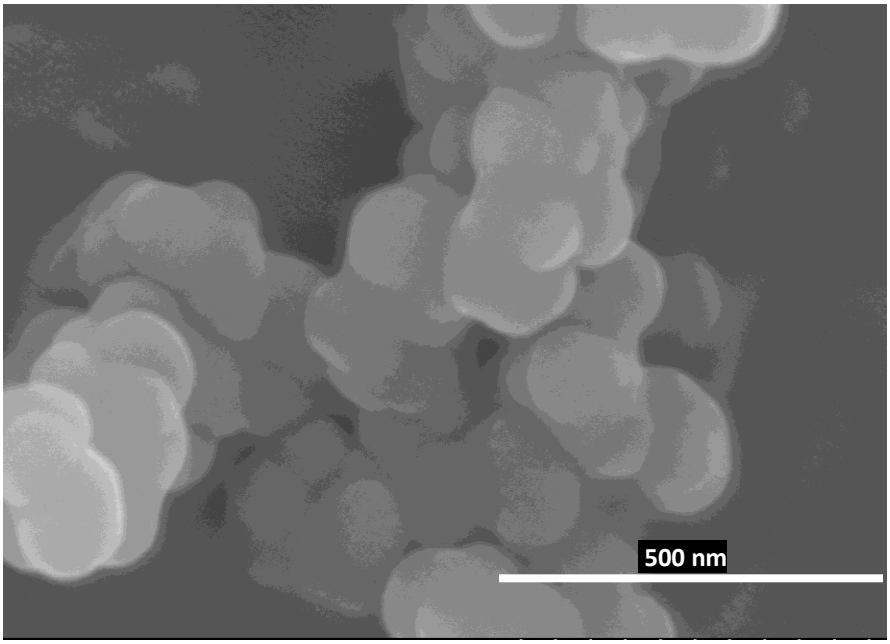

Figure 3.12: SEM image of BLP-12(H) revealing a uniform platelet morphology.

Given the fact that borazine is isostructural to the boroxine unit found in COFs such as COF-1 and COF-102, we anticipated BLPs to be thermally stable and highly porous. Therefore we subjected BLPs to thermogravimetric analysis and nitrogen porosity measurements. BLP-1(H) and BLP-12(H) were analyzed by TGA to determine the thermal stability of the material produced as well as confirm that all guests have been removed. Samples were run on a TA Instruments Q-5000 series thermal gravimetric analyzer with samples held in platinum pans under an atmosphere of nitrogen. The TGA traces of the as-prepared materials undergo substantial weight loss, presumably due to pore evacuation of solvent molecules and unreacted adducts, upon heating under nitrogen atmosphere and remain stable up to 400 °C. This is a typical behavior of porous materials in general and has been reported for porous covalent frameworks.[76]

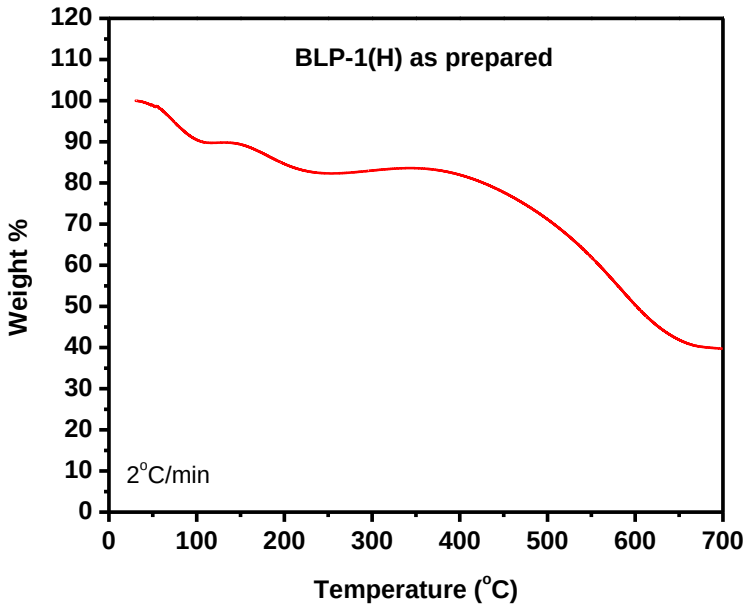

Figure 3.13: TGA trace for an unactivated sample of BLP-1(H).

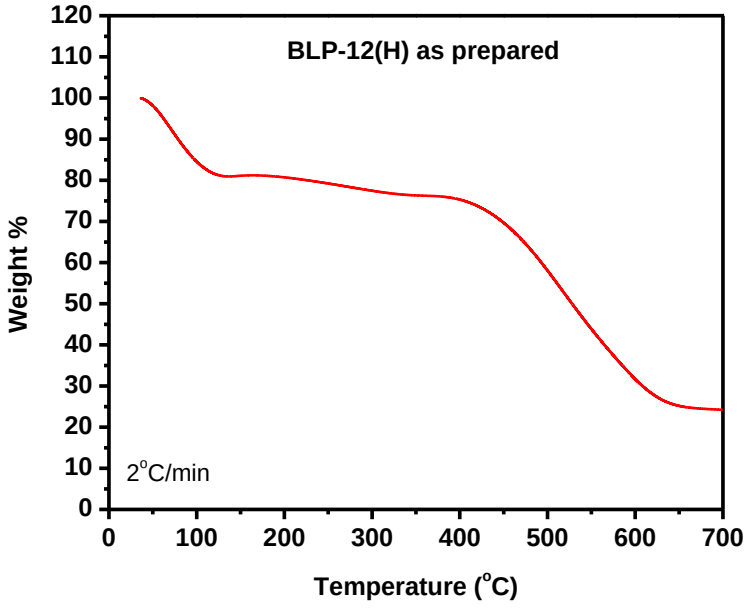

Figure 3.14: TGA trace for an unactivated sample of BLP-12(H).

Based on TGA studies and the thermal stability of BLPs we activated both materials by degassing at 120 °C and 1 x 10^{-5} torr for 16 hrs prior to nitrogen porosity measurements. The Type I nitrogen isotherms (Figure 3.15) are consistent with permanent microporous materials that are characterized by a sharp uptake at $P/P_o = 10^{-4}$ to 10^{-2}, while the final rise in the nitrogen uptake is due to condensation in intermolecular cavities created by the packing of BLP particles. The Brunauer-Emmett-Teller (BET) model was applied to each isotherm for P/P_o between 0.05 and 0.15 and resulted in surface areas of 1360 and 2244 m^2/g for BLP-1(H) and BLP-12(H), respectively. The Langmuir model (P/P_o = 0.05-0.30) gave surface area values of 1744 and 2866 m^2/g. The surface area of BLP-1(H) is considerably higher than related covalent nets: COF-1 (711 m^2/g),[76] CTF-1 (791 m^2/g),[79] and halogenated BLPs (503-1364 m^2/g),[7] while the surface area of BLP-12(H) is among the highest for organic polymers. The pore volumes (Vp) calculated at P/P_o = 0.90 were 0.69 cm^3/g for BLP-1(H) and 1.08 cm^3/g for BLP-12(H). Pore size distributions were estimated using density functional theory (DFT) calculations which revealed narrow pore-size distributions centered at about 12.7 Å.

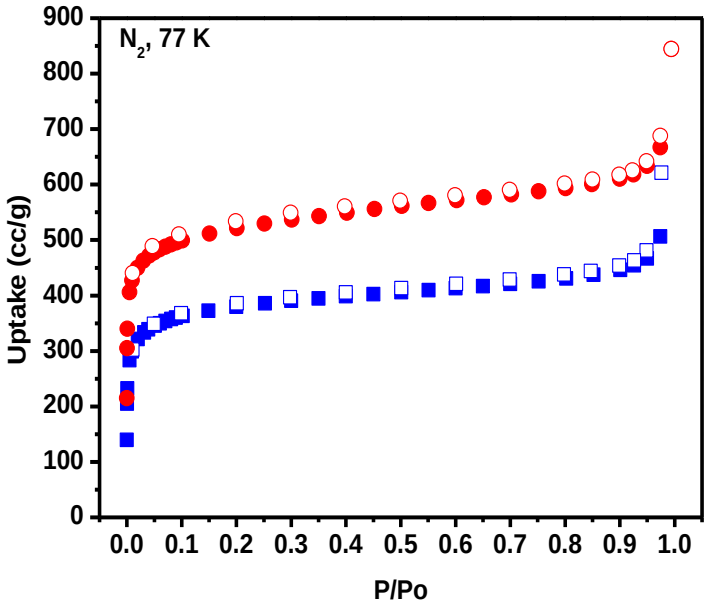

Figure 3.15: N_2 adsorption isotherm for BLP-1(H) (blue) and BLP-12(H) (red) measured at 77 K. The filled squares are adsorption points and the empty squares are desorption points.

Pore Size Distributions (PSDs) were calculated using Non-Local Density Functional Theory (NLDFT) on the adsorption branch with a cylindrical/sphere pore model on the nitrogen experiments combined with data taken from carbon dioxide sorption experiments performed at 273 K as has been reported previously.[76] Experimental N_2 adsorption isotherm for BLP-1(H) and BLP-12(H) measured at 77 K is shown in Figure 3.16 and 3.17 as filled squares. The calculated NLDFT isotherm is overlaid as open squares. Note that a fitting error of < 1 % indicates the validity of using this method for assessing the porosity of BLPs. The fitting error is indicated. BET plot for BLP-1(H) calculated from the N_2 adsorption isotherm at 77 K. The model was applied from P/P_o= 0.05-0.15. The correlation factor is indicated in the graphs. The Langmuir plots for BLP-1(H) and BLP-12(H) calculated from the N_2 adsorption isotherm at 77 K are also shown. The model was applied from P/P_o= 0.05-0.30. The correlation factor is indicated.

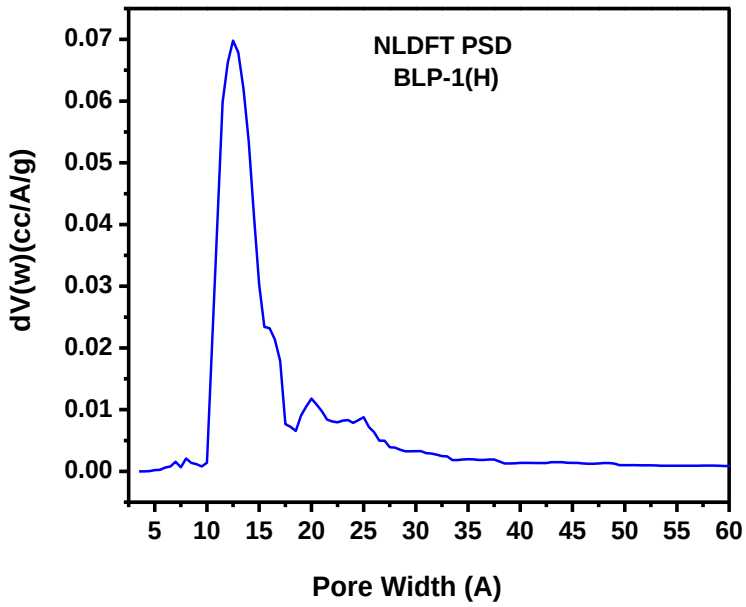

Figure 3.16: NLDFT Pore Size Distribution for BLP-1(H)

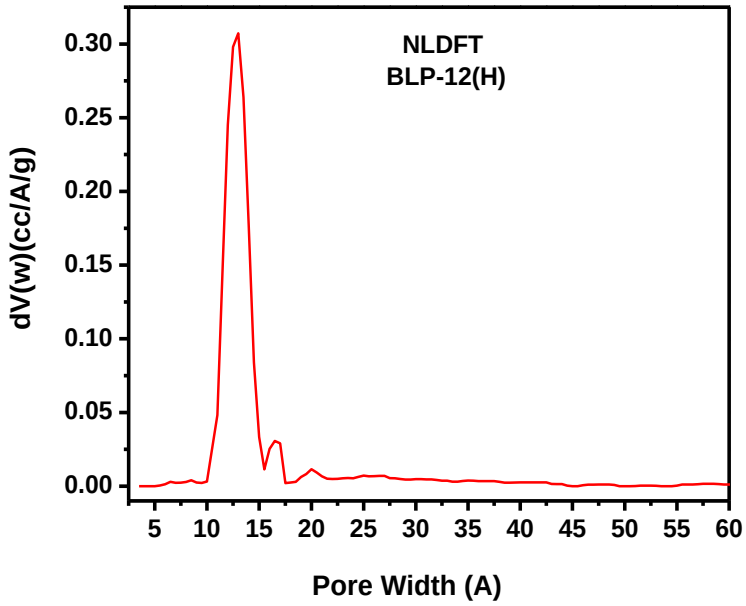

Figure 3.17: NLDFT Pore Size Distribution for BLP-12(H)

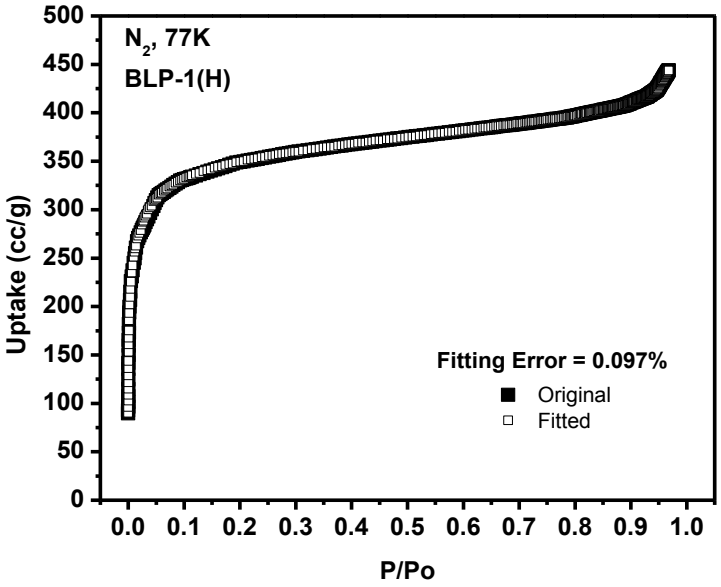

Figure 3.18: Experimental N_2 adsorption vs. calculated NLDFT isotherm for BLP-1(H)

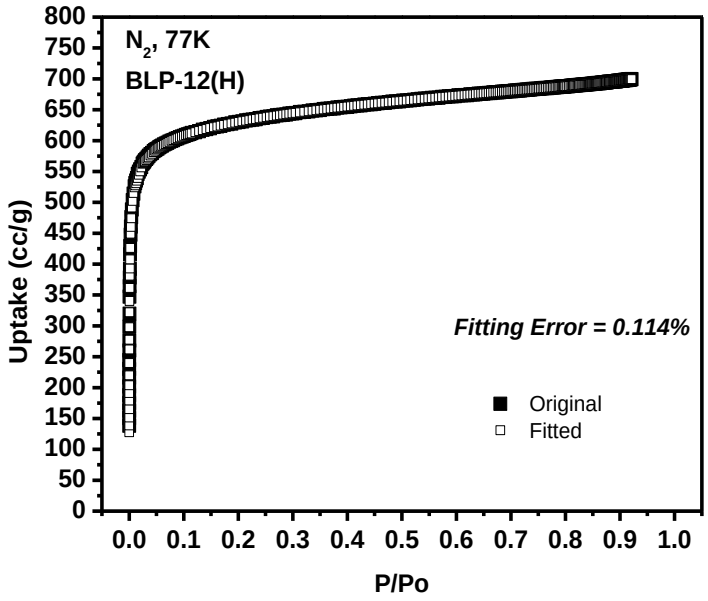

Figure 3.19: Experimental N_2 adsorption vs. calculated NLDFT isotherm for BLP-12(H)

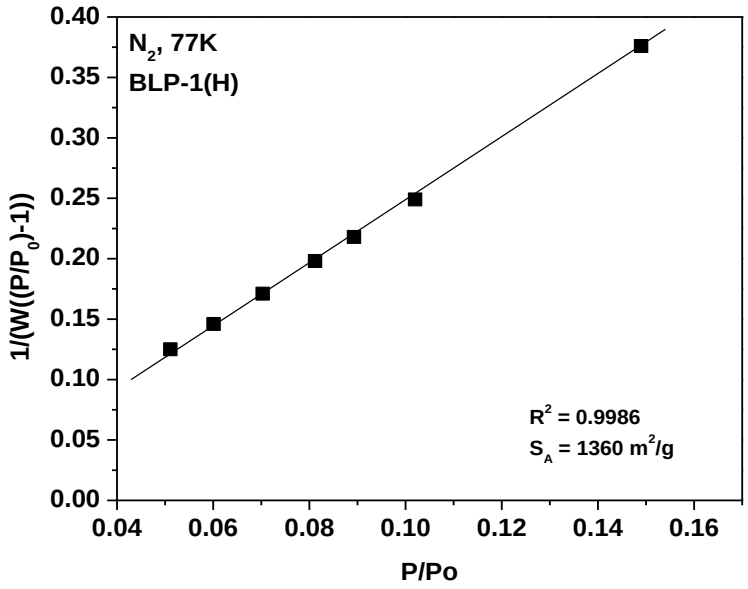

Figure 3.20: BET plot for BLP-1(H)

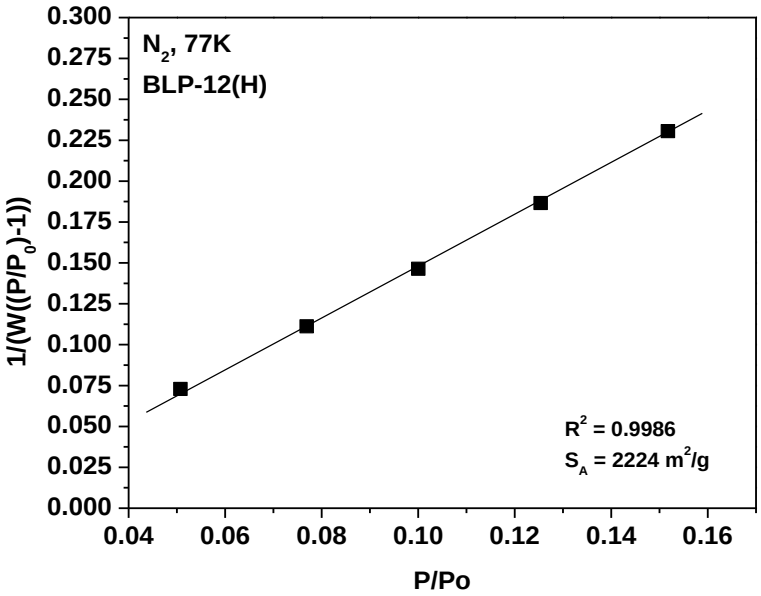

Figure 3.21: BET plot for BLP-12(H)

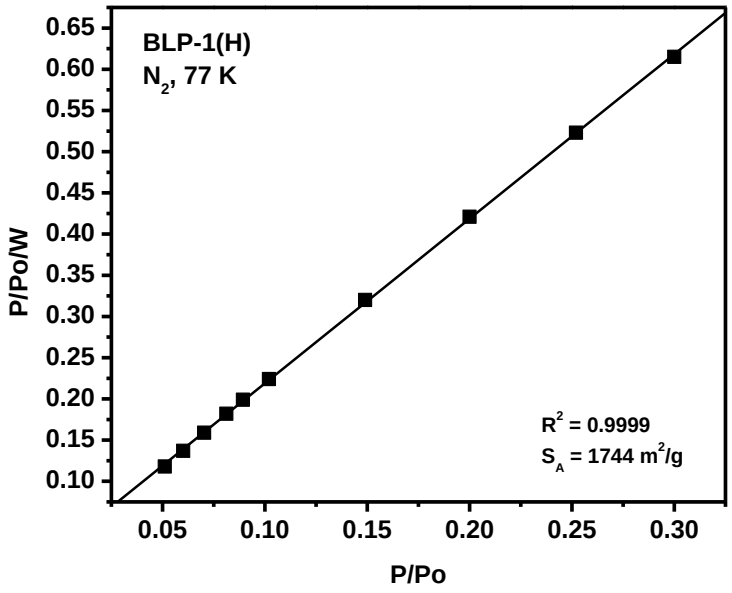

Figure 3.22: Langmuir plot for BLP-1(H)

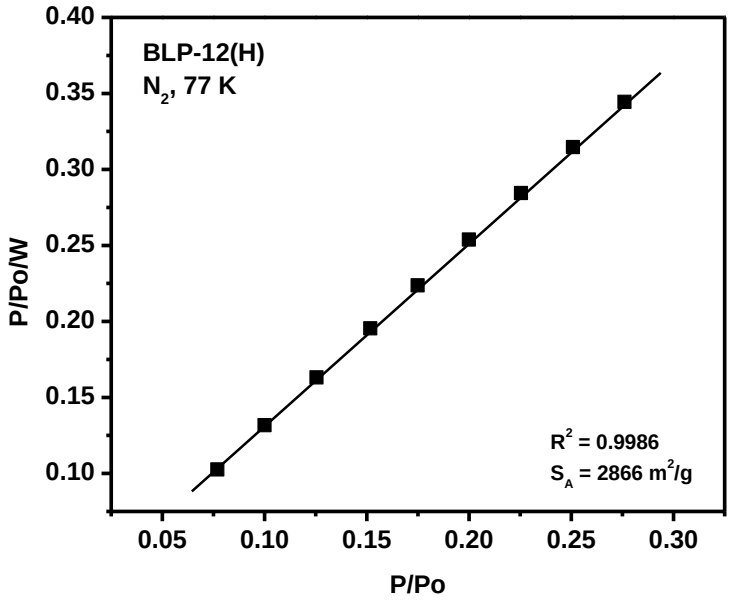

Figure 3.23: Langmuir plot for BLP-12(H)

Once the porosity of BLPs had been established, we considered their performance in gas storage. Hydrogen is among the leading candidates for future use in automotive applications because of its abundance, renewability, and clean aspects.[158] Physisorbed hydrogen storage is highly attractive because of the rapid uptake and release of hydrogen.[157-159] However, the weak interactions between hydrogen molecules and pore walls necessitate the use of low temperatures and elevated pressure conditions to offset the usually low heat of adsorption. Therefore, developing new materials with enhanced storage properties to meet targets set by the US Department of Energy for 2015 (5.5 wt% hydrogen and 0.040 kg hydrogen/L) remains a considerable challenge.[33]

We collected hydrogen isotherms at 77 K and 87 K (Figure 3.24) and calculated the hydrogen isosteric heats of adsorption (Q_{st}) using the virial method.[160] The H_2 uptake for BLP-1(H) (1.33 wt%) is lower than that of BLP-12(H) (1.93 wt%) yet both are higher than our previously reported halogenated BLPs (0.68-1.30 wt%).[95] Moreover, despite their amorphous nature, the performance of BLPs in hydrogen storage is very comparable with other organic polymers of similar surface areas. For example, under similar conditions the analogous crystalline COF-1[5] and CTF-1[79] store 1.28 and 1.55 wt% of H_2, respectively, the hydrogen uptake by BLPs is also similar to those of purely organic polymers such as hypercrosslinked polymer networks synthesized by the self-condensation of bischloromethyl monomers (0.89-1.69 wt%),[85] nitrogen-linked nanoporous networks of aromatic rings (0.01-0.85 wt%),[161] and polymers of intrinsic microporosity (PIMs) which recently have been reported to be among the best organic polymers for hydrogen uptake (0.74-1.83 wt%).[162] In contrast, activated carbon such as PICACTIF-SC, AX-21, and zeolite-templated show a noticeably higher uptake (1.90, 2.40, and 2.60 wt%, respectively) due to their ultrafine pores.[49,163] The Q_{st} values for hydrogen

at low coverage were found to be 6.8 kJ/mol (BLP-1(H)) and 6.0 kJ/mol (BLP-12(H)) and drop at higher loading to reach 5.5 and 4.8 kJ/mol, repectively (Fig, S27, S29, ESI). These Q_{st} values are similar to those reported for organic polymers such as POFs (5.8-8.3),[138,139] 2D COFs (6.0-7.0 kJ/mol),[5] polyimide networks (5.3-7.0 kJ/mol),[136,137] PPNs (5.5-7.6 kJ/mol),[140] and BILP-1 (7.9 kJ/mol)[125] and are much higher than values reported for 3D COFs: COF-102 (3.9 kJ/mol), COF-103 (4.4 kJ/mol), and the carbon-based porous aromatic framework PAF-1 (4.6 kJ/mol).[93] As expected, these Q_{st} values fall below those of the halogenated BLPs (7.1-7.5 kJ/mol)[95] which is most likely due to the higher polarization level of the borazine rings in halogen decorated BLPs.

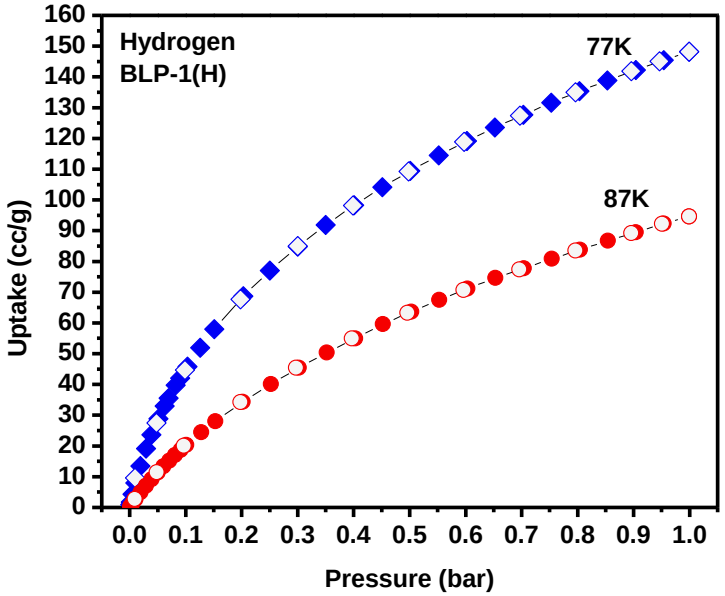

Figure 3.24: H_2 adsorption isotherms for BLP-1(H) measured at 77 K (red circles) and 87K (blue diamonds). The filled shapes are adsorption points and the empty shapes are desorption points.

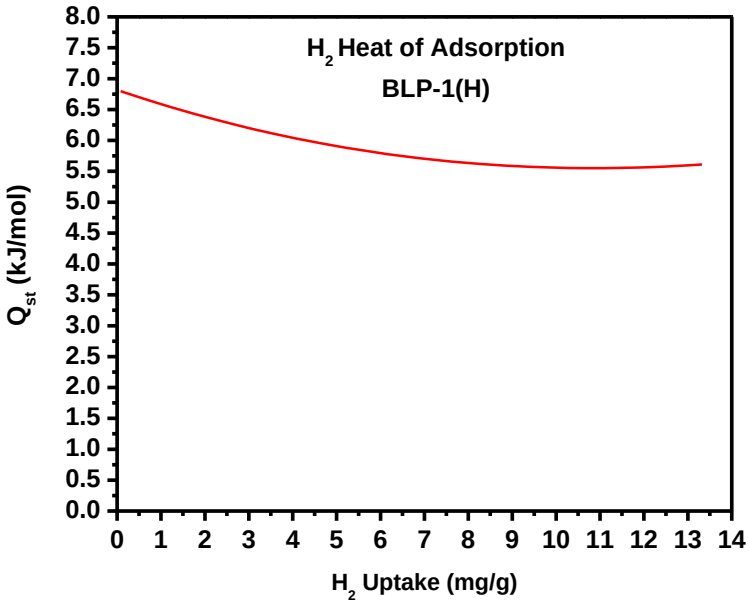

Figure 3.25: Hydrogen isosteric heat of adsorption (Q_{st}) for BLP-1(H).

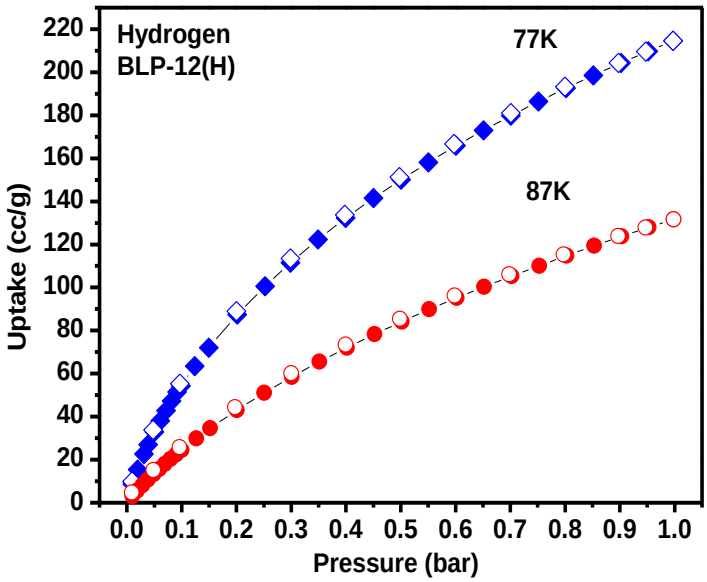

Figure 3.26: H_2 adsorption isotherms for BLP-12(H) measured at 77 K (red circles) and 87K (blue circles). The filled shapes are adsorption points and the empty shapes are desorption points.

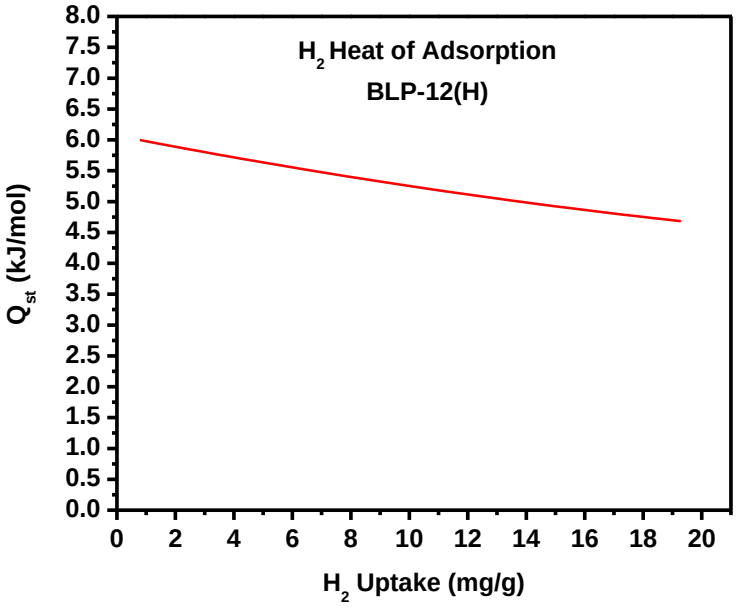

Figure 3.27: Hydrogen isosteric heat of adsorption (Q_{st}) for BLP-12(H).

We have also investigated the performance of BLPs in low pressure CH_4 and CO_2 storage at 273 K and 298 K (Figure 3.28 and 3.30). Interest in storing CH_4 stems from its potential in automotive applications due to its abundance and low carbon footprint, whereas CO_2 capture or separation from flue gases or coal-fired plants is highly attractive due to environmental and economic reasons.[164-167] The maximum CO_2 uptake at 273/298 K was 7.4/4.1 wt% (BLP-1(H)) and 12.8/7.4 wt% (BLP-12(H)) with Q_{st} values of 25.3 kJ/mol and 25.2 kJ/mol, respectively. The uptake capacities of BLPs exceed values reported for other organic polymers including diimide based porous organic polymers (POPs) (9.1 and 6.6 wt%)[168], and unfunctionalized MOFs which include MIL-53 (9.6 wt%), IRMOF-1 (4.7 wt%), ZIF-100 (4.3 wt%) and MOF-177 (3.5 wt%).[165,166] However, CO_2 uptakes are lower than those of amine functionalized MOFs or organic polymers and molecules such as HKUST-1 (17.9 wt%), Cu–BTC (17.9 wt%) and BioMOF-11 (26.4 wt%),[169] and BILP-1 (18.8 wt%).[125] At zero coverage, the Q_{st} values 25.3 kJ/mol and 25.2 kJ/mol are higher than the values reported for COFs,[5] imine-linked organic cages[170] or diimide polymers,[136,137] and lower than those of CO_2-selective MOFs[169,171-174] or ZTFs[175] which generally feature $–NH_2$ or –OH functionalized pores.

The maximum uptake for CH_4 at 273 K was 13.7 cc/g for BLP-1(H) and 18.1 cc/g for BLP-12(H) with respective Q_{st} values of 16.7 kJ/mol and 17.0 kJ/mol at low coverage. A very recent study on the use of COFs illustrated their potential in methane uptake where heat of adsorption depended strongly on pore size and spanned a range of 8 to 25 kJ/mol, with higher values for narrower pores.[167] Both materials reported in this study have relatively similar pore apatures (~12.7 Å) that resemble those of microporous 2D and 3D COFs.[5] The CH_4 storage capacity and isosteric heat of adsoption of BLPs are in line with those of COFs and organic

polymers under similar conditions.[5,6] The relatively high CO_2 uptake and binding by BLPs may arise due to favorable interactions between the polarizable CO_2 molecules and borazine rings.

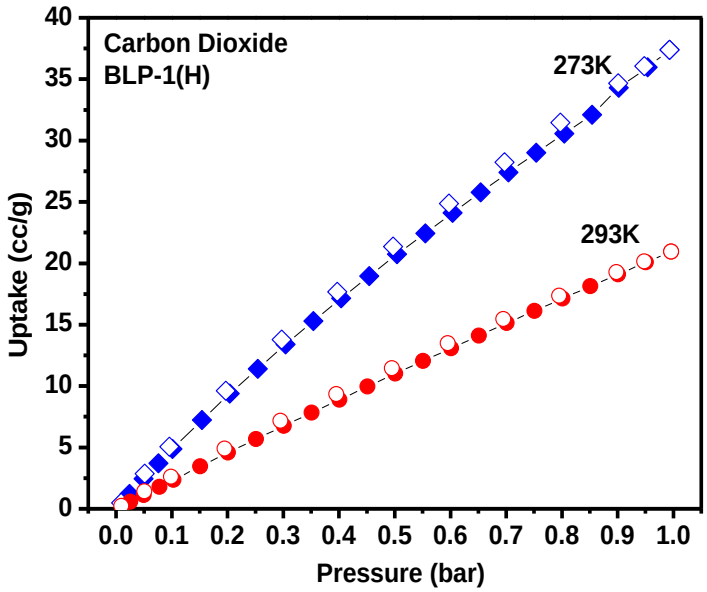

Figure 3.28: Carbon dioxide adsorption isotherms for BLP-1(H).

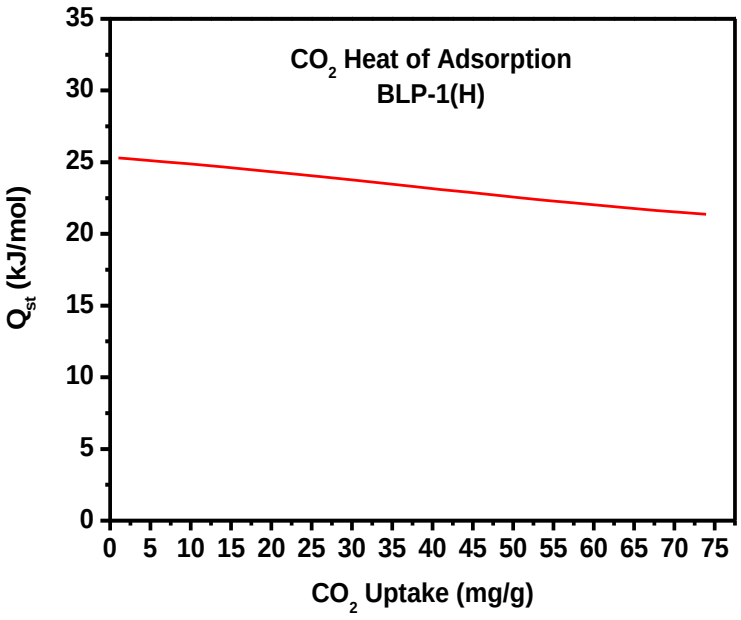

Figure 3.29: Carbon dioxide isosteric heat of adsorption (Q_{st}) for BLP-1(H).

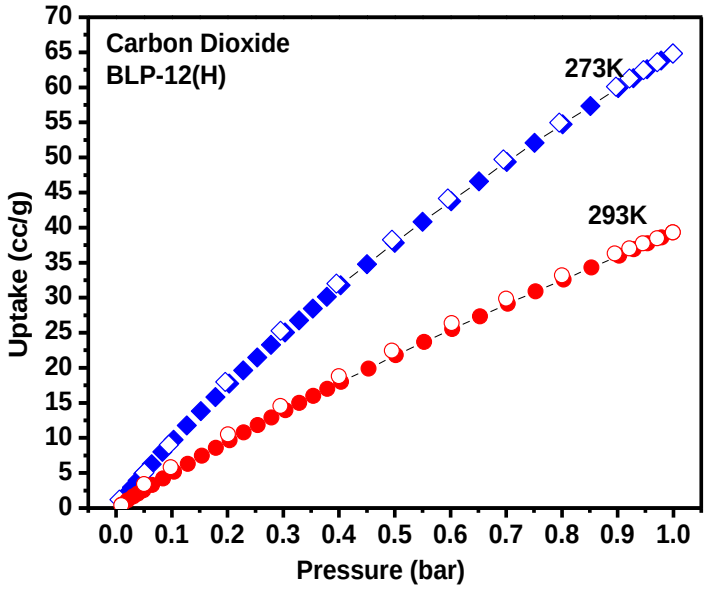

Figure 3.30: Carbon dioxide adsorption isotherms for BLP-12(H)

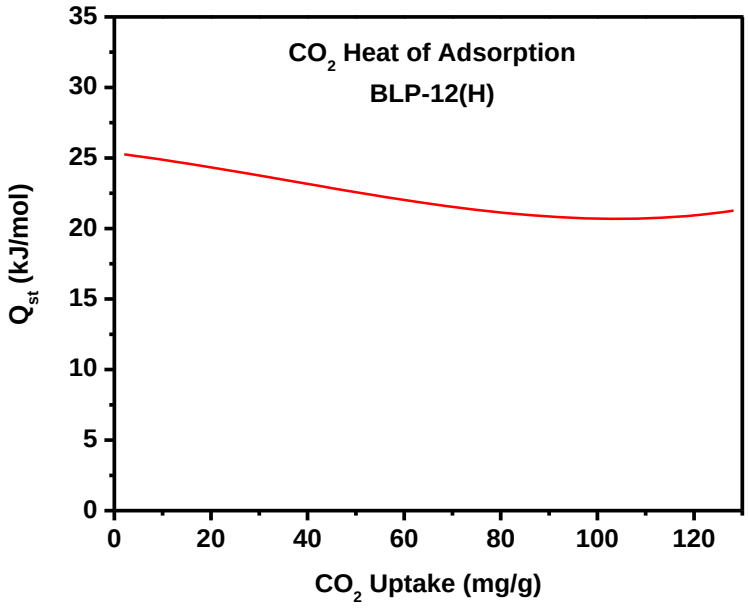

Figure 3.31: Carbon dioxide isosteric heat of adsorption (Q_{st}) for BLP-12(H).

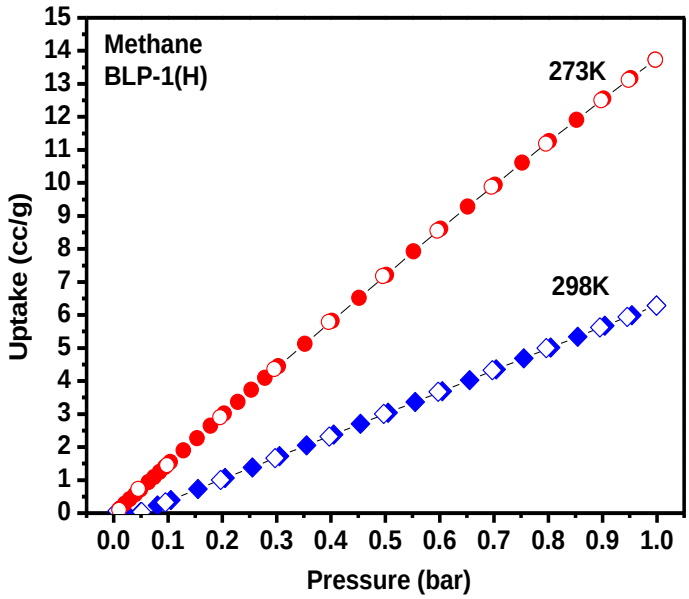

Figure 3.32: Methane adsorption isotherms for BLP-1(H).

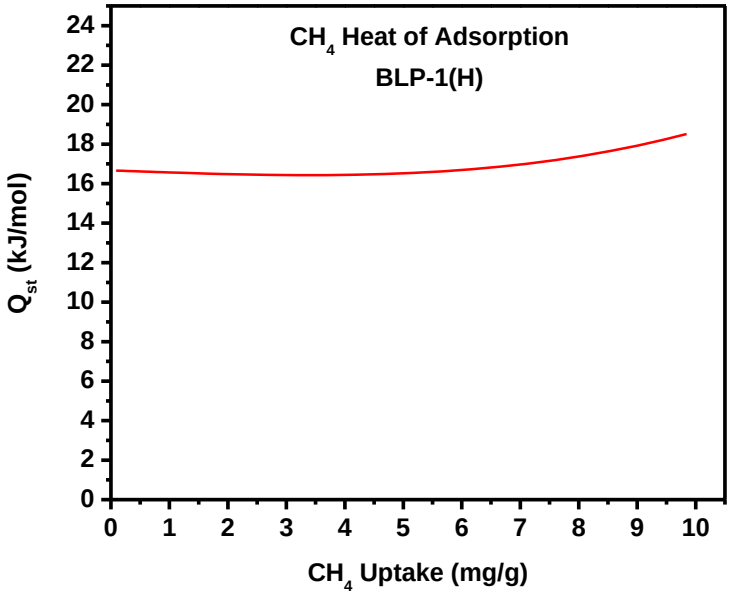

Figure 3.33: Methane isosteric heat of adsorption (Q_{st}) for BLP-1(H).

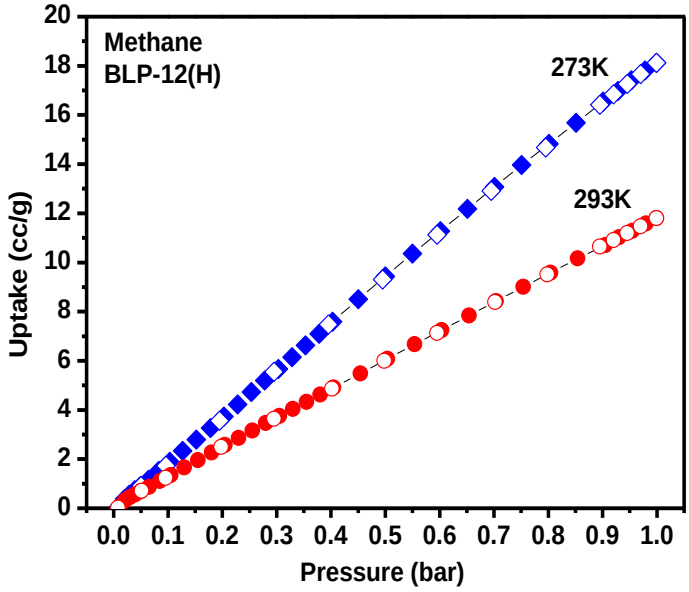

Figure 3.34: Methane adsorption isotherm for BLP-12(H)

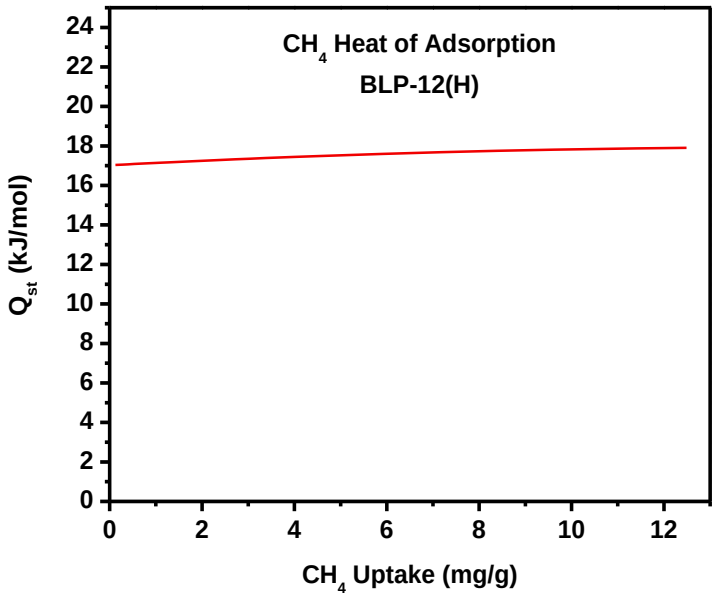

Figure 3.35: Methane isosteric heat of adsorption (Q_{st}) for BLP-12(H).

In the following tables, BLPs gas storage capacities along with their corresponding heats of adsorption are displayed.

Table 3.1: Hydrogen Storage Properties of BLP-1(H) and BLP-12(H)

BLP	H_2				
	cc/g	mmol/g	mg/g	wt%	Q_{st} (kJ/mol)
BLP-1(H)	148	6.66	13.3	1.33	6.8
BLP-12(H)	214	9.64	19.3	1.93	5.9

Table 3.2: Carbon Dioxide Storage Properties of BLP-1(H) and BLP-12(H)

BLP	CO_2				
	cc/g	mmol/g	mg/g	wt%	Q_{st} (kJ/mol)
BLP-1(H)	37.4	1.68	73.9	7.39	25.3
BLP-12(H)	64.8	2.91	128	12.8	25.2

Table 3.3: Methane Storage Properties of BLP-1(H) and BLP-12(H)

BLP	CH_4				
	cc/g	mmol/g	mg/g	wt%	Q_{st} (kJ/mol)
BLP-1(H)	10.8	0.48	7.74	0.77	23.9
BLP-12(H)	17.4	0.78	12.5	1.25	17.0

3.4 Conclusion

In conclusion, we have demonstrated the synthesis of highly porous borazine-linked polymers by thermolysis of arylamine-borane adducts and investigated their performance under ambient pressure and cryogenic conditions. The hydrogen sorption experiments indicate that BLPs have high hydrogen storage capacities at low pressure and display somewhat higher hydrogen isosteric heat of adsorption than analogous COFs; however, higher pressure conditions are required to fully explore the potential of BLPs in gas storage applications.

Chapter 4: Targeted Synthesis of A Microcrystalline Borazine-Linked Covalent Organic Framework

4.1 Introduction

Covalent-organic frameworks (COFs) are a new class of highly porous crystalline materials with promising potential in gas storage,[5] optoelectronics,[176] and catalysis. [7-13] COFs can be tailored to possess exceptionally high porosities, very low densities, and pore metrics that span the microporous and mesoporous ranges. To impart crystallinty into these covalent frameworks, covalent dynamic bonds such as B-O and C-N, have been used to guide 2D and 3D solid-state growth and packing of COFs networks. [133,76-79] In contrast to organic polymers which are usually amorphous because they are usually synthesized only under kinetic control, the reversible bond-formation provide convenient routes for microcrystallinty in COFs. In the absence of reversible synthetic conditions, covalently-linked polymers lack long range ordering and tend to be amorphous. To circumvent poor pore formation and enhance the overall porosity, the use of building blocks that dictate the spatial growth of the polymer has been instrumental. One potential building block is borazine which is structurally similar to the boroxine units found in COFs prepared by boronic acid self-condensation reactions or triazine. Borazine has been mainly used for the fabrication of BN-based ceramics[177] or in organic optoelectronics. [142-146] However, to date, the use of borazine as a building block for the preparation of porous polymers remains scarce. Polymers linked by B-N bonds are highly sought after, but their preparation remains a great challenge. Along this line, we sought after the inclusion of borazine (B_3N_3)

as a functionalized and polarizable building block into porous organic polymers.[95,96] One of the well-established synthetic avenues for the synthesis of monomeric borazine molecules is thermal decomposition of primary amine-borane adducts. Catalytic and thermal dehydrogenation of amine-borane (AB) adducts have been under intensive investigation mainly due to their potential use in hydrogen storage applications.[178-180] However, their use as precursors for porous architectures remains undocumented.

With these considerations in mind we set out to construct highly porous borazine-linked materials and to investigate their use in gas storage applications. In this section we describe the targeted synthesis of the first crystalline borazine-linked polymer, BLP-2(H), by the thermal decomposition of 1,3,5-tris(p-aminophenyl)benzene-borane in toluene-mesitylene mixture at 120 ºC for 48 hrs. BLP-2(H) exhibits an eclipsed packing of the 2D layers with high surface area and thermal stability.

Scheme 4.1. Synthesis of BLP-2(H) from in situ thermal decomposition of 1,3,5-tris(p-aminophenyl)benzene-borane.

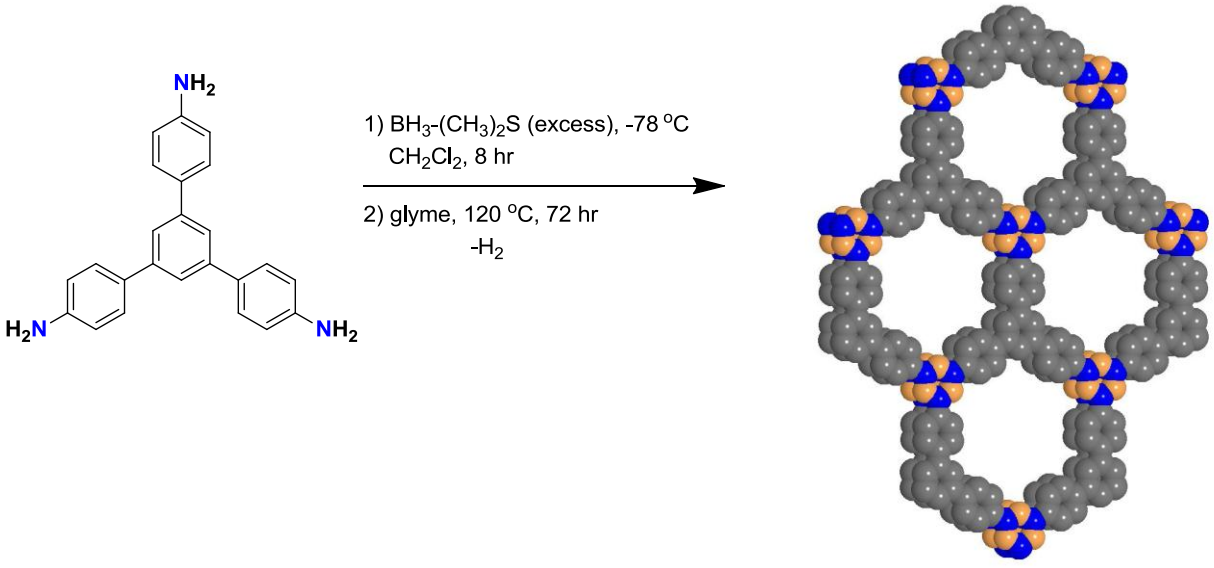

BLP-2(H), 73%

4.2 Experimental

All starting materials and solvents, unless otherwise noted, were obtained from the Aldrich Chemical Co. and used without further purification. Dichloromethane (DCM) was dried over CaH_2. Toluene and mesitylene were dried over sodium. The isolation and handling of all products were performed under an inert atmosphere of nitrogen using either glove box or Schlenk line techniques. 1,3,5-*tris*(p-aminophenyl)benzene was synthesized using methods reported in literature.[181]

Scheme 4.2. Synthesis of 1,3,5-*tris*(p-aminophenyl)benzene from trimerization of p-nitroacetophenone.

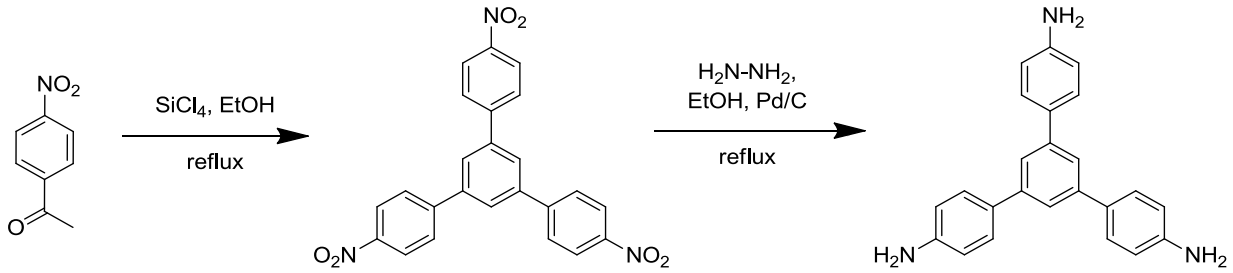

Synthesis of 1,3,5-*Tris*(p-nitrophenyl)benzene. $SiCl_4$ (20 mL, 0.18 mol) was added dropwise to a dry ethanol solution (60 mL) containing 10 g (0.06 mol) p-nitroacetophenone at 0 ºC. A yellow precipitate was formed immediately and then the mixture was refluxed for 10 h. After the mixture was cooled to room temperature, saturated NH_4Cl aqueous solution (100 mL) was added and stirred for 10 min. The obtained yellow precipitate was filtered and dried and directly added in 100 mL ethanol containing Pd/C (10%, 0.8 g). The mixture was heated to reflux, then 25 ml of 64% $NH_2NH_2 \cdot H_2O$ was added drop-wise to the hot solution. After refluxing overnight,

the precipitate was collected by filtration, the solution was cooled to room temperature, and a pale yellow precipitate was collected. The solid was recrystallized in ethanol and dried under vacuum and white solid was obtained (5.6 g, 80% yield). ^{1}H NMR (DMSO-d_6, 300 MHz): 7.48 (s, 3H, ArH), 7.47 (d, J_{HH} = 9.0, 6H, ArH), 6.66 (d, J_{HH} = 8.4, 6H, ArH), 5.20 (s, 6H, NH_2). ^{13}C NMR (DMSO-d_6, 75 MHz): δ 114.9, 121.1, 128.2, 128.8, 142.3, 149.0.

Synthesis of 1,3,5-*Tris*(p-aminophenyl)benzene-borane ($C_6H_3(PhNH_2{\cdot}BH_3)_3$**.** A 100 ml Schlenk flask was charged with 100 mg (0.285 mmol) of 1,3,5-*tris*(p-aminophenyl)benzene and 80 ml of anhydrous DCM. The solution was cooled -78 ºC in an acetone/dry ice bath and treated with 2.5 ml (2.5 mmol) of 1M borane·dimethylsulfide in drop-wise. The clear solution was allowed to warm to room temperature while stirring overnight. On the following day, a white precipitate had formed. The solid white product was filtered and rinsed several times with DCM. ^{1}H NMR (DMSO-d_6): δ 7.82 (d, J_{HH} = 2.4, ArH), 7.28 (d, J_{HH} = 8.7, ArH), 7.75 (s, ArH), 7.314 (s, NH_2), 1.59 (br, BH_3). ^{13}C NMR (75 MHz, DMSO-d_6) δ 123.4, 124.8, 128.3, 138.1, 141.8, 143.8.

Further characterization by Mass Spectrometry and elemental analysis were unsuccessful due to the instability of the amine-borane adduct in the absence of solvents and due to polymerization upon heating under elemental analysis testing conditions.

Synthesis of BLP-2(H). Pyrex tubes were charged with 30 mg of dry adduct and 2.0 ml of a mesitylene:toluene (1:4) solution. The tubes were then sonicated for 30 min before they were flash-frozen, evacuated and sealed. The reaction tubes were slowly heated in an oven to 120 ºC overnight to afford a fluffy white polymer which was isolated by filtration over a medium glass frit and washed with anhydrous DCM. The product was immersed in anhydrous DCM (20 ml)

for 24 h, during which the activation solvent was decanted and freshly replenished twice. Anal. Calcd. for (C_8H_6BN): C, 75.56%; H, 4.76%; N, 11.02%. Found: C, 72.96%; H, 5.19%; N, 9.34%.

Organoboron compounds typically give lowered carbon values in elemental microanalysis due to the formation of non-combustible boron carbide byproducts.[76]

Activation of BLP-2(H) for gas adsorption measurements. Inside a glove-box, about 150 mg of as-prepared sample of BLP was loaded into an Autosorb cell then heated to 120°C under dynamic vacuum (1.0×10^{-5} torr) for 16 h. The sample was back-filled with nitrogen to exclude adsorption of moisture prior to N_2 adsorption measurements.

Gas Sorption Measurements. Nitrogen experiments were run using a Quantachrome Autosorb 1-C analyzer at 77 K. Pore Size Distribution (PSD) was calculated using Non-Local Density Functional Theory (NLDFT) on the adsorption branch with a spherical/cylindrical pore model. Hydrogen sorption experiments were run on the same Quantachrome Autosorb 1-C analyzer at both 77 K and 87 K. Methane and carbon dioxide experiments were run at 273 K and 293 K each. Ultrahigh purity helium (99.999%) was used to calibrate the free volume in the sample cell before each measurement. For H_2 uptake measurement, hydrogen with purity of 99.999% was used. CO_2 (99.9%) and CH_4 (99.999%) were obtained from Airgas Inc. (Radnor, PA).

Heat of Adsorption Calculations. Using the data taken at 77 K and 87 K, the isosteric heat of adsorption for BLP-2(H) was calculated according to previous reports[148] by solving the virial-type expression:

$$\ln P = \ln N + (1/T)\sum_{i=0}^{m} a_i N^i + \sum_{i=0}^{n} b_i N^i$$

where P is pressure in torr, T is temperature in Kelvin, and N is the mmol of gas adsorbed per gram of sample. The values for *m* and *n* were varied such that $m \geq n$ and resulted in the best fit as determined by the sum of the squares of the errors. The values for a_0, a_1,…a_m were used in the calculation for the isosteric heat of adsorption, Q_{st}:

$$Q_{st} = -R \sum_{i=0}^{m} a_i N^i$$

The calculated values were plotted as they relate to surface coverage, and the isosteric heat of adsorption values at the point of zero-coverage is highlighted in the text.

4.3 Results and Discussion

We first established the formation of the expected bonds by FT-IR. By observing the loss of certain stretches expected for dehydrocoupling reactions combined with the appearance of borazine-characteristic peaks, the formation of the expected products can be confirmed. FT-IR spectra of BLP-2(H) and starting materials were obtained as KBr pellets using a Nicolet - Nexus 670 spectrometer. FT-IR spectra strongly revealed the presence of borazine indicated by the characteristic stretch at 1395 cm^{-1}, which was not present in starting material. There is also substantial reduction of the N-H stretching of amine/amine-borane adducts at ~3400 cm^{-1} and the B-H stretch at ~2550 cm^{-1} which is indicative of the near exhaustive dehydrogenation of nitrogen and boron sites in forming the borazine rings. A residual N-H stretch at 3300 cm^{-1} is present due to unreacted amine site on the particle surfaces and incompletely reacted groups at defects in the material.

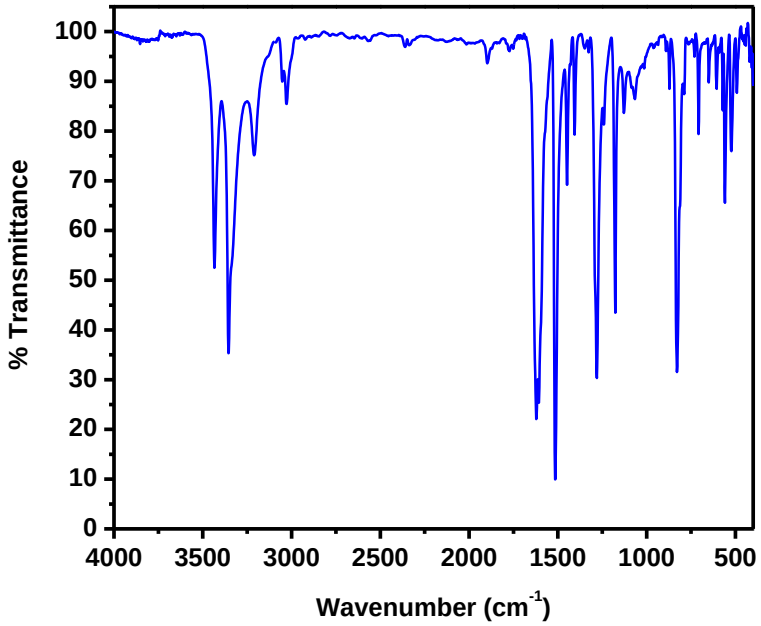

Figure 4.1: FT-IR spectrum of 1,3,5-*tris*(p-aminophenyl)benzene.

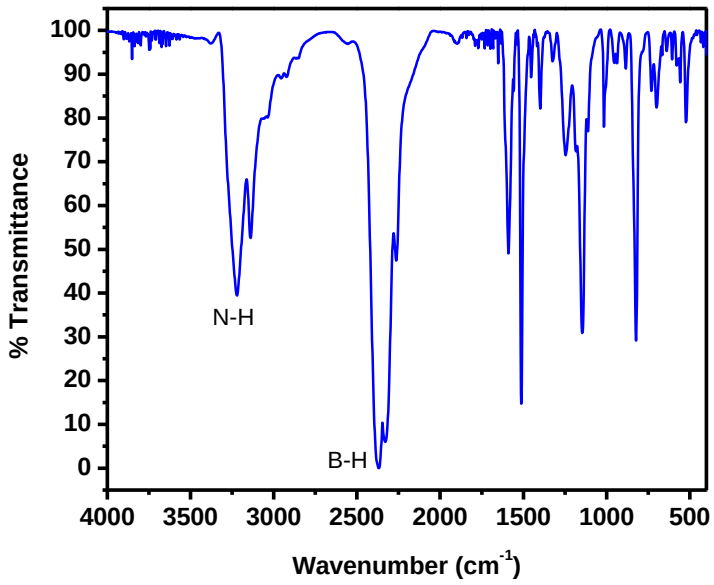

Figure 4.2: FT-IR spectrum of 1,3,5-*tris*(p-aminophenyl)benzene-borane.

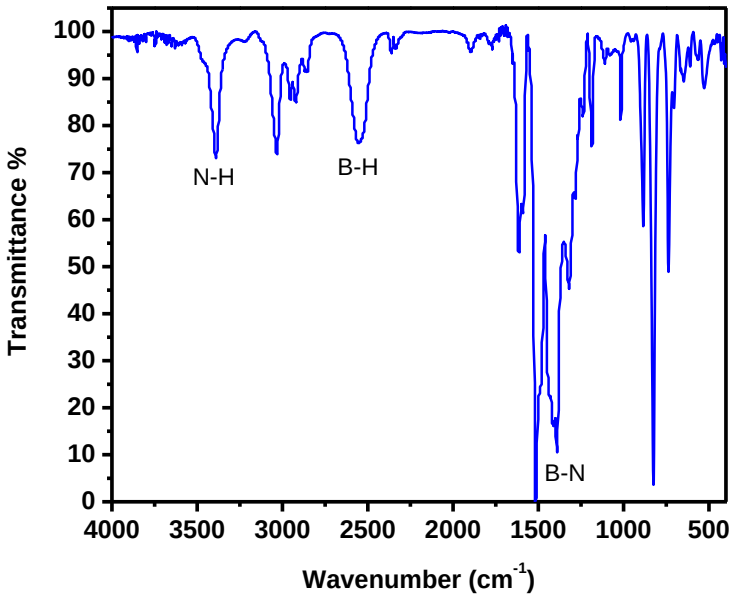

Figure 4.3: FT-IR spectrum of BLP-2(H)

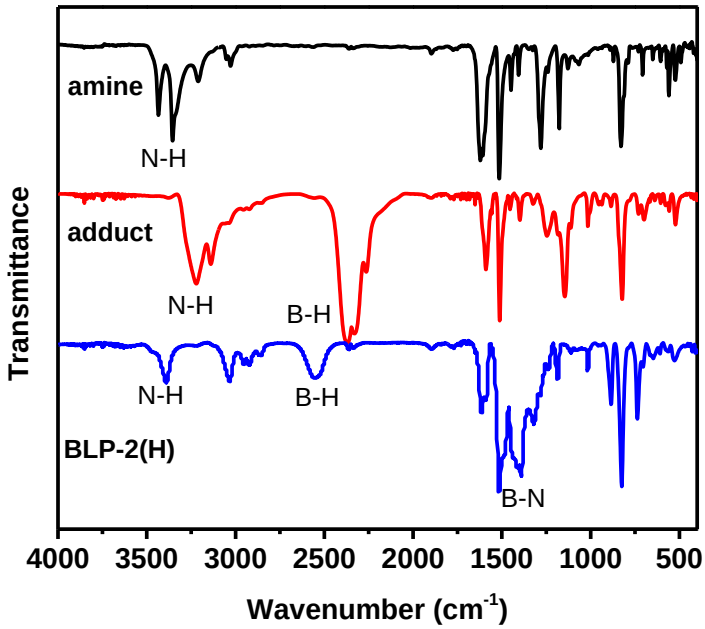

Figure 4.4: FT-IR spectrum of BLP-2(H) and starting materials.

To ensure the incorporation of intact building units into the polymer framework, we have also considered solid state ^{13}C CP-MAS NMR spectroscopy. Solid state ^{11}B MAS NMR spectroscopy was used to investigate the geometry and connectivity of the boron sites. Solid-state NMR spectra were recorded at ambient temperature on a 360-1 instrument by Spectral Data Services, Inc., Champaign, IL. ^{11}B MAS NMR data were collected with a 45 degree ^{11}B pulse length and a recycle delay of two seconds. High-power H-1 decoupling was employed during acquisition only. Samples were spun at the magic angle at about 7 kHz. Chemical shifts are referenced to external neat boron trifluoroetherate. There are two broad signals in the ^{13}C CP-MAS spectrum centered around 140 and 126 ppm that originate from 1,3,5-(p-aminophenyl)benzene core. The signal in the 140 region arises from three separate peaks; two from the two carbon environments of the central benzene (3 C-H and 3 C-C) and one from the three carbons on the phenyl rings directly bonded to the central benzene. The signal in the 126 region arises from three peaks as well; two from the C-H carbons on the phenyl rings and one from the three C-N carbons as is apparent by observation of the amine-borane ^{13}C NMR spectra. The ^{11}B MAS spectrum reveals a broad doublet (9 and 21 ppm) which is consistent with tri-coordinate boron at 116 MHz and is in sharp contrast to tetra-coordinate boron seen in amine-borane adducts or cycloborazanes which usually appear in the negative region (0 to -45 ppm)[154-156]. A similar observation has been documented by Gervais et al, in which the ^{11}B signal appears at similar range and is sensitive to the magnetic field strength.[152,253]

A

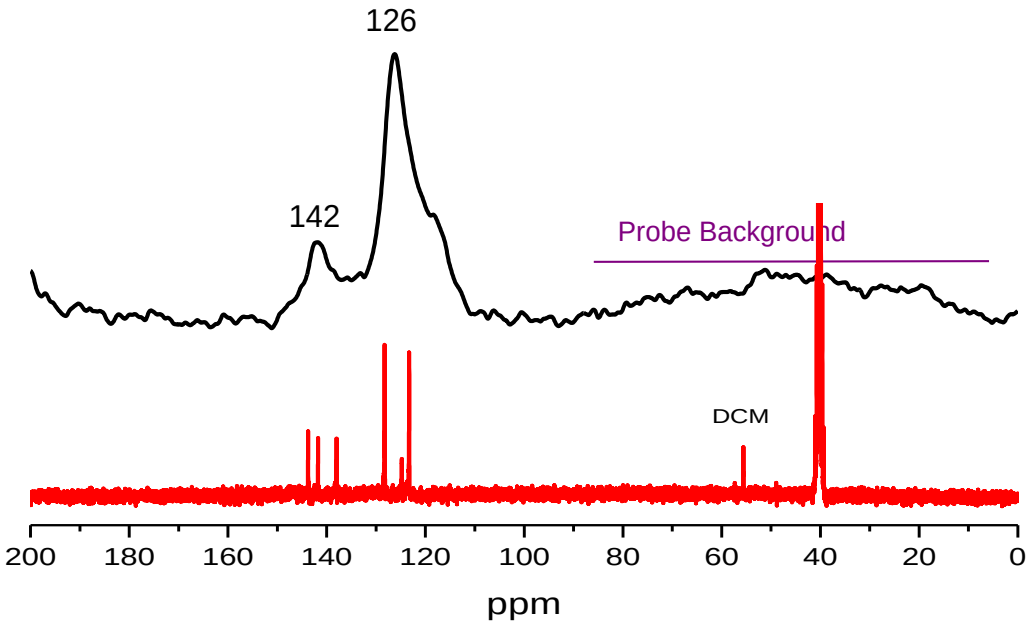

B

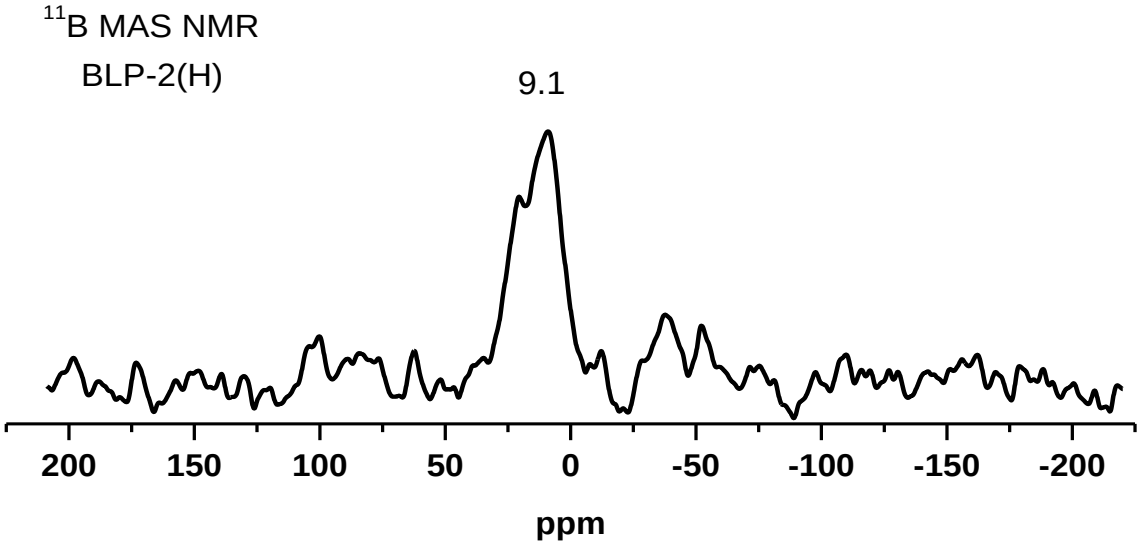

Figure 4.5: Solid state ^{13}C CP-MAS NMR (A) and ^{11}B MAS NMR (B) spectra for BLP-2(H). Red line – ^{13}C NMR of 1,3,5-*tris*(p-aminophenyl)benzene-borane.

The morphology and phase purity of BLP-2(H) were investigated by scanning electron microscopy. Samples were prepared by dispersing the material onto a sticky carbon surface attached to a flat aluminum sample holder. The sample was then platinum-coated using a Denton Vacuum V TSC HP Cold Sputtering Platform at $1x10^{-4}$ mbar of pressure in a nitrogen atmosphere for 120 seconds. Samples were analyzed on a Hitachi SU-70 Scanning Electron Microscope using an accelerating voltage of 15 kV. Images magnified 35 – 400k times revealed well-defined rectangular prisms ~100 nm in width of various lengths. The difference in particle shape from those of all other BLPs is due to its high crystallinity and the use of nonpolar solvent in the reaction process.

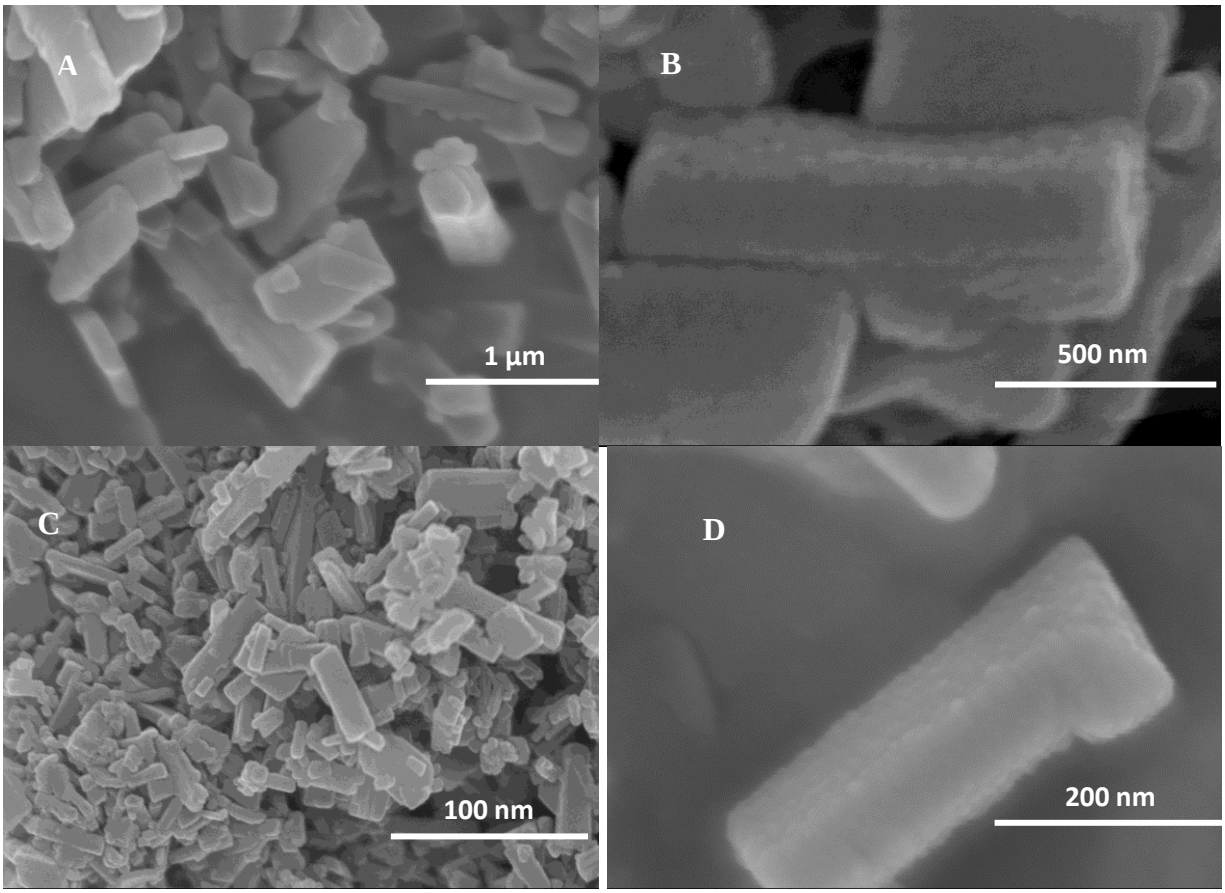

Figure 4.6: SEM image of BLP-2(H) particles revealing a rectangular prism-shaped morphology at x35 (A) x90 (B) x250 (C) and x100 (D) magnification.

The crystalline nature of BLP-2(H) was further conformed by powder x-ray diffraction studies (PXRD) as depicted in Figure 4.7. Powder X-ray diffraction data of BLP-2(H) were collected on a Panalytical X'pert Pro Multipurpose Diffractometer (MPD). Samples were mounted on a zero background sample holder measured in transmission mode using Cu Kα radiation with a 2θ range of 5-35°. The experimental PXRD pattern was compared against calculated patterns for theoretical models that exhibit eclipsed and staggered confirmations of the anticipated 2D sheets following methods reported for 2D COFs. Both models where the 2D sheets pack in an eclipsed boron nitride like stacking (AA) or in a staggered graphene like stacking conformation (AB) were constructed using Materials Studio Visualizer and their geometry were optimized using the Forcite module.[129] The powder diffraction patterns for the modeled topologies were determined using *Mercury 2.4.*[130] As shown in Figure 4.7, the diffraction pattern of the eclipsed conformation which has a P-6m2 space group corresponds well with the experimental data and is in sharp contrast to the staggered conformation. Studies have been done on the stacking patterns of various derivatives of triphenylbenzene showing interesting self-assembly based on the π-conjugated core.[182] Therefore, we anticipate the layers of BLP-2(H) to be stabilized by similar forces. The broad peaks in the XRD pattern of BLP-2(H) arise from poor packing of the 2D layers and possible defects in the structure. In the aforementioned studies, deviations in packing were found to be dependent upon constituent groups. Manners and co-workers reported the crystal structure of N-triphenylborazine where the phenyl groups are not coplanar with the B_3N_3 ring but are slightly twisted, with angles between the two planes of 48.8°, 43.7° and 42.3°,[111] which may be more consequential to the structure of BLP-2(H).

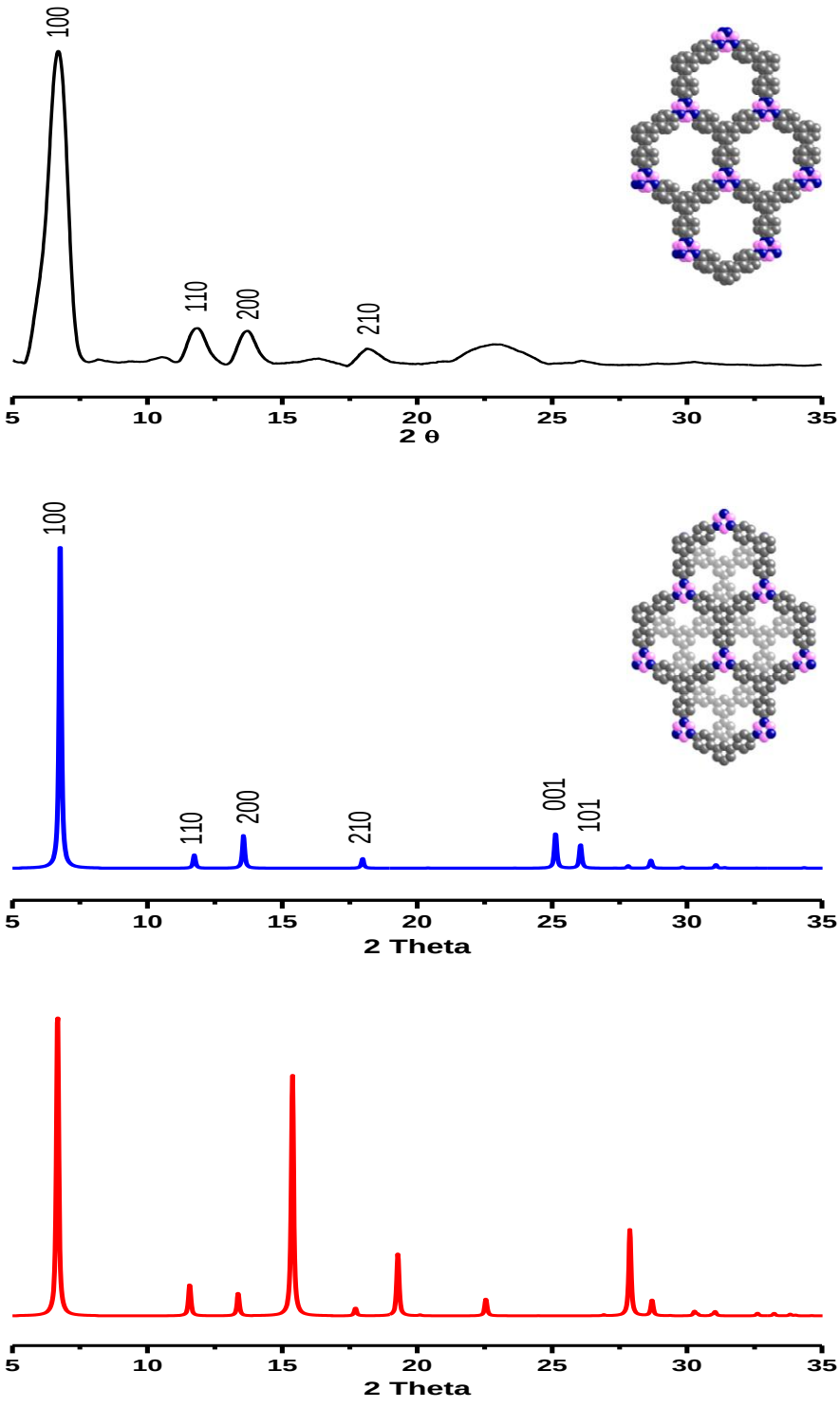

Figure 4.7: PXRD pattern of BLP-2(H) compared to patterns calculated from *Mercury 2.4* with the stacking of the layers in staggered and eclipsed conformations. Note the pattern from the eclipsed model more closely resembles the pattern of BLP-2(H).

To assess the thermal stability and porosity of BLP-2(H), we subjected the as-synthesized material to thermogravimetric analysis (Figure 4.8) under a flow of nitrogen. Samples were run on a TA Instruments Q-5000 series thermal gravimetric analyzer with samples held in platinum pans under an atmosphere of nitrogen. The TGA trace is typical of porous materials and shows a ~19 wt% loss up to 150 °C as a result of a loss of solvent molecules from the pores, then the material remains stable until ~ 420 °C where it starts to decompose. The thermal stability is very similar to those exhibited by analogous COFs. It is interesting to note that the percent mass of the decomposition residue is 20% which is very close to the BN content (19.6%) in BLP-2(H).

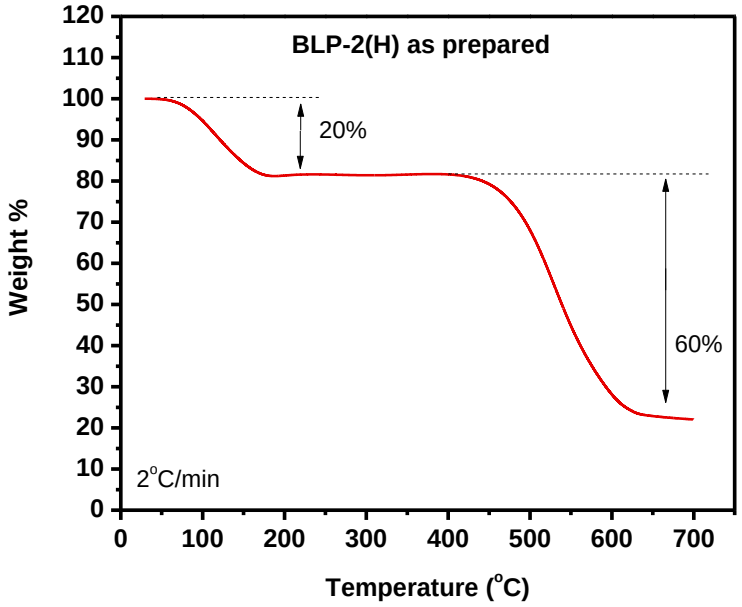

Figure 4.8: TGA trace for an as prepared sample of BLP-2(H).

The porous nature of BLP-2(H) was evaluated by argon uptake measurements at 87 K and 0-1 bar. Prior to sorption experiments, the sample was degassed at 120 °C and 1 x 10^{-5} torr for 16 hrs. The Type I argon isotherms (Figure 4.9) are consistent with permanent microporous materials that are characterized by a sharp uptake at $P/P_o = 10^{-4}$ to 10^{-2}. A surface area of 1178 $m^2\ g^{-1}$ was calculated using the Brunauer-Emmett-Teller (BET) for P/P_o between 0.05 and 0.15. Using the Langmuir model (P/P_o = 0.05-0.30), the surface area value was determined to be 1564 m^2/g. BLP-2(H) outperforms those of related covalent networks such as COF-1 (711 m^2g)[5] and CTF-1 (791 m^2g),[79] in this regard as well as chlorinated and brominated BLPs (503-1364 m^2/g).[95] The pore volume (V_p) calculated at P/P_o = 0.90 was 0.59 cm^3/g for BLP-2(H). Pore Size Distribution (PSD) were calculated using Non-Local Density Functional Theory (NLDFT) on the adsorption branch with a cylindrical/sphere pore model on the nitrogen experiments combined with data taken from carbon dioxide sorption experiments performed at 273 K as has been reported previously.[76]

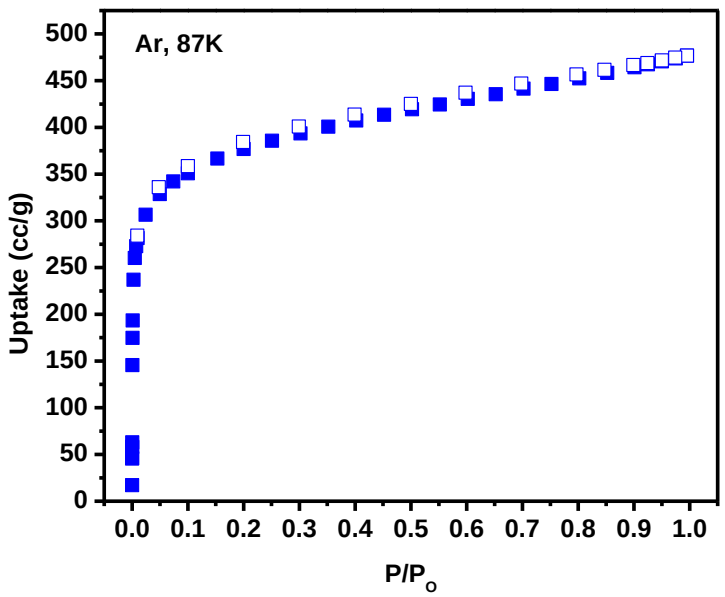

Figure 4.9: Ar adsorption isotherm for BLP-2(H) measured at 87 K. The filled squares are adsorption points and the empty squares are desorption points.

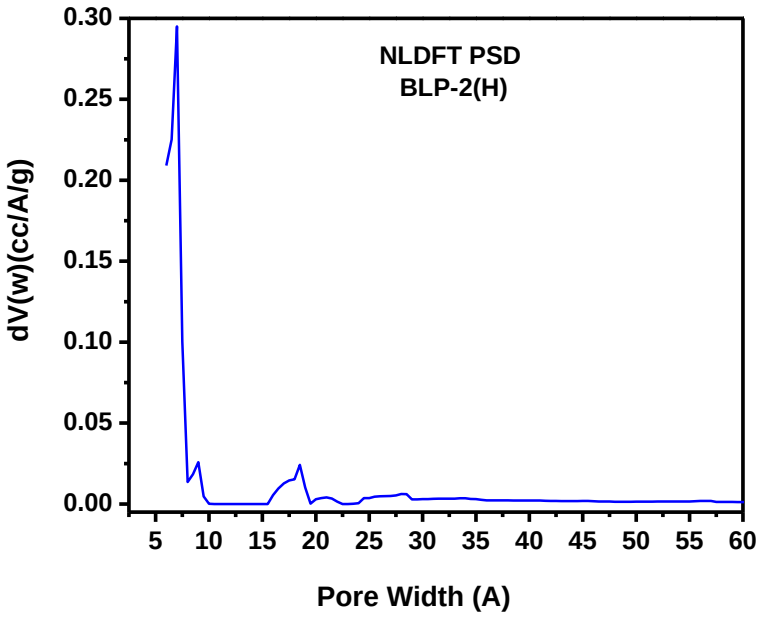

Figure 4.10: NLDFT Pore Size Distribution for BLP-2(H)

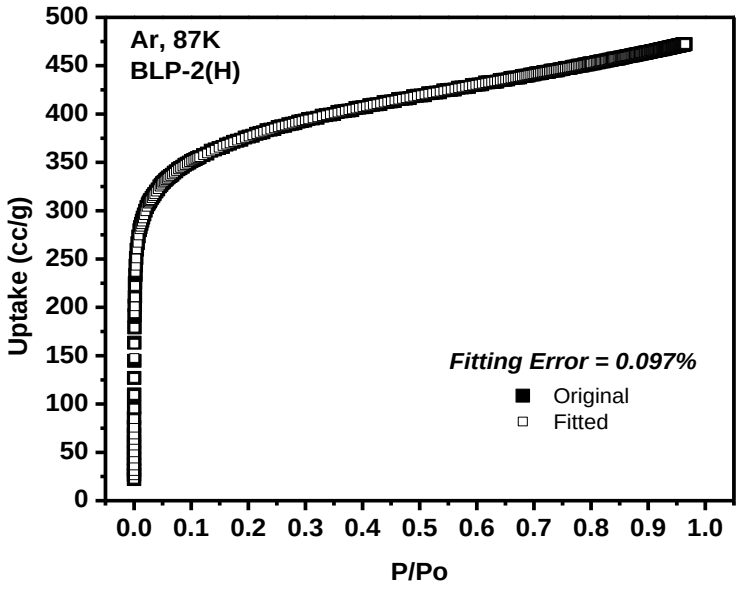

Figure 4.11: Experimental N_2 adsorption isotherm for BLP-2(H) measured at 87 K is shown as filled squares. The calculated NLDFT isotherm is overlaid as open squares. *Note that a fitting error of < 1 % indicates the validity of using this method for assessing the porosity of BLP-2(H).*

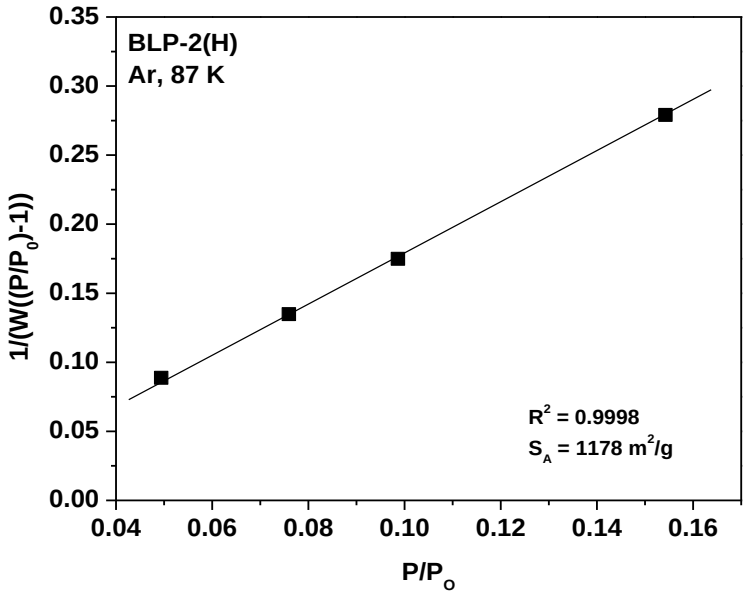

Figure 4.12: BET plot for BLP-2(H) calculated from the N_2 adsorption isotherm at 77 K. The model was applied from P/P_o = 0.05-0.15.

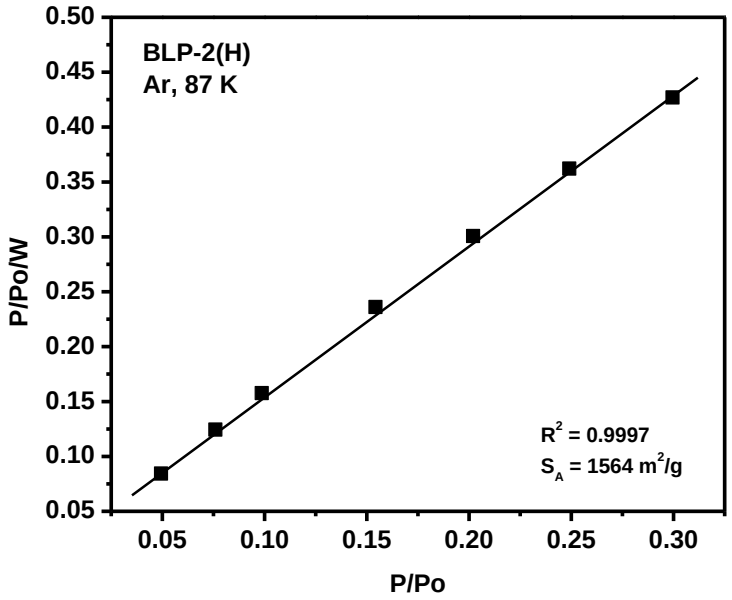

Figure 4.13: Langmuir plot for BLP-2(H) calculated from the Ar adsorption isotherm at 87 K. The model was applied from P/P_o = 0.05-0.30.

Considering its high porosity, we decided to investigate the performance of BLP-2(H) in H_2, CH_4 and CO_2 uptake. Hydrogen, because of its abundance, burning cleanly in fuel cells to generate electricity and water, has become a top candidate for replacing fossil fuels. However because of weak interactions between molecular hydrogen and pore walls, high volume storage is still a great challange at ambient conditions. We have collected low pressure hydrogen isotherms at 77 and 87 K and calculated the isosteric heat of adsorption (Q_{st}) using the virial method.[160] At 1 bar and 77 K, the hydrogen uptake for BLP-2(H) is 1.5 wt %, which exceeds those of halogenated BLPs and is comparable to similar crystalline organic polymers such as COF-1 (1.28 wt%) and CTF-1 (1.55 wt%). The Q_{st} value was calculated to be 6.8 kJ/mol at zero coverage. This value is similar to those of previously reported organic polymers which usually lie somewhere between 5.0-8.0 kJ/mol.[5,125,138-140]

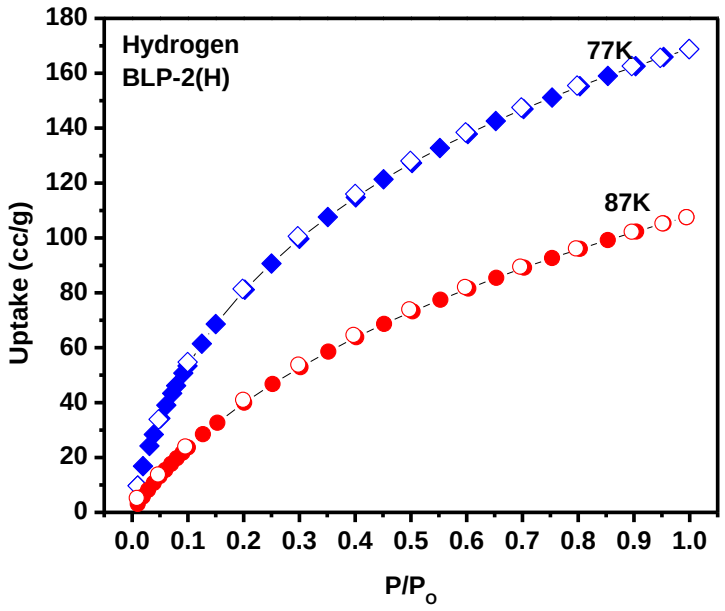

Figure 4.14: Hydrogen adsorption isotherm for BLP-2(H) measured at 77 K (red circles) and 87K (blue diamonds). The filled shapes are adsorption points and the empty shapes are desorption points.

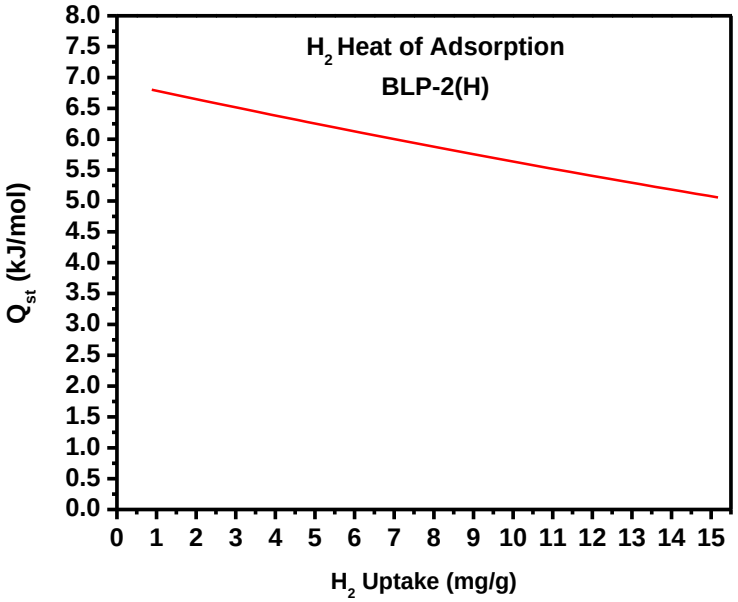

Figure 4.15: Hydrogen isosteric heat of adsorption (Q_{st}) for BLP-2(H).

The storage of methane and carbon dioxide in porous polymers has also been of great interest recently. Methane, because of its natural abundance and low carbon footprint is investigated for its potential in automotive applications. CO_2 capture or separation from flue gases or coal-fired plants is highly attractive for economic and environmental reasons. CH_4 and CO_2 isotherms were taken at 273 and 298 K each, and Q_{st} values were calculated in a similar manner to H_2. All isotherms were fully reversible without any notable hysteresis. The maximum CO_2 uptake at 273 K was 8.1 wt% which is in the range of other organic polymers previously mentioned and unfunctionalized MOFs which include MIL-53 (9.6 wt%), IRMOF-1 (4.7 wt%), ZIF-100 (4.3 wt%) and MOF-177 (3.5 wt%).[165,166] The BLP-2(H) CO_2 Qst value was calculated to be 22.1 kJ/mol at zero coverage. This value stays constant throughout entire pressure range indicating that BLP-2(H) has no preferred bonding site for CO_2. Q_{st} are higher than the values reported for COFs,[5] imine-linked organic cages[170] or diimide polymers,[136,137] yet expectedly lower than those of CO_2 selective MOFs[169,171-174] or ZTFs[175] which generally feature $–NH_2$ or –OH functionalized pores. The maximum uptake for CH_4 at 273 K was 14.3 cc/g (1.4 wt%) for BLP-2(H) with a Qst value of 16.2 kJ/mol at low coverage. The CH_4 storage capacity and isosteric heat of adsoption of BLPs are in-line with those of COFs and other organic polymers.

Table 4.1: H_2, CO_2, and CH_4 Storage Properties of BLP-2(H)

	cc/g	mmol/g	mg/g	wt%	Q_{st} (kJ/mol)
H_2	169	7.59	15.2	1.50	6.8
CO_2	40.9	1.83	80.8	8.08	22.1
CH_4	14.3	0.64	10.3	1.03	17.4

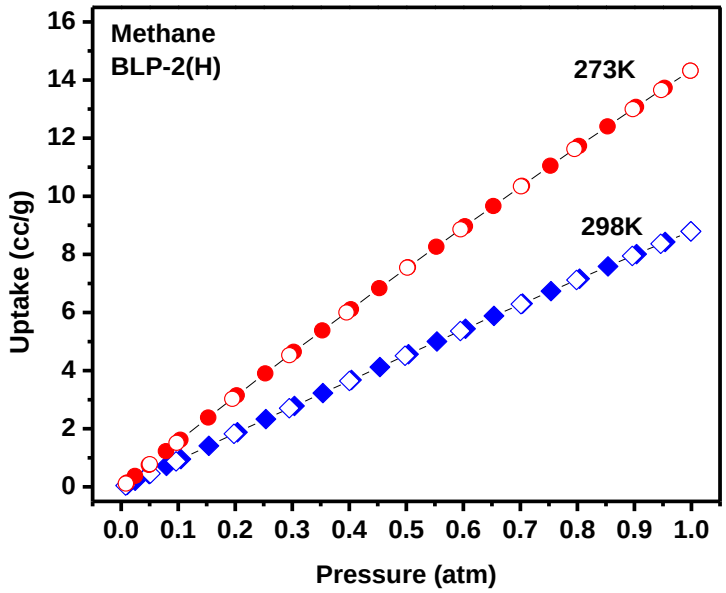

Figure 4.16: Methane adsorption isotherm for BLP-2(H).

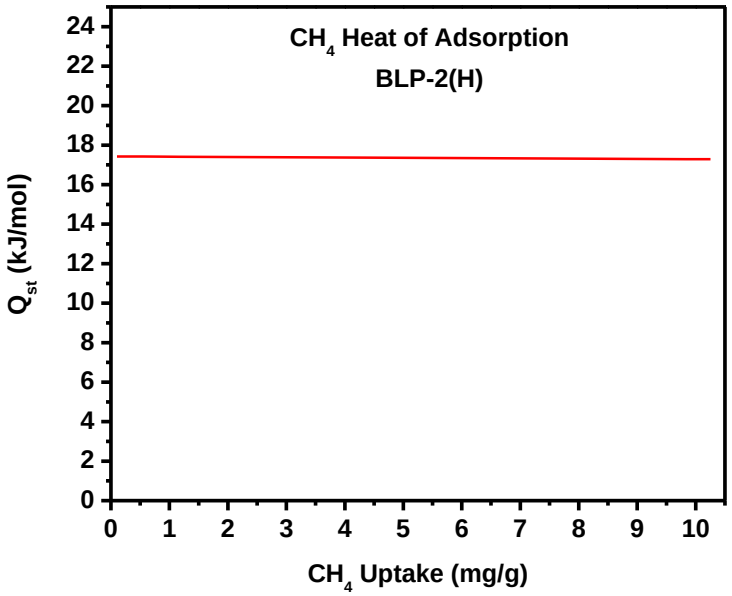

Figure 4.17: Methane isosteric heat of adsorption (Q_{st}) for BLP-2(H).

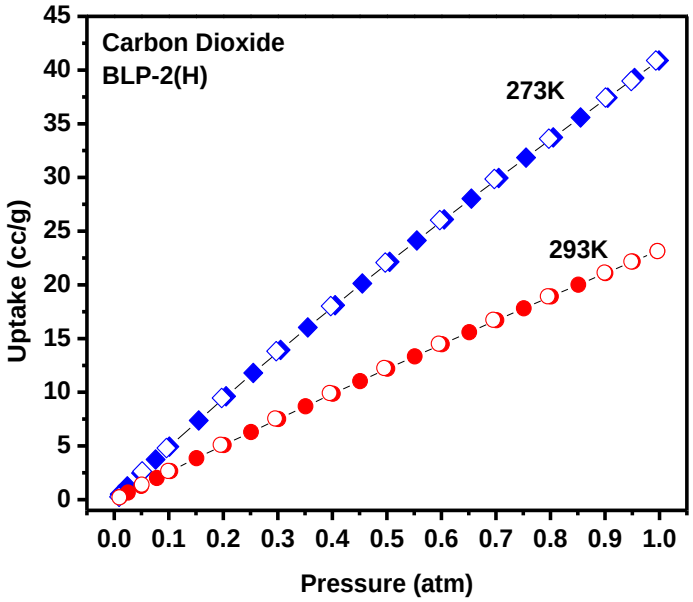

Figure 4.18: Carbon dioxide adsorption isotherm for BLP-2(H).

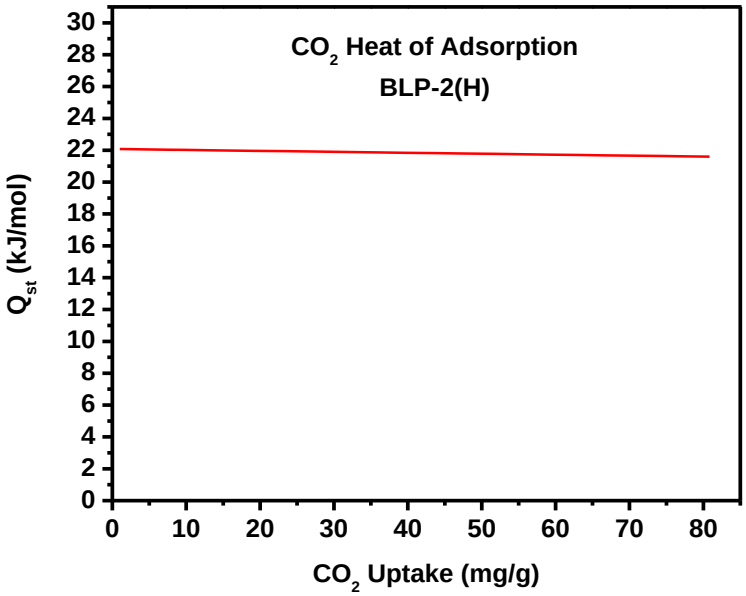

Figure 4.19: Carbon dioxide isosteric heat of adsorption (Q_{st}) for BLP-2(H).

4.4 Conclusion

In conclusion, we have shown that thermolysis of arylamine-borane adducts can lead to highly porous and crystalline borazine-linked polymers. We have investigated the gas sorption performance of BLP-2(H) under ambient pressure and cryogenic conditions. The resulting polymer is thermally stable and exhibits permanent microporosity. Considering the results, this new class of polymers along with its 3D analogs is expected to increase potential gas storage and separation capabilities in the field of porous polymers. Later on we describe high pressure gas (CH_4, CO_2, H_2) uptake in BLP-2(H).

Chapter 5: Synthesis and Characterization of BLP-4(H) and BLP-10(H)

5.1 Introduction

Reported here are the synthesis and characterization of two new borazine-linked polymers. We have recently reported the synthesis of BLP-1(H) and BLP-12(H) which occur under solvothermal conditions via dehydrogenation of their corresponding amine-borane precursors. Here, BLP-4(H) and BLP-10(H) are synthesized in a similar fashion. BLP-4(H) employs m-phenylenediamine-borane as a precursor, representing the use of a bent-shaped building unit for the first time in a BLP. Benzidine-borane is used as the starting material in the synthesis of BLP-10(H), which is an extended analog of BLP-1(H) having two phenyl groups between each borazine unit instead of one. Benzidine-borane, however is dissolved in diglyme instead of monoglyme in the synthesis of BLP-10(H).

Scheme 5.1. Synthesis of BLP-4(H) and BLP-10(H) from in situ thermal decomposition of arylamine-borane adducts.

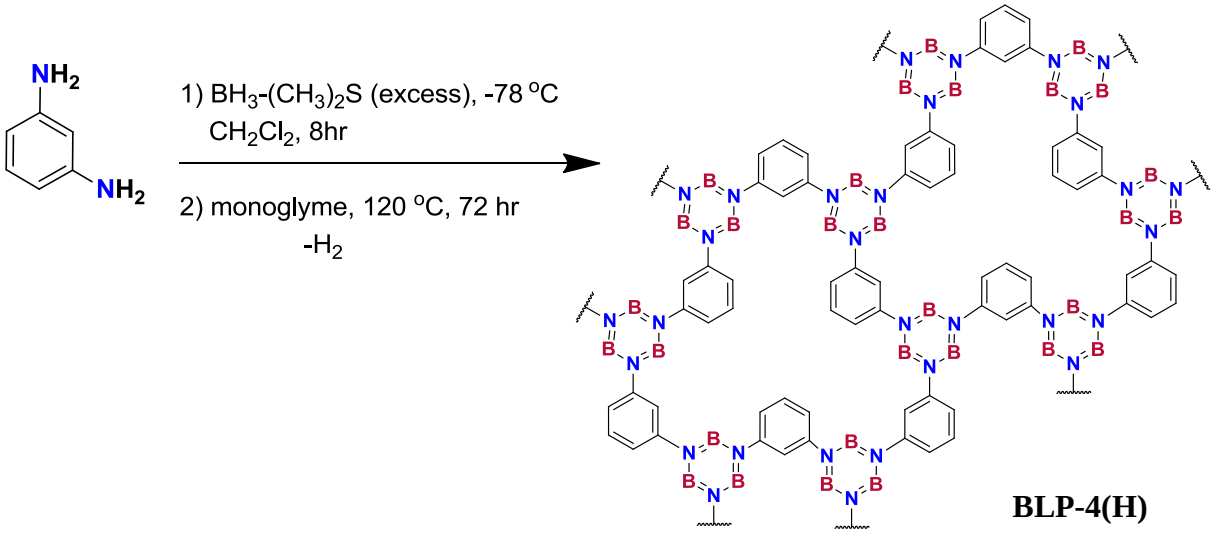

BLP-4(H)

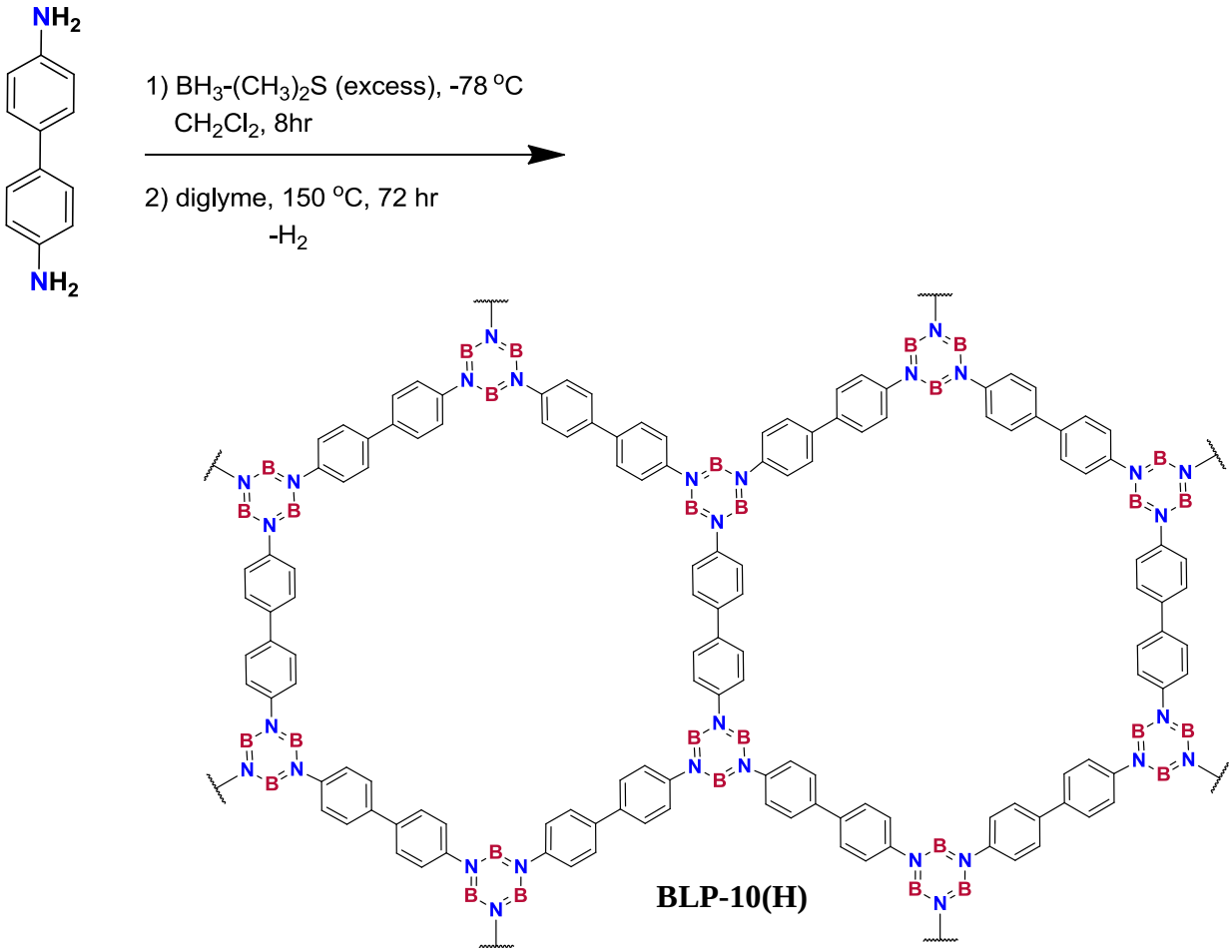

BLP-10(H)

5.2 Experimental

All starting materials and solvents, unless otherwise noted, were obtained from the Acros Organics Co. and used without further purification. Benzidine and *m*-phenylenediamine were purified by sublimation. Tetrahydrofuran (THF), monoglyme, and diglyme were dried over sodium and benzophenone. Dichloromethane (DCM) was dried over CaH_2. The isolation and handling of all polymer products were performed under an inert atmosphere of nitrogen using either glove box or Schlenk line techniques.

***m*-phenylenediamine-borane, $C_6H_4(NH_2{\cdot}BH_3)_2$**. A 100 ml Schlenk flask was charged with *m*-phenylenediamine (200 mg, 1.85 mmol) and 100 ml of anhydrous DCM. The solution was cooled to -78 ºC in an acetone/dry ice bath and treated with borane-dimethylsulfide (1.05 ml, 11.1 mmol, Aldrich) drop-wise under a flow of nitrogen. The clear solution was allowed to warm to room temperature while stirring overnight. On the following day, the white solid material is filtered and washed with DCM (3x15ml).^{1}H NMR: (300 MHz, DMSO-d_6) δ 7.47 (s, 4H), 7.11 (s, 4H), 1.51 (s, br, 6H).^{13}C NMR (75 MHz, DMSO-d_6) δ 144.4, 129.7, 120.0, 117.0.

BLP-4(H). A Pyrex tube was charged with *p*-$C_6H_4(NH_2{\cdot}BH_3)_2$ (35 mg, 0.26 mmol) and 2 ml of glyme. The tube was flash frozen at 77 K, evacuated and flame sealed. The reaction mixture was heated in a programmable oven at 0.1 ºC/min to 120 ºC for 72 h to afford a fluffy white polymer which was isolated by filtration over a medium glass frit and washed with anhydrous THF (3 x 15 ml) (82% yield).

Benzidine-borane, $C_6H_4(NH_2{\cdot}BH_3)_2$. A 100 ml Schlenk flask was charged with benzidine (200 mg, 1.08 mmol) and 100 ml of anhydrous DCM. The solution was cooled to -78 ºC in an acetone/dry ice bath and treated with borane-dimethylsulfide (1.05 ml, 11.1 mmol, Aldrich)

drop-wise under a flow of nitrogen. The clear solution was allowed to warm to room temperature while stirring overnight. On the following day, the white solid material is filtered and washed with DCM (3x15ml).^{1}H NMR: (300 MHz, d_6-DMSO) δ 7.59 (d, 4H), 7.52 (s, 4H), 7.26 (d, 4H), 1.59 (s, br, 6H).^{13}C NMR (75 MHz, d_6-DMSO) δ 123.3, 127.7, 137.6, 143.4

BLP-10(H). A Pyrex tube was charged with 35 mg of benzidine-borane (0.26 mmol) and 2 ml of diglyme. The tube was flash frozen at 77 K, evacuated and flame sealed. The reaction mixture was heated in a programmable oven at 0.1 ºC/min to 120 ºC for 24 h to afford a fluffy white polymer which was isolated by filtration over a medium glass frit and washed with anhydrous THF (3 x 15 ml) (60% yield). Anal. Calcd.for ($C_9H_9B_3N_3$): C, 70.7%; H, 4.9%; N, 13.7%. Found: C, 65.7%; H, 5.3%; N, 11.9%.

Inside a glove-box, about 150 mg of an as-prepared sample of BLP was loaded into an Autosorb cell then heated to 120 °C under dynamic vacuum (1.0 x 10^{-5} torr) for 16 h. The sample was back-filled with nitrogen to exclude adsorption of moisture prior to N_2 adsorption measurements.

Gas Sorption Analysis. Nitrogen experiments were run using a Quantachrome Autosorb 1-C analyzer at 77 K. Pore Size Distributions (PSDs) were calculated using Non-Local Density Functional Theory (NLDFT) on the adsorption branch with a cylindrical pore model.

5.3 Results and Discussion

The chemical composition and connectivity of the building units were investigated by spectral and analytical methods which included FT-IR, and elemental analysis. By observing the

loss of certain stretches expected for dehydrocoupling reactions combined with the appearance of borazine-characteristic peaks, the formation of the expected products can be confirmed. FT-IR spectra of starting materials, BLP-4(H) and BLP-10(H) were obtained as KBr pellets using Nicolet - Nexus 670 spectrometer. Consistent with previously reported BLPs, the bands at 3300-3500 cm^{-1} that correspond to the N-H stretching of amine/amine-borane adducts are significantly reduced after polymerization indicating a release of the amine hydrogen atoms from the starting material. Weak signals remain due to N-H stretches from unreacted $–NH_2$ on the surface of the polymers' particles and incompletely reacted groups at defects in the material. The aromatic C-H stretching observed around 2800-3100 cm^{-1} is more prevalent in BLP-10(H) which is expected due to the greater presence of phenyl groups. Borane B-H peaks in adducts were observed at approximately 2400 cm^{-1} while a slight shift to about 2550 cm^{-1} occurs as is typically seen in BLP formation.[95,96] The intensity of the B-H band in the amine-borane adducts is significantly reduced upon borazine formation. The strong stretch appearing at 1400 cm^{-1} also supports the formation of the B-N bonds of the borazine ring.[149-151]

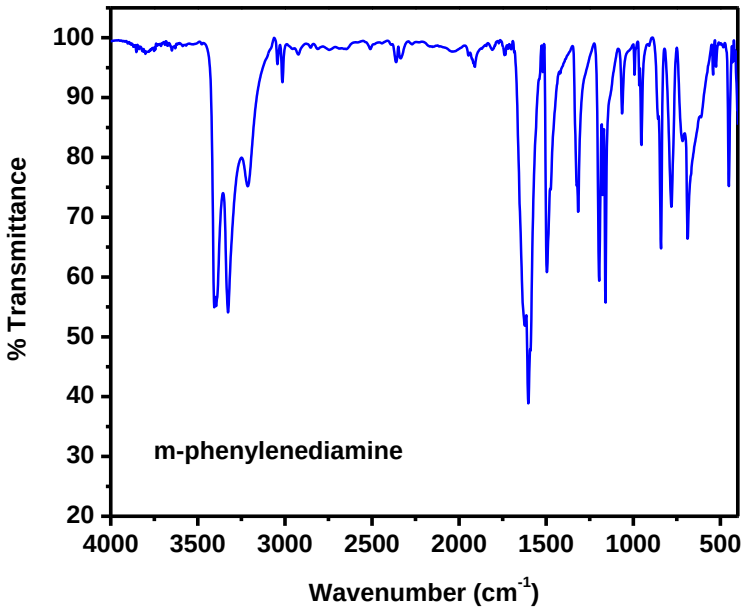

Figure 5.1: FT-IR spectrum of *m*-phenylenediamine.

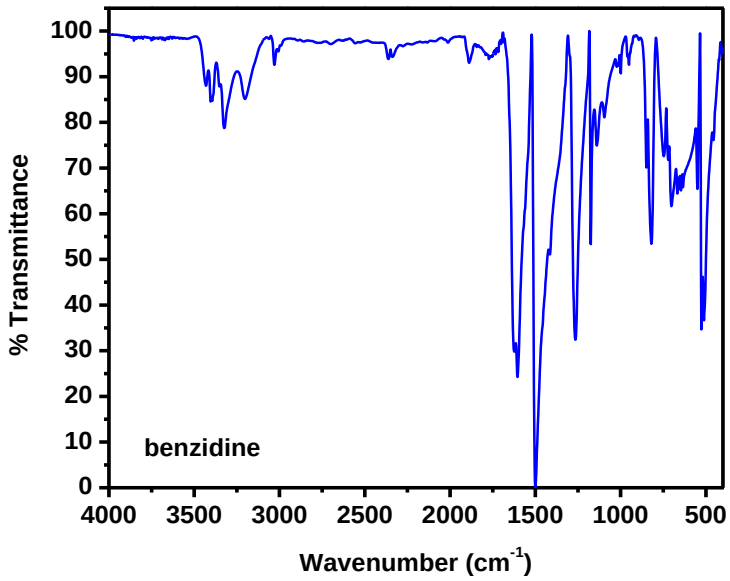

Figure 5.2: FT-IR spectrum of benzidine.

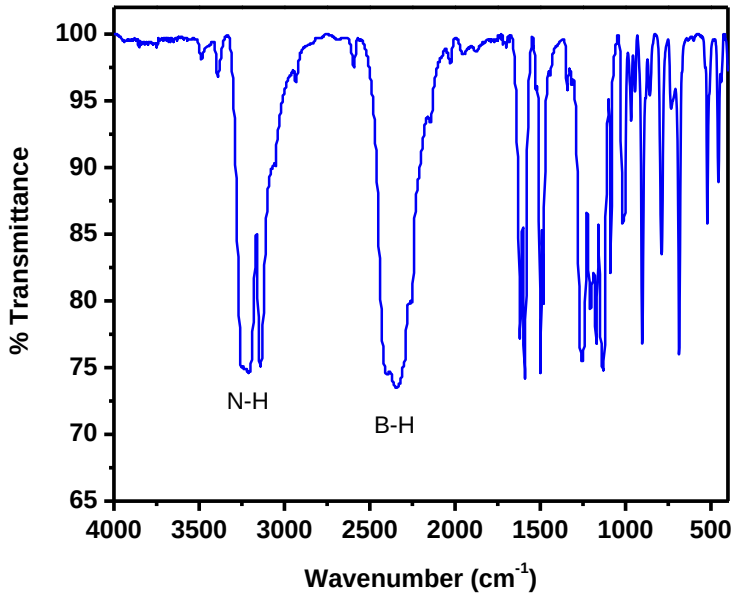

Figure 5.3: FT-IR spectrum of *m*-$C_6H_4(NH_2 \cdot BH_3)_2$.

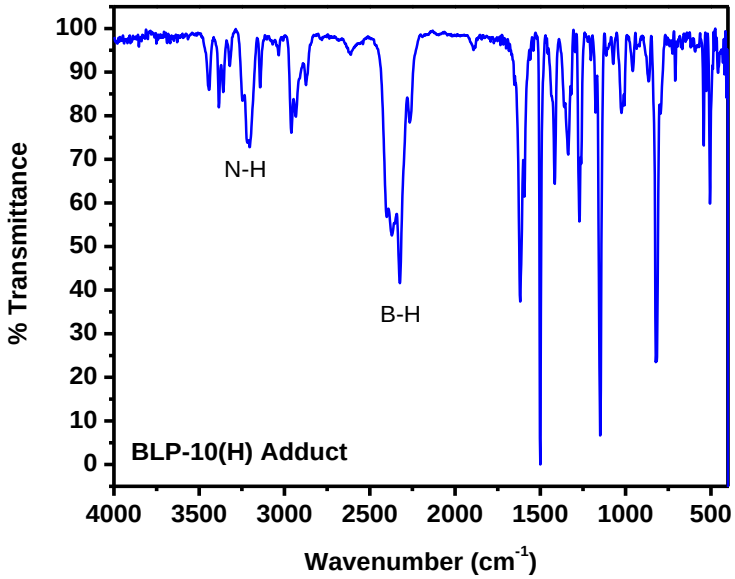

Figure 5.4: FT-IR spectrum of benzidine-borane.

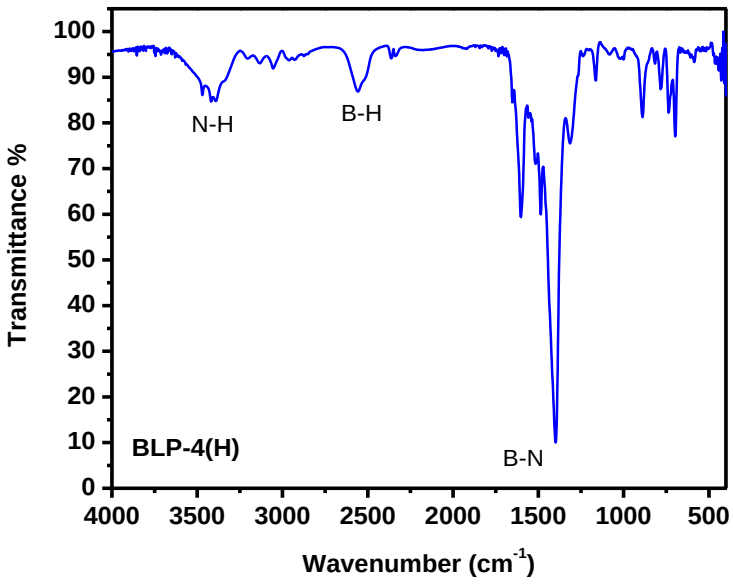

Figure 5.5: FT-IR spectrum of BLP-4(H).

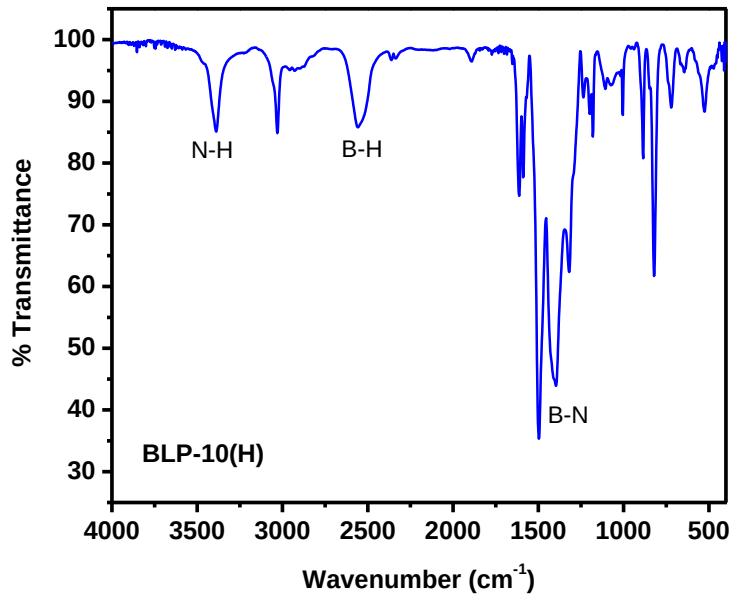

Figure 5.6: FT-IR spectrum of BLP-10(H).

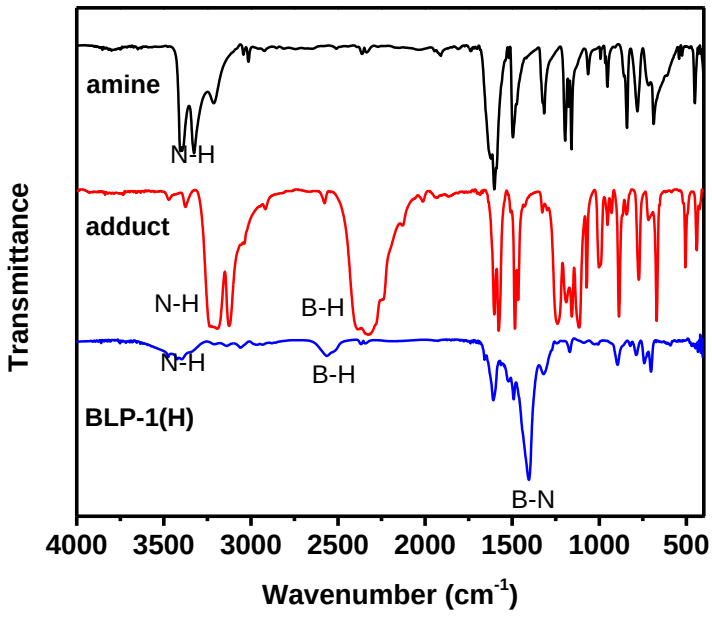

Figure 5.7: FT-IR spectrum of BLP-4(H) and starting materials.

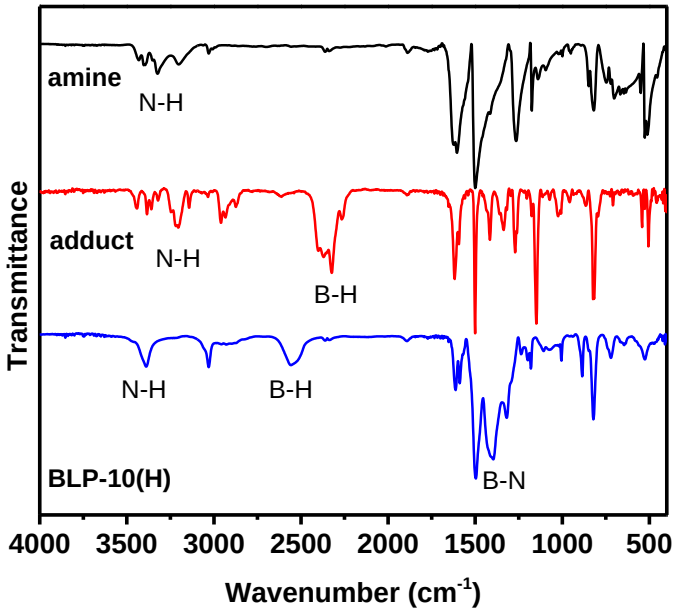

Figure 5.8: FT-IR spectrum of BLP-10(H) and starting materials.

BLPs were isolated under an inert atmosphere followed by degassing at 120°C / 1.0 x 10^{-5} torr for 16 hrs. In order to determine the morphology of products, scanning electron microscopy (SEM) was used. Samples were prepared by dispersing the material onto a sticky carbon surface attached to a flat aluminum sample holder. BLP-4(H) sample was platinum-coated using a Denton Vacuum V TSC HP Cold Sputtering Platform at $1x10^{-4}$ mbar of pressure in a nitrogen atmosphere for 120 seconds. BLP-4(H) was analyzed on a Hitachi SU-70 Scanning Electron Microscope using an accelerating voltage of 15 kV. For BLP-10(H), the sample was gold coated using an EMS (Electron Microscopy Sciences) 550x Sputter Coater at $1x10^{-1}$ mbar of pressure in a nitrogen atmosphere for 120 seconds while maintaining 20 mA of current. BLP-10(H) was analyzed on a Zeiss EVO XVP Scanning Electron Microscope using the SEI detector with accelerating voltages ranging from 10 kV to 20 kV. SEM images of as-prepared materials revealed a homogeneous morphology of spherical particles for BLP-4(H) and an irregularly shaped particle for BLP-10(H) indicating phase purity (Figures 5.9 and 5.10). BLP-4(H) has particle sizes of approximately 100 nm while BLP-10(H) has particles sizes of ~300 nm. Powder x-ray diffraction studies on as-prepared and activated materials indicated that both polymers are amorphous.

A

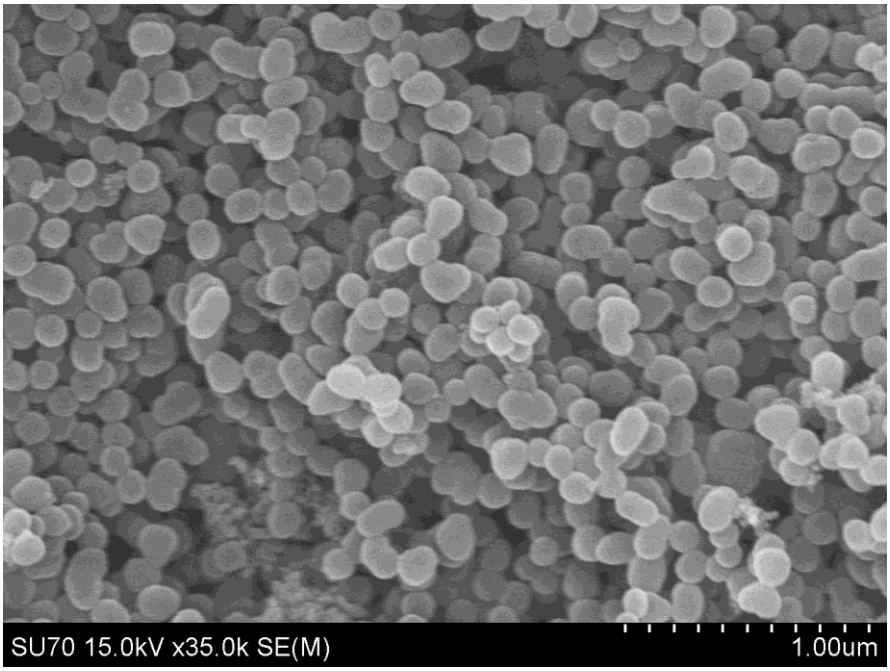

B

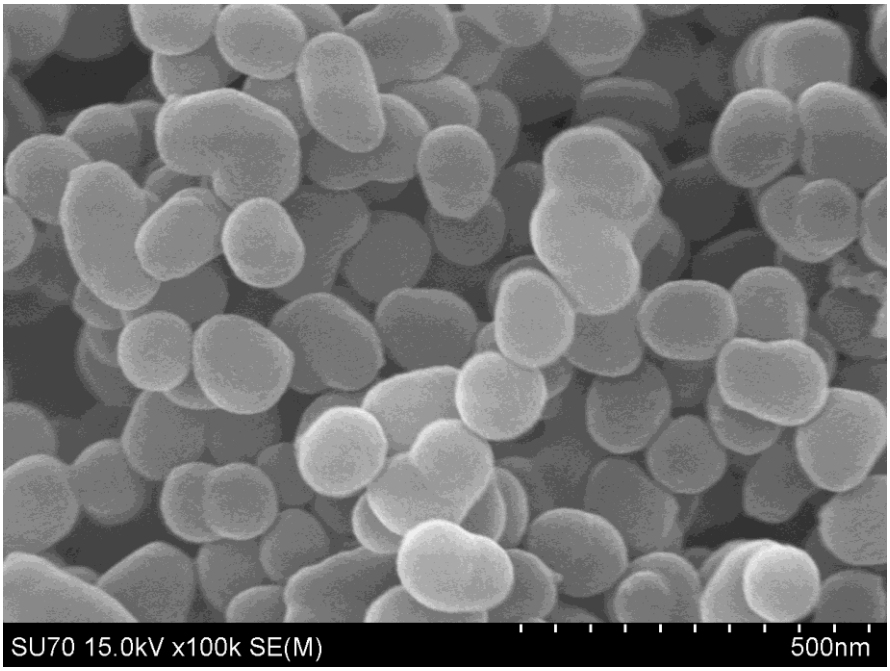

Figure 5.9: SEM image of BLP-4(H) revealing a spherical morphology.

A

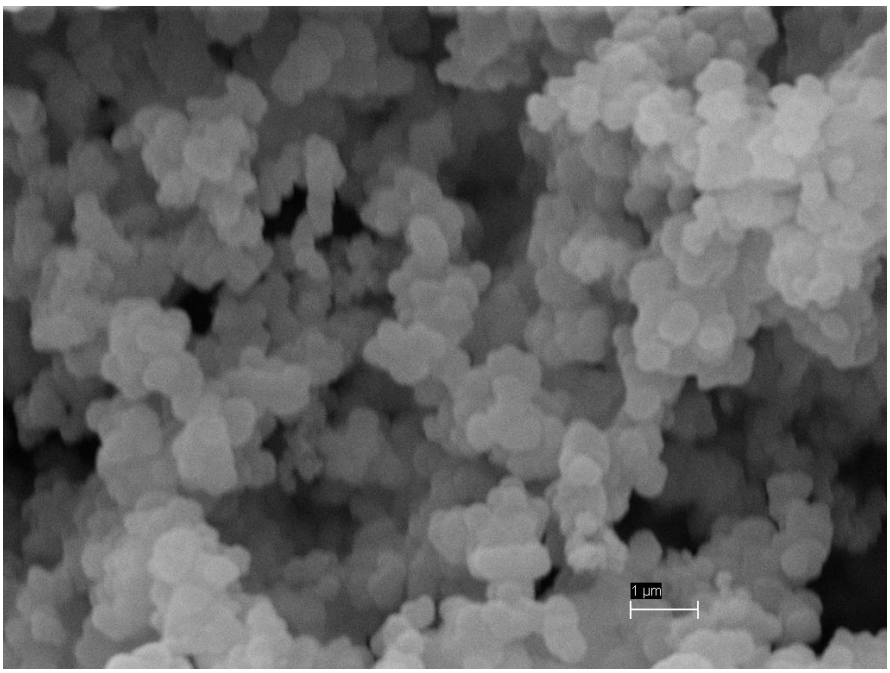

B

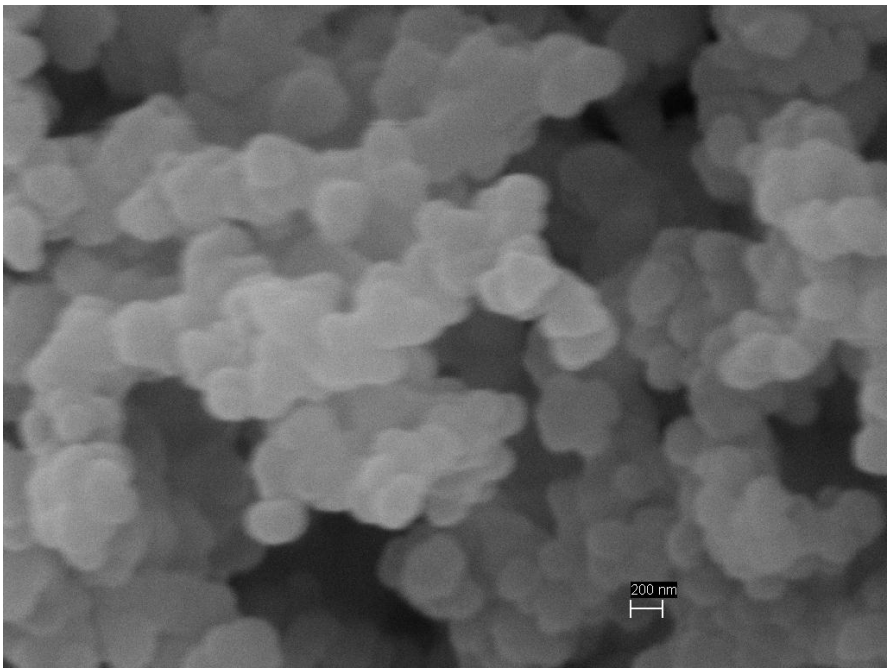

Figure 5.10: SEM image of BLP-10(H) revealing a spherical morphology.

To investigate porosity and thermal stability, BLPs were subjected to thermogravimetric analysis. BLP-4(H) and BLP-10(H) were analyzed by TGA to determine the thermal stability of the material produced as well as to confirm that all guests molecules have been removed. Samples were run on a TA Instruments Q-5000 series thermal gravimetric analyzer with samples held in platinum pans under an atmosphere of nitrogen. The TGA trace of the as-prepared BLP-4(H) represents an initial 10% weight loss due to the evacuation of solvent molecules and unreacted starting materials. Upon heating under nitrogen atmosphere BLP-4(H) remain stable up to 400 °C. This is a typical behavior of porous materials in general and has been reported for porous covalent frameworks.[76] BLP-10(H) undergoes substantial initial weight (30%) indicating a high degree of porosity. This could be explained by the difference in solvent used during synthesis. Monoglyme, which is used in the synthesis of BLP-1(H), 4(H) and 12(H), compared to diglyme which is used in BLP-10(H), is more volatile therefore much of the surface solvent in the former evaporates at room temperature before analysis. The longer biphenyl linkers compared to those of other BLPs also contribute to an increase in porosity. BLP-10(H) begins to decompose around 400 °C as is seen with BLP-4(H) and all other hydrogen-BLPs.

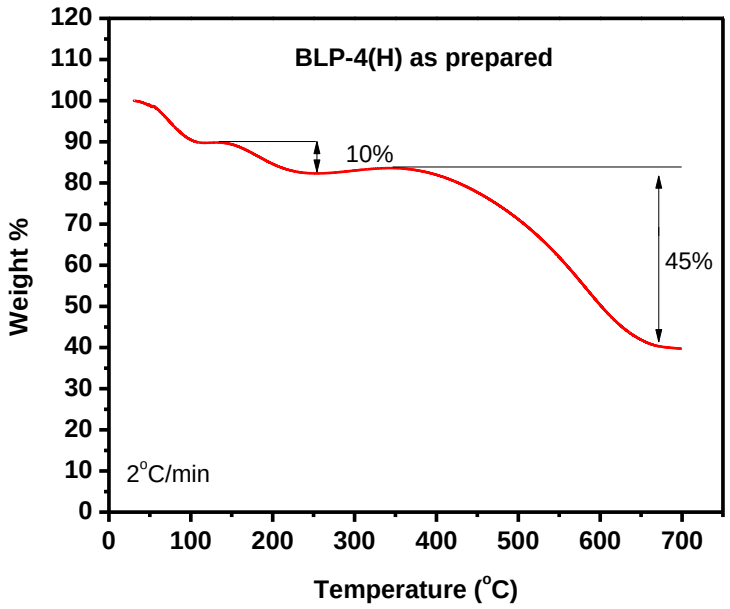

Figure 5.11: TGA trace for an unactivated sample of BLP-4(H).

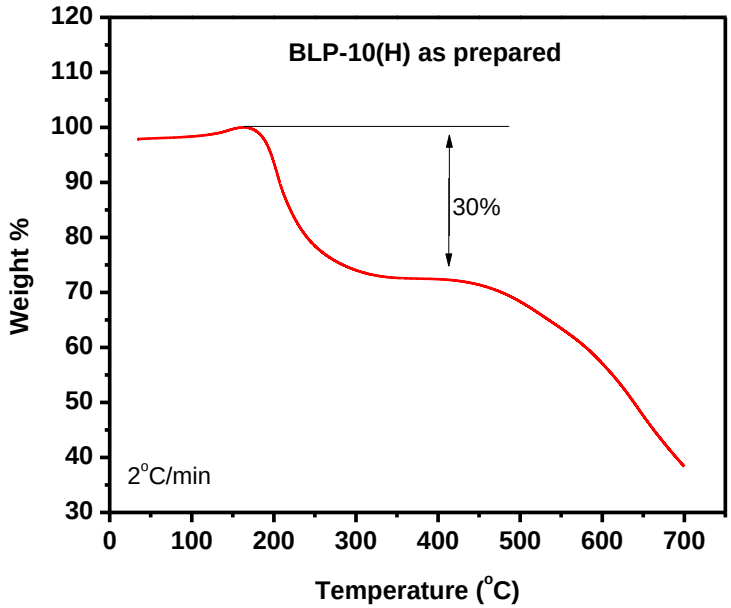

Figure 5.12: TGA trace for an unactivated sample of BLP-10(H).

Based on TGA studies and the thermal stability of BLPs we activated BLP-4(H) by degassing at 120 °C and BLP-10(H) at 150 ºC; both at 1 x 10^{-5} torr for 16 hrs prior to nitrogen porosity measurements. The Type I nitrogen isotherms are consistent with permanent microporous materials that are characterized by sharp uptakes at P/P_o = 10^{-4} to 10^{-2}, while the final rise in the nitrogen uptake is due to condensation in intermolecular cavities created by the packing of BLP particles. BLP-10(H) displays a slight bit of hysteresis toward higher pressures. The classical explanation is based on a change in geometry during adsorption and desorption.[183] Kitagawa reports a similar phenomenom in MOFs called a guest-induced transformation of pores.[184] Because of the longer benzidine building unit, BLP-10(H) is more flexible hence more susceptible to a "breathing" effect. The Brunauer-Emmett-Teller (BET) model was applied to each isotherm for P/P_o between 0.05 and 0.15 and resulted in surface areas of 885 and 843 m^2/g for BLP-4(H) and BLP-10(H), respectively. The Langmuir model (P/P_o = 0.05-0.30) gave surface area values of 1199 and 1132 m^2/g. The pore volumes (Vp) calculated at P/P_o = 0.90 were 0.54 cm^3/g for BLP-4(H) and 0.51 cm^3/g for BLP-10(H). Pore size distributions were estimated using density functional theory (DFT) calculations which revealed narrow pore-size distributions centered at 15.6 and 15.0 Å.

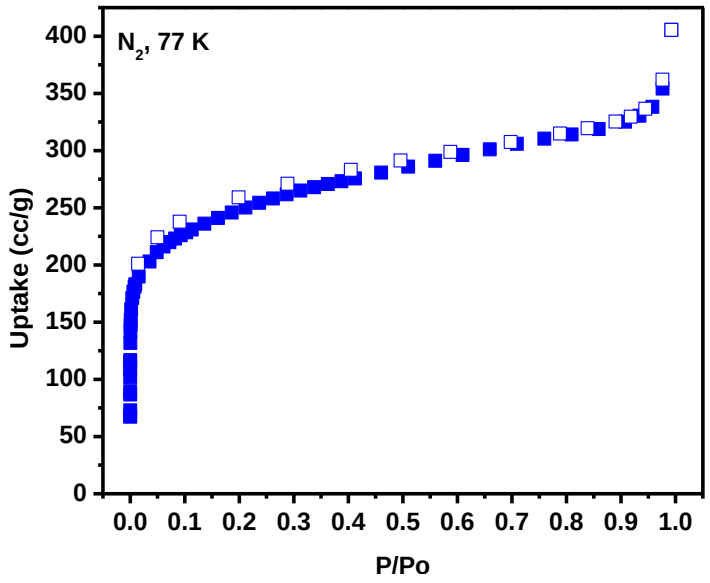

Figure 5.13: N_2 adsorption isotherm for BLP-4(H) (measured at 77 K. The filled squares are adsorption points and the empty squares are desorption points.

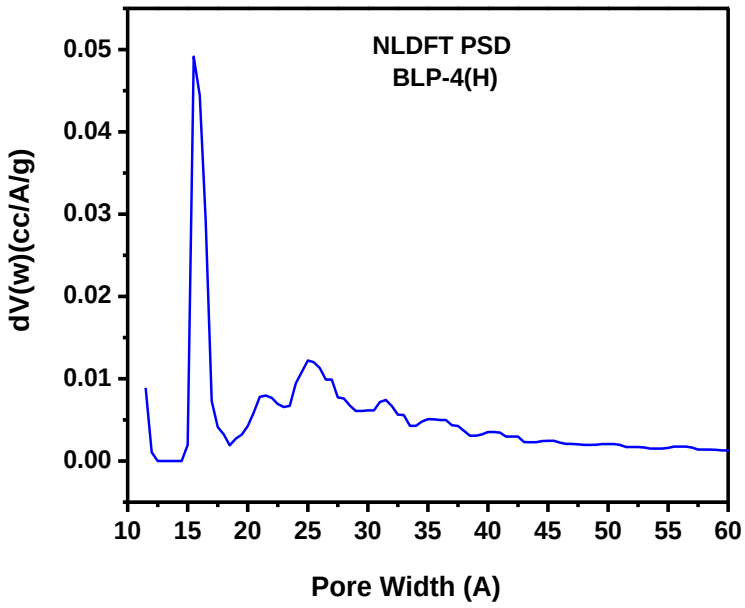

Figure 5.14: NLDFT Pore Size Distribution for BLP-4(H)

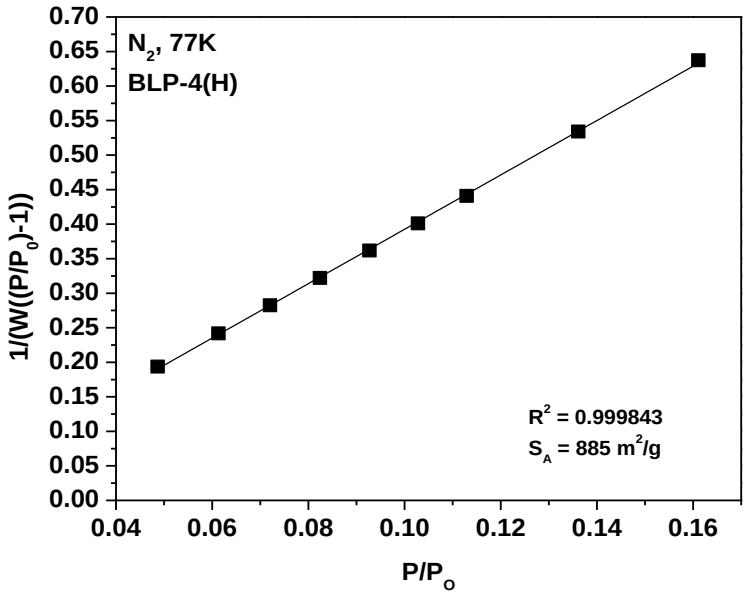

Figure 5.15. BET plot for BLP-4(H)

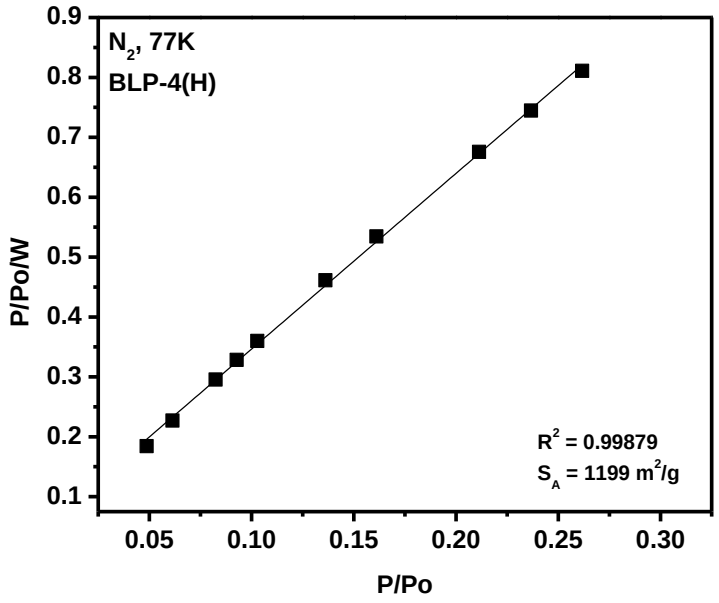

Figure 5.16. Langmuir plot for BLP-4(H)

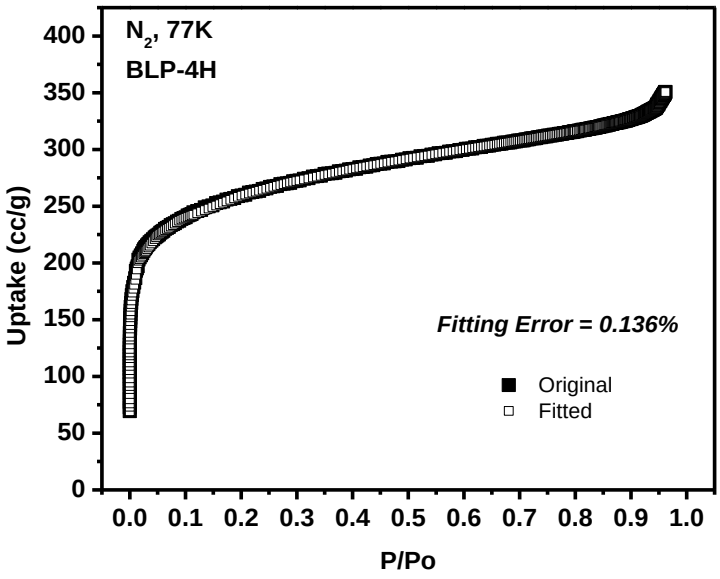

Figure 5.17: Experimental N_2 adsorption vs. calculated NLDFT isotherm for BLP-4(H)

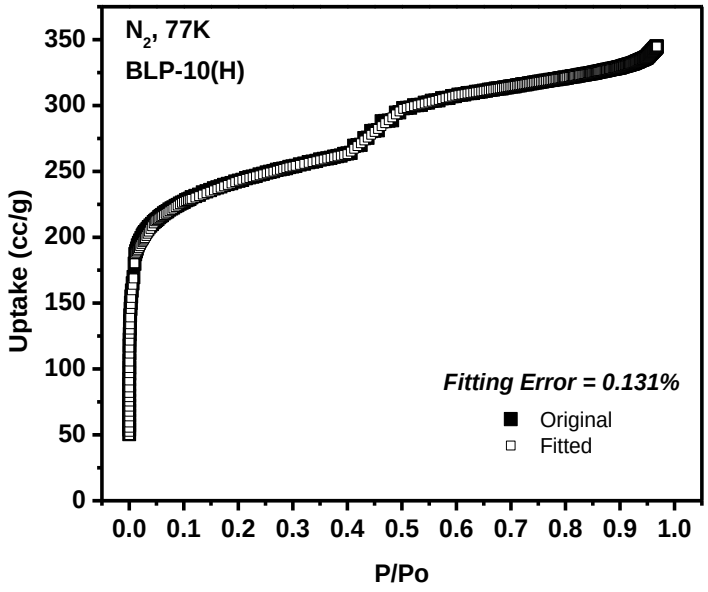

Figure 5.18 Experimental N_2 adsorption vs. calculated NLDFT isotherm for BLP-10(H)

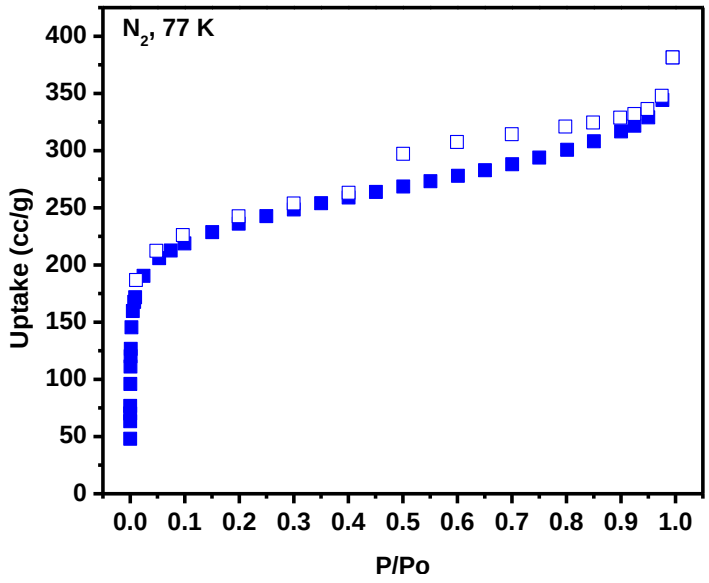

Figure 5.19. N_2 adsorption isotherm for BLP-10(H) measured at 77 K. The filled squares are adsorption points and the empty squares are desorption points.

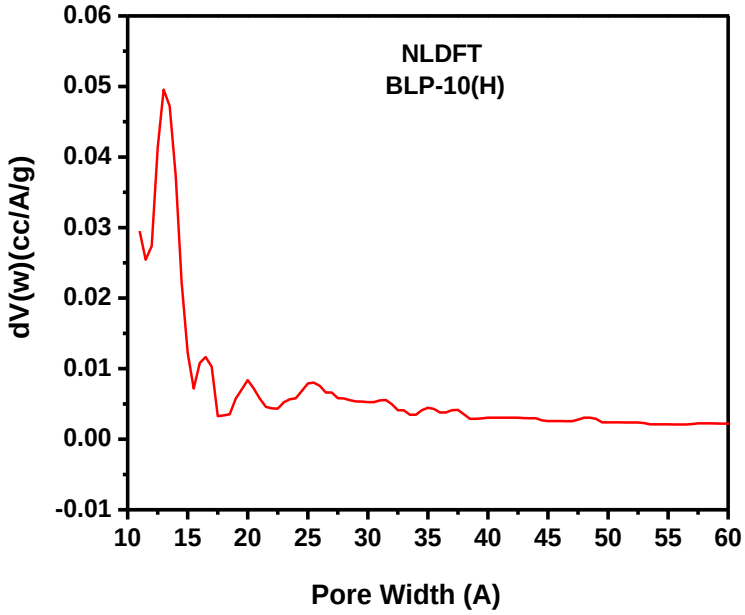

Figure 5.20. NLDFT Pore Size Distribution for BLP-10(H)

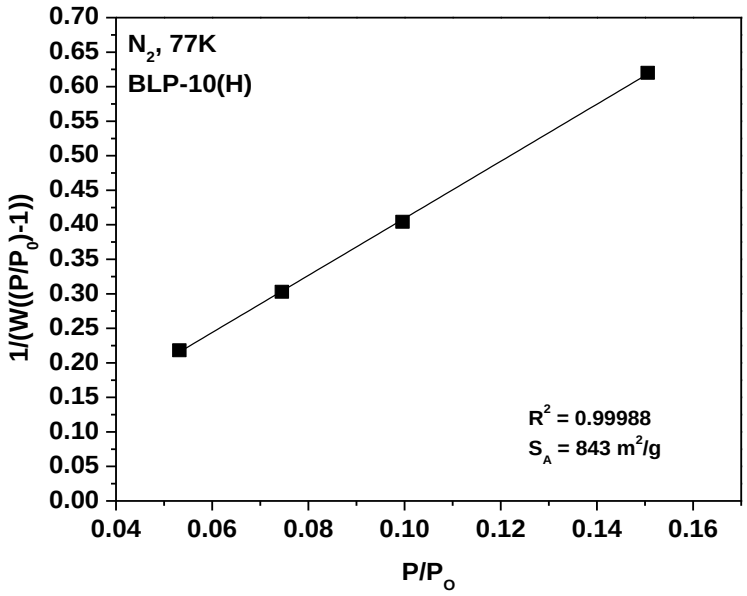

Figure 5.21 BET plot for BLP-10(H)

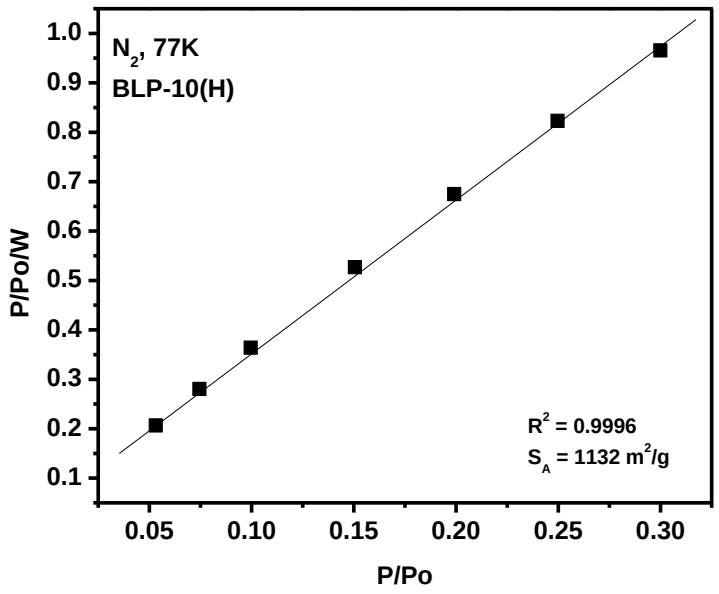

Figure 5.22 Langmuir plot for BLP-10(H)

5.4 Conclusion

We have synthesized and characterized two new BLPs: BLP-4(H) and BLP-10(H). The synthesis of these highly porous borazine-linked polymers by thermolysis of new arylamine-borane adducts and investigated their porosity via nitrogen adsorption experiments. Pore sizes and surface areas are in the range of previously reported BLPs though BLP-10(H) was expected to have a much higher porosity due to the longer organic linker. From this study, we can conclude that the extended linker my increase the possibility of forming interpenetrated nets leading to lower porosity.

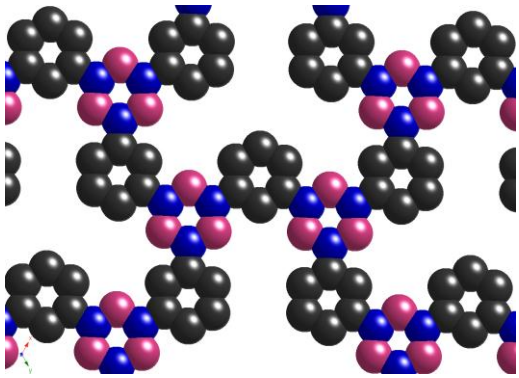

Figure 5.23. Model representation of BLP-4(H) using Materials Studio (pink spheres – boron; blue spheres – nitrogen; gray spheres – carbon; hydrogen atoms are omitted for clarity)

Chapter 6: Borazine-Linked Polymers: An investigation of High Pressure H_2, CH_4, and CO_2 Sorption and Selectivity

6.1 Introduction

Environmental issues have become increasingly important around the world with emphasis on finding solutions to the problems of climate change and sustainable development. Separation and removal of CO_2 from a variety of industrial gases is crucial to the development of a cleaner and more sustainable environment. Coal, for example, is a resource that is heavily relied upon for energy; therefore, the reduction of CO_2 emissions from coal-fired plants is a necessary goal for a future in clean energy.[185] If a suitable adsorbent is developed, it is very promising that these goals will be achievable. Recently there has been great interest in the design and synthesis of highly porous organic architectures for physical adsorption of environmentally relevant gases such as H_2, CH_4, and CO_2. The chemical composition, physical and textural properties are dictated during synthesis that allow for materials with enhanced properties relevant to their respective applications. These polymeric materials can possess considerable porosity and well-defined cavities which render them highly attractive especially in adsorptive gas storage. In addition to customized porosity, polymerization processes can lead to pore wall functionalization that significantly enhance gas uptake and selectivity as have been demonstrated for benzimidazole-linked polymers.[125] We have also recently reported on the inclusion of borazine (B_3N_3) as a functionalized and polarizable building block into porous borazine-linked polymers and their low pressure gas sorption

performances.[95,96] Borazine has been mainly used for the fabrication of BN-based ceramics or in organic optoelectronics.[142-146] However, up to date, the use of borazine for the preparation of porous polymers for gas storage and separation remains fairly undeveloped.

In this section, we describe high pressure H_2, CH_4, and CO_2 sorption studies on BLPs, the synthesis and characterization of a new melamine-based BLP, and extensive CO_2 selectivity studies using the ideal adsorption solution theory (IAST). The synthesis of BLP-3(H) was performed by thermolysis of the melamine-borane adduct in monoglyme to afford the corresponding polymers as white powder in good yields.

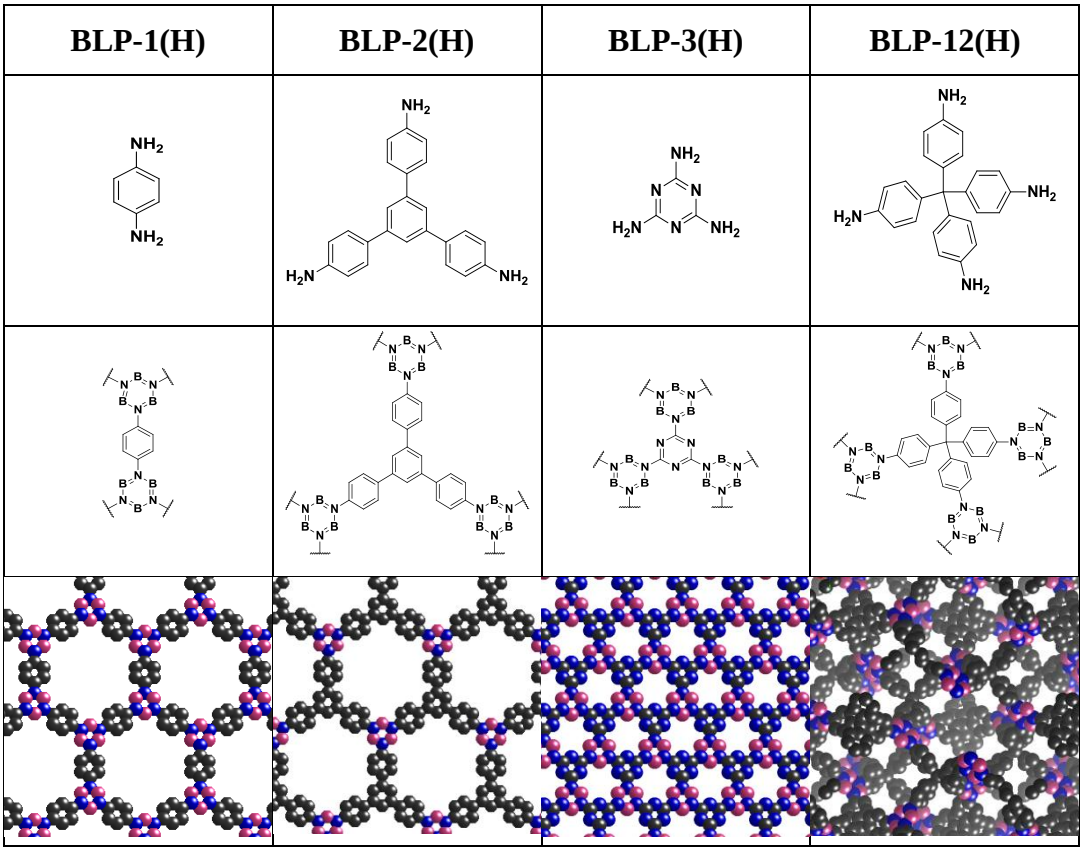

Figure 6.1. Amine building units (top) and their corresponding BLPs (middle) after treatment with borane and thermolysis. Theoretical representation and structure of products (bottom) of

BLP-1(H), -2(H), -3(H) and -12(H). B, pink; N, blue; C, black; hydrogen atoms are omitted for clarity.

6.2 Experimental

General Considerations. All starting materials and solvents, unless otherwise noted, were obtained from Acros Organics Co. and used without further purification. Melamine and *p*-phenylenediamine were purified by sublimation. Tetrahydrofuran (THF, Fisher) and monoglyme (Sigma-Aldrich) were distilled over sodium and benzophenone and dichloromethane (DCM, Fisher) was distilled over CaH_2. Toluene and mesitylene were dried over sodium. *Tetra*-(4-aminophenyl)methane and 1,3,5-tris(p-aminophenyl)benzene were synthesized according to published methods. The isolation and handling of all polymer products were performed under an inert atmosphere of nitrogen using either glove box or Schlenk line techniques.

FT-IR spectra of starting materials and BLPs were obtained as KBr pellets using Nicolet - Nexus 670 spectrometer. Solid-state NMR spectra were recorded at ambient temperature on a 360-1 instrument by Spectral Data Services, Inc., Champaign, IL. ^{11}B MAS NMR data were collected with a 45 degree ^{11}B pulse length and a recycle delay of two seconds. High-power H-1 decoupling was employed during acquisition only. Samples were spun at the magic angle at about 7 kHz. Chemical shifts are referenced to external neat boron trifluoroetherate. Samples for SEM were prepared by dispersing BLPs onto a sticky carbon surface attached to a flat aluminum sample holder. The sample was then platinum-coated using a Denton Vacuum V TSC HP Cold Sputtering Platform at $1x10^{-4}$ mbar of pressure in a nitrogen atmosphere for 120 seconds. Samples were analyzed on a Hitachi SU-70 Scanning Electron Microscope using an accelerating voltage of 15 kV. Thermogravimetric analysis was run on a TA Instruments Q-

5000 series thermal gravimetric analyzer with samples held in platinum pans under an atmosphere of nitrogen.

melamine-borane, $C_3N_3(NH_2{\cdot}BH_3)_3$. A 100 ml Schlenk flask was charged with melamine (200 mg, 1.58 mmol) and 100 ml of anhydrous DCM. The solution was cooled to -78 ºC in an acetone/dry ice bath and treated with borane-dimethylsulfide (1.50 ml, 15.8 mmol, Aldrich) drop-wise under a flow of nitrogen. The mixture was allowed to warm to room temperature while stirring overnight. On the following day, the white solid material is filtered and washed with DCM (3x15ml) (90% yield).^{1}H NMR: (300 MHz, d_6-DMSO) δ 6.75 (s, 4H), 1.50 (s, br, 6H).

BLP-3(H). A Pyrex tube was charged with melamine-borane (35 mg, 0.21 mmol) and 2 ml of glyme. The tube was flash frozen at 77 K, evacuated and flame sealed. The reaction mixture was heated in a programmable oven at 0.1 ºC/min to 120 ºC for 72 h to afford a fluffy white polymer which was isolated by filtration over a medium glass frit and washed with anhydrous THF (3 x 15 ml) (53% yield). Anal. Calcd.for ($C_9H_9B_3N_3$): C, 23.2%; H, 1.9%; N, 54.8%. Found: C, 25.9%; H, 4.7%; N, 33.6%.

Gas Sorption Measurements. Nitrogen experiments were run using a Quantachrome Autosorb 1-C analyzer at 77 K. Pore Size Distributions (PSDs) were calculated using Non-Local Density Functional Theory (NLDFT) on the adsorption branch with a spherical/cylindrical pore model. Hydrogen sorption experiments were run on the same Quantachrome Autosorb 1-C analyzer at both 77 K and 87 K. Methane and carbon dioxide experiments were run at 273 K and 293 K each. Ultrahigh purity helium (99.999%) was used to calibrate the free volume in the sample

cell before each measurement. For H_2 uptake measurement, hydrogen with purity of 99.999% was used. CO_2 (99.9%) and CH_4 (99.999%) were obtained from Airgas Inc. (Radnor, PA).

Heat of Adsorption Calculations. Using the data taken at two separate temperatures, the isosteric heat of adsorption for BLP-3(H) was calculated according to previous reports[148] by solving the virial-type expression:

$$\ln P = \ln N + (1/T)\sum_{i=0}^{m} a_i N^i + \sum_{i=0}^{n} b_i N^i$$

where P is pressure in torr, T is temperature in Kelvin, and N is the mmol of gas adsorbed per gram of sample. The values for *m* and *n* were varied such that $m \geq n$ and resulted in the best fit as determined by the sum of the squares of the errors. The values for a_0, a_1,…a_m were used in the calculation for the isosteric heat of adsorption, Q_{st}:

$$Q_{st} = -R\sum_{i=0}^{m} a_i N^i$$

The calculated values were plotted as they relate to surface coverage, and the isosteric heat of adsorption values at the point of zero-coverage are highlighted in the text.

Selectivity Calculations via IAST. CO_2/CH_4 selectivities were calculated using the ideal adsorption solution theory (IAST) of Myers and Prausnitz.[186] Pure component CO_2, H_2 and CH_4 isotherms obtained using a *Micromeritics High Pressure Volume Analyzer* (HPVA) measured at 275 and 298 K were fitted using a dual-site Langmuir-Freundlich (DSLF) model

$$q_i = a\frac{b\,p_{i,A}^{1/c}}{1 + bp_{i,A}^{1/c}} + d\frac{ep_{i,B}^{1/f}}{1 + ep_{i,B}^{1/f}}$$

The calculations were performed for binary mixtures with equal partial pressures in the bulk gas phase, i.e., p1= p2., where q_i is the saturation capacity of species *i*, mol kg^{-1}; *a* and *d* the molar loading of species *i*, mol kg^{-1}; *b* and *e* are the dual Langmuir-Freundlich constants for species i; p_i, the bulk gas phase pressure of species *i*, *A* and *B* referring to adsorption sites *A* and *B*; and *c* and *f* are the dual Langmuir-Freundlich isotherm fits for species *i*. The integrals were computed numerically and the adsorbed phase composition that minimized the difference between the integrals of the two spreading pressures was found using Mathematica®[187]

$$\int_0^{f_1^0} N_1^0(f_1)dlnf_1 = \int_0^{f_2^0} N_2^0(f_2)dlnf_2$$

the single-component adsorption amount and selectivity are further obtained from the above equation by numerical integration and root exploration. The adsorption selectivities, S_{ads}, for binary mixtures of CO_2/CH_4 and CO_2/H_2 were defined by

$$S_{ads} = \frac{q_1/q_2}{p_1/p_2}$$

6.3 Results and Discussion

6.3.1 Synthesis and Characterization of BLP-3(H).

The geometrical similarity between boroxine and borazine rings and the versatile synthetic routes of the latter encouraged us to consider a new class of highly porous borazine-linked polymers (BLPs), derived from amine-borane adducts. Amine-borane adducts can be synthesized by treatment of an amine with a borane source or from ammonium chloride salt and $LiBH_4$.[4] Primary and secondary amine-borane adducts have been shown to undergo dehydrocoupling at temperatures above 100 ˚C to yield cyclic aminoborane (4 or 6-membered rings) and borazine derivatives.[105-109] Manners and co-workers[110-111] demonstrated the first

well-characterized examples of boron-nitrogen bond formation under mild reaction conditions using transition metal catalysts (Rh, Ir, Ru and Pd). Since the development of these heterogeneous catalytic systems, several homogeneous catalytic transition metal systems have been developed including an Ir-pincer complex[188], $[TiCp_2]$[189] and $RhCl(PHCy_2)_3$[190] to form B-N bonds.

We have recently reported the synthesis of BLP-1(H), BLP-2(H), and BLP-12(H)[96] which occur under solvothermal conditions via dehydrogenation of the their corresponding amine-borane precursors. BLP-3(H) and its corresponding precursor, Melamine-borane was synthesized in a similar fashion. Melamine however, was not soluble in DCM, the reaction solvent. The experiment proceeded, however in adequate yields without completely solubilizing the starting material. BLP-3(H) is synthesized by heating the dissolved amine-borane in monoglyme then filtered as a fluffy white powder.

From FT-IR spectra, by observing the loss of certain stretches expected for dehydrocoupling reactions combined with the appearance of borazine-characteristic peaks, the formation of the expected products can be confirmed. For melamine and melamine-borane, the peaks at 3000-3500 correspond to the N-H stretching. A large stretch at 1650 cm^{-1} is due to the C=N bonds of the triazine ring.[191] The spectrum of melamine-borane and BLP-3(H) is considerably unresolved. It is obvious, however, due to the appearance of the broad peak at ~2500 cm^{-1} that borane is successfully incorporated in the spectrum of the melamine-borane. There is a reduction of peaks in the 3000-3500 region, after polymerization representing dehydrogenation though signals remain more than usual, due to N-H stretches from unreacted – NH_2 on the surface of the polymer's particles. The apparent larger portion of incompletely reacted material and terminal groups is expected due to the insolubility of the starting material.

The borazine peak typically seen at 1400 cm^{-1} is evident, however partially concealed due to a high overlap of the more prevalent triazine stretch at 1650 cm^{-1}.

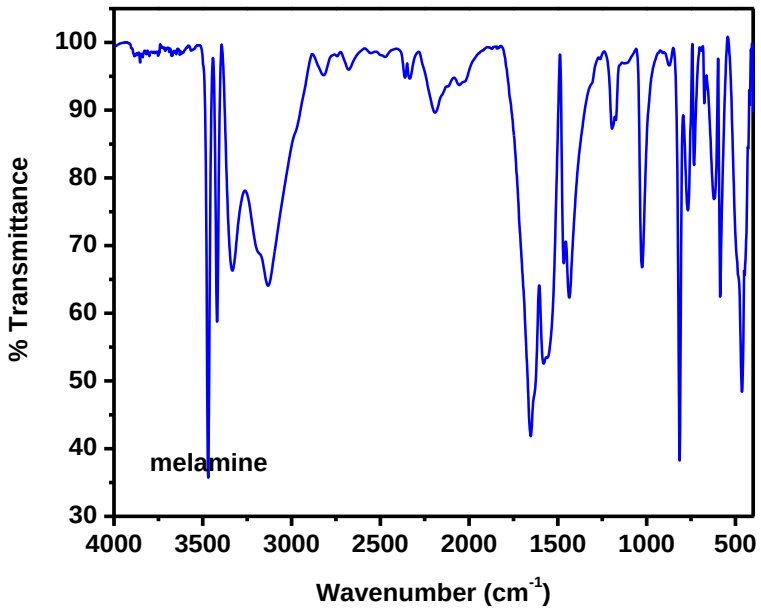

Figure 6.2. FT-IR spectrum of melamine

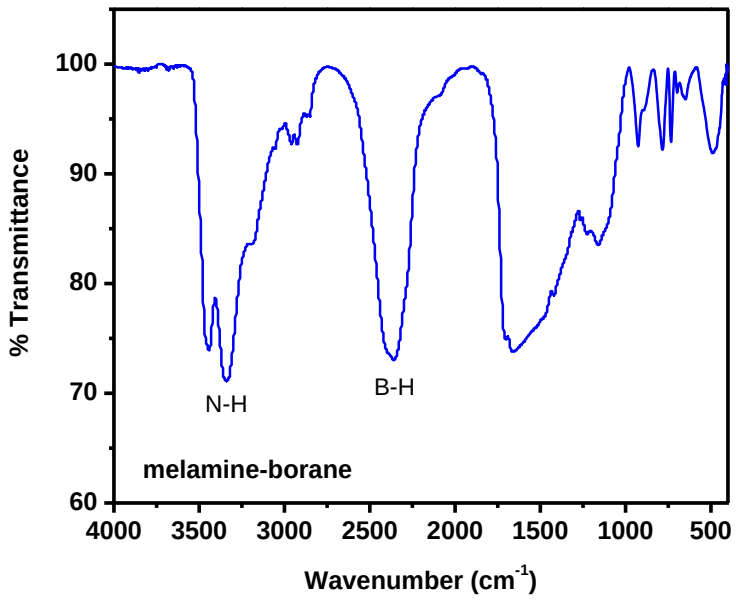

Figure 6.3. FT-IR spectrum of melamine-borane.

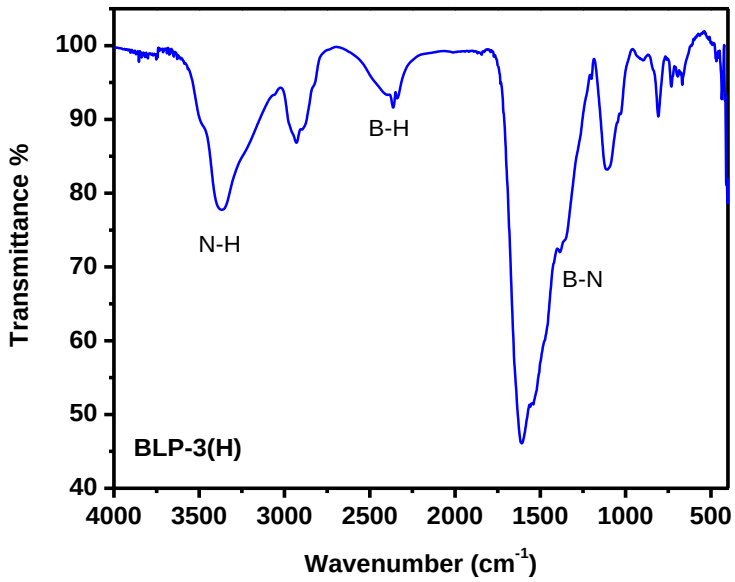

Figure 6.4. FT-IR spectrum of BLP-3(H).

^{11}B MAS and ^{13}C CP-MAS NMR spectra were used to establish the connectivity and coordination number of boron and to verify the inclusion of intact building units into the framework of BLPs. The ^{13}C CP-MAS signals which appear as broad peaks in the aromatic range support the incorporation of the intact melamine core into the network of BLP-3(H) as seen in Figure 6.5 (*asterisks represent spinning side bands)*. The ^{11}B signal for BLP-3(H) appears as a very broad peak similar to previously reported BLPs and other borazine-containing polymers (0-40 ppm).[12]

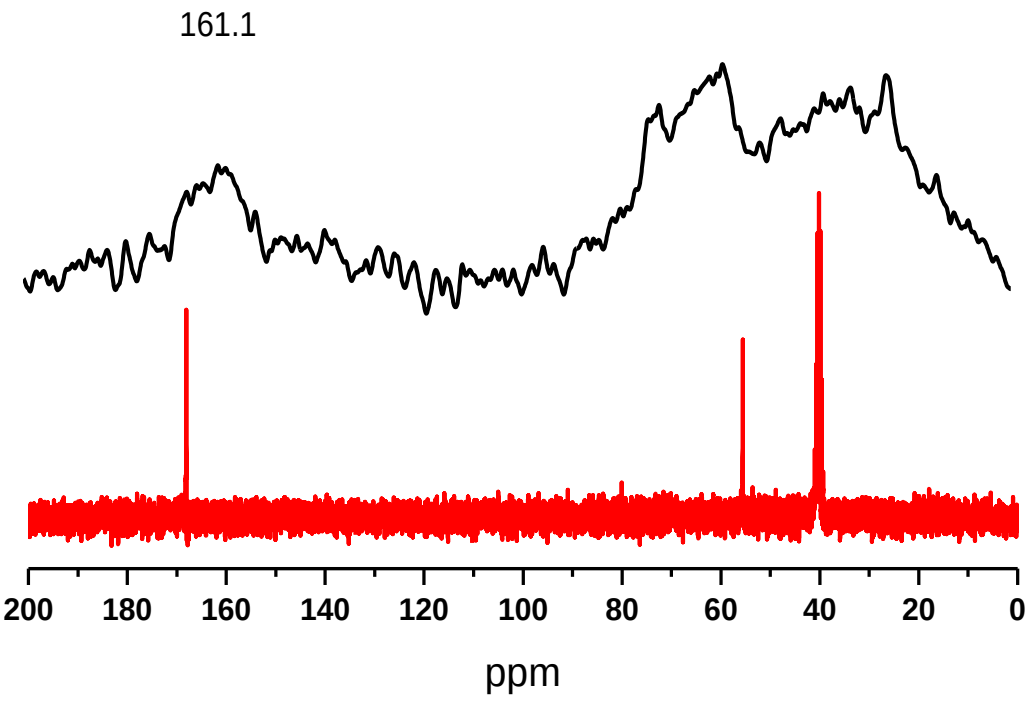

Figure 6.5. Solid state ^{13}C CP-MAS NMR spectra for BLP-3(H). Red line – ^{13}C NMR of starting material. *Signals at 55 and 40 are DCM and DMSO-d_6, respectively.*

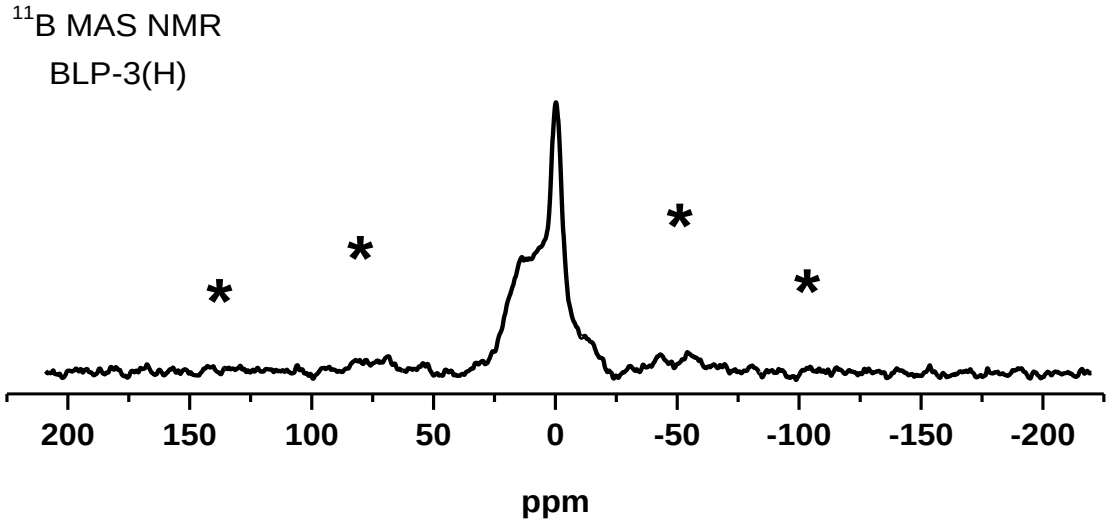

Figure 6.6. Solid state ^{11}B MAS NMR spectra for BLP-3(H).

In order to determine the morphology of products, scanning electron microscopy (SEM) was used. A sample of BLP-3(H) was isolated under an inert atmosphere followed by degassing at 120°C / 1.0 x 10^{-5} torr for 16 hrs. SEM images of activated material revealed irregularly shaped particles ~200 nm in diameter. Only one type of morphology was found to exist in each polymer, confirming the purity of the material produced. Powder x-ray diffraction studies on as-prepared and activated materials indicated that both polymers are amorphous.

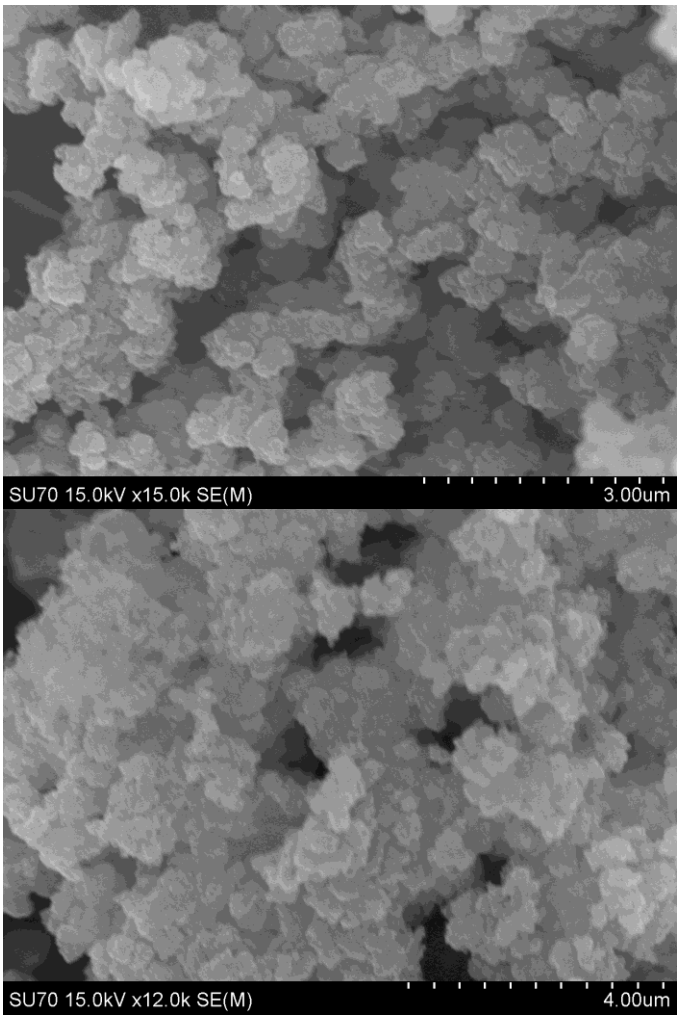

Figure 6.7: SEM image of BLP-3(H) revealing an irregular morphology.

We anticipated BLPs to be thermally stable and highly porous. Therefore we subjected BLPs to thermogravimetric analysis and nitrogen porosity measurements. BLP-3(H) was analyzed by TGA to determine the thermal stability of the material produced as well as confirm that all guests have been removed. Samples were run on a TA Instruments Q-5000 series thermal gravimetric analyzer with samples held in platinum pans under an atmosphere of nitrogen. The TGA trace of an as-prepared sample shows an initial 10% weight loss due to pore evacuation of solvent molecules. The polymer remains stable until about 250 ºC where a gradual loss in weight begins to occur, which is followed by a sharp decrease at ~400 ºC. This gradual weight loss is thought to be due to interlayer cross-linking. This behavior has been observed previously reported borazine-containing polymers.[192,193]

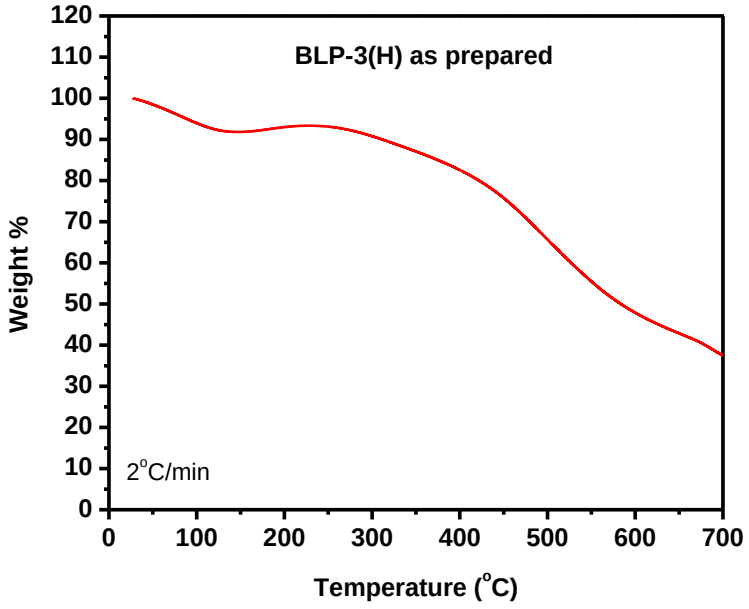

Figure 6.8: TGA trace for an unactivated sample of BLP-3(H).

Based on TGA studies and the thermal stability of BLPs we activated both materials by degassing at 120 °C and 1 x 10^{-5} torr for 16 h prior to nitrogen porosity measurements. BLP-3(H) displays a type I nitrogen isotherm which is consistent with permanent microporous materials that are characterized by a sharp uptake at $P/P_o = 10^{-4}$ to 10^{-2}, while the final rise in the nitrogen uptake is due to condensation in intermolecular cavities created by the packing of BLP particles. Using the Brunauer-Emmett-Teller (BET) model to P/P_o between 0.05 and 0.15, surface area was calculated to be 1071 m^2/g . The Langmuir model (P/P_o = 0.05-0.30) gave a surface area value of 1387 m^2/g. The surface area of BLP-3(H) is among the lowest reported for BLPs but still surpasses crystalline covalent nets such as COF-1 (711 m^2/g),[2a] and CTF-1 (791 m^2/g).[3a] The pore volume (V_p) of BLP-3(H) calculated at P/P_o = 0.90 was 0.53 cm^3/g. Using the Non-Local Density Functional Theory (NLDFT) we were able to calculate pore size distribution (PSD) on the adsorption branch with a cylindrical pore model on the nitrogen experiments combined with data taken from carbon dioxide sorption experiments performed at 273 K (Figure 6.10) as has been reported previously. PSD revealed a narrow pore-size distributions centered at about 13.8 Å.

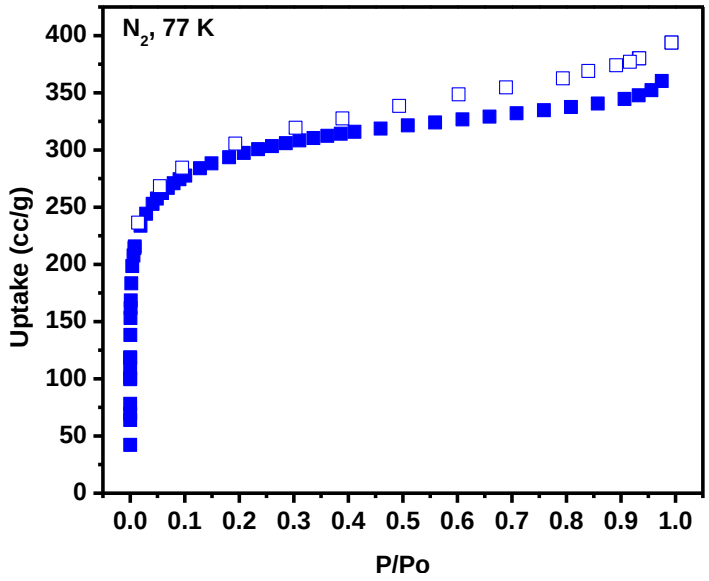

Figure 6.9: N_2 adsorption isotherm for BLP-3(H) measured at 77 K. The filled squares are adsorption points and the empty squares are desorption points.

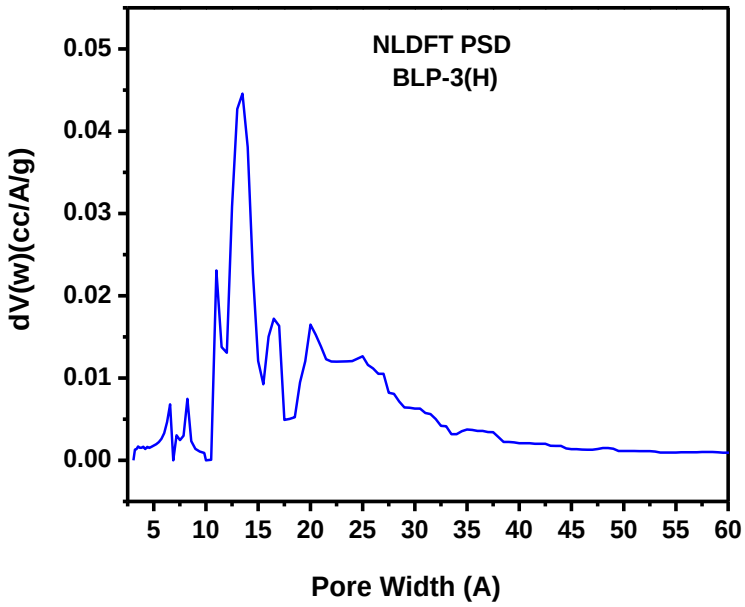

Figure 6.10: NLDFT pore size distribution for BLP-3(H)

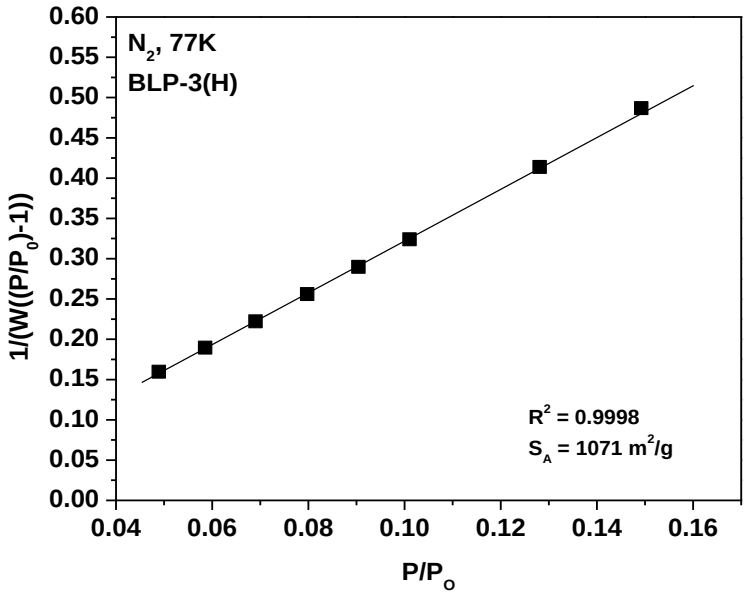

Figure 6.11: BET plot for BLP-3(H)

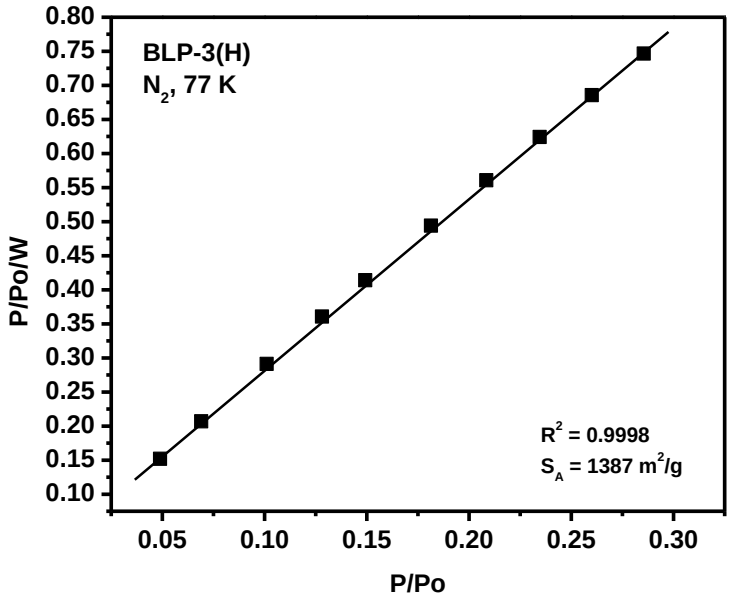

Figure 6.12: Langmuir plot for BLP-1(H)

6.3.2 Low Pressure (1 bar) Gas Storage in BLP-3(H).

Low pressure hydrogen, methane, and carbon dioxide isotherms were measured at various temperatures and used to calculate heats of adsorption for BLP-3(H). The maximum H_2 uptake for BLP-3(H) at 1 bar and 77 K was found to be 148 cc/g. From the 77 K and 87 K isotherms, we calculated the hydrogen isosteric heat of adsorption (Q_{st}) using the virial method. At zero coverage, BLP-3(H) displays a H_2 Qst of 7.7 kJ/mol which the highest of all reported BLPs to date. The maximum uptake for CH_4 and CO_2 at 273 K was 13.1 cc/g and 53.7 cc/g with a respective Q_{st} values of 10.1 kJ/mol and 22.1 kJ/mol at low coverage. It is noteworthy that maximum CO_2 uptake for BLP-3(H) is higher than those of BLP-1(H) and BLP-2(H), though its surface area and pore volume is lower. This is thought to be due to its high borazine content and will be discussed in more detail in the selectivity section. CO_2 and CH_4 Q_{st} values were calculated by fitting isotherms run at 273 and 298 K to the virial equation as was done with hydrogen. A summary of low pressure data and Q_{st} values are displayed in Table 6.1.

Table 6.1. Low pressure uptake values (1 bar) and heats of adsorption for selected BLPs

	SA_{BET} (m^2/g)	H_2 Uptake (cc/g)	CH_4 Uptake (cc/g)	CO_2 Uptake (cc/g)	Q_{st} (kJ/mol)		
					H_2	CH_4	CO_2
BLP-1(H)	1360	148.2	13.7	37.4	6.8	16.7	25.3
BLP-2(H)	1178	168.8	14.3	40.9	6.8	16.2	22.1
BLP-3(H)	1071	135.3	13.1	53.7	7.7	10.1	22.1
BLP-12(H)	2244	222.5	18.1	64.8	6.0	17.0	25.2

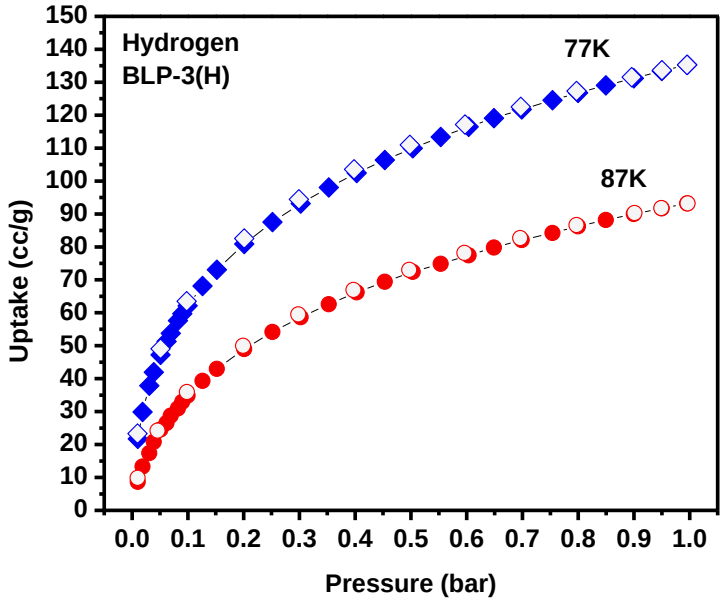

Figure 6.13: H_2 adsorption isotherms for BLP-3(H) measured at 77 K (blue diamonds) and 87K (red circles). The filled shapes are adsorption points and the empty shapes are desorption points.

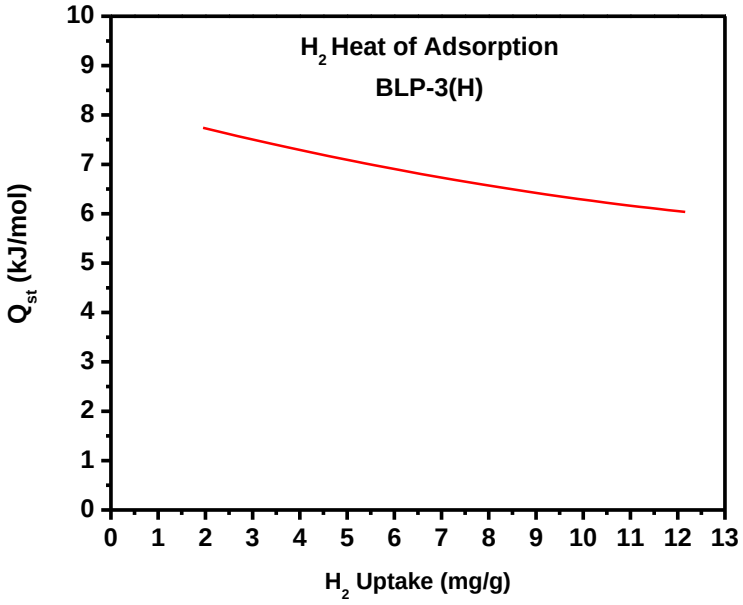

Figure 6.14: Hydrogen isosteric heat of adsorption (Q_{st}) for BLP-3(H).

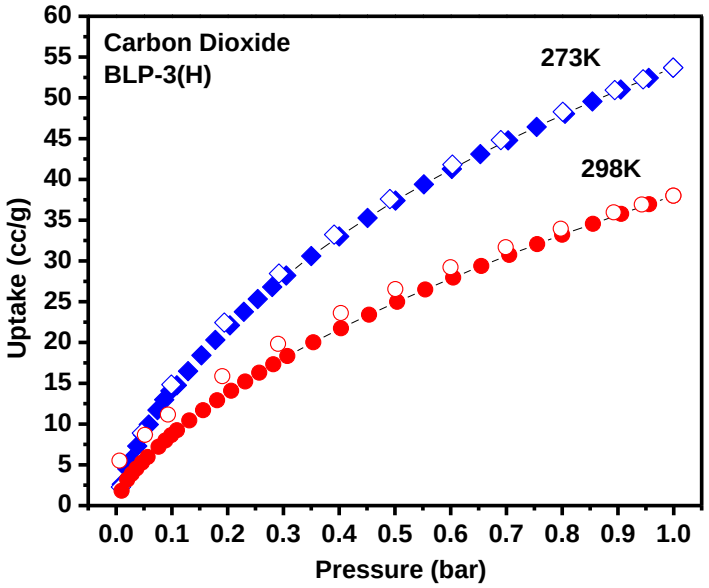

Figure 6.15: Carbon dioxide adsorption isotherms for BLP-3(H).

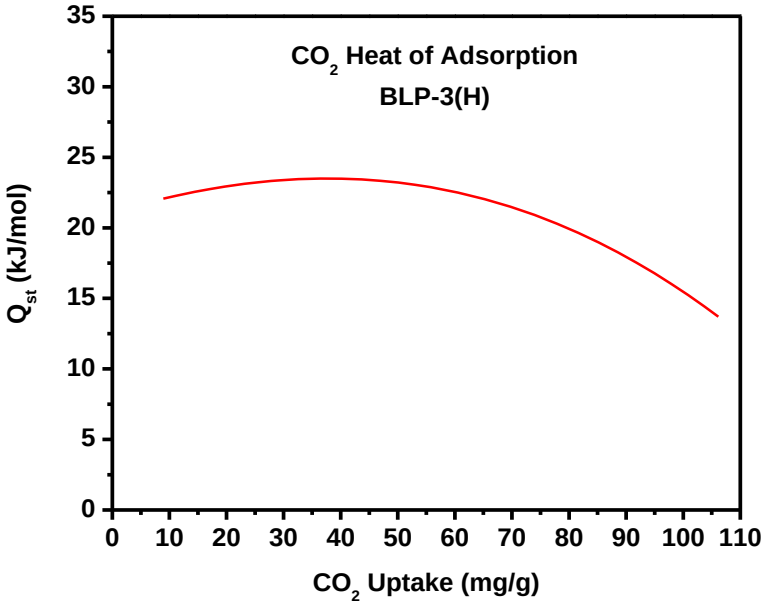

Figure 6.16: Carbon dioxide isosteric heat of adsorption (Q_{st}) for BLP-3(H).

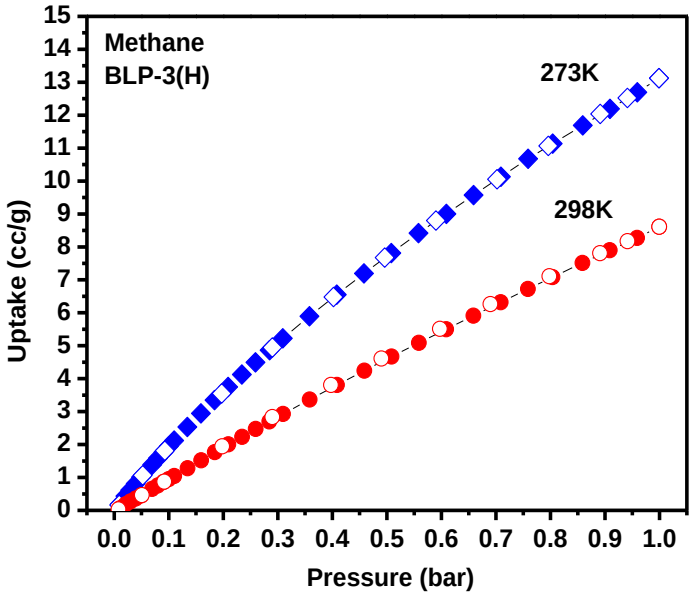

Figure 6.17: Methane adsorption isotherms for BLP-3(H).

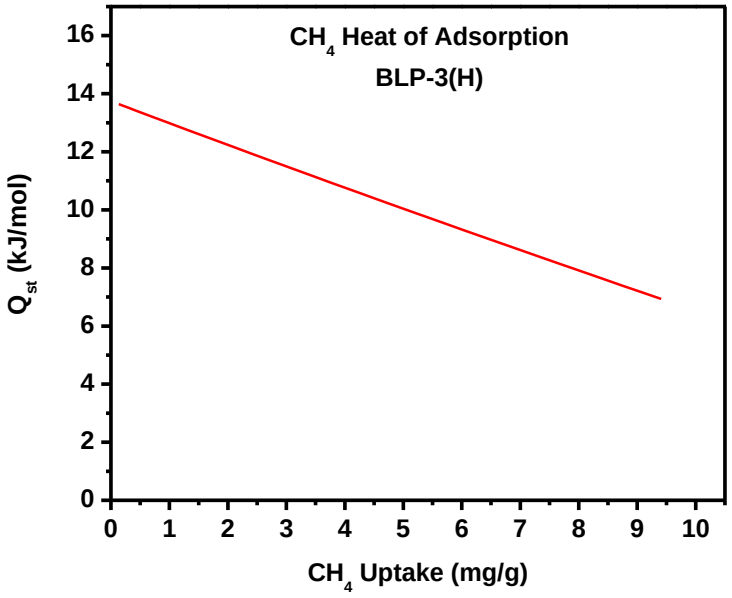

Figure 6.18: Methane isosteric heat of adsorption (Q_{st}) for BLP-3(H).

6.3.3 High Pressure Gas Sorption in BLPs

Hydrogen Storage in BLPs. Because of great interest in the use of hydrogen as an alternative fuel, we investigate the high pressure uptake capacity in BLPs. We have previously reported low pressure measurements on BLP-1(H), -2(H), and -12(H) which perform competitively compared to similar polymers in the field. Here, we take a further look into how increased pressure affects gas uptake in borazine containing polymers at various temperatures. At low pressures, the three dimensional BLP-12(H), solidly outperforms the 2D BLPs in terms of gas uptake having the hightest surface area and pore volume. However, surface area in porous polymers seems to play a major role as pressure is increased. Though BLP-12(H) remains the best hydrogen storage material at 40 bar with an uptake of 4.2 wt %, BLP-1(H) however is well within range with an uptake of ~4.0 wt %. BLP-12(H) at 77 K reaches saturation at around 35 bar while the 87 K isotherm steadily increases at higher pressures. At some point shortly after 40 bar hydrogen uptake capacities at 77 and 87 K are expected to become indistinguishable. In BLP-1(H), temperature also has less of an effect on uptake in that the uptake values at 40 bar for 77 and 87 K are overlapping, both adsorbing ~4.0 wt% H_2. BLP-2(H) displays a maximum uptake of ~2.6 wt % at 77 K and 22 bar, but gradually decreases as pressure is increased, losing up to approximately 0.1 wt% by the time 40 bar is reached. At 87 K, saturation is in not observed, therefore isotherms are expected to converge near this pressure as seen with BLP-1(H). BLP-3(H) displays a surprisingly low hydrogen uptake of 1.5 wt %, though saturation is not being approached at 40 bar in isotherms run at 77 or 87 K.

Table 6.2 High pressure hydrogen uptakes of nanoporous organic polymers and selected BLPs

	SA_{BET} (m^2/g)	$V_{p,}$ (cm^3/g)	H_2 Qst (kJ/mol)	H_2 Uptake (wt%)	P (bar)
BLP-1(H)	1360	0.69	6.8	3.97	40
BLP-2(H)	1178	0.59	7.7	2.48	40
BLP-3(H)	1071	0.53	6.0	1.47	40
BLP-12(H)	2244	1.08	6.8	4.25	40
COF-1	750	0.30	6.2	1.48	40
COF-6	750	0.32	7.0	2.26	20
COF-102	3620	1.55	3.9	7.74	40
COF-103	3530	1.54	4.4	7.05	40
PAF-1	5600	-	-	7.0	48
PAF-3	2932	-	-	5.5	60
PAF-4	2246	-	-	4.2	60
PPN-4	6461	-	-	8.34	55

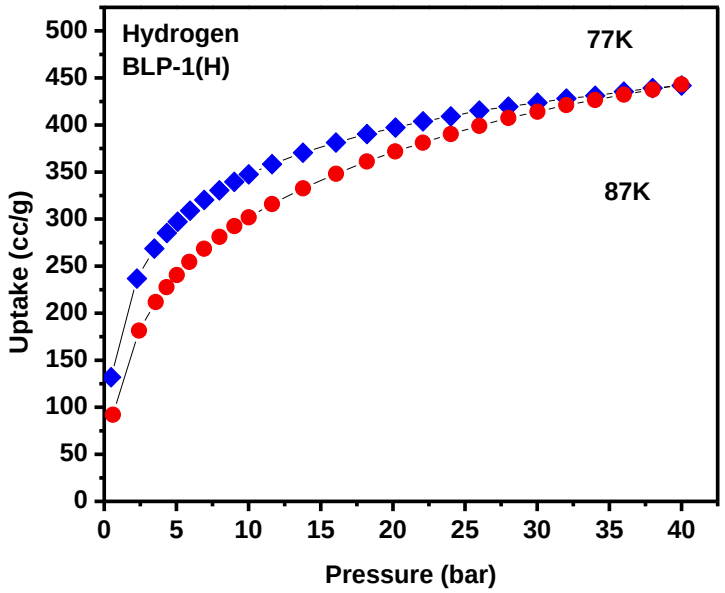

Figure 6.19. H_2 adsorption isotherms for BLP-1(H) measured at 77 K (red circles) and 87 K (blue diamonds).

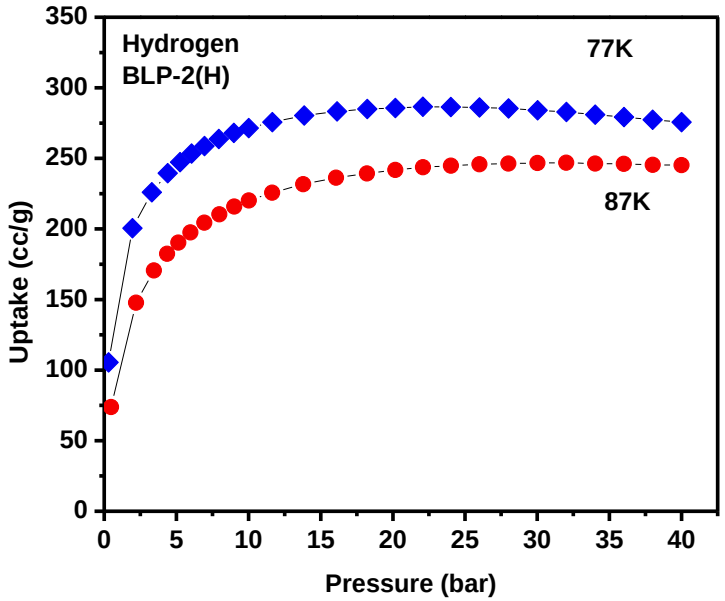

Figure 6.20. H_2 adsorption isotherms for BLP-2(H) measured at 77 K (red circles) and 87 K (blue diamonds).

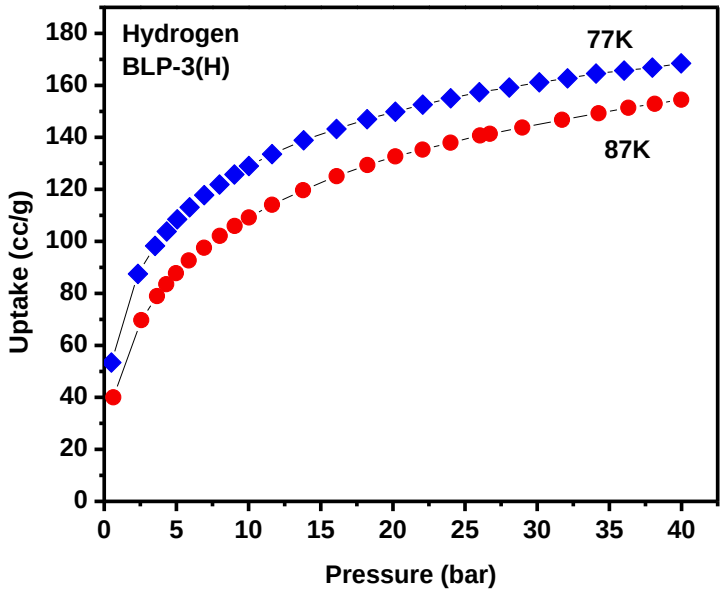

Figure 6.21. H_2 adsorption isotherms for BLP-3(H) measured at 77 K (red circles) and 87 K (blue diamonds).

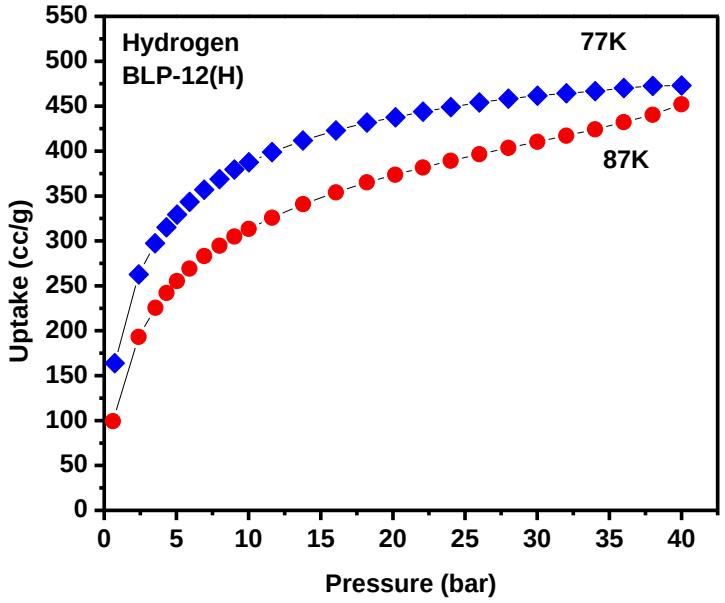

Figure 6.22. H_2 adsorption isotherms for BLP-12(H) measured at 77 K (red circles) and 87 K (blue diamonds).

Methane and Carbon Dioxide Adsorption. Methane and carbon dioxide are two other major players in clean energy. Methane, the primary component in natural gas, is a cleaner source of energy than conventional fuels such as gasoline releasing lower amounts of carbon emissions. It has also become of interest because of its low cost and abundance. Consequently, we have investigated the high pressure methane storage capacity of BLPs. Unlike hydrogen adsorption experiments, methane adsorption behavior seems to be consistent regardless of pressure. In all methane experiments, uptake increases continuously with pressure. Isotherms run at 273 K, as expected, show higher uptake than 298 K in all cases. As is seen in low pressure isotherms, methane uptake varies directly with pore volume and surface area. BLP-1(H), -2(H), -3(H) and -12(H) have maximum uptake capacities at 273 K of 13.4, 10.5, 5.5, and 15.5 wt % respectively. Considering the pore volumes calculated from low pressure isotherms nitrogen and argon isotherms, these values are consistent with values reported in a similar study on COFs in reported in 2009. In this study, COFs were classified by pore size. Group 1 consisted of 2D structures with 1D small pores (9 Å), group 2 included 2D structures with large 1D pores (16, 27, and 32 Å) and group 3 was comprised of 3D structures with 3D medium-sized pores (12 Å). It was found that group 1 stored up to 10 wt %, group 2 between 10 and 15 wt %, and group 3 above 20 wt %.

CO_2, a primary contributor to global warming, is produced in large quantities during the combustion of fossil fuels in vehicles and industrial plants. Porous polymers such as BLPs can act as sorbents to capture CO_2 from an exhaust gas, which is known as post-combustion. They can also be used to capture CO_2 from contaminated natural gas reserves or a from a mixture of fuel gases which is known as pre-combustion.[194,195] Pre-combustion conditions are at high pressure, separating high contents of CO_2 from methane or hydrogen. Post-combustion

conditions occur around atmospheric pressure with low contents of CO_2 in N_2 at temperatures between 40 and 60 ºC.[195] We have recently reported the low pressure CO_2 uptake capacity in BLPs[95,96] and present here the high pressure performance of BLP-1(H), -2(H), -3(H) and -12(H). BLPs compare well at high pressures with organic polymers such as HCPs[196] and some COFs, however, polymers such as PAF-1 and PPN-4 with exceptionally high surface areas dwarf their CO_2 uptake capacity as shown in Table 6.3.

Table 6.3 High pressure methane and carbon dioxide uptakes of nanoporous organic polymers and selected BLPs

	SA_{BET} (m^2/g)	Pore Width (Å)	V_p (cm^3/g)	Uptake at 298 K (mmol/g)		P (bar)
				CH_4	CO_2	
BLP-1(H)	1360	12.7	0.69	6.7	15.4	40
BLP-2(H)	1178	6.4	0.59	5.5	11.5	40
BLP-3(H)	1071	13.8	0.53	2.5	7.98	40
BLP-12(H)	2244	12.7	1.08	7.2	16.4	40
COF-1	750	9	0.30	2.5	5.23	50
COF-6	750	9	0.32	4.1	7.03	50
COF-102	3620	12	1.55	11.7	27.3	50
COF-103	3530	12	1.54	10.9	27.0	50
PAF-1	5640	-	-	-	29.6	40
PPN-1	1249	-	-	-	11.0	60
PPN-2	1764	-	-	-	19.0	60
PPN-3	2840	-	-	-	25.3	60
PPN-4	6461	-	-	17.1	38.9	50

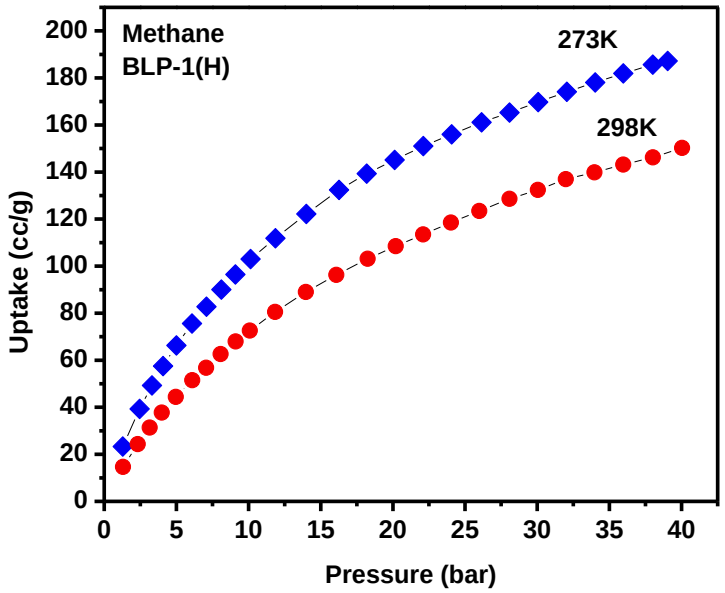

Figure 6.23 CH_4 adsorption isotherms for BLP-1(H) measured at 273 K (blue diamonds) and 298K (red circles).

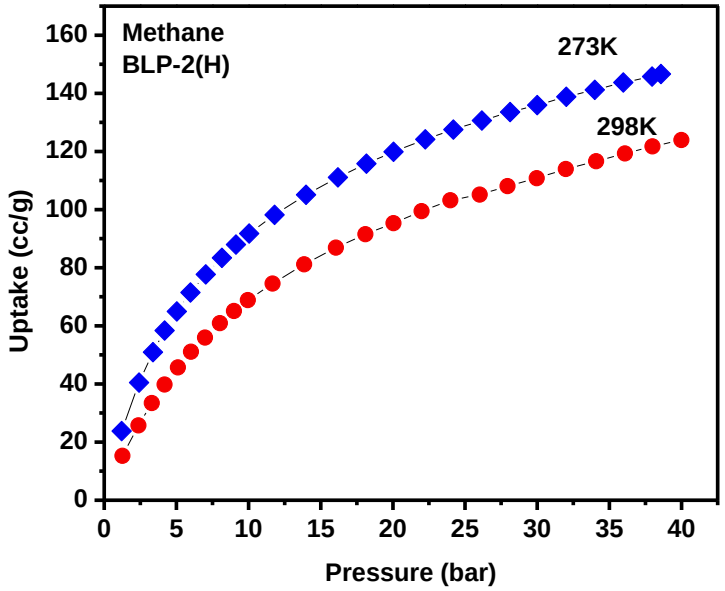

Figure 6.24 CH_4 adsorption isotherms for BLP-2(H) measured at 273 K (blue diamonds) and 298K (red circles).

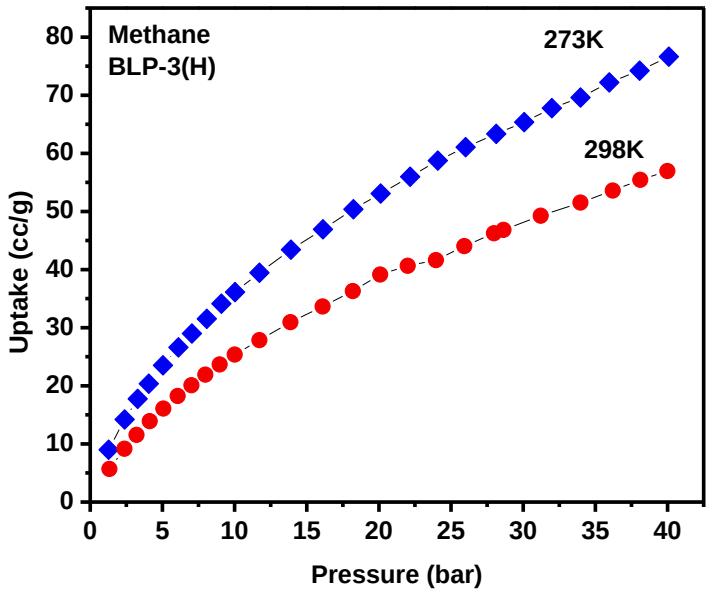

Figure 6.25 CH_4 adsorption isotherms for BLP-3(H) measured at 273 K (blue diamonds) and 298K (red circles).

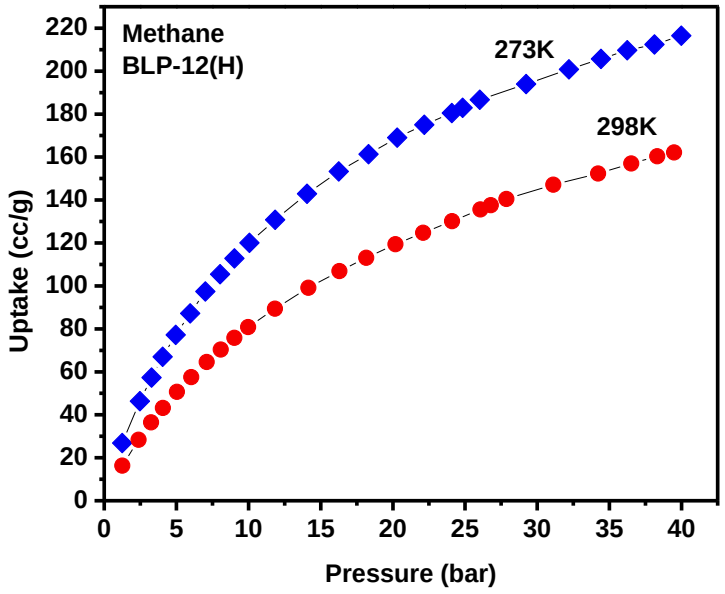

Figure 6.26 CH_4 adsorption isotherms for BLP-12(H) measured at 273 K (blue diamonds) and 298K (red circles).

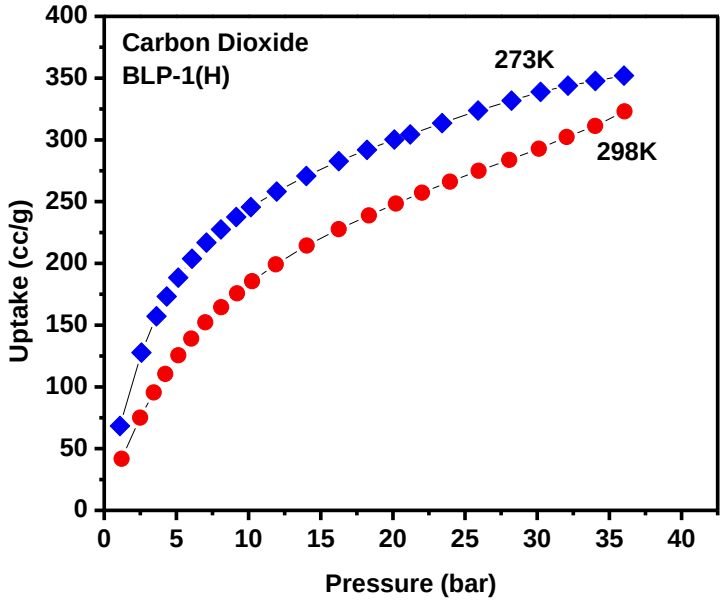

Figure 6.27 CO_2 adsorption isotherms for BLP-1(H) measured at 273 K (blue diamonds) and 298K (red circles).

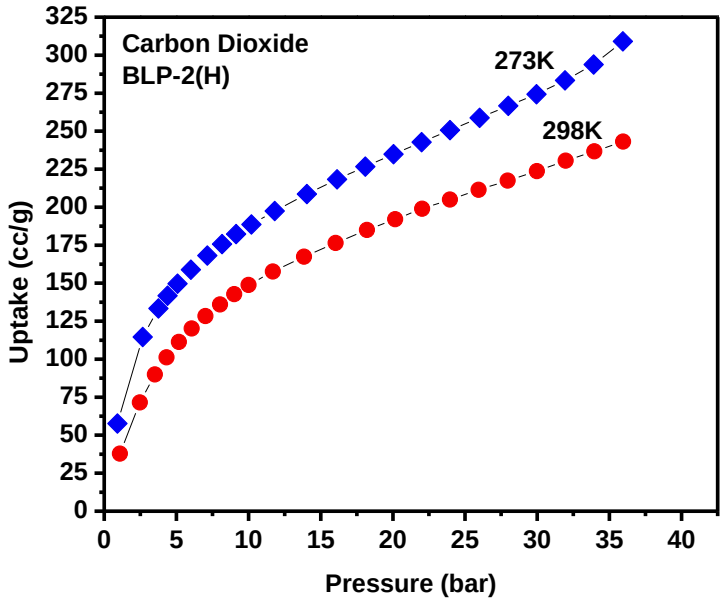

Figure 6.28. CO_2 adsorption isotherms for BLP-2(H) measured at 273 K (blue diamonds) and 298K (red circles).

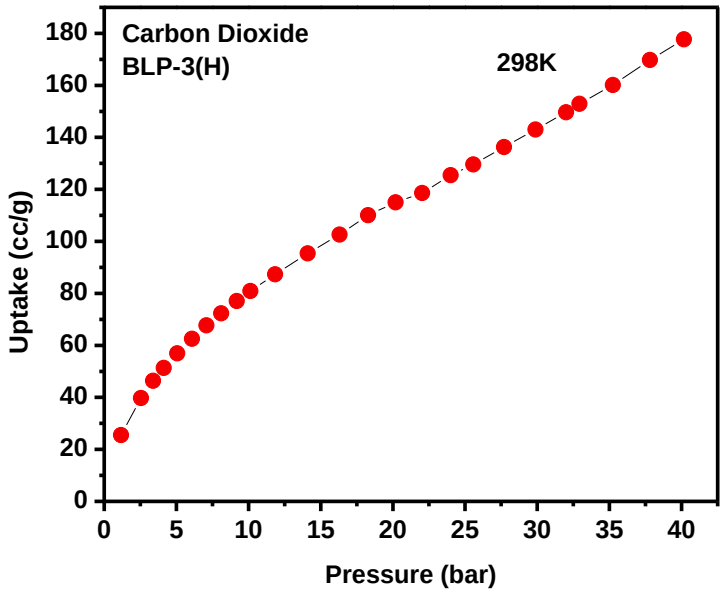

Figure 6.29. CO_2 adsorption isotherm for BLP-3(H) 298K (red circles).

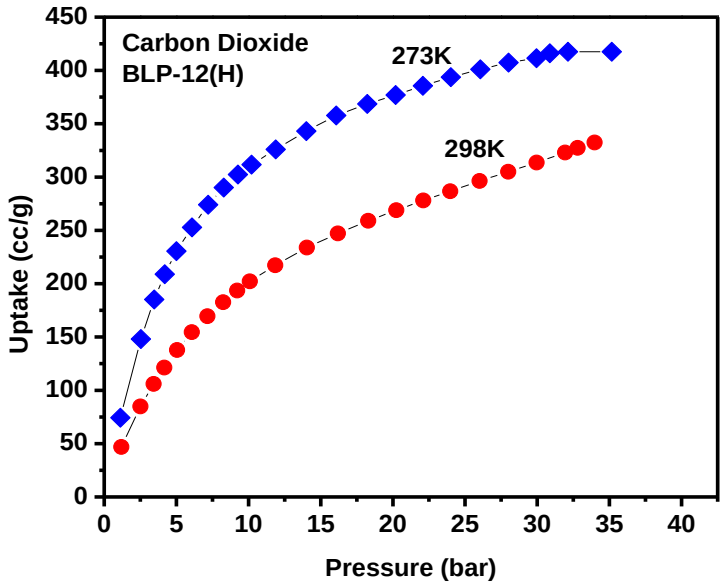

Figure 6.30. CO_2 adsorption isotherms for BLP-12(H) measured at 273 K (blue diamonds) and 298K (red circles).

6.3.4 Selectivity in BLPs

From the experimental CO_2 and CH_4 isotherms, binary mixture adsorption was predicting using IAST. IAST calculations have been used recently to accurately predict gas mixture adsorption in several zeolites[197-199], MOFs[197,200,201] and porous organic polymers. Although other theories exist for such predictions, IAST is the most reliably used for the prediction of mixed-gas adsorption equilibria from single component isotherms.[197,200,202-204] In order to perform the integrations required by IAST, the single-component isotherms should be fitted by a proper model. The single-site and dual-site Langmuir-Freundlich equation were used depending on the best fit as determined by R^2 values for all the fitted isotherms. All R^2 were >0.999 indicating that the single-component isotherms are in good agreement with the models. The selectivity $S_{A/B}$ in a binary mixture of components A and B is defined as $(x_A/y_A)/ (x_B/y_B)$, where *xi* and *yi* are the mole fractions of component *i* in the adsorbed and bulk phases, respectively (*i* = A,B).

Adsorption selectivity for CO_2/CH_4 mixtures. The IAST-predicted CO_2/CH_4 selectivities at different mixture compositions and different pressures for BLPs are shown in Figure 6.31. As expected, CO_2 is preferentially adsorbed over CH_4 in all BLPs because of stronger interactions between CO_2 and the pore walls of each BLP. In BLP-1(H), 2(H), and 12(H), selectivities increase modestly as pressure increases. Selectivities are in the range of 3 to 5 for these three BLPs. BLP-3(H) however exhibits a sharp increase in selectivity at the lower pressures reaching values >7. This higher selectivity can be explained by the high nitrogen content. It has been shown that by introducing amine functionality, accessible nitrogen, or open metal sites into the pore wall of metal organic frameworks (MOFs), [169,171-174] zeolitic imidazolate frameworks (ZIFs)[205] or zeolitic tetrazolate frameworks (ZTFs)[145,146] gas uptake and

selectivity can drastically be increased. In particular, the selective uptake of CO_2 over CH_4 or N_2 is believed to arise from enhanced CO_2-framework interactions through hydrogen bonding and/or dipole-quadrupole interactions.[125,126] Overall, the selected BLPs exhibit selectivities higher than MOF-5 (2-3)[197,199] and 2D and 3D COFs (2-4)[206] and are consistent with PPNs (2-6),[140] and MCM-41 (~6)[207] at similar conditions.

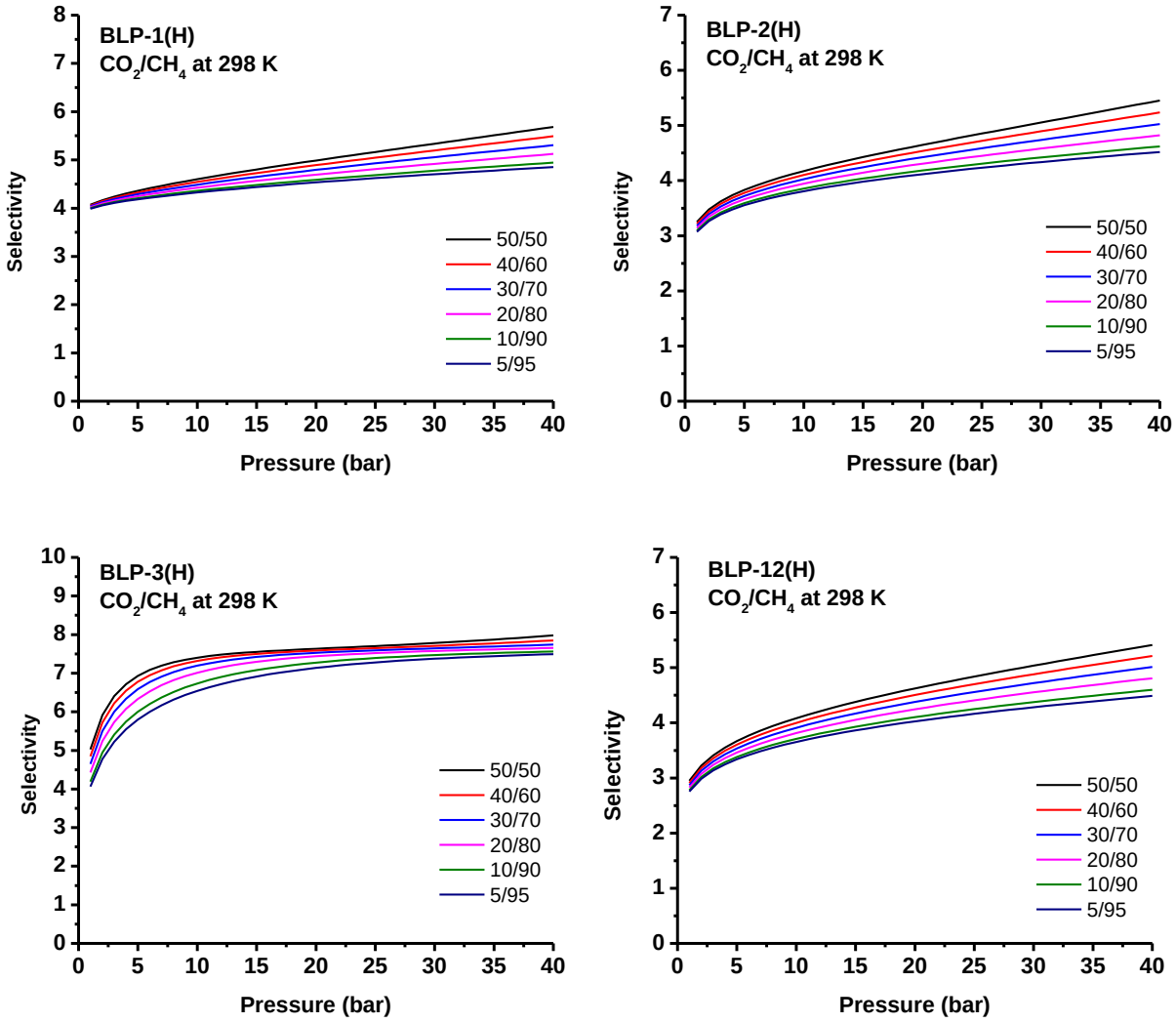

Figure 6.31. IAST predicted CO_2/CH_4 selectivities at various mixture compositions for BLP-1(H), -2(H), -3(H), and -12(H) at 298 K.

6.4 Conclusion

In conclusion, we have demonstrated the synthesis of a new highly porous melamine-based borazine-linked polymer by thermolysis and investigated its gas storage performance under ambient pressure and cryogenic conditions. BLP-3(H) exhibits noteworthy CO_2 uptake at low pressure due its high content of nitrogen. High pressure gas storage investigations and selectivity studies on BLPs via IAST confirm that CO_2 selectivity of highly porous materials tend to increase with pressure while materials with lower porosities tend to decrease with pressure. BLP-3(H) also stands out by having the highest selectivity among the BLP(H) family. These studies place BLPs among the most attractive candidates for clean energy applications.

Chapter 7: Nickel-catalyzed Synthesis of Nanoporous Organic Frameworks and Their Potential Use In Gas Storage Applications

7.1 Introduction

The design and synthesis of highly porous organic polymers with predefined porosity has attracted considerable attention due to their potential in applications that entail gas storage and separation, catalysis, and conductivity.[14,53,131,208] Among this class of materials are covalent-organic frameworks (COFs), which can be tailored to possess exceptional porosities, very low densities, and pore metrics that span the micro- and meso-porous ranges.[76-80,209-212] The crystalline nature of COFs stem from the dynamic nature of covalent bonds involved in their construction. Unfortunately, the dynamic nature of B–O bonds in COFs renders them prone to hydrolysis, which leads to framework decomposition and loss of porosity. In the absence of reversible bond formation, covalently linked polymers lack long-range ordering and tend to be amorphous. Nevertheless, such polymers can be designed to possess well-defined cavities through the use of building blocks that dictate the spatial growth of the polymer. Interestingly, high surface areas are typically imparted to these porous architectures without the use of templating processes. Recent efforts in this field have been directed towards the synthesis of more thermally and chemically robust materials in order to enhance material durability.[213-229] For example, Ben et al.[93] used the nickel(0)-catalyzed Yamamoto coupling reaction to link tetrahedral monomers (tetraphenylmethane) by C–C bond into a highly porous aromatic

framework, PAF-1. PAF-1 has high specific surface area (Langmuir surface area: 7,100 m^2/g), remarkable thermal and chemical stability, and remains the most porous purely organic material reported to date. Moreover, the oxidative Eglinton coupling of terminal alkynes has been utilized for the construction of alkyne-linked frameworks such as porous polymer networks (PPNs) reported by Zhou and coworkers,[140] which also exhibited high Langmuir surface areas (827–2,790 m^2/g). The same report also described the synthesis of PPN-3 (5,323 m^2/g) by linking tetraphenyladamantane using the same method reported by Ben et al. Cooper et al. have synthesized porous poly(aryleneethynylene) networks using palladium-catalyzed Sonogashira–Hagihara cross-coupling.[216-223] These conjugated microporous polymers (CMPs) are amorphous and have Brunauer–Emmett–Teller (BET) surface areas of up to 834 m^2/g. It has been reported that the use of unfused benzene rings in the pore walls of porous architectures is essential for obtaining exceptionally high porosity.[75] Introducing high porosity into materials has a direct impact on several applications including hydrogen storage by physisorption in particular.[159] Hydrogen storage remains one of the major hurdles facing the widespread use and commercialization of this highly flammable fuel.[28,44,230] There have been intensive research efforts in this area to meet targets set by the US Department of Energy for on-board hydrogen storage for 2015 (volumetric 40 g/l; gravimetric 5.5 wt%).[231] With these considerations in mind, we report herein on the synthesis and characterization of highly porous organic polymers using nickel-catalyzed Yamamoto coupling reactions. The use of various building blocks with a variable number of unfused benzene rings leads to enhanced porosity. The resultant polymers are chemically and thermally robust and most importantly permanently porous with very high surface area, which makes them an ideal candidate for hydrogen storage applications.

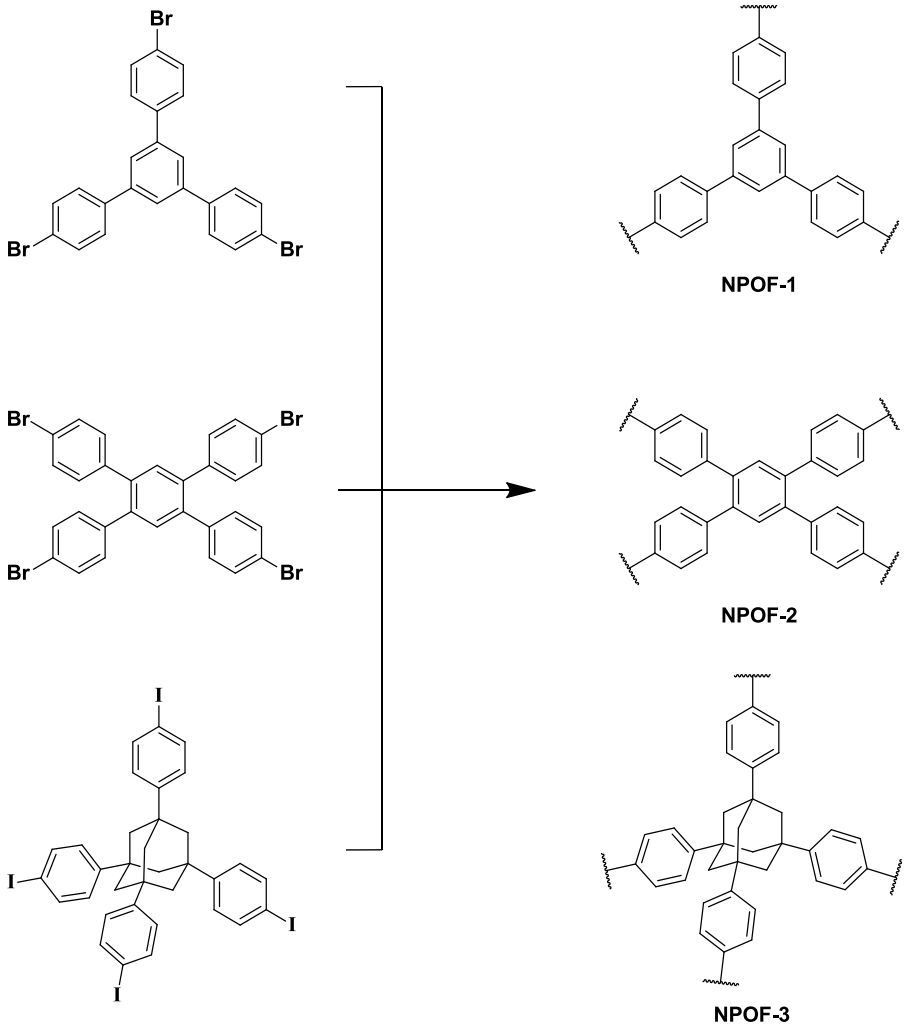

Figure 7.1. Monomers of NPOFs generated by coupling reactions.

7.2 Experimental

General Considerations. All starting materials, unless noted otherwise, were obtained from Thermo Fisher Scientific Inc. and used without further purification. Anhydrous DMF (99.98%) was purchased from Acros Chemicals. 1,5-cyclooctadiene (COD) was distilled from calcium hydride, and toluene was distilled from sodium 1,3,5,7-tetrakis(4-iodophenyl)adamantane, 1,3,5-tris(4-bromophenyl)benzene, and 1,2,4,5-tetrakis (4-

bromophenyl)benzene were prepared according to literature methods.[230,232-231865] All reactions were performed under a nitrogen atmosphere using glovebox or Schlenk line techniques. Elemental analyses were performed by Midwest Microlab, Indianapolis, IN. (Lower carbon contents are due to unreacted halide at the surface of the polymers or unreacted starting material inside pores).[140]

Instrumentation. FT-IR spectra were collected using KBr pellets in transmission mode using a Nicolet Nexus 670 spectrometer. All spectra were measured with 32 scans at a resolution of 4 cm^{-1} using a blank KBr disk as background, followed by baseline correction. Thermogravimetric analysis (TGA) was carried out using a Q5000IR analyzer (TA Instruments). The samples were heated at the rate of 5 ºC/min under a nitrogen atmosphere up to 700 ºC. Powder X-ray diffraction data were collected on a Panalytical X'pert Pro Multipurpose Diffractometer (MPD). Samples were mounted on a zero-background sample holder and measured using Cu Kα radiation with a 2 h range of 5–30. Scanning electron microscopy (SEM) images were taken on a Hitachi SU-70 scanning electron microscope. The samples were mounted onto aluminum holders, and then coated with platinum at 1 x 10^{-4} mbar of pressure in a nitrogen atmosphere for 120 s before imaging. Solid-state nuclear magnetic resonance (NMR) spectra were recorded at ambient temperature on a 363-MHz NMR system. ^{13}C CP-MAS spectra were obtained with a 1-ms contact time and a 3-s recycle delay.

Gas sorption analysis. Low-pressure N_2 and H_2 adsorption measurements (0–1 bar and 77 K) were performed on an Autosorb-1 C (Quantachrome) volumetric analyzer. All samples were degassed at 200 ºC/10^{-5} Torr for 12 h before analysis. Ultra-high-purity grade N_2 and H_2 (99.999% purity) were used throughout the adsorption experiments. Surface areas were calculated in the relative pressure (P/P_o) range from 0.05 to 0.3. Pore size distributions (PSDs)

and pore volumes were derived from N_2 adsorption branches using the nonlocal density functional theory (NLDFT) cylindrical pore model.

Scheme 7.1: Synthetic pathways to (a) 1,3,5-tris(4-bromophenyl)benzene, (b) 1,2,4,5-tetrakis (4-bromophenyl)benzene, and (c) 1,3,5,7-tetrakis(4-iodophenyl)adamantane

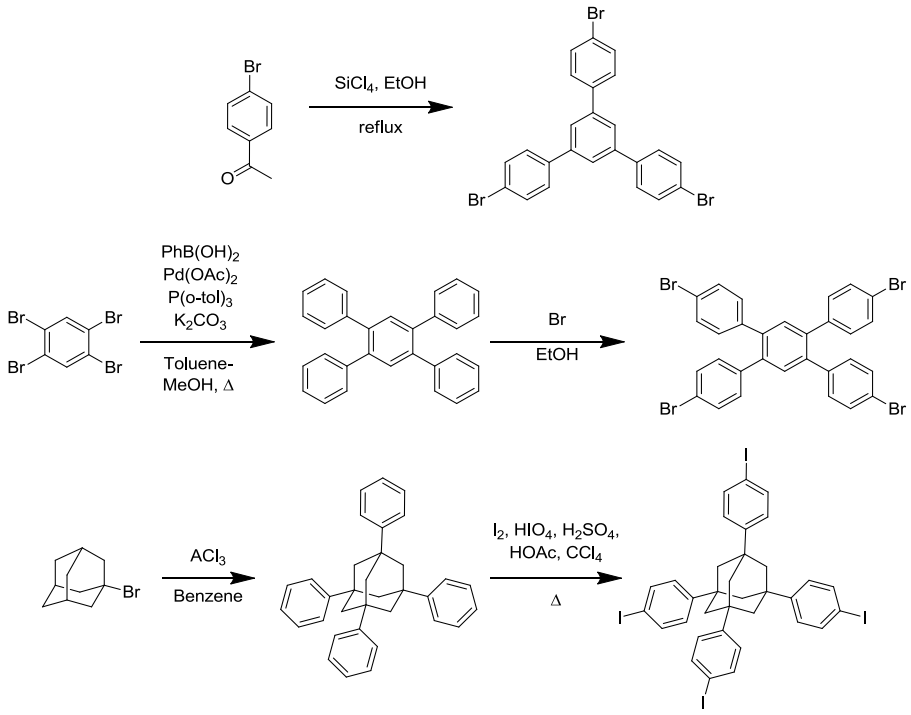

NPOF-1. To a 250-mL Schlenk flask equipped with a stir bar was added COD (520 mg, 4.8 mmol), $Ni(cod)_2$ (1.32 g, 4.80 mmol), 2,20-bipyridyl (750 mg, 4.80 mmol), and DMF (60 ml). The mixture was heated at 80 ºC for 1 h to afford a dark purple solution. To the resultant solution was added 1,3,5-Tris(4-bromophenyl)benzene (500 mg, 0.92 mmol) in DMF (20 ml) and the resultant suspension was kept stirring for an additional 24 h at 80 ºC. The mixture was cooled to room temperature and the dark residue was filtered off over a medium glass frit. Concentrated HCl (12 M, 20 ml) was added drop-wise to the residue. Afterwards, the residue was washed with acetone (5 x 10 ml), $CHCl_3$ (5 x 10 ml), THF (5 x 10 ml) and H_2O (5 x 10 ml),

respectively, and dried under reduced pressure to afford NPOF-1 as an off-white powder (460 mg, 99% based on 1,3,5-Tris(4-bromophenyl)benzene); Anal. Calcd. for C_8H_5: C, 95.02; H, 4.98. Found: C, 89.95; H, 5.53. FT-IR (ν, cm^{-1}) 3,434 (s, br), 3,034 (w), 2,925 (w), 1606 (m), 1,496 (m), 1,112 (m), 992 (s), 811 (s); H 5.04. ^{13}C CP-MAS (100 MHz) δ = 140.3, 126.6.

NPOF-2. In a fashion similar to the preparation of NPOF-1, COD, (484 mg, 4.5 mmol), $Ni(cod)_2$ (1.24 g, 4.5 mmol), 2,2-bipyridyl (703 mg, 4.5 mmol), and DMF (60 ml) were combined. The mixture was heated at 80 ºC for 1 h. To the resulting purple solution was added a DMF (20 ml) solution of 1,2,4,5-Tetrakis(4-bromophenyl) benzene (0.86 mmol, 600 mg). Post-synthesis treatment and isolation afforded NPOF-2 as an off-white powder (510 mg, 95% yield). Anal. Calcd. for C_5H_3: C, 95.21; H, 4.79. Found: C, 88.95; H, 5.20. FT-IR (ν, cm^{-1}) 3,433 (s, br), 3,034 (m), 1,606 (m), 1,491 (s), 1,201 (w), 992 (s), 811 (s), 744 (w), 702 (w); ^{13}C CP-MAS (100 MHz) δ = 146.0, 139.1, 130.7, 125.1.

NPOF-3. In a fashion similar to the preparation of NPOF-1, COD, (310 mg, 2.73 mmol), $Ni(cod)_2$ (750 mg, 2.73 mmol), 2,2-bipyridyl (430 mg, 2.73 mmol), andDMF (60 ml) were combined. The mixture was heated at 80ºC for 1 h. To the resulting purple solution was added a DMF (20 ml) solution of 1,3,5,7-Tetrakis(4-iodophenyl) adamantane (0.53 mmol, 500 mg). Post-synthesis treatment and isolation afforded NPOF-3 as an off-white powder (217 mg, 94%). Anal. Calcd. for $C_{34}H_{27}$: C, 93.75;H, 6.25. Found: C, 87.69; H, 6.35. FT-IR (ν, cm^{-1}) 3,439 (s, br), 3,034 (s), 2,930 (s), 2,847 (s), 1,606 (m), 1,507 (s), 1,449 (m), 1,351 (s), 1,091 (s), 998 (s), 821 (s), 738 (m), 691 (m), 557 (m), 468 (m); ^{13}C CP-MAS (100 MHz) δ = 147.8, 125.2, 47.7, 45.4, 38.9.

7.3 Results and Discussion

The synthesis of NPOFs was established using methods described by Ben et al. and the monomeric building units were specifically chosen to increase the surface area of the resultant polymers for subsequent use in adsorptive hydrogen storage studies. NPOFs are insoluble in common organic solvents such as dimethylformamide, tetrahydrofuran, toluene, dichloromethane, methanol, and acetone, which facilitate their purification steps. Additionally, NPOFs exhibit a remarkable chemical stability and remain intact in 12 M HCl or 6 M NaOH solutions. The chemical composition and structural aspects of NPOFs were investigated by spectral and analytical methods while their porous nature was examined by N_2 porosity measurements. Unlike COFs, all NPOFs were amorphous, which prevented their solid-state investigation by powder X-ray diffraction techniques. Amorphous materials are generally obtained, as in the case of organic polymers such as polymers of intrinsic microporosity (PIMs), CMPs, PPNs, etc., due to the lack of bond formation reversibility.

In spite of their lack of long-range ordering, these polymers can be highly porous and suitable for multifaceted applications. To investigate phase purity of NPOFs, we collected SEM images, which revealed that NPOF-1 and NPOF-2 exist as platelets of ~200–300 nm in size. The formation of platelet morphology is most likely due to the 2D nature of the NPOF-1 and NPOF-2 frameworks that are facilitated by π-staking of the conjugated phenyl rings. In contrast, the particles of NPOF-3 are more spherical as a result of the 3-D building unit (tetraphenyladamantane) employed for the construction of this framework.

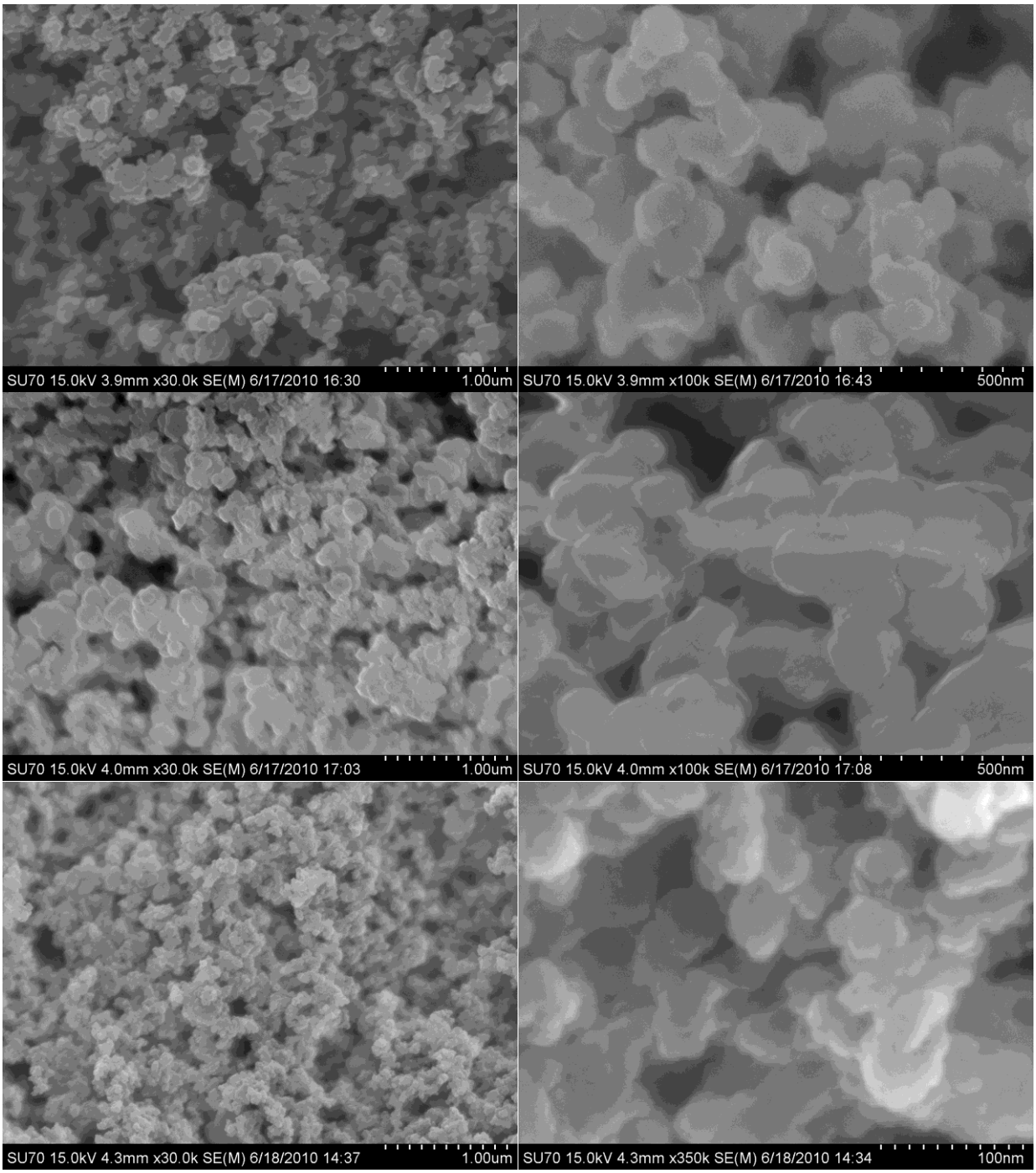

Figure 7.2: SEM image of (A and B) NPOF-1, (C and D) NPOF-2 and (E and F) NPOF-3 particles, revealing spherical morphologies.

The chemical composition of NPOFs was first investigated by elemental analysis, which provided lower carbon contents than expected for all NPOFs. A similar observation has been reported for other materials constructed using coupling reactions that entail aryl halides as in the case of CMPs and PPNs. The lower carbon contents recorded for all NPOFs may originate from trapped starting materials inside the pores or unreacted halides at the surface of the polymers.[18-31,38] It has been suggested that the surface of such polymers is terminated by unreacted carbon-halide bonds, however their concentrations are very low, which does not allow for their detection by NMR methods. The presence of carbon-halide in NPOFs was supported by FT-IR spectroscopy studies, which revealed vibration stretches at ~750 cm^{-1} that are consistent with aryl halide functionality.

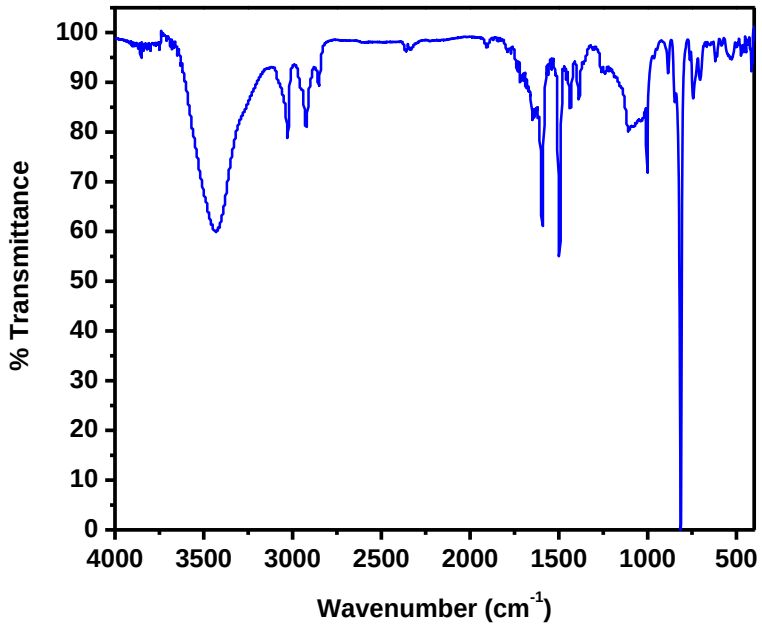

Figure 7.3: IR spectra of an activated POF-1.

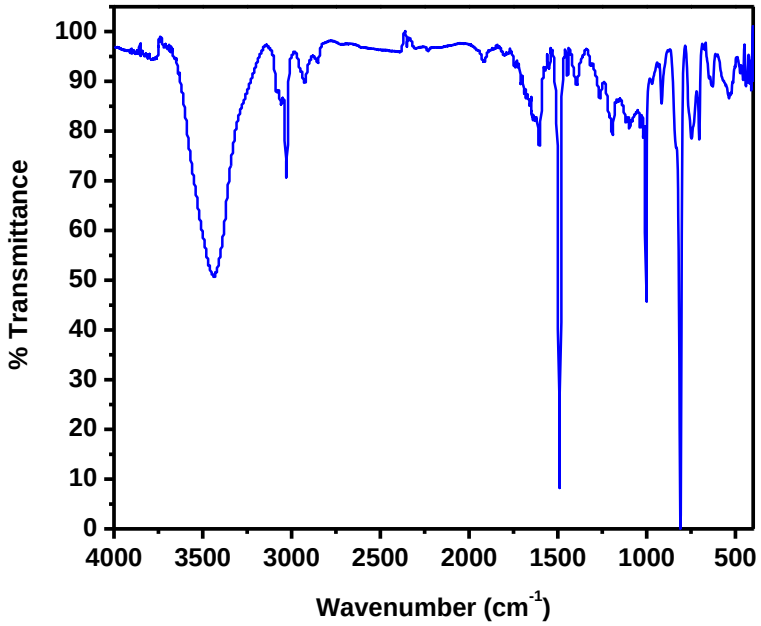

Figure 7.4: IR spectra of an activated POF-2.

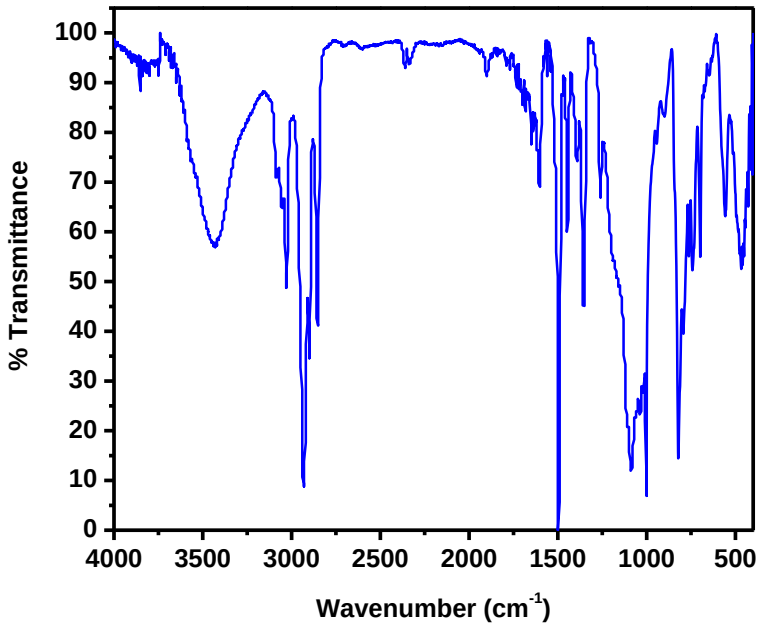

Figure 7.5: IR spectra of an activated POF-3.

To establish the incorporation of monomeric building units into NPOF networks through the formation of C–C bonds, we collected solid-state ^{13}C CP-MAS NMR experiments on activated samples (Figure 7.6). CP-MAS NMR techniques have been widely used for the characterization of porous organic materials, especially amorphous polymers, to help illustrate their solid-state structure and connectivity between building units. The activation process of NPOFs involved treatment with 12 M HCl followed by washing with organic solvents and water to remove residual nickel and soluble oligomers or starting materials. After several washing steps, NPOFs were subjected to heating under reduced pressure (200 $^{o}C/10^{-5}$ Torr) for 12 h. In all spectra, the ^{13}C signals at δ = 122 ppm (C–Br) or 94 ppm (C–I) that correspond to the carbon-halide in the starting monomers were absent and under NMR detection levels. In the ^{13}C CP MAS spectrum of NPOF-1, the signals at δ = 140.2 and 126.6 ppm correspond to the new C–C bond formed upon aryl–aryl coupling and the ortho-CH carbon, respectively, while the signal for C–Br that usually appears at δ = 122.3 ppm is absent. In the spectrum of NPOF-2, the signals at δ = 146.0 and 139.1 ppm correspond to the new C–C bond formed while signals at 130.7 and 125.1 ppm correspond to the ortho-CH carbons. Also, the C–Br signal at d = 121.4 ppm is absent. For NPOF-3, the signal at δ = 147.8 and 125.2 ppm correspond to the new C–C bond formed and the ortho-CH carbon, respectively. Also, the C–I signal at δ = 91.7 ppm is absent.

A.

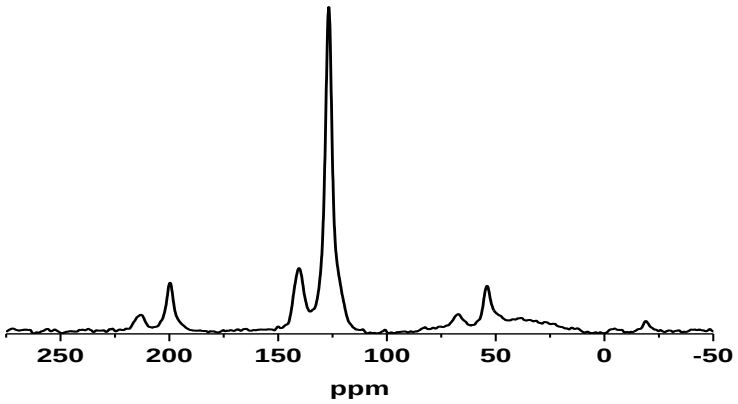

B

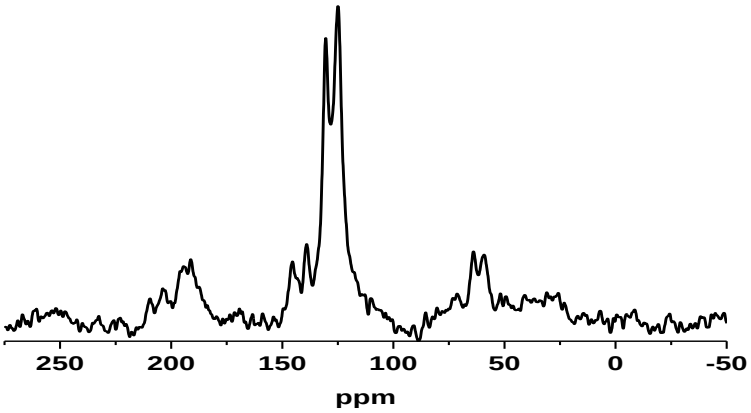

C

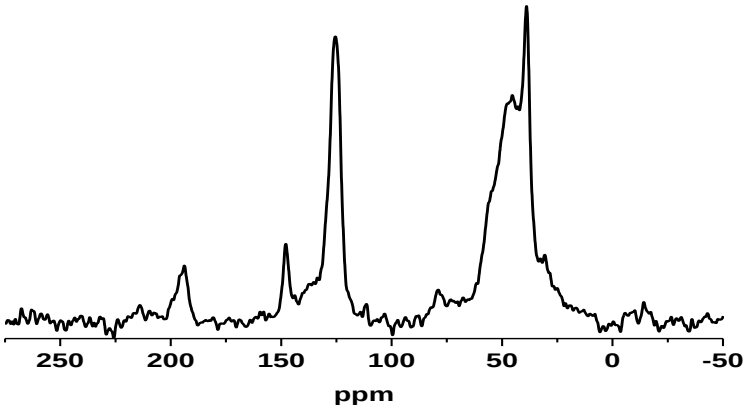

Figure 7.6. Solid state ^{13}C CP-MAS NMR spectra for (A) NPOF-1, (B) NPOF-2 and (C) NPOF-3.

The covalent nature of NPOFs was also manifested in their high thermal stability during TGA studies (Figure 7.7-7.9). TGA traces collected from studies conducted on activated samples revealed that NPOF-1 and NPOF-3 remain stable up to 450 ºC, whereas NPOF-2 starts to decompose about 350 ºC. These decomposition temperatures are typical for covalent polymers that show higher thermal stability than most of their MOF counterparts. This feature makes NPOFs very attractive for use in industrial applications where thermal and chemical stability is generally needed.

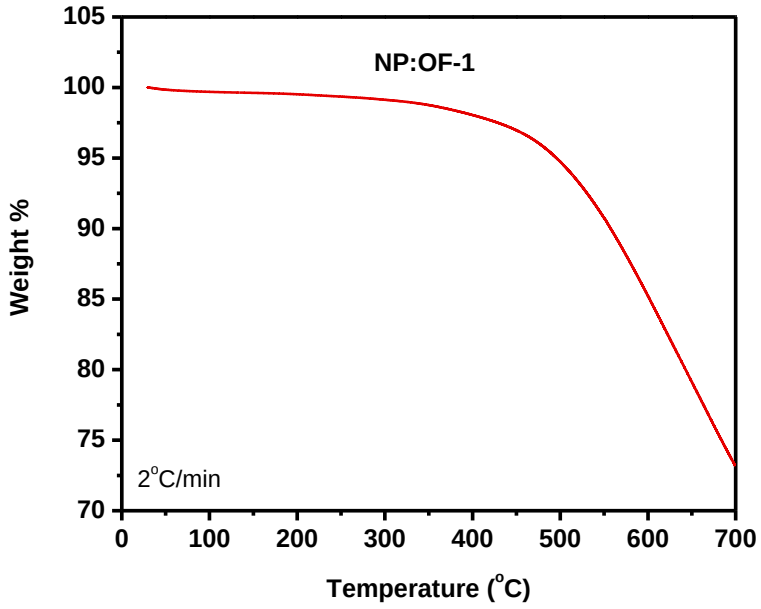

Figure 7.7. TGA trace for an as prepared sample of NPOF-1.

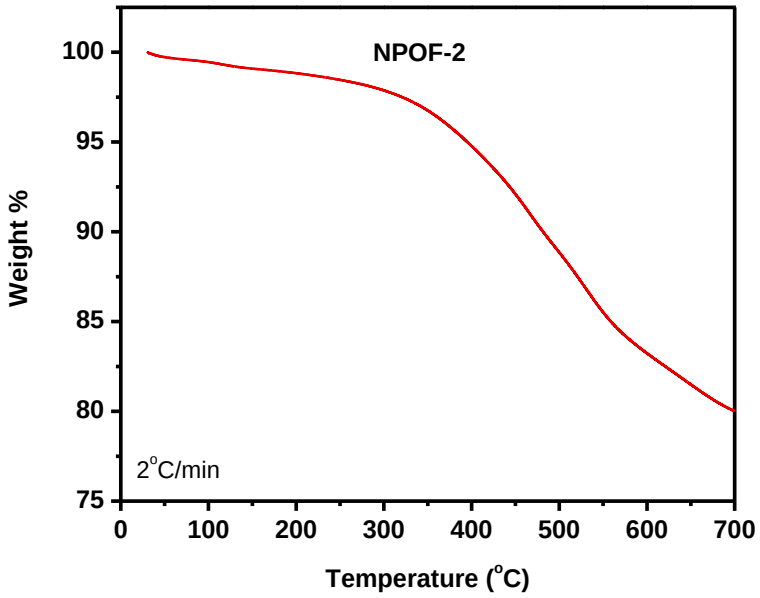

Figure 7.8. TGA trace for an as prepared sample of NPOF-2.

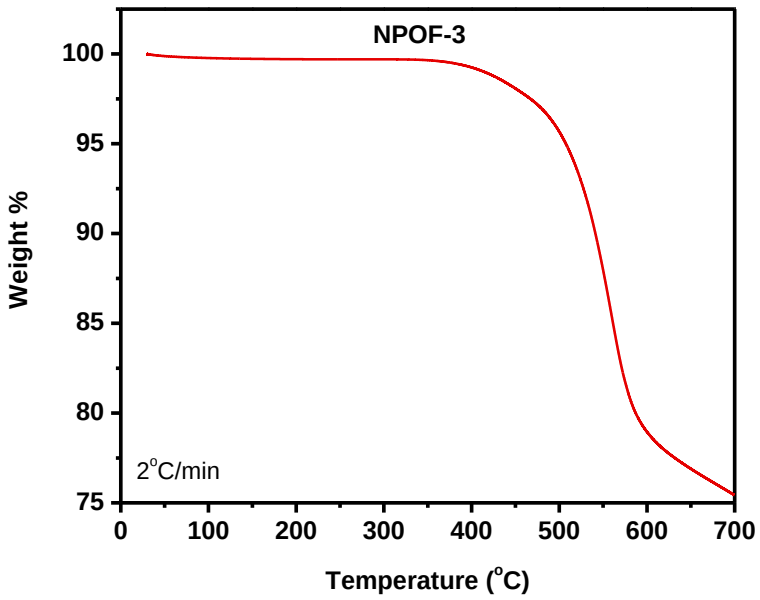

Figure 7.9. TGA trace for an as prepared sample of NPOF-3.

Of particular interest to us is the ability to tailor the porosity in NPOFs and to investigate its impact on the physisorption of dihydrogen, which has been under intensive investigation, as it represents a clean and renewable energy source. The porosity of NPOFs was established using N2 sorption–desorption experiments on the activated materials. NPOF samples were degassed at 200 ºC and 10^{-5} Torr for 12 h prior to nitrogen sorption analysis. The nitrogen uptakes indicate that NPOFs have permanent porosity evidenced by the fully reversible uptake release of nitrogen for all materials. The steep rise in the nitrogen uptake at P/P_o = 0–0.1 and the type I isotherms indicate microporosity. There is notable hysteresis for all samples and a gradual increase in nitrogen uptake until saturation pressure (P/P_o = 1), which may indicate that NPOFs have a flexible ‘‘soft’’ nature.[241] Surface area measurements were conducted using the adsorption branch from the N_2 isotherms at P/P_o = 0.05–0.30 and are listed along with other textural properties in Table 7.1. NPOFs exhibit considerably high Langmuir surface area values: 2635 m^2/g (NPOF-1); 4227 m^2/g (NPOF-2); and 2423 m^2/g (NPOF-3). PSD was calculated using NLDFT using the uptake branch of the nitrogen isotherm.[62] Both NPOF-1 and NPOF-3 show a narrow PSD of about 1.27 nm while NPOF-2 exhibits a boarder PSD in the range of 1.56–2.50 nm and therefore has both micro- and mesopores. It was surprising to us to see that NPOF-3 has a lower surface area than its related PPN-3 (5,323 m^2/g) that was synthesized using 1,3,5,7-Tetrakis(4-bromophenyl)adamantane under similar reaction conditions. The lower surface area observed for NPOF-3 may result from a faster coupling rate associated with the iodo-building block, 1,3,5,7-Tetrakis(4-iodophenyl) adamantine, which could hamper organized pore formation and the overall porosity of NPOF-3. The experimental surface areas (SA_{BET}) for NPOFs were compared against those of purely organic porous materials such as CMPs, PPNs, COFs, and PIMs. The surface area of NPOFs, especially that of NPOF-2, exceeds that of most

of PIMs (430–1760 m^2/g), or CMPs (522–1631 m^2/g) and are similar to those of highly porous 3-D COFs (e.g., COF-103, ~10 m^2/g), PAF-1 (5600 m^2/g) and PPNs (1249–2840 m^2/g).

Table 7.1: Porous properties and hydrogen uptake of NPOFs

Polymer	SA_{Lang} $(m^2/g)^a$	SA_{BET} $(m^2/g)^b$	P_{vol} $(cm^3/g)^c$	PSD $(nm)^d$	H_2 (wt%)
NPOF-1	2635	1907	1.5722	1.27	1.28
NPOF-2	4227	3127	2.4418	1.56	1.45
NPOF-3	2423	1794	1.1925	1.27	0.82

[a]Calculated by the Langmuir method. [b]Calculated by the BET method [c]Calculated from nitrogen adsorption branch at P/P_o = 0.9. [d]Calculated from NLDFT.

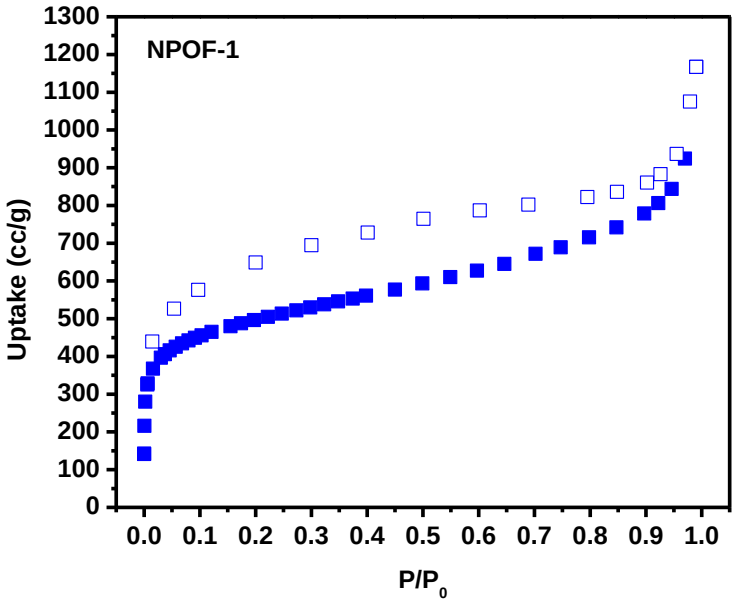

Figure 7.10. N_2 adsorption isotherm for NPOF-1 measured at 77 K. The filled squares are adsorption points and the empty squares are desorption points.

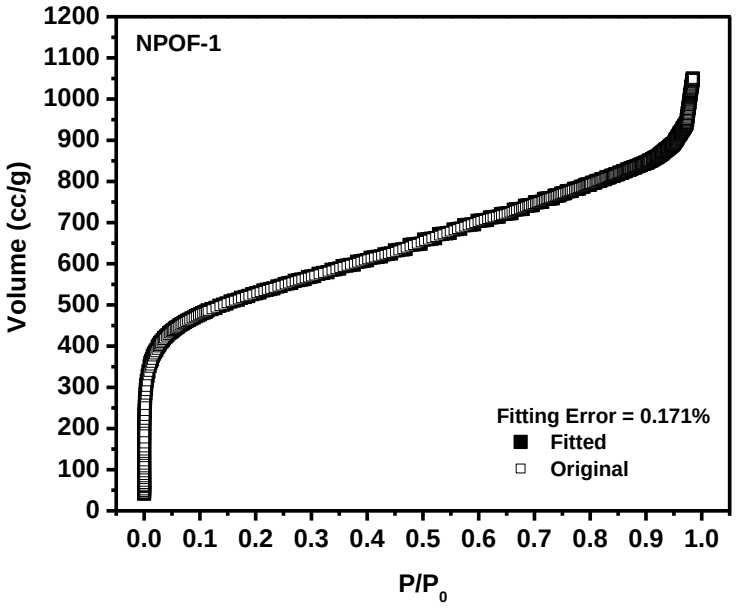

Figure 7.11. Experimental N_2 adsorption isotherm for NPOF-1 measured at 77 K is shown as filled squares. The calculated NLDFT isotherm is overlaid as open squares.

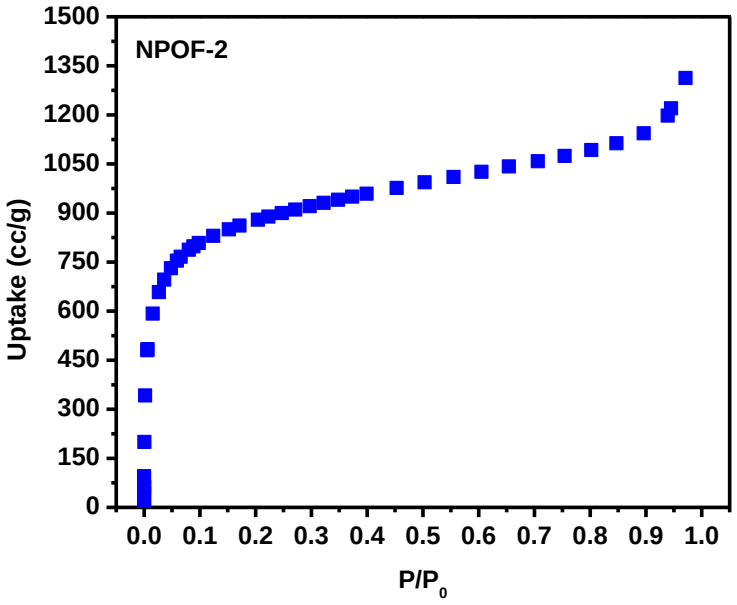

Figure 7.12. N_2 adsorption isotherm for NPOF-2 measured at 77 K.

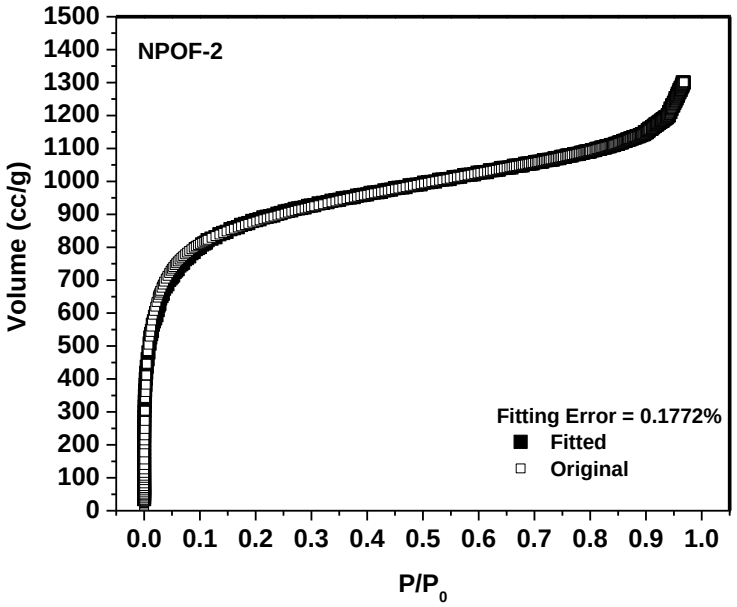

Figure 7.13. Experimental N_2 adsorption isotherm for NPOF-2 measured at 77 K is shown as filled squares. The calculated NLDFT isotherm is overlaid as open squares.

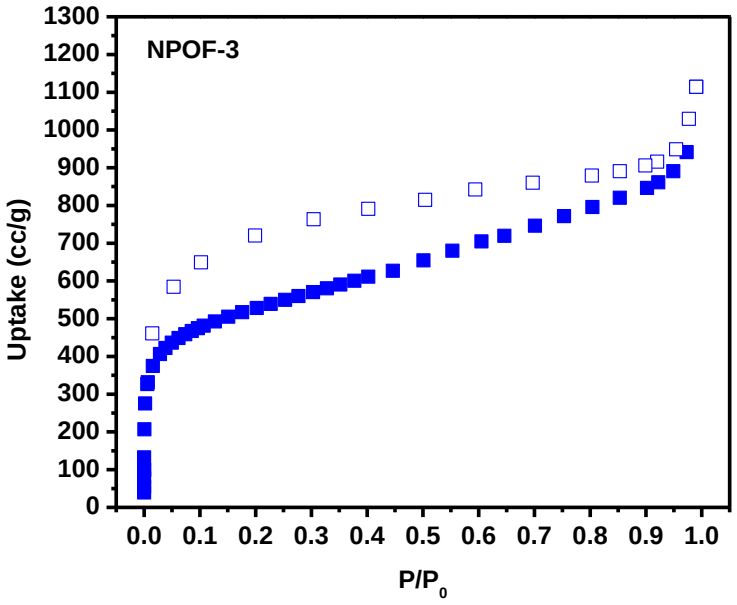

Figure 7.14. N_2 adsorption isotherm for NPOF-3 measured at 77 K. The filled squares are adsorption points and the empty squares are desorption points.

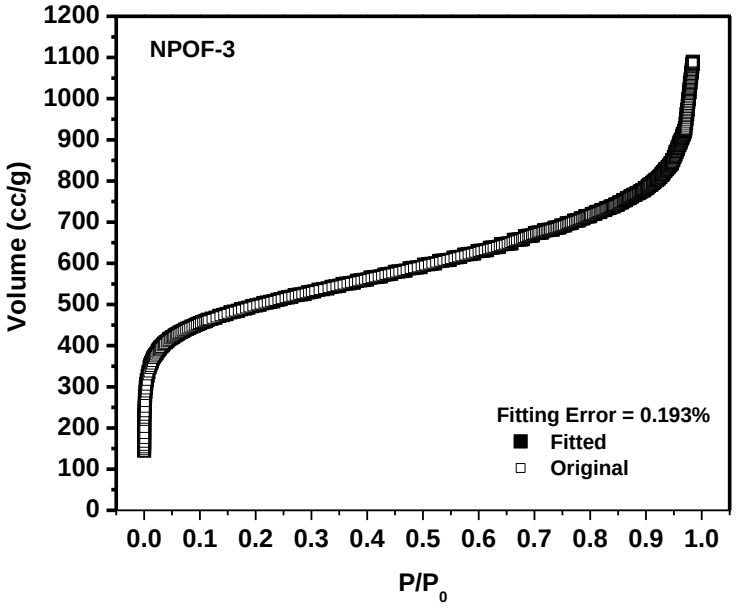

Figure 7.15. Experimental N_2 adsorption isotherm for NPOF-3 measured at 77 K is shown as filled squares. The calculated NLDFT isotherm is overlaid as open squares.

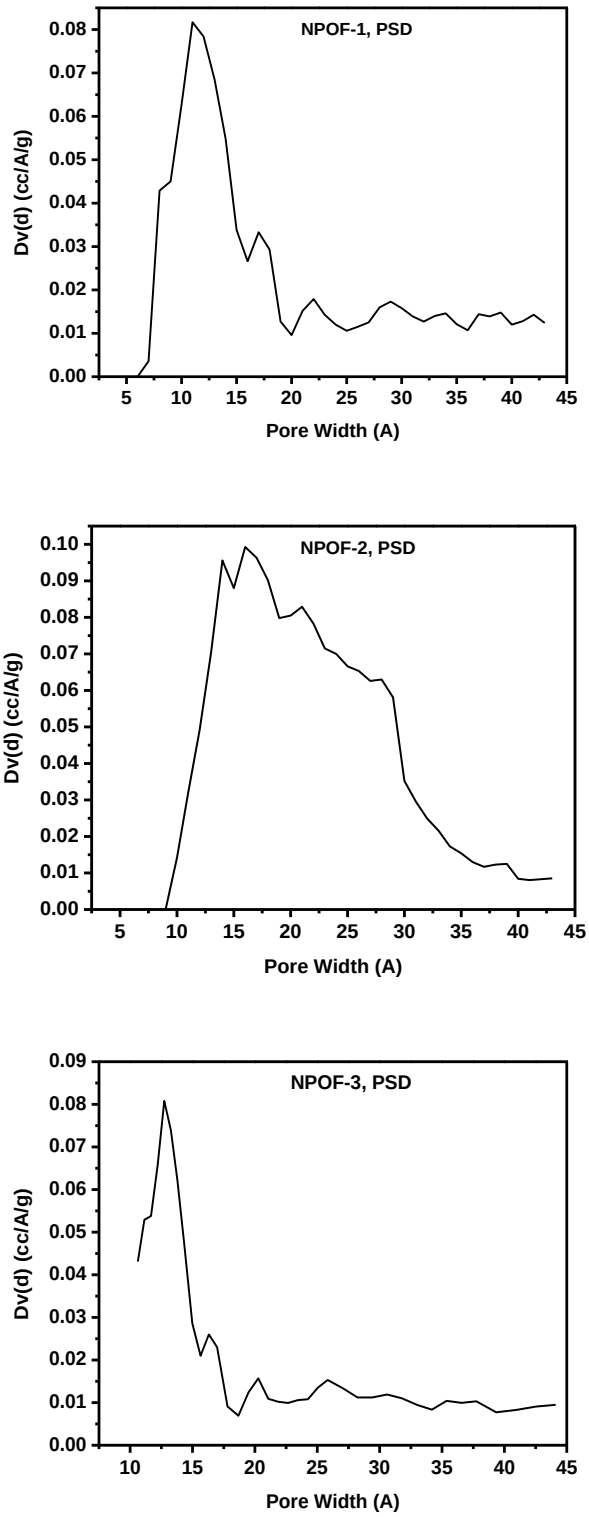

Figure 7.16: NLDFT Pore Size Distribution for (A) NPOF-1, (B) NPOF-2, and (C) NPOF-3

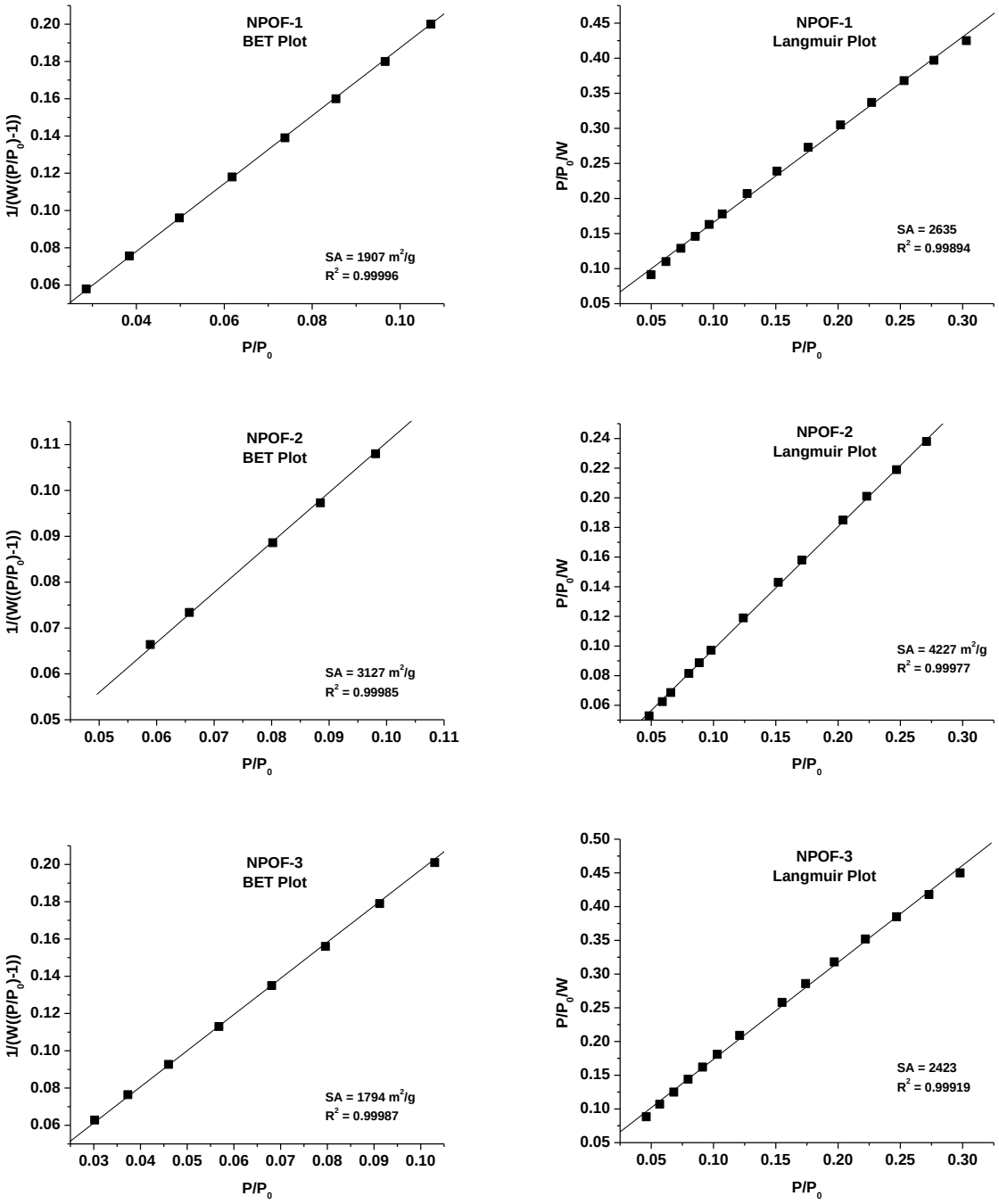

Figure 7.17. BET (P/P_o = 0.05-0.15) and Langmuir (P/P_o = 0.05-0.30) plots for NPOF-1, NPOF-2 and NPOF-3 calculated from the nitrogen adsorption.

Hydrogen storage remains one of the major hurdles facing the widespread use and commercialization of this highly flammable fuel. It is now well recognized that physisorption of H2 is a function of surface area in porous materials such as organic polymers, MOFs, COFs, etc. Given the high surface areas of NPOFs, we investigated their low pressure hydrogen storage performance at 77 K and 0–1 bar (Figure 7.18-19). The H_2 uptakes listed in Table 7.1 were higher for NPOFs of higher surface area as expected, and the PSD seems to have a modest impact on the final uptake at the above-mentioned conditions. Previous studies have documented the impact of pore size on hydrogen storage, which can be enhanced by pores having dimensions close to the kinetic diameter of the H_2 molecule. The storage enhancement is a result of increased interaction between the H_2 and the pore walls. Even though NPOF-1 and NPOF-3 have relatively smaller pores than NPOF-2, the storage capability of the latter exceeds the other NPOFs due to its higher surface area. We have also compared hydrogen storage by NPOFs to other related organic and inorganic porous architectures. For example, under similar conditions, the related COFs and CTFs store 0.9–1.2 and 1.55 wt% of H_2, respectively.[80,226] Other purely organic polymers such as hypercrosslinked polymer networks synthesized by the self-condensation of bischloromethyl monomers (0.89–1.69 wt%), nitrogen-linked nanoporous networks of aromatic rings (0.01–0.85 wt%),[161] and PIMs, which recently have been reported to be among the best organic polymers for hydrogen uptake (0.74–1.83 wt%), show comparable uptakes.[134] Moreover, the H_2 uptakes of NPOFs are in line with those recently reported for PAF-1 (1.5 wt%) or PPNs (1.37–1.58 wt%). In contrast, activated carbon such as PICACTIF-SC, AX-21, and zeolite-templated show higher uptake (1.90, 2.40, and 2.60 wt%, respectively)[49,163] however, we anticipate NPOFs to exhibit higher hydrogen uptake under high-pressure and cryogenic conditions.

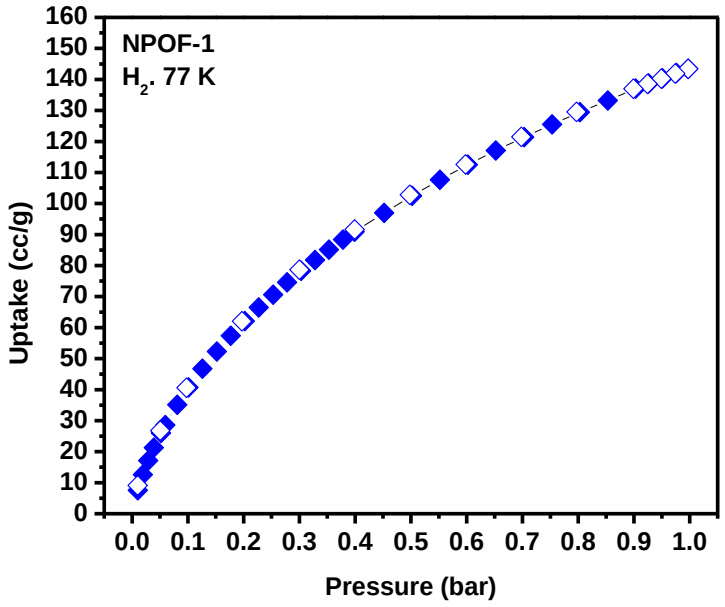

Figure 7.18. Hydrogen uptake isotherms for NPOF-1

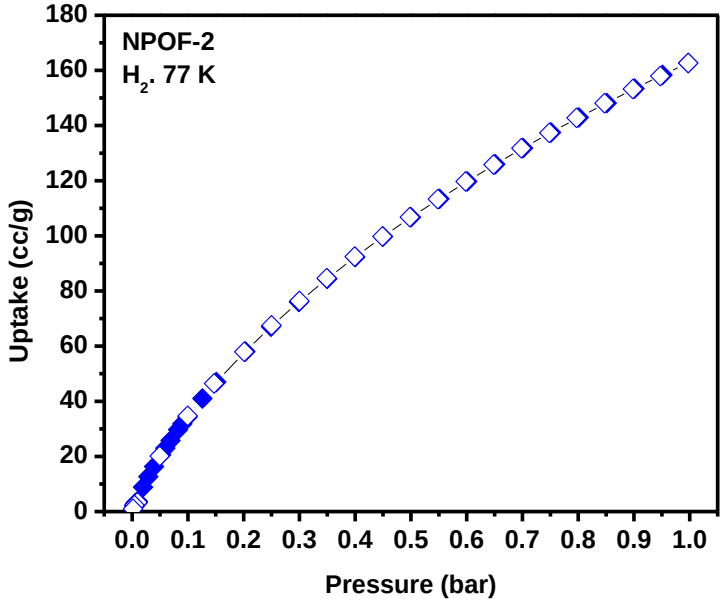

Figure 7.19. Hydrogen uptake isotherms for NPOF-2

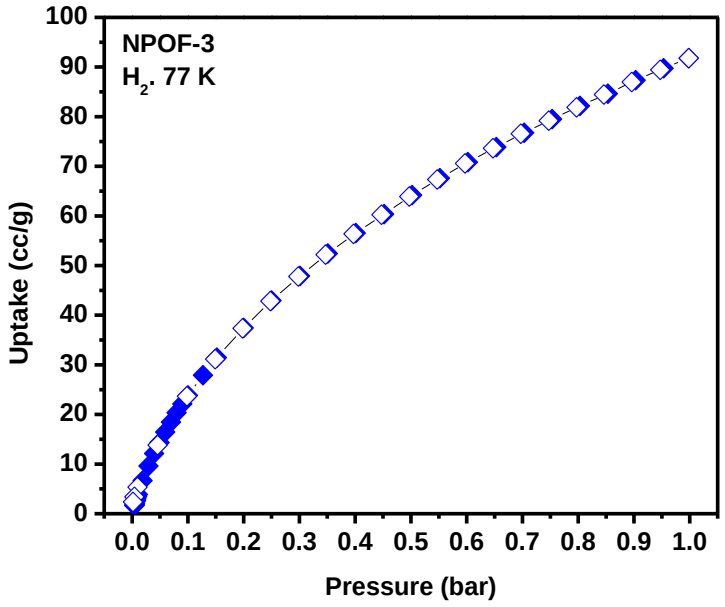

Figure 7.20. Hydrogen uptake isotherms for NPOF-3

7.4 Conclusions

In conclusion, a series of highly porous organic polymers of permanent porosity and high thermal and chemical stability has been prepared using nickel-catalyzed Yamamoto coupling reactions of 2-D and 3-D aryl halide building blocks. The surface areas and pore sizes in these polymers are directly impacted by the dimensionality and metrics of the building blocks. We anticipate these polymers to undergo post-synthesis chemical modification that would install several functional groups into the pore wall which could enhance gas uptake and selectivity, ion-capture, and separation applications. The accessible high surface area in NPOFs makes them attractive for high-pressure gas uptake studies, which are currently being addressed in our laboratory.

Chapter 8. Conclusion

Over the past few years, porous organic materials have shown exceptional capabilities in terms of gas storage and separation. Since the discovery of COFs in 2005, there have been numerous attempts to develop the optimum metal-free, low-density material for storage of small gases such as H_2, CH_4, and CO_2. Few of the attempts have resulted in crystalline, well-characterizable polymers; however, in many cases, amorphous polymers have been proven to exhibit higher surface areas and selective gas sorption properties than their crystalline counterparts. To this end, several major advances have been achieved and have been reported throughout this dissertation.

First, a new class of porous materials connected by B-N bonds has been developed, successfully synthesizing and fully characterizing six new BLPs in addition to three new NPOFs. This concept was first demonstrated in the synthesis of BLP-1(H) and BLP-12(H) as potential representative 2D and 3D BLPs, respectively. A design strategy similar to that used in the synthesis of COFs was applied. By replacing the boronic acid starting materials used in COFs with amine-boranes, we were able to successfully include the borazine ring into a tailored predetermined COF-like system. BLP-1(H), though amorphous, exhibited a 55% higher surface area and 43% higher pore volume than the analogous COF-1, which confirms that crystallinity is not a prerequisite for high porosity. BLP-12(H), synthesized from the 3D tetra(4-aminophenyl)methane building unit exhibited an even higher surface area than BLP-1(H). Though, its surface area and pore size was not comparable to 3D COFs such as COF-102 and

COF-103, characterization of BLP-12(H) still shows potential for increased gas sorption properties.

Another major accomplishment was the completion of the investigation on H_2, CH_4, and CO_2 storage capabilities in BLPs through low pressure and high pressure gas sorption measurements comparing the results to other organic polymers in the field. The high sorptive potential of BLP-12(H) was confirmed by measurements at atmospheric pressure exhibiting the highest hydrogen uptake of any reported organic polymers. Using these measurements we were also able to determine the heats of adsorption using the virial method. These calculations revealed heats of adsorption typical of porous organic frameworks for 2D BLPs, however a much higher H_2 heat of adsorption in BLP-12(H) compared to analogous 3D COFs. CO_2/CH_4 selectivity using the Ideal Adsorbed Solution Theory was applied to high pressure isotherms, resulting in a modest overall separation potential.

Thirdly, the crystallization of the first porous borazine-containing polymer, BLP-2(H), was realized via the dehydrogenation 1,3,5-tris(p-aminophenyl)benzene-borane. It is widely believed that the crystallization of organic polymers is difficult due to required microscopic reversibility in bond formation and impossible in the absence thereof. BLP-2(H), however, which under the given conditions may proceed through irreversible B-N bond formation, was successfully crystallized as confirmed by PXRD. The development of this novel synthesis has been a significant feat in that the related boron nitride ceramic material is typically crystallized at temperatures around 1000 ºC. BLP-2(H) was synthesized using a facile route under relatively mild conditions (120 ºC, 72 h). Through XRD experiments we were able to match experimental patterns to the modeled pattern confirming the predicted eclipsed structure. SEM images of

BLP-2(H) show uniformed well-defined rectangular prism-shaped particles approximately 50-100 nm in width.

The successful incorporation of melamine into a BLP structure, BLP-3(H) has been another significant advance in the field of porous polymers. In doing this, we have synthesized the polymer with the highest borazine content and therefore the highest potentially accessible hydrogen (4.8 wt%) content for chemisorptive hydrogen storage. In addition, BLP-3(H) exhibits desirable gas sorption properties; having the lowest surface area, its CO_2 uptake surprisingly surpasses those of BLP-1(H) and BLP-2(H) at 1 bar and has the highest CO_2/CH_4 selectivity among the BLPs reported herein.

In addition to our investigations on BLPs, we have included studies on another series of highly porous organic polymers prepared using the nickel-catalyzed Yamamoto coupling reactions of 2-D and 3-D aryl halide building blocks. The surface areas and pore sizes in these polymers were directly impacted by the dimensionality and metrics of the building blocks. These non-borazine containing nanoporous organic polymers, NPOFs, consisting of all carbons atoms were subjected to low pressure hydrogen storage measurements. It was interesting to find that though NPOFs exhibit higher surface areas than BLPs, their hydrogen uptake capacities were inferior. This finding suggests that the borazine content of BLPs plays a significant role in hydrogen storage properties; possibly due to the more polarized nature of borazine compared to benzene.

There are several potential avenues to take in further investigating BLPs now that a solid foundation has been established. It was mentioned that BLP-3(H) stands out by having the highest borazine content, which makes it a good candidate for chemisorption studies. If a successful system is developed whereby hydrogen can be reintroduced into the borazine

framework forming borazane units, it would be significant in that the chemisorption, which would be complementary to the intrinsic physisorptive potential, would permit the storage of large amounts hydrogen. Another future work would involve the crystallization of a tetraphenylbenzene containing BLP. A BLP made from the starting material 1,2,4,5-tetrakis(4-aminophenyl)benzene, is likely to be very porous due to its exposed ring faces and edges as described in the design of high surface area materials in Chapter 2. In addition, this molecule possesses similar properties to the amine used in BLP-2(H) which suggests the feasibility of crystallization. 1,3,5,7-tetrakis(4-aminophenyl)adamantane would also act as an interesting building unit to incorporate into a BLP framework (BLP-15(H) in Chapter 2). Having a tetrahedral geometry with longer more isolated extensions, it has the potential to outperform even BLP-12(H) in gas storage capacity.

In summary, we have demonstrated the synthesis of highly porous borazine-linked polymers by thermolysis of arylamine-borane adducts and investigated their gas storage performance under ambient pressure and cryogenic conditions. For the first time we have proved that thermolysis of an amine-borane can lead to a porous and crystalline borazine-linked polymer. We have demonstrated the synthesis of a new porous melamine-based borazine-linked polymer by thermolysis which exhibits exceptional gas storage properties. Finally, we have synthesized a new series of high surface area NPOFs and studied their H_2 sorption capacity relative to BLPs. The work presented here represents a major advance in the development of porous materials, placing BLPs among the most attractive candidates for clean energy applications. There is still, however, much more room for additional scientific contributions through investigations in the field of BLPs.

References

References

1. McKeown, N. B.; Budd, P. M.; Msayib, K. J.; Ghanem, B. S.; Kingston, H. J.; Tattershall, C. E.; Makhseed, S.; Reynolds, K. J.; Fritsch, D. *Chem. Eur. J.* **2005**, 11, 2610.
2. Budd, P. M.; Msayib, K. J.; Tattershall, C. E.; Ghanem, B. S.; Reynolds, K. J.; McKeown, N. B.; Fritsch, D. *J. Membr. Sci.* **2005,** 251, 263.
3. McKeown, N. B.; Ghanem, B. S.; Msayib, K. J.; Budd, P. M.; Tattershall, C. E.; Mahmood, K.; Tan, S.; Book, D.; Langmi; Walton, A. *Angew. Chem. Int. Ed.* **2006**, 45, 1804.
4. Han, S. S.; Furukawa, H.; Yaghi, O. M.; Goddard, W. A. *J. Am. Chem. Soc.* **2008**, 130, 11580.
5. Furukawa, H.; Yaghi, O. M.; *J. Am. Chem. Soc.* **2009**, 25, 8876.
6. Schwab , M. G.; Lennert, A.; Pahnke, J.; Jonschker,, G.; Koch, M; Senkovska, I.; Rehahn, M.; Kaskel, S. *J. Mater. Chem.* **2011**, 21, 2131.
7. Mackintosh, H. J.; Budd, P. M.; McKeown, N. B.; *J. Mater. Chem.* **2008**, 18, 573.
8. McKeown, N. B.; Hanif, S.; Msayib, K. J.; Tattershall, C. E.; Budd, P. M. *Chem. Commun.* **2002**, 2782.
9. McKeown, N. B.; Makhseed, S.; Budd, P. M. *Chem. Commun.* **2002**, 2780.
10. Xie, Z.; Wang, C.; deKrafft, K. E.; Lin, W. *J. Am. Chem. Soc.* **2011**, 133, 2056.
11. Chen, L.; Yang, Y.; and Jiang, Donglin J. *J. Am. Chem. Soc.* **2011**, 132, 9138.

12. Du, X.; Sun, Y.; Tan, B.; Teng, Q.; Yao, X.; Su, C.; Wang, Wei, W. *Chem. Commun.*, **2010**, 46, 970.

13. Palkovits, R.; Antonietti, M.; Kuhn, P.; Thomas, A.; and Schuth, F. *Angew. Chem. Int. Ed.* **2009**, 48, 6909.

14. Thomas, A.; Kuhn, P.; Weber, J.; Titirici, M.; Antonietti, M. *Macromol. Rapid Commun.* **2009**, 30, 221.

15. Domenech-Carbo, A. *Electrochemistry of Porous Materials*, CRC Press, Taylor and Francis Group, Boca Raton, FL, **2007.**

16. Rakow, N. A.; Wendland, M. S.; Trend, J. E.; Poirier, R. J.; Paolucci, D.M.; Maki, S. P.; Lyons, C. S.; Swierczek, M. J. *Langmuir* **2010**, 26, 3767.

17. Groves, W.A.; Zellersa, E.T.; Frye, G.C. *Anal. Chem. Acta* **1998**, 371, 131.

18. Gao, J.B.; Sansinena, J.M. Wang, H-.L. *Synth. Metals* **2003**, 135, 809.

19. Perez, G. P.; Crooks, R. M. *Anal. Chem.* **2004**, 76, 4137.

20. Du, X.; Ying, Z.; Jiang, Y.; Liu, Z.; Yang, T.; Xie, G. *Sens. Actuat. B* **2008**, 134, 409.

21. Barton, T. J.; Bull, L. M.; Klemperer, W. G.; Loy, D. A.; McEnaney, B.; Misono, M.; Monson, P. A.; Pez, G.; Scherer, G. W.; Vartuli, G. C.; Yaghi, O. M. *Chem. Mater.***1999**, 11, 2633.

22. Rohrman, F. A; Steigerwald, B. J.; Ludwig, J. H. *Science* **1967**, 156, 931.

23. Greene, D. L.; Kahn, J. R.; Gibson, R. C. *The Energy Journal* **1999**, 20, 1.

24. Greene, D. L. *Contemp. Pol. Issues*, 1990, 8, 118.

25. Zuttel, A. *Materials Today* **2003**, 6, 24.

26. Ritter, J. A.; Ebner, A. D.; Wang, J.; Zidan, R. *Materials Today* **2003**, 6, 18.

27. Ogden, J. M. *Annu. Rev. Energy Env.* **1999**, 24, 227.

28. Schlapbach, L., Zuttel, A. *Nature* **2001**, 414, 353.

29. U. S. Department of Energy, Hydrogen and Fuel Cells Program, http://www.hydrogen.energy.gov/

30. Grimes, C. A.; Varghese, O. K.; Ranjan, S. *Light, Water, Hydrogen: The Solar Generation of Hydrogen by Water Phtoelectrolysis.* Springer Sci. and Business Media, LLC., **2008.**

31. Ball, M. and Wierschel, M.; *The Hydrogen Economy: Oppurtunities and Chellenges.* Cambridge Univ. Press, **2009**.

32. Bossel, U.; Eliasson, B. *Energy and The Hydrogen Economy.* **2003**. http://www.methanol.org/pdf/HydrogenEconomyReport2003.pdf

33. *Hydrogen, Fuel Cells, & Infrastructure Technologies Program: Multi-year Research, Development, and Demonstration Plan;* U.S. DOE, http://www1.eere.energy.gov/hydrogenandfuelcells/storage/current_technology.html.

34. Stephens, F. H.; Pons, V.; Baker, R. T. *Dalton Trans.* **2007**, 25, 2613.

35. Nguyen, V. S.; Matus, M. H.; Grant, D. J.; Nguyen, M. T.; Dixon, D. A. *Phys. Chem. A* **2007**, 111, 8844.

36. Pun, D.; Lobkovsky, E.; Chirik, P. J. *Chem. Commun.* **2007**, 31, 3297.

37. Mohajeri, N.; T-Raissi, A.; Adebiyi, O. *J. Power Sources* **2007**, 167, 482-485.

38. Langmi, H. W.; McGrady, G. S. *Chem. Rev.* **2007**, 251, 925-935.

39. Keaton, R. J.; Blacquiere, J. M.; Baker, R. T. *J. Am. Chem. Soc.* **2007**, 129, 1844-1845.

40. Stephens, F. H.; Baker, R. T.; Matus, M. H.; Grant, D. J.; Dixon, D. A. *Angew. Chem. Int. Ed.* **2007**, 46, 746.

41. Orimo, S. I.; Nakamori, Y.; Eliseo, J. R.; Zuttel, A.; Jensen, C. M. *Chem. Rev.* **2007**, 107, 4111.

42. Zhao, D.; Yuan, D. Q.; Zhou, H. C. *Energy Environ. Sci.* **2008**, 1, 222.

43. Dinca, M.; Long, J. R. *Angew. Chem. Int. Ed.* **2008**, 47, 6766.

44. Collins, D. J.; Zhou, H. C. *J. Mater. Chem.* **2007**, 17, 3154.

45. Lin, X.; Jia, J. H.; Hubberstey, P.; Schroder, M.; Champness, N. R. *Cryst. Eng. Comm.* **2007**, 9, 438.

46. Rowsell, J. L. C.; Yaghi, O. M. *Angew. Chem. Int. Ed.* **2005**, 44, 4670.

47. Seayad, A. M.; Antonelli, D. M. *Adv. Mater.* **2004**, 16, 765.

48. Xia, Y.; Mokaya, R. *J. Phys. Chem. C* **2007**, 111, 10035.

49. Yang, Z. X.; Xia, Y. D.; Mokaya, R. *J. Am. Chem. Soc.* **2007**, 129, 1673.

50. McKeown, N. B.; Budd, P. M.; Book, D. *Macromol. Rapid Commun.* **2007**, 28, 995.

51. Budd, P. M.; Butler, A.; Selbie, J.; Mahmood, K.; McKeown, N. B.; Ghanem, B.; Msayib, K.; Book, D.; Walton, A. *Phys. Chem. Chem. Phys.* **2007**, 9, 1802.

52. Ghanem, B. S.; Msayib, K. J.; McKeown, N. B.; Harris, K. D. M.; Pan, Z.; Budd, P. M.; Butler, A.; Selbie, J.; Book, D.; Walton, A. *Chem. Commun.* **2007**, 1, 67.

53. McKeown, N. B.; Budd, P. M. *Chem. Soc. Rev.* **2006**, 35, 675.

54. Maffei, A. V.; Budd, P. M.; McKeown, N. B. Adsorption studies of a microporous phthalocyanine network polymer. Langmuir 2006, 22, 4225.

55. Budd, P. M.; McKeown, N. B.; Fritsch, D. *J. Mater. Chem.* **2005**, 15, 1977.

56. Brunauer, S.; Deming, L. S.; Deming, W. E.; Teller, E. *J. Am. Chem. Soc.* **62,** 1940 1723.

57. Gregg, S. J.; Sing, K. S. W. *Adsorption, Surface Area and Porosity*; Academic Press Inc. Ltd.: London, **1982**.

58. Langmuir, I. *J. Am. Chem. Soc.* **1916**, 38, 2221.

59. Brunauer, S.; Emmett, P. H.; Teller, E. *J. Am. Chem. Soc.* **1938**, 60, 309.

60. Autosorb-1 Operating Manual Ver1.53 Quantachrome Instruments.

61. Lozano-Castello, D.; Cazorla-Amoros, D.; Linares-Solano, A. Carbon 42 (2004) 1231–1236

62. Ravikovitch, P. I.; Vishnyakov, A.; Russo, R.; and Neimark, A. V. *Langmuir* **2000,** *16,* 2311.

63. Manocha, S. M. *Sadhana* **2003,** 28, 335.

64. Daley, M. A. Mangun, C. L.; DeBarrb, J. A.; Riha, S.; Lizzio, A. A.; Donnals, G. L.; Economy, J. *Carbon* **1997**, 35, 411.

65. Mochida, I.; Kawabuchi, Y.; Kawano, S.; Matsumura, Y.; Yoshikawa, M. *Fuel* **1997,** 76, 543.

66. Rolando, M. A. Roque-Maherbe, R. *Adsorption and Diffusion in Nanoporous Materials,* CRC Press, Taylor and Francis Group, Boca Raton, FL, **2007.**

67. Roque-Malherbe R, Marquez-Linares F, Del Valle W, Thommes M. *J Nanosci Nanotechnol*. **2008**, 11, 5993.

68. Beck, J. S.; Yartuli, J. C.; Roth, W. J.; Leonowicz, M. E.; Kresge, C. T.; Schmidt, K. D.; Chu, C. T.-W.; Olson, D. H.; Sheppard, E. W.; Mccullen, S. B.; Higgns, J. B.; Schlenker, J. L. *J. Amer. Chem. Soc.* **1992**, 114, 10834.

69. Zeolites http://www.asdn.net/asdn/chemistry/zeolites.shtml

70. Davis, M. E.; Saldarriaga, C.; Montes, C.; Garces, J.; Crowder, C. *Zeolites* **1988**, 362.

71. Nalwa, H. S., Ed., *Handbook of Surfaces and Interfaces of Materials,* Academic Press, New York, **2000**, 1.

72. Hoskins, B. F.; Robson, R. *J. Am. Chem. Soc.* **1989,** *111*, 5962.

73. David J. Tranchemontagne, Jose´ L. Mendoza-Corte´ s, Michael O'Keeffe and Omar M. Yaghi Chem. Soc. Rev., 2009, 38, 1257.

74. Hailian Li, Mohamed Eddaoudi, Thomas L. Groy, and O. M. Yaghi, *J. Am. Chem. Soc.* **1998,** *120*, 8571.

75. Furukawa, H,; Ko, N.; Go, Y. B.; Aratani, N.; Choi, S. B.; Choi, E.; Yazaydin, A. O.; Snurr, R. Q.; O'Keeffe, M.; Kim, J.; Yaghi, O. M. *Science* **2010**, 239, 424.

76. Côté, A. P.; Benin, A. I.; Ockwig, N. W.; Matzger, A. J.; O'Keeffe, M.; Yaghi, O. M. *Science* **2005**, *310*, 1166.

77. Côté, A. P.; El-Kaderi, H. M.; Furukawa, H.; Hunt, J. R.; Yaghi, O. M. *J. Am. Chem. Soc.* **2007**, *129*, 12914.

78. El-Kaderi, H. M.; Hunt, J. R.; Mendoza-Cortés, J. L.; Côté, A. P.; Taylor, R. E.; O'Keeffe, M.; Yaghi, O. M. *Science* **2007,** 316, 268.

79. Kuhn, P.; Antonietti, M.; Thomas, A. *Angew. Chem. Int. Ed.* **2008**, 47, 3450.

80. Uribe-Romo, F. J.; Hunt, J. R.; Furukawa, H.; Klock, C.; O'Keeffe, M.; Yaghi, O. M. *J. Am. Chem. Soc.*, **2009**, 131, 4570.

81. Davankov, V. A.; Tsyurupa, M. P. *React. Polym.* **1990**, 13, 27.

82. Tsyurupa, M. P.; Davankov, V. A. *React. Funct. Polym.* **2002**, 53,193.

83. Ahn, J. -H.; Jang, J. -E.; Oh, C. -G.; Ihm, S. -K.; Cortez, J.; Sherrington, D. C. *Macromolecules* **2005**, 39, 627.

84. Lee, J. Y.; Wood, C. D.; Bradshaw, D.; Rosseinsky, M. J.; Cooper, A. I. *Chem. Commun*. **2006**, 2670.

85. Wood, C. D.; Tan, B.; Trewin, A.; Niu, H.; Bradshaw, D.; Rosseinsky, M. J.; Khimyak, Y. Z.; Campbell, N. L.; Kirk, Stoeckel, E.; Cooper, A. I. *Chem. Mater.* **2007**, 19, 2034.

86. Jiang, J.-X.; Su, F.; Trewin, A.; Wood, C. D.; Campbell, N. L.; Niu, H.; Dickinson, C.; Ganin, A. Y.; Rosseinsky, M. J.; Khimyak Y. Z.; Cooper, A. I. *Angew. Chem., Int. Ed.*, **2007**, 46, 8574.

87. Cooper, A. I. *Adv. Mater.* **2009**, 21, 1291.

88. Schmidt, J.; Weber, J.; Epping, J.; Antonietti, M.; Thomas, A. *Adv. Mater.* **2009**, 21, 702.

89. Weber, J.; Thomas, A. *J. Am. Chem. Soc.* **2008**, 130, 6334.

90. Jiang, J. X.; Su, F.; Trewin, A.; Wood, C. D.; Niu, H.; Jones, J.; Khimyak, Y. Z.; Cooper, A. I. *J. Am. Chem. Soc.* **2008**, 130, 7710.

91. Chen, L.; Honsho, Y.; Seki, S.; Jiang, D. *J. Am. Chem. Soc.* **2010**, 132, 6742.

92. Dawson, R.; Laybourn, A.; Clowes, R.; Khimyak, Y. Z.; Adams, D. J.; Cooper, A. I. *Macromolecules* **2009**, 42, 8809.

93. Ben, T.; Ren, H.; Ma, S. Q.; Cao, D. P.; Lan, J. H.; Jing, X. F.;Wang, W. C.; Xu, J.; Deng, F.; Simmons, J. M.; Qiu, S. L.; Zhu, G. S. *Angew. Chem., Int. Ed*. **2009**, *48*, 9457.

94. Yuan, D.; Lu, W.; Zhao, D.; Zhou, H-. C. *Adv. Mater.* **2011**, 23, 3723.

95. Reich, T. R.; **Jackson, K. T.**; Li, S.; Jena, P.; El-Kaderi, H. M. *J. Mater. Chem.* **2011**, 21, 10629.

96. **Jackson, K. T.**; Rabbani, M. G.; Reich, T. E.; El-Kaderi, H. M. *Polym. Chem.* DOI: 10.1039/C1PY00374G

97. Gay-Lussac, J. L.; Thenard, J. L. *Mem de Phys. et de Chim. De la Soc. D'arcueil* 2, **1809**, 210.

98. Davy, J. *Anne Chimie* **1813**, 86, 178.

99. Stock, A.; Pohland, E. B. *Ber. Dtsch. Chem. Ges.* **1926**, 59, 2215.

100. Niedenzu, K.; Dawson, J. W. *Boron-Nitrogen Compounds*, Academic Press Inc.: New York, **1965**.

101. Lane, C. F. *N-B-H Survey*, Contract # DE-FC36-05GO15060, Northern Arizona University, April 17, **2006**.

102. Schaeffer, G. W.; Schaeffer, R.; Schlesinger, H. I. *J. Am. Chem. Soc.* **1951**, 73, 1612.

103. Hough, W. V.; Guibert, C. R.; Hefferan, G. T. US Patent 4150097, April 17, **1979**.

104. Wideman, T.; Sneddon, L. G. *Inorg. Chem.* **1995**, *34*, 1002.

105. Bissot, T. C.; Parry, R. W. *J. Am. Chem. Soc.* **1955**, 77, 3481.

106. Gaines, D. F.; Schaeffer, R. *J. Am. Chem. Soc*. **1963**, 85, 395.

107. Meller, A.; Schaschel, E. *Inorg. Nucl. Chem. Lett.* **1966**, 2, 41.

108. Brown, M. P.; Heseltine, R. W.; Sucliffe, L. H. *J. Chem. Soc. A* **1968**, 612.

109. Framery, E.; Vaultier, M. *Heteroatom Chem.* **2000**, *11*, 218-225.

110. C. A. Jaska, K. Temple, A. J. Lough, I. Manners, Chem. Commun. **2001**, 962.

111. C. A. Jaska, K. Temple, A. J. Lough, I. Manners, *J. Am. Chem. Soc.* **2003**, 125, 9424.

112. Skoog, D. A.; Holler, F. J.; Niemon, T. A.; *Principles of Instrumental Analysis, 5th Ed.*, **1998**, Harcourt Brace and Co.; Orlando, FL.

113. Wells, A. F. *Three-Dimensional Nets and Polyhedra*. Wiley: New York, **1977**.

114. Wells, A. F. *Further Studies of Three-Dimensional Nets*; Monograph 9; Am. Cryst. Assoc.: Littleton, CO, **1979**.

115. MacGillivray, L. R. Metal-Organic Frameworks: Design and Application; Wiley: New Jersey, **2010**.

116. O'Keeffe, M.; Yaghi, O. M. *Chem. Rev.* **2011**, dx.doi.org/10.1021/cr200205j.

117. Yaghi, O. M.; O'Keeffe, M.; Ockwig, N. W.; Chae, H. K.; Eddaoudi, M.; Kim, J. Nature **2003**, 423, 705.

118. Ohrstrom, L.; Larsson, K. Molecular Based Materials: The Structural Network Approach; Elsevier: Amsterdam, **2005**.

119. Delgado-Friedrichs, O.; O'Keeffe, M.; Yaghi, O. M. *Phys. Chem. Chem. Phys*. **2007**, 9, 1035.

120. O'Keeffe, M.; Peskov, M. A.; Ramsden, S. J.; Yaghi, O. M. *Acc. Chem. Res.* **2008**, 41, 1782. RCSR can be accessed at rcsr.anu.edu.au.

121. Chae, H. K.; Siberio-Perez, D. Y.; Kim, J.; Go, Y. –B.; Eddaoudi, M.; Matzger, A. J.; O'Keeffe, M.; Yaghi, O. M. *Nature* **2004**, 427, 523.

122. Kesanli, B.; Cui, Y.; Smith, M. R.; Bittner, E. W.; Bockrath, B. C.; Lin, W. *Angew. Chem., Int. Ed.* **2005**, 44, 72.

123. Chun, H.; Dybtsev, D. N.; Kim H.; Kim, K. *Chem. Eur. J.* **2005**, 11, 3521.

124. Shengqian Ma Pure Appl. Chem., Vol. 81, No. 12, pp. 2235

125. Rabbani, M. G.; El-Kaderi, H. M. *Chem. Mater.* **2011**, 23, 1650.

126. Zheng, B.; Bai, J.; Duan, J.; Wojtas, L.; Zaworotko, M. J. *J. Am. Chem. Soc.* **2011**, 133, 748.

127. *Materials Studio 4.3 V*; Accelrys, Inc: San Diego, CA, **2003**.

128. O'Keeffe, M.; Eddaoudi, M.; Li, H.; Reineke, T. M.; Yaghi, O. M. *J. Solid State Chem.* **2000**, 152, 3.

129. Accelrys Software, Inc. *Forcite*, http://accelrys.com/products/datasheets/forcite.pdf

130. *Mercury 2.4*, Cambridge Crystallographic Data Centre: Cambridge, UK, **2010.**

131. McKeown, N. B.; Budd, P. M. *Macromolecules* **2010**, 43, 5163.

132. Jiang, J. X.; Cooper, A. I. *Top. Curr. Chem.* **2010**, 293, 1.

133. Kuhn, P.; Forget, A.; Su, D.; Thomas, A.; Antonietti, M. *J. Am. Chem. Soc.* **2008**, 130, 13333.

134. Ghanem, B. S.; Hashem, M.; Harris, K. D. M.; Msayib, K. J.; Xu, M.; Budd, P. M.; Chaukura, N.; Book, D.; Tedds, S.; Walton, A.; McKeown, N. B. *Macromolecules* **2010**, 43, 5287.

135. Kassab, R. M.; Jackson, K. T.; El-Kadri O. M.; El-Kaderi, H. M. *Res. Chem. Intermed.* **2011**, 37, 747.

136. Wang, Z.; Zhang, B.; Yu, H.; Sun, L.; Jiaob, C.; Liua, E. *Chem. Commun.* **2010**, 46, 7730.

137. Farha, O. K.; Spokoyny, A. M.; Hauser, B. G.; Bae, Y. –S.; Brown, S. E.; Snurr, R. Q.; Mirkin, C. A.; Hupp, J. T. *Chem. Mater.* **2009**, 21, 3033.

138. Pandey, P.; Katsoulidis, A. P.; Eryazici, I.; Wu, Y.; Kanatzidis, M. G.; Nguyen, S. T. *Chem. Mater.* **2010**, 22, 4974.

139. Katsoulidis, A. P.; Kanatzidis, M. G. *Chem. Mater.* **2011**, 23, 1818.

140. Lu, W.; Yuan, D.; Zhao, D.; Schilling, C. I.; Plietzsch, O.; Muller, T.; Br€ase, S.; Guenther, J.; Bl€umel, J.; Krishna, R.; Li, Z.; Zhou, H. -C.*Chem. Mater.* **2010**, 22, 5964.

141. Belof, J. L.; Stern, A. C.; Eddaoudi, M.; Space, B. *J. Am. Chem. Soc.* **2007**, 129, 15202.

142. Salles, V.; Bernard, S.; Li, J.; Brioude, A.; Chehaidi, S.; Foucaud, S.; Miele, P. *Chem. Mater.* **2009**, 21, 2920.

143. Duperrier, S.; Bernard, S.; Calin, A.; Sigala, C.; Chiriac, R.; Miele, P.; Balan, C. *Macromolecules* **2007**, 40, 1028.

144. Sham, I. H. T.; Kwok, C. -C.; Che, C. -M.; Zhu, N. *Chem. Commun.* **2005**, 3547.

145. Wakamiya, A.; Ide, T.; Yamaguchi, S. *J. Am. Chem. Soc.* **2005**, 127, 14859.

146. Yamaguchi, S.; Wakamiya, A.; *Pure Appl. Chem.* **2006**, 78, 1413.

147. Ganesan, P.; Yang, X.; Loos, J.; Savenije, T. J.; Abellon, R. D.; Zuilhof, H.; Sudhölter, E. J. R. *J. Am. Chem. Soc.* **2005**, 127, 14530.

148. Jagiello, J.; Bandosz, T. J.; Putyera, K.; Schwarz, J. A. *J. Chem. Eng. Data* 1995, **40**, 1288.

149. Kaldor, A.; Porter, R. F.; *Inorg. Chem.* **1971**, 10, 775.

150. Li, J. S.; Zhang, C. R.; Li, B.; Cao, F.; Wang, S. Q. *Inorg. Chim. Acta* **2011**, 366, 173.

151. Moon, K. T.; Min D. S.; Kim, D. P. *J. Ind. Eng. Chem.* **1997**, 3, 288.

152. Gervais, C.; Babonneau, F. *J. Organomet. Chem.* **2002**, 657, 75.

153. Gervais, C.; Framery, E.; Duriez, C.; Maquet, J.; Vaultier, M.; Babonneau, F. *J. Eur. Ceram. Soc.* **2005**, 25, 129.

154. Gervais, C.; Babonneau, F.; Maquet, J.; Bonhomme, C.; Massiot, D.; Framery, E.; Vaultier, M. *Magn. Reson. Chem.* **1998**, 36, 407.

155. Li, J.; Zhang, C.; Li, B.; Cao, F.; Wang, S. *Eur. J. Inorg. Chem.* **2010**, 1763.

156. Chen, X.; Bao, X.; Zhao, J. -C.; Shore, S. G. *J. Am. Chem. Soc.* **2011**, 133, 14172.

157. Murray, L. J.; Dinca, M.; Long, J. R. *Chem. Soc. Rev.* **2009**, 38, 1294;

158. Zhou, H. -C. *Chem. Commun.* **2010**, 46, 44.

159. Germain, J.; Frechet, J. M. J.; Svec, F. *Small* **2009**, 5, 1098.

160. Rowsell, J. L. C.; Yaghi, O. M. *J. Am. Chem. Soc.* **2006**, 128, 1304.

161. Germain, J.; Svec, F.; Frechet, J. M. J. *Chem. Mater.* **2008**, 20, 7069.

162. Ghanem, B. S.; Hashem, M.; Harris, K. D. M.; Msayib, K. J. Xu, M. C.; Budd, P. M.; Chaukura, N.; Book, D.; Tedds, S.; Walton, A.; McKeown, N. B. *Macromolecules* **2010**, 43, 5287.

163. Texier-Mandoki, N.; Dentzer, J.; Piquero, T.; Saadallah, S.; David, P.; Vix-Guterl, C. *Carbon* **2004**, 42, 2744.

164. D'Alessandro, D. M.; Smit, B.; Long, J. R. *Angew. Chem., Int. Ed.* **2010**, 49, 2.

165. Ma, S. Q.; Zhou, H. -H. *Chem. Commun.* **2010**, 46, 44.

166. Keskin, S.; van Heest, T. M.; Sholl, D. S. *Chem. Sus. Chem.* **2010**, 3, 879.

167. Mendoza-Cortes, J. L. J.; Han, S. S.; Furukawa, H.; Yaghi, O. M.; Goddard, W. M.; *J. Phys. Chem. A* **2010**, 114, 10824.

168. Farha, O. K.; Bae, Y. -S.; Hauser, B. G.; Spokoyny, A. M.; Snurr, R. Q.; Mirkin, C. A.; Hupp, J. T. *Chem. Commun.* **2010**, 46, 1056.

169. An, J.; Geib, J. S.; Rosi, N. L. *J. Am. Chem. Soc.* **2010**, 132, 38.

170. Jin, Y.; Voss, B. A.; Jin, A.; Long, H.; Noble, R. D.; Zhang, W. *J. Am. Chem. Soc.* **2011**, 133, 6650.

171. Demessence, A.; D'Alessandro, D. M.; Foo, M. L.; Long, J. R. *J. Am. Chem. Soc.* **2009**, 131, 8784.

172. Arstad, B.; Fjellv_ag, H.;Kongshaug, K. O.; Swang, O.; Blom, R. *Adsorption* **2008**, 14, 755.

173. Vaidhyanathan, R.; Iremonger, S. S.; Dawson, K. W.; Shimizu,G. K. H. *Chem. Commun.* **2009**, 5230.

174. Vaidhyanathan, R.; Iremonger, S. S.; Shimizu, G. H. K.; Boyd, P. G.; Alavi, S.; Woo., T. K. *Science* **2010**, 330, 650.

175. Panda, T.; Pachfule, P.; Chen, Y.; Jiangb, J.; Banerjee, R. *Chem. Commun.* **2011**, 47, 2011.

176. Hutchinson, N. J.; Coquil, T.; Navid, A.; Pilon, L. *Thin Solid Films* **2010**, 518, 2141.

177. Wideman, T.; Fazen, P. J.; Su, K.; Remsen, E. E.; Zank, G. A.; Sneddon, L. G. *Appl. Organometal. Chem.* **1998**, 12, 681.

178. Clark, T. J.; Lee, K.; Manners, I. *Chem. Eur. J.* **2006**, 12, 8634.

179. Jaska, C. A.; Manners, I. Inorganic Chemistry in Focus II, ed. By G. Meyer, D. Naumann, L. Wesemann, Wiley-VCH, Weinheim, **2005**, pp. 5364.

180. Hamilton, C. W.; Baker, R. T.; Staubitz, A.; Manners, I. *Chem. Soc. Rev.* **2009**, 38, 279.

181. Bao, C.; Lu, R.; Jin, M.; Xue, P.; Tan, C.; Xu, T.; Liu, G.; Zhao, Y. *Chem. Eur. J.* **2006**, 12, 3287.

182. Bao, C.; Jin, M.; Lu, R.; Song, Z.; Yang, X.; Song, D.; Xu, T.; Liu, G.; Zhao, Y. *Tetrahedron* **2007**, 63, 7443.

183. Heimens, P. C.; Rajagopalan, R., *Principles of /Colloid and Surface Chemistry, 3rd ed*; Marcel Dekker;: New York, **1997**; Chapter 6.

184. Maji, T. K.; Mostafa, G.; Matsuda, R.; Kitagawa, S. *J. Am. Chem. Soc.* **2005**, 127, 17152.

185. Chu, S. *Science* **2009**, 325, 1599.

186. Myers, A. L.; Prausnitz, J. M. *AIChE J.* **1965**, 11, 127.

187. Wolfram Research, Inc., *Mathematica*, Version 8.0, Champaign, IL **2010.**

188. Denney, M. C.; Pons, V.; Hebden, T. J.; Heinekey, D. M.; Goldberg, K. I. *J. Am. Chem. Soc.* **2006**, 128, 12048.

189. Clark, T. J.; Russell, C. A.; Manners, I. *J. Amer. Chem. Soc.* **2006**, 128, 9582.

190. Sloan, M. E.; Clark, T. J,; Manners, I. *Inorg. Chem.*. **2009**, 48, 2429.

191. Mauer, L. J.; Chernyshova, A. A.; Hiatt, A.; Deering, A.; Davis, R. *J. Agric. Food Chem.* **2009,** 57, 3974.

192. Rye, R. R.; Tallant, D. R. *Chem. Mater.* **1991**, 3, 286.

193. Jeon, J. -K.; Uchimaru, Y.; Kim, D. –P. *Inorg. Chem.* **2004**, *43*, 4796.

194. Dawson, R.; Cooper, A, I.; Adams, D. J. *Prog. Polym. Sci.* **2011** doi:10.1016/j-progpolymsci.2011.09.002

195. D'alessandro, D. M.; Smit, B.; Long, J. R. *Angew. Chem Int. Ed*. **2010**, 49, 6058.

196. Martin, C. F.; Stockel, E.; Clowes, R.; Adams, D. J.; Cooper, A. I.; Pis, J. J.; Rubiera, F.; Pevida, C. *J. Mater. Chem.* **2011**, 21, 5475.

197. Babarao, R.; Hu, Z. Q.; Jiang, J. W.; Chempath, S.; Sandler, S. I. *Langmuir***2007**, *23*, 659.

198. Challa, S. R.; Sholl, D. S.; Johnson, J. K. *J. Chem. Phys.* **2002**, *116*, 814.

199. Goj, A.; Sholl, D. S.; Akten, E. D.; Kohen, D. *J. Phys. Chem. B* **2002**,*106*, 8367.

200. Chen, Y.; Jiang, J. *ChemSusChem* **2010**, 3, 982

201. Bae, Y. -S.; Mulfort, K. L.; Frost, H.; Ryan, P.; Punnathanam, S.; Broadbelt, L. J.; Hupp, J. T.; Snurr, R. Q. *Langmuir* **2008,** *24,* 8592.

202. Goetz, V.; Pupier, O.; Guillot, A. *Adsorption* **2006**, *12*, 55.

203. Murthi, M.; Snurr, R. Q. *Langmuir* **2004**, *20*, 2489.

204. Wu, J. Q.; Zhou, L.; Sun, Y.; Su, W.; Zhou, Y. P. *AIChE J.* **2007**, *53*, 1178.

205. Phan, A.; Doonan, C. J.; Uriberomo, F. J.; Knobler, C. B.; O'Keeffe, M.; Yaghi, O. M. *Acc. Chem. Res*. **2010**, *43*, 58.

206. Liu, Y. H.; Liu, D. H.; Yang, Q. Y.; Zhong, C. L.; Mi, J. G. *Ind. Eng. Chem. Res.* **2010**, *49*, 2902.

207. Cao, D., Wu, J., *Carbon* **2005**, 43, 1364.

208. Maly, K. E. *J. Mater. Chem.* **2009**, 19, 1781.

209. Tilford, W. R.; Gemmil, W. R.; zur Loye, H. C.; Lavigne, J. J. *Chem. Mater.* **2006**, 18, 5296.

210. Wan, S.; Guo, J.; Kim, J.; Ihee, H.; Jiang, D. *Angew. Chem. Int. Ed.* **2008**, 47, 8826.

211. Wan, S.; Guo, J.; Kim, J.; Ihee, H.; Jiang, D. *Angew. Chem. Int. Ed.* **2009**, 48, 5439.

212. Hunt, J. R.; Doonan, C. J.; LeVangie, J. D.; Cote, A. P.; Yaghi, O. M. *J. Am. Chem. Soc.* **2008**, 130, 11872.

213. Kuhn, P.; Thomas, A.; Antonietti, M. *Macromolecules* **2009**, 42, 319.

214. Bojdys, M. J.; Jeromenok, J.; Thomas, A.; Antonietti, M. *Adv. Mater*. **2010**, 22, 2202.

215. Bojdys, M. J.; Wohlgemuth, S. A.; Thomas, A.; Antonietti, M. *Macromolecules* **2010**, 43, 6639.

216. Jiang, J. X.; Su, F.; Wood, C. D.; Campbell, N. L.; Niu, H.; Dickinson, C.; Ganin, A. Y.; Rosseinsky, M. J.; Khimyak, Y. Z.; Cooper, A. I.; Trewin, A. *Angew. Chem. Int. Ed.* **2007**, 46, 8584.

217. Dawson, R.; Su, F.; Niu, H.; Wood, C. D.; Jones, J. T. A.; Khimyak, Y. Z.; Cooper, A. I. *Macromolecules* **2008**, 41, 1591.

218. Jiang, J. X.; Su, F.; Niu, H.; Wood, C. D.; Campbell, N. L.; Khimyak, Y. Z.; Cooper, A. I. *Chem. Commun.* **2008**, 486.

219. Yuan,S.; Kirklin, S.; Dorney, B.; Liu, D. J.; Yu, L. *Macromolecules* **2009**, 42, 1554.

220. Schmidt, J.; Werner, M.; Thomas, A. *Macromolecules* **2009**, 42, 4426.

221. Xia, J.; Yuan, S.; Wang, Z.; Kirklin, S.; Dorney, B.; Liu, D. J.; Yu, L. *Macromolecules* **2010**, 43, 3325.

222. Dawson, R.; Laybourn, A.; Khimyak, Y. Z.; Adams, D. J.; Cooper, A. I. *Macromolecules* **2010,** 43, 8524.

223. Sprick, R. S.; Thomas, A.; Scherf, U. *Polym. Chem.* **2010** 1, 283.

224. Budd, P. M.; Ghanem, B. S.; Makhseed, S.; McKeown, N. B.; Msayib, K. J.; Tattershall, C. E. *Chem. Commun.* **2004,** 2, 230.

225. McKeown, N. B.; Gahnem, B.; Msayib, K. J.; Budd, P. M.; Tattershall, C. E.; Mahmood, K.; Tan, S.; Book, D.; Langmi, H. W.; Walton, A. *Angew. Chem.* **2006,** 118, 1836.

226. Kuhn, P.; Antonietti, M.; Thomas, A. *Angew. Chem.* **2008,** 120, 3499.

227. Weber, J.; Antonietti, M.; Thomas, A. *Macromolecules* **2008,** 41, 2880.

228. Schwab, M. G.; Fassbender, B.; Spiess, H. W.; Thomas, A.; Feng, X. L.; Mullen, K. *J. Am. Chem. Soc.* **2009,** 131, 7216.

229. Trewin, A.; Cooper, A. I. *Angew. Chem. Int. Ed.* **2010,** 49, 1533.

230. Klerke, A.; Christensen, C. H.; Nørskov, J. K.; Vegge, T. *J. Mater. Chem.* **2008,** 18, 2304.

231. DOE Targets for On-Board Hydrogen Storage Systems for Light-Duty Vehicles, https://www1.eere.energy.gov/hydrogenandfuelcells/storage/pdfs/targets_onboar_hydro_storage_explanation.pdf

232. Cao, X. Y.; Liu, X. H.; Zhou, X. H.; Zhang, Y.; Jiang, Y.; Cao, Y.; Cui, Y. X.; Pei, J. *J. Org. Chem.* **2004,** 69, 6050.

233. Li, Z. H.; Wong, M. S.; Tao, Y. *Tetrahedron* **2005,** 61, 5277.

234. Rathore, R.; Burns, C. L.; *Org. Synth.* **2005,** 82, 30.

235. Reichert, V. R.; Mathias, L. J. *Macromolecules* **1994,** 27, 7015.

Vita

Karl T. Jackson
Born April 16, 1984 in Petersburg, VA
U.S. Citizen

Education

Ph.D. Chemistry **Aug. 2007 to Dec. 2011**
Virginia Commonwealth Univ., Richmond, VA 23284

B.S. Chemistry **Aug. 2002 to May 2006**
Virginia State University, Petersburg, VA 23806

Work Experience

Virginia Commonwealth University
Research Assistant **May 2009 to Dec. 2011**
Teaching Assistant **Aug. 2007 to May 2009**

Dinwiddie County Public Schools
High School Chemistry and Active Physics Teacher **Aug. 2006 to Jun. 2007**

Research Experience

Virginia Commonwealth University
Research Assistant **Dec. 2007 to Dec. 2011**
(Advisor: Dr. Hani M. El-Kaderi)

Virginia State University
Advanced Laboratory. **Aug. 2005 to May 2006**
(Advisor: Dr. Colleen M. Taylor)

Competitive Honors

- Gerald and Susan Bass Scholarship (2011)
- Provost Scholarship (2002-2004)
- VSU Chemistry Departmental Scholarship (2002-2004)

Publications

1. **Jackson, K. T.**; Rabbani, M. G.; Reich, T. E.; El-Kaderi, H. M. "Synthesis of Highly Porous Borazine-Linked Polymers and Their Application to H_2, CO_2, and CH_4 Storage" *Polym. Chem.* **2011**, 2, 2775.
2. Reich, T. R.; **Jackson, K. T.**; Li, S.; Jena, P.; El-Kaderi, H. M. "Synthesis and Characterization of Highly Porous Borazine-Linked Polymers and Their Performance in Hydrogen Storage Application" *J. Mater. Chem.* **2011**, 21, 10629.
3. Kassab, R. M.; **Jackson, K. T.**; El-Kaderi, O. M.; El-Kaderi, H. M. "Nickel-Catalyzed Synthesis of Soft Nanoporous Organic Frameworks and Their Potential Use in Gas Storage Applications" *Res. Chem. Intermed.* **2011**, 7, 747.
4. Rabbani, M. G.; Reich, T. E.; Kassab, R.; **Jackson, K. T.**; El-Kaderi, H. M. " High CO_2 Uptake and Selectivity by Triptycene-Derived Benzimidazole-Linked Polymers" *Chem. Comm.* **2012** DOI**:** 10.1039/C2CC16986J.
5. Reich, T. R.; Behera, S.; **Jackson, K. T.**; Jena, P. El-Kaderi, H. M. "Highly Selective CO_2/CH_4 Gas Uptake by a Halogen-Decorated Borazine-Linked Polymer" (submitted).
6. **Jackson, K. T.**; Reich, T. E.; El-Kaderi, H. M. "Targeted Synthesis of A Microcrystalline Borazine-Linked Covalent Organic Framework" (in preparation).

Posters and Presentations

1. **Jackson, K. T.**, El-Kaderi, H. M. "Synthesis and Characterization of Porous Borazine-Linked Polymers under Solvothermal Conditions" International Symposium of Clusters and Nanostructures (ISCAN), Richmond, VA Nov. 7, 2011.
2. **Jackson, K. T.**, El-Kaderi, H. M. "Synthesis and Characterization of Highly Porous Borazine-Linked Polymers and Selected Gas Sorption Studies" ACS-Southeastern Regional Meeting, Oct. 26, 2011.
3. **Jackson, K. T.** "Development of Porous Borazine-Linked Polymers *via* Thermal Dehydrogenation of Amine-Borane Adducts" Virginia State University, April 29, 2011.
4. Reich, T. E.; **Jackson, K. T.**; Rabbani, M. G.; El-Kaderi, H. M., "Design, Synthesis, and Characterization of Multifunctional Nanoporous Organic Architectures," First United Arab Emirates Conference on Pure and Applied Chemistry (ECPAC11), American University of Sharjah, March 1-3, 2011.

Affiliations

- American Chemical Society
- Chemistry Graduate Student Organization
- Alpha Phi Alpha Fraternity, Inc